



**HAL**  
open science

# Searching for gravitational waves produced by cosmic strings in LIGO-Virgo data

Imène Belahcene

► **To cite this version:**

Imène Belahcene. Searching for gravitational waves produced by cosmic strings in LIGO-Virgo data. Cosmology and Extra-Galactic Astrophysics [astro-ph.CO]. Université Paris Saclay (COMUE), 2019. English. NNT : 2019SACLS406 . tel-02878783

**HAL Id: tel-02878783**

**<https://theses.hal.science/tel-02878783>**

Submitted on 23 Jun 2020

**HAL** is a multi-disciplinary open access archive for the deposit and dissemination of scientific research documents, whether they are published or not. The documents may come from teaching and research institutions in France or abroad, or from public or private research centers.

L'archive ouverte pluridisciplinaire **HAL**, est destinée au dépôt et à la diffusion de documents scientifiques de niveau recherche, publiés ou non, émanant des établissements d'enseignement et de recherche français ou étrangers, des laboratoires publics ou privés.

# Searching for gravitational waves produced by cosmic strings in LIGO-Virgo data

Thèse de doctorat de l'Université Paris-Saclay  
préparée à l'Université Paris-Sud

École doctorale n°576 Particules, Hadrons, Énergie, Noyau,  
Instrumentation, Imagerie, Cosmos et Simulation (PHENIICS)

Spécialité de doctorat: Astroparticules et Cosmologie

Thèse présentée et soutenue à Orsay, le 25 Octobre 2019, par

NNT: 2019SACLS406

**Imène Belahcene**

Composition du Jury :

Marie-Hélène Schune Directeur de recherche, LAL (UMR8607)	Président
Christophe Ringeval Associate Professor, IRMP	Rapporteur
Ed Porter Directeur de recherche, APC (UMR7164)	Rapporteur
Danièle Steer Professeur, APC (UMR7164)	Examineur
Tania Regimbau Directeur de recherche, LAPP (UMR5814)	Examineur
Patrice Hello Professeur, LAL (UMR8607)	Directeur de thèse
Florent Robinet Chargé de recherche, LAL (UMR8607)	Co-Directeur de thèse

Searching for gravitational waves produced by cosmic  
strings in LIGO-Virgo data.

Belahcene Imène

# Contents

<b>Remerciements</b>	<b>5</b>
<b>Synthèse</b>	<b>8</b>
<b>Introduction</b>	<b>20</b>
<b>1 Gravitational waves</b>	<b>23</b>
1.1 General Relativity	24
1.1.1 Geometry in General Relativity	24
1.1.2 The Einstein equations	25
1.2 Linearized General Relativity	28
1.3 Gravitational waves in vacuum	29
1.3.1 Generalities	29
1.3.2 Example	30
1.3.3 Gravitational-wave effects on matter	31
1.4 Gravitational-wave generation	32
1.5 Gravitational waves sources	36
1.5.1 Continuous waves	37
1.5.2 Gravitational wave bursts	38
1.5.3 Stochastic gravitational wave background	39
<b>2 Gravitational Wave Detectors</b>	<b>41</b>
2.1 History	41
2.1.1 The Role of the 1957 Chapel Hill Conference	41
2.1.2 The first gravitational wave detectors: Weber bars	42
2.2 Interferometric gravitational-wave detectors	44
2.2.1 Detection principle	44
2.2.2 Angular response	47
2.3 Fundamental noise sources	49
2.3.1 Shot noise	50
2.3.2 Radiation pressure noise	51

2.3.3	Seismic noise	52
2.3.4	Thermal noise	53
2.4	Current ground-based detectors network	53
2.4.1	Virgo and Advanced Virgo	53
2.4.2	LIGO and Advanced LIGO	59
2.4.3	Observing Runs	60
2.4.4	Detections	64
2.5	Data Quality	66
2.5.1	Glitches	67
2.5.2	Vetoos	70
2.5.3	Data quality tools	71
<b>3</b>	<b>Cosmic Strings</b>	<b>75</b>
3.1	The standard cosmological model	75
3.1.1	The cosmological principle	75
3.1.2	The FLRW metric	75
3.1.3	The Friedmann equations	76
3.1.4	A brief history of the Universe	81
3.2	Cosmic strings	83
3.2.1	Spontaneous symmetry breaking	83
3.2.2	The Nielsen-Olesen string formation	87
3.2.3	Phase transition	90
3.2.4	The Nambu-Goto action	92
3.2.5	String dynamic	94
3.2.6	Intercommutation	97
3.2.7	Cusps and Kinks	99
3.3	Gravitational waves emitted by cosmic strings	102
3.3.1	Waveform from cusps and kinks	102
3.3.2	Propagation in an expanding space	104
3.3.3	Radiation power from a loop	104
3.4	Other observational signatures of cosmic strings	105
3.4.1	Gravitational properties of cosmic strings	106
3.4.2	Gravitational lensing	107
3.4.3	CMB anisotropies	108
<b>4</b>	<b>Cosmic String analysis for O1/O2</b>	<b>111</b>
4.1	O1 and O2 data set	113
4.2	Detecting gravitational-wave with matched filter	114
4.3	Power spectral density estimation	118
4.4	Searching for cosmic strings with templates	119
4.4.1	Search with one template	119
4.4.2	Search with a set of templates	121
4.4.3	$\chi^2$ consistency test	122
4.5	Trigger selection	124

4.6	Time coincidence between triggers	127
4.6.1	The zero-lag	127
4.6.2	Background estimation	129
4.7	Ranking Statistic	131
4.7.1	Bayesian coincidence test	131
4.7.2	Signal sample	132
4.7.3	Probability density functions	133
4.8	Data quality	137
4.8.1	The impact of data quality flags	138
4.8.2	Background event identification	141
4.8.3	UPV	142
4.8.4	Highest ranked background events	143
4.9	O1 results	144
4.9.1	Cusp and kink search	144
4.9.2	Search sensitivity	146
4.10	O2 analysis	147
4.10.1	Results	148
4.10.2	Search using Advanced Virgo data	149
<b>5</b>	<b>Upper limits on cosmic string parameters</b>	<b>154</b>
5.1	Loop distribution models	154
5.1.1	String network in a FLRW Universe	155
5.1.2	Model 1	157
5.1.3	Model 2	159
5.1.4	Model 3	160
5.2	The rate of bursts	164
5.3	Stochastic gravitational-wave background	169
5.4	Results	173
5.4.1	Constraints	174
5.4.2	O1/O2 results	176
5.5	Searching for kink-kink collisions	180
5.5.1	Burst search	180
5.5.2	Constraints	181
	<b>Conclusion and prospects</b>	<b>186</b>
	<b>Bibliography</b>	<b>190</b>

# Remerciements

Tout d'abord, je souhaite exprimer ma gratitude envers les rapporteurs de cette thèse, Ed Porter et Christophe Ringeval, qui ont pris le temps nécessaire pour l'évaluer justement, ainsi que les examinatrices, Danièle Steer et Tania Regimbau, en particulier pour les discussions intéressantes que nous avons pu avoir. Je suis reconnaissante à Marie-Hélène Schune d'avoir pris en charge la présidence du jury, mais aussi pour tout les conseils pertinents et avisés qu'elle m'a donnée, ainsi que pour sa générosité.

Je remercie Florent Robinet qui a eu la patience de m'avoir encadrée durant cette thèse, avec la rigueur qui lui est associée. Je lui suis reconnaissante pour sa disponibilité de chaque instant, il a toujours été prêt à répondre à mes questions, à partager avec moi ses compétences, et aussi à me soutenir avant chaque présentation que j'ai pu donner. De plus, grâce à ses nombreuses relectures il a pu rendre ce manuscrit compréhensible, tant du point de vue du fond que de la forme. Je remercie également Patrice Hello, aussi bien pour avoir pris le temps de lire et de corriger ce manuscrit que pour son soutien, et plus spécialement pour la qualité de ses commentaires sur la Physique toujours intéressants et pertinents.

Merci à l'ensemble du groupe Virgo à Orsay. En particulier, Nicolas pour sa bonne humeur, et ses réponses claires à mes nombreuses questions sur un peu tout, Marie-Anne pour ses nombreux conseils, toujours intéressants aussi bien d'un point de vue scientifique qu'humain. Je remercie les "jeunes", Pierre pour son grand optimisme et pour m'avoir fait bien rire, Jean Gregoire pour ses petits gateaux et ses drôles de commentaires, David pour ses bon conseils et ses encouragements. Je n'oublie pas de remercier les autres membres du groupe, Fabien, Angélique, Sarah, Nicolas A., David C., Shaymaa, Pierre Alexandre, Valentin et Tito. Je remercie également Sylvie Teullet pour l'assistance dans mes missions, et sa belle énergie.

Mes remerciements vont aussi vers ceux qui m'ont enseigné la Physique pendant mes études, en particulier, Pierre Binétruy, Sylvain Chaty, Nathalie Deruelle, Éric

## *Remerciements*

---

Gourgoulhon, Éric Huguet, Jacques Le Bourlot et Jihad Mourad. Ainsi que vers tous ceux qui se sont donnés la peine d'écrire des livres scientifiques d'une belle qualité, faisant le travail de fond essentiel à toute transmission du savoir.

J'ai une pensée émue pour mes amis, je pense tout particulièrement à Adèle, Antoine, Bernardo, Eric, Eslam, Gaspard, Hanna, Julien, Marie, Mikel, Tijani, Thiebaut, Thomas et Stefano. Merci pour votre soutien.

Mes derniers remerciements vont vers ma famille. À ma mère, Abla, pour m'avoir donné le gout des mathématiques et de la physique depuis mon plus jeune age. À mon père, Kamel, pour sa grande sagesse, et pour m'avoir toujours soutenue et pour m'avoir donné tout ce dont j'avais besoin. Sans oublier mes deux plus jolies petites soeurs, Meriem et Leila, pour avoir toujours cru en moi.

*Remerciements*

---

# Synthèse

Les ondes gravitationnelles sont l'une des prédictions de la théorie de la Relativité Générale d'Einstein. Les ondes gravitationnelles sont des solutions de ses équations qui correspondent à des perturbations de l'espace-temps se propageant à la vitesse de la lumière. La gravitation étant très faible en intensité, de telles ondes sont très difficiles à détecter. Grâce à cette même propriété, les ondes gravitationnelles sont un messager direct des sources les plus compactes de l'Univers, car elles se propagent à travers l'espace, sans être dispersées ou absorbées par la matière intermédiaire, contrairement aux ondes électromagnétiques qui constituent la lumière. Même des phénomènes extrêmement puissants n'engendrent que des amplitudes d'ondes gravitationnelles très faibles. Ainsi, il a fallu développer des instruments extrêmement sensibles: les détecteurs LIGO et Virgo. Les ondes gravitationnelles ont été détectées pour la première fois de façon directe le 14 septembre 2015, par ces mêmes expériences. Depuis, plusieurs dizaines de détections ont été faites ouvrant la voie à une astronomie multi-messagers.

Cette thèse est dédiée à l'analyse des données des détecteurs d'ondes gravitationnelles de seconde génération Advanced LIGO et Advanced Virgo. En particulier nous nous intéressons à la détection d'ondes gravitationnelles qui pourraient être émises par des structures à une dimension créées dans l'Univers primordial: les cordes cosmiques. Ces objets ont une densité d'énergie particulièrement élevée et vibrent à des vitesses relativistes, ce qui indique qu'elles sont une source naturelle d'ondes gravitationnelles. Au terme des analyses, aucune signature d'ondes gravitationnelles correspondant à celle attendue pour les cordes cosmiques n'a pu être identifiée. Cependant, grâce à ce travail, nous avons pu déterminer des limites sur les différents paramètres caractérisant les cordes cosmiques afin de préciser les conditions d'existence de ces dernières.

## **Propriétés des ondes gravitationnelles**

La théorie de la Relativité Générale décrit le mouvement d'objets sous l'influence de l'interaction gravitationnelle. À la différence de la mécanique galiléenne, la Relativité générale affirme que le temps et l'espace sont inextricablement liés en un

seul continuum appelé “espace-temps”. La géométrie de l’espace-temps est décrite par la métrique, qui définit le concept de distance entre deux points. La masse-énergie courbe l’espace et en retour la courbure de l’espace détermine comment les objets se déplacent. Les équations d’Einstein:

$$G_{\alpha\beta} = \frac{8\pi G}{c^4} T_{\alpha\beta}, \quad (1)$$

décrivent la structure de l’espace-temps en incluant le mouvement des objets. Le tenseur d’Einstein  $G_{\alpha\beta}$  est seulement fonction de la métrique et de ses deux premières dérivées spatio-temporelles, alors que le tenseur énergie-impulsion  $T_{\alpha\beta}$  est le terme source qui décrit la distribution de masse-énergie, d’impulsion et de tension dans l’Univers.

Les équations d’Einstein sont non linéaires, et par conséquent il n’existe pas de solution analytique générale pour une distribution quelconque de matière. Cependant, dans la limite d’un champ faible, c’est-à-dire un espace quasiment plat et sans source de champ gravitationnel, ces équations peuvent être linéarisées. On peut utiliser l’invariance de jauge, pour choisir une jauge dite “harmonique” ou jauge de Lorenz, pour réécrire les équations d’Einstein sous la forme d’une équation d’onde. Dans ces conditions, les solutions sont appelées ondes gravitationnelles. Une onde gravitationnelle est décrite par deux degrés de liberté ou états de polarisation. Les deux polarisations linéaires se distinguent par leur effet sur un cercle de masses libres, le plan du cercle étant perpendiculaire à la direction de propagation de l’onde. Une onde polarisée “plus” déforme le cercle en une ellipse qui est périodiquement compressée dans une direction et étirée dans l’autre. Une onde polarisée “croix” a le même effet, mais suivant une direction tournée de  $45^\circ$ . Toutes les combinaisons linéaires de ces deux polarisations sont possibles. Ainsi, le passage d’une onde gravitationnelle engendre une variation de distance entre deux points.

Les équations d’Einstein décrivent aussi les mécanismes de génération d’ondes gravitationnelles par des masses en mouvement. Dans ce cadre, si l’on se situe suffisamment loin de la source et que celle-ci possède une vitesse bien inférieure à celle de la lumière, l’émission des ondes gravitationnelles est bien décrite par l’évolution du moment quadrupolaire de ces masses. L’amplitude d’un rayonnement quadrupolaire est beaucoup plus faible que celle d’un rayonnement dipolaire et ceci, associé au couplage faible de la matière à la gravité, justifie que l’amplitude d’un rayonnement gravitationnel est typiquement beaucoup plus petite qu’un rayonnement électromagnétique. De plus, l’émission quadrupolaire à l’ordre le plus bas implique une brisure de la symétrie sphérique de la source pour émettre des ondes gravitationnelles.

Les seules ondes gravitationnelles que l’on peut espérer détecter sont celles provenant de sources astrophysiques. Ces sources peuvent être classées en familles, selon la morphologie du signal qu’elles émettent. En particulier, les signaux transitoires qui durent de quelques millisecondes à quelques secondes, sont émis par des phénomènes cataclysmiques comme l’effondrement du cœur d’une étoile en fin de vie ou la fusion de trous noirs. Les signaux continus et stables par rapport à l’échelle de la durée d’observation, sont émis par exemple par les pulsars. La superposition incohérente

d'ondes gravitationnelles émises par l'ensemble des sources transitoires et continues constituent un fond de rayonnement gravitationnel stochastique. De plus, la génération d'ondes gravitationnelles dans l'Univers primordial, nous parviendrait aujourd'hui aussi sous la forme d'un fond, similaire au rayonnement de fond diffus cosmologique dans le domaine électromagnétique. Le fond stochastique d'ondes gravitationnelles n'a toujours pas été détecté, mais pourra entre autres, permettre de "sonder" l'Univers primordial.

### Détecteurs d'ondes gravitationnelles

Le passage d'une onde gravitationnelle modifie la distance entre deux masses libres. La variation de distance relative est proportionnelle à l'amplitude de l'onde gravitationnelle. C'est sur cet effet que repose le principe de détection des détecteurs interférométriques d'ondes gravitationnelles Virgo et LIGO. Le concept de base est celui de l'interféromètre de Michelson. Pour que l'interféromètre soit utilisé en tant que détecteur d'ondes gravitationnelles, il faut que les miroirs soient suspendus. Ainsi, ils peuvent être considérés comme des masses libres dans le plan horizontal du détecteur pour des ondes gravitationnelles de fréquence large devant la fréquence de résonance des suspensions. Une onde gravitationnelle qui se propage perpendiculairement au plan de l'interféromètre, alternativement, allonge un bras de l'interféromètre et raccourcit l'autre. Les interférences des deux faisceaux lumineux se trouvent ainsi modifiées. Une onde gravitationnelle est détectée comme une variation de puissance mesurée en sortie de l'interféromètre.

On peut assimiler un détecteur interférométrique à une antenne possédant une réponse angulaire qui dépend de la position de la source dans le ciel et qui diffère pour chacune des polarisations. L'amplitude de l'onde gravitationnelle mesurée par un détecteur est une combinaison linéaire des facteurs d'antenne qui représentent la réponse angulaire du détecteur. La réponse est optimale quand l'onde arrive perpendiculairement au plan du détecteur, et nulle quand celle-ci se propage selon les bissectrices du détecteur.

Un interféromètre de Michelson de base n'a pas la sensibilité pour mesurer des différences de longueurs relatives de l'ordre de  $10^{-21}$  m. Plusieurs améliorations ont été nécessaires pour construire les détecteurs Virgo et LIGO.

De plus, les ondes gravitationnelles ne sont pas le seul phénomène physique induisant une fluctuation de la puissance transmise par l'interféromètre. Pour évaluer les performances d'un détecteur, c'est-à-dire sa sensibilité, il faut comparer sa réponse à une onde gravitationnelle aux nombreux bruits qui limitent la mesure. Par exemple, la précision de la mesure de la puissance transmise par l'interféromètre est, entre autres, limitée par les fluctuations quantiques du nombre de photons détecté par une photodiode pour une puissance incidente donnée.

Les détecteurs LIGO et Virgo se sont arrêtés plusieurs années pour une mise à jour majeure pour donner naissance à la seconde génération de détecteurs: Advanced LIGO et Advanced Virgo. Ces développements ont conduit à une augmentation significative de la sensibilité des détecteurs. La première prise de données (O1)

a débuté en septembre 2015, où Advanced LIGO a recueilli des données jusqu'en janvier 2016. C'est pendant cette période qu'on a été détecté pour la première fois de façon directe, des ondes gravitationnelles émises par la coalescence de trous noirs, GW150914. La seconde période d'observation (O2) commence en Novembre 2016 et se termine en Août 2017. Advanced Virgo a rejoint les détecteurs Advanced LIGO durant le dernier mois. Cette période est riche en détections, en particulier avec la première détection d'ondes gravitationnelles émises par la coalescence d'étoiles à neutrons, GW170817. L'ajout d'Advanced Virgo au réseau des détecteurs a joué un rôle crucial sur la localisation de la source.

Les données des détecteurs sont largement contaminées par des bruits transitoires appelés "glitches", qui dégradent la sensibilité des recherches de signaux d'ondes gravitationnelles, en particulier pour les signaux transitoires d'ondes gravitationnelles ou "bursts". Les bruits transitoires peuvent provenir de nombreuses sources, et il est nécessaire de comprendre leurs origines afin de les supprimer des données. Pour ce faire, les détecteurs sont surveillés par un millier de sondes, et différents outils ont été développés pour identifier et classifier ces bruits transitoires. Grâce à l'identification de familles de bruit transitoires, on génère des data quality flags qui marquent certaines périodes de temps de prise de données comme étant du bruit. Une partie du travail de cette thèse a été consacrée à la compréhension de ces bruits transitoires dans Advanced Virgo. En particulier, pour les détections pendant la seconde période d'observation (O2), j'ai vérifié qu'il n'y a pas de corrélation entre l'évènement détecté et les sondes auxiliaires. J'ai par la suite isolé et caractérisé tous les bruits transitoires autour de chaque évènement dans une fenêtre temporelle de  $\pm 5$  min. Ce travail a été utilisé pour s'assurer que ces bruits transitoires n'avaient pas d'incidence sur la localisation de la source et l'estimation des paramètres de l'évènement.

## Les cordes cosmiques

L'Univers en se refroidissant subit une série de transitions de phase, qui peuvent conduire à des brisures spontanées de symétrie dans l'Univers primordial. Kibble a été le premier à montrer que des défauts topologiques du vide formés lors de ces transitions de phase pouvaient survivre au cours de l'évolution de l'Univers. Les cordes cosmiques sont des défauts topologiques unidimensionnels étendus sur des distances cosmologiques prédits dans de nombreux modèles de physiques de très hautes énergies. L'énergie par unité de longueur d'une corde cosmique,  $\mu$ , est donnée par la température à laquelle la transition de phase se produit  $\mu \sim T_c^2$ . Ainsi, des cordes formées dans l'Univers primordial, encore très chaud, sont caractérisées par une énergie extrêmement élevée. La dynamique d'un réseau de cordes cosmiques est donnée par l'action de Nambu-Goto dans le cas de cordes infiniment fines. L'interaction des cordes cosmiques entre elles conduit à la formation de boucles qui oscillent de façon périodique au cours du temps. Le mouvement de ces boucles est relativiste. La tension d'une corde de Nambu-Goto est égale à son énergie

par unité de longueur  $\mu$  et force toute corde cosmique qui n'est pas complètement droite à se déplacer relativistiquement. Il est très courant dans la littérature de se référer à la quantité sans dimension  $G\mu/c^2$  comme étant la tension de la corde. Les simulations numériques de l'évolution d'un réseau de cordes montrent que les cordes échangent toujours leurs branches lorsqu'elles se croisent. Ce mécanisme est appelé intercommutation. Les développements de la théorie des cordes suggèrent que les cordes fondamentales peuvent être étirées à des tailles macroscopiques et jouer le rôle de super cordes cosmiques. La différence majeure avec les cordes cosmiques topologiques est que lorsqu'elles se rencontrent, elles se reconnectent avec une probabilité  $p$  qui peut être inférieure à l'unité. Une des conséquences majeures du mécanisme d'intercommutation, est la formation incessante de boucles de cordes cosmiques. Le mouvement d'oscillation des boucles peut conduire à l'apparition de points de rebroussement dans la forme de la corde ou "cusps", qui se propagent à la vitesse de la lumière. Un autre type de discontinuités, apparaît lors de l'intercommutation des cordes autour du point d'échange. Ces discontinuités, qui ressemblent à un "coin" sur les boucles de cordes cosmiques sont appelées "kinks". Les "cusps" et "kinks" émettent des puissants sursauts d'ondes gravitationnelles dont la forme d'onde a été déterminée par Damour et Vilenkin. La région d'émission d'onde gravitationnelle est conique. Un autre type de sursauts est engendré par la rencontre de deux "kinks" qui se propagent dans des directions opposées. Dans ce cas, il s'agit d'une émission dans toutes les directions de l'espace. Mais les cordes cosmiques peuvent également être la source d'autres phénomènes observables, comme des phénomènes de lentilles gravitationnelles, des variations dans le fond diffus cosmologique, ou encore des émissions de rayons cosmiques à haute énergie.

### Analyse des données-Résultats

Les données récoltées par un détecteur interférométrique se présentent sous la forme d'une série temporelle:

$$s(t) = n(t) + h(t). \quad (2)$$

Le but de l'analyse de données des détecteurs d'ondes gravitationnelles est de déceler le signal  $h(t)$  qui serait éventuellement caché dans les données  $s(t)$  par le bruit  $n(t)$ . La forme attendue de l'onde gravitationnelle émise par des cordes cosmiques est bien connue. On appelle "template" un modèle de la forme de l'onde gravitationnelle prédite par la théorie. La chaîne d'analyse ou "pipeline", dédiée à la recherche de sursauts d'ondes gravitationnelles produites par des cordes cosmiques utilise la technique de filtrage adapté pour détecter la présence d'un signal dans les données. Cette méthode consiste à faire la corrélation croisée entre le signal mesuré par le détecteur et un template du signal attendu. Pour détecter la présence d'un signal dans du bruit et mesurer son intensité, il faut un outil: le rapport signal sur bruit ("Signal to Noise Ratio", SNR). Si le SNR est grand, cela indique qu'autre chose que du bruit seul est présent dans les données. On applique ainsi un seuil sur le SNR afin de discriminer un vrai signal d'ondes gravitationnelles d'un bruit. Une partie de mon travail à consister à étudier la distribution des événements qui ont passé un

seuil fixé de SNR ou “triggers”. Pour un bruit gaussien, en l’absence de signal caché, la distribution de SNR sera distribuée selon une gaussienne. La figure. 1 représente une distribution typique obtenue lors des analyses conduites. Cette distribution n’est pas gaussienne, on note la présence d’une queue d’évènements à haut SNR. En effet, la technique de filtrage adapté est optimale si le bruit du détecteur est gaussien et stationnaire, ce qui n’est pas le cas. J’ai étudié la distribution des “triggers” à la sortie de cette première étape du pipeline. Le but de ce travail est d’ajuster le seuil en SNR pour pouvoir discriminer au mieux le signal du bruit. Chaque “trigger” est décrit par un ensemble de paramètres. Une grande partie du travail sur les distributions d’évènements a été consacrée à la réduction des queues d’évènements non gaussiennes. Ce travail a permis d’identifier des familles de bruits transitoires et de les supprimer des données dans la suite de l’analyse.

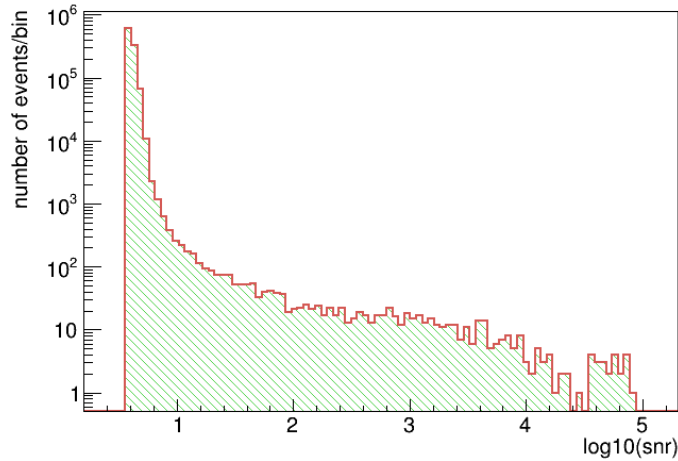


Figure 1: Distribution statistique du SNR pour les triggers dans H1 pendant O1.

Contrairement à un évènement de bruit, un signal d’onde gravitationnelle doit être observé de façon corrélée dans un intervalle de temps court dans les différents interféromètres. On peut donc chercher des évènements en coïncidence temporelle entre plusieurs détecteurs, afin de réduire les bruits transitoires qui peuvent imiter un signal de corde cosmique. La fenêtre de coïncidence est suffisamment large pour tenir compte non seulement du temps maximal de propagation de l’onde gravitationnelle entre les détecteurs, mais aussi de la durée du signal et de l’incertitude temporelle.

Enfin pour améliorer le pipeline, on utilise une technique bayésienne pour distinguer les vrais signaux des évènements de bruit. On calcule un rapport de vraisemblance (likelihood ratio)  $\Lambda(\vec{x})$ , où  $\vec{x}$  représente l’ensemble des paramètres utilisés pour décrire un évènement coïncident. Cette fonction augmente de façon monotone avec la probabilité qu’un évènement coïncident soit le résultat d’une onde gravitationnelle. On peut ainsi classer les évènements coïncidents du plus probable au moins probable

d’être une onde gravitationnelle.

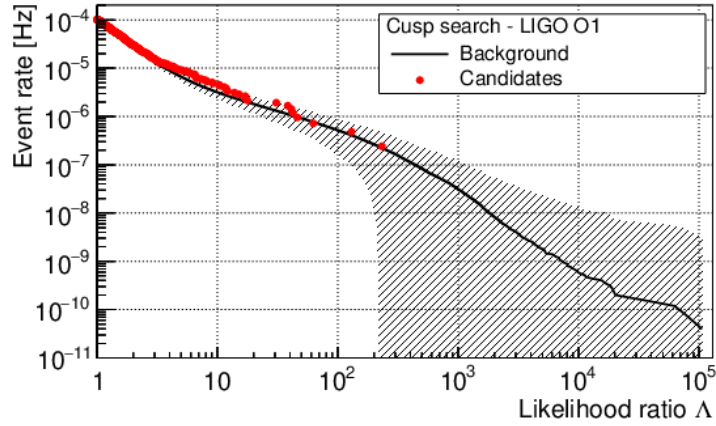
Pour estimer l’importance d’un candidat, nous devons caractériser le bruit des détecteurs d’ondes gravitationnelles qui n’est ni gaussien ni stationnaire. Pour cela, on va décaler temporellement d’une certaine durée (méthode des time-slides) les données des détecteurs. Un éventuel signal de cordes cosmiques ne sera ainsi plus coïncident dans les détecteurs. En augmentant plusieurs fois le décalage temporel, on obtient plusieurs lots de données de bruits indépendants les uns des autres qu’on utilise pour estimer la distribution du bruit de fond. L’étude de la distribution du bruit de fond permet de caractériser entièrement notre analyse.

Enfin, en l’absence de détection on détermine la sensibilité de notre analyse aux signaux recherchés, en ajoutant dans les données des formes d’ondes gravitationnelles simulées. L’efficacité de la recherche est ainsi définie comme la fraction de signaux de cordes cosmiques simulés retrouvés par la chaîne d’analyse.

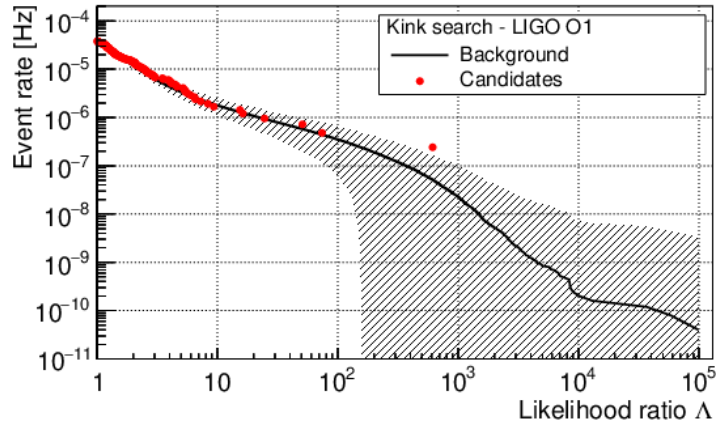
## Résultats

J’ai cherché des sursauts d’ondes gravitationnelles produits par des “cusps” ou des “kinks” dans les données collectées lors de la première période d’observation des détecteurs Advanced LIGO. J’ai conduit deux analyses distinctes en parallèle. La période analysée correspond à un total de 49 jours, où les deux détecteurs fonctionnaient simultanément. Une partie essentielle de ce travail a consisté à comprendre et réduire le bruit des détecteurs. Pour cela j’ai testé séparément l’impact de tous les data quality flags sur la distribution d’évènements coïncidents fortuits (bruit de fond de l’analyse). À chaque fois que j’ai appliqué une liste de data quality flags sur les données, j’ai relancé l’analyse et j’ai étudié à nouveau la distribution d’évènements coïncidents fortuits qui a été modifiée. Ce travail est itératif. Grâce à cela, j’ai pu améliorer la sensibilité des analyses en minimisant le risque de supprimer un candidat des données. J’ai ensuite conduit une étude détaillée sur une large partie des événements de la queue de la distribution du bruit de fond de l’analyse. J’ai utilisée des méthodes différentes afin d’isoler et d’identifier les familles de bruits qui limitent la recherche. En particulier, j’ai montré que la recherche est largement limitée par un type particulier de bruits transitoires qui sont semblables au signal attendu des cordes cosmiques: les “blip glitches”. Avec la liste de “blip glitches” trouvées, j’ai essayé de comprendre l’origine de ces bruits en cherchant des corrélations dans toutes les canaux auxiliaires. Aucune corrélation significative n’a été mise en évidence.

Pour les deux recherches (“cusps” et “kinks”), il n’y a pas de candidats qui s’écartent de manière significative de la distribution de bruit, cf. Fig 2. L’évènement le mieux classé est mesuré avec un rapport de vraisemblance  $\Lambda_h = 232$  pour la recherche des “cusps” et  $\Lambda_h = 611$  pour la recherche des “kinks”, associé à un taux de fausse alarme  $\text{FAR}_{O1} = 2.40 \times 10^{-7}$  Hz. Une enquête sur ces événements montre qu’ils semblent appartenir à la famille des “blip glitches”. En l’absence de détection,



(a)



(b)

Figure 2: En rouge, la distribution cumulative du nombre d'évènements en fonction de la statistique  $\Lambda$  pour l'analyse des (a) cusps (b) kinks (O1). L'estimation du bruit de fond est représentée par la courbe noire, avec une erreur de  $1\sigma$  illustrée par la zone hachurée.

j'ai estimé la sensibilité de la recherche définie comme la fraction de signaux simulés retrouvés avec  $\Lambda > \Lambda_h$ , cf. Fig x3. Il est intéressant de comparer la courbe de sensibilité des “cusps” à celle obtenue dans l'analyse précédente lors des périodes d'observations S5/S6 (2005-2010) pour un même taux de fausse alarme. La sensibilité de la recherche est améliorée d'un facteur 10. Ce gain en sensibilité s'explique par l'amélioration significative de la sensibilité à basse fréquence des détecteurs Advanced LIGO.

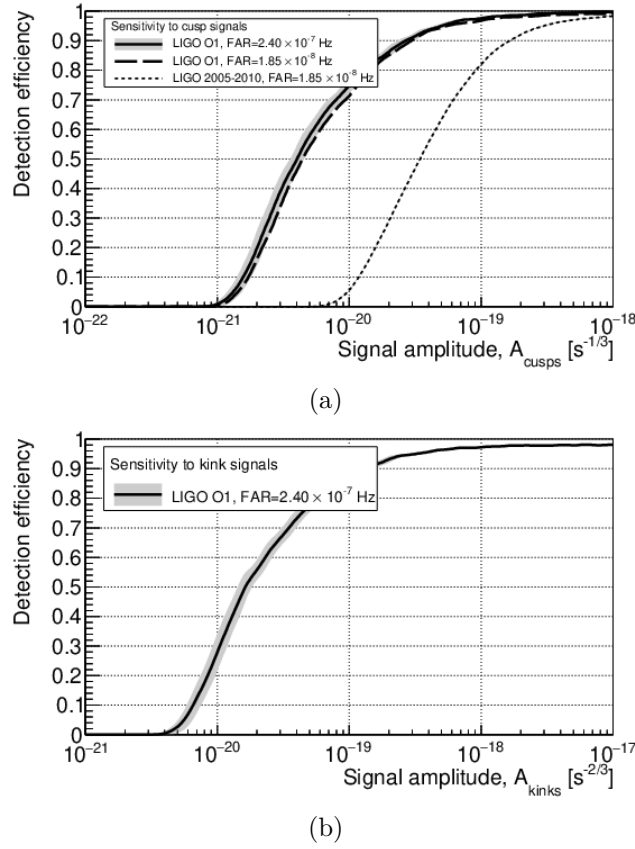


Figure 3: Sensibilité de la recherche en fonction de l'amplitude du signal pour les (a) cusps (b) kinks.

De façon similaire j'ai conduit une recherche d'ondes gravitationnelles produites par des "cusps", en utilisant les données de la seconde période d'observation d'Advanced LIGO. La période analysée correspond à un total de 155.9 jours. Mon travail sur la qualité des données a permis d'augmenter la sensibilité de la recherche. Aucun signal n'a été détecté, cf Fig. 4. En parallèle, j'ai également effectué une recherche à trois détecteurs à l'aide des données recueillies par Advanced Virgo en août 2017, correspondant à un total de 17 jours de données. J'ai montré que malgré le fait que les blip glitches sont bien compris dans Virgo, il ne limitent pas la recherche. Mon étude sur la qualité des données dans Virgo a permis d'augmenter la sensibilité de la recherche de façon significative à haute amplitude. Mais, j'ai montré qu'inclure Virgo dans l'analyse semble légèrement dégrader la sensibilité de la recherche à basse amplitude. Ceci est dû à la faible sensibilité de Virgo par rapport à celle des détecteurs LIGO. Finalement, j'ai estimé la sensibilité de la recherche en combinant cette fois les données des deux périodes d'observations (O1 et O2), cf. 4.

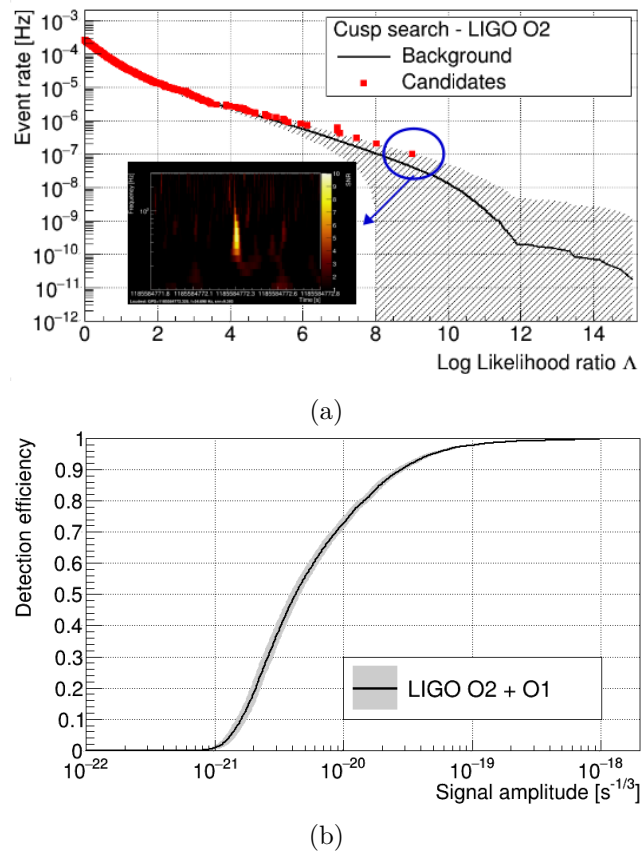


Figure 4: (a) En rouge, la distribution cumulative du nombre d'évènements en fonction de la statistique  $\Lambda$  pour l'analyse des cusps (O2). L'estimation du bruit de fond est représentée par la courbe noire, avec une erreur de  $1\sigma$  illustrée par la zone hachurée. (b) Sensibilité de la recherche en fonction de l'amplitude du signal pour les cusps.

### Contraintes-Résultats

Nous avons vu qu'un réseau de cordes cosmiques formé dans l'Univers primordial est d'abord caractérisé par la tension des cordes  $G\mu/c^2$ . Un autre paramètre est la probabilité d'intercommutation (avec  $p < 1$  pour les super cordes cosmiques). En l'absence de détection, j'ai pu contribuer à poser des limites sur ces deux paramètres en utilisant les courbes d'efficacité obtenues lors des analyses. Il était important et nécessaire de dériver le taux de sursauts d'ondes gravitationnelles produit par des cordes cosmiques. À cette fin, trois modèles qui prédisent la distribution de boucles de cordes cosmiques: M=1, M=2 et M=3 ont été considérés. Les modèles M=1 et M=2 sont assez similaires, mais diffèrent par des facteurs de normalisation. La conséquence est que le modèle M=2 prédit une distribution de boucles plus faible que celle du modèle M=1. Le modèle M=3 est très différent des autres, et fait

intervenir une physique plus complexe. C'est le modèle qui prédit la distribution de boucle la plus grande, en particulier pour les très petites boucles de cordes cosmiques. Pour cette raison, l'analyse de sursauts d'ondes gravitationnelles a pu contraindre ce modèle pour les cordes topologiques ( $p=1$ ) avec  $G\mu < 8.5 \times 10^{-10}$ . Nous avons mis à jour ces résultats lors de l'analyse de la seconde période de prise de données d'Advanced LIGO et d'Advanced Virgo avec  $G\mu < 4.2 \times 10^{-10}$  pour le modèle  $M=3$ . De plus, un nouveau type d'émission d'ondes gravitationnelles a été étudié. En effet, quand il y a plus d'un "kink" par oscillation de boucles, les "kinks" peuvent se rencontrer et produire un sursaut d'onde gravitationnelle. Par comparaison avec l'émission produite par un "cusp" ou un "kink", cette émission est isotrope. J'ai ajouté cette nouvelle forme d'onde à la chaîne d'analyse et j'ai analysé les données de la première et de la seconde période d'observation d'Advanced LIGO et Advanced Virgo. Grâce à ces résultats, j'ai posé des limites sur un nouveau paramètre: le nombre de "kinks"  $N_k$  par oscillation de boucle. J'ai montré que l'analyse de sursauts d'ondes gravitationnelles émis par les cordes cosmiques n'est pas assez sensible pour poser des contraintes fortes sur ce paramètre. Ces résultats posent les fondations de l'analyse future de la troisième période d'observation des détecteurs de seconde génération.



# Introduction

The notion of gravitational waves begins with the confirmation of the existence of electromagnetic waves in 1887 by Heinrich Hertz. However, a mathematical derivation of gravitational waves was only possible thanks to the formulation of the theory of General Relativity in 1915. One year later, Einstein postulated the existence of gravitational waves in 1916. Nevertheless, the physical reality of a gravitational-wave solution of Einstein equations was not showed until the Chapel Hill conference in 1957. It was at this point that a young physicist, Joseph Weber, decided to design the first gravitational-wave detector. Gravitational interaction is very weak, and gravitational waves have only tiny effects on matter. On the other hand, it is this same property that makes the gravitational-wave study so important. Indeed, this allows gravitational waves to be a direct messenger of the most compact sources in the Universe, as they propagate essentially unscathed through space, without being scattered or absorbed from intervening matter. The first evidence for their existence is due to the work of 1993 Nobel laureates Joseph Taylor and Russell Hulse. While this observation did not directly detect gravitational waves, it pointed to their existence.

In the early seventies Robert L. Forward (former student of Joseph Weber) built the first prototype of a laser interferometer (with 8.5m long arms) and Rainer Weiss laid the groundwork with the first design study of a real interferometric detector. This led to the development of the LIGO detectors. In parallel, Alain Brillet initiated the development of a European project of a gravitational-wave detector, the Virgo interferometer. The first generation of ground-based interferometric gravitational-wave detectors LIGO and Virgo stopped to take data in 2011 without making any detection. In order to improve the sensitivity of these detectors, a series of upgrades have led to the second generation of detector: Advanced LIGO and Advanced Virgo. Finally, on September 2015, gravitational waves emanating from a binary black hole coalescence, were finally detected during the first observing run of Advanced LIGO. A bit later, on August 2017, the LIGO-Virgo gravitational-wave network registered a gravitational-wave signal from the inspiral of neutron stars. Since then, several other detections have been made. This marks the dawn of a

new era in astronomy, opening an original window with which to observe the Universe.

The existence of cosmic strings has been proposed in the mid-seventies by Tom W.B. Kibble. These are one-dimensional topological defects; structures of extremely high energy density with infinitesimal widths and lengths of cosmological size. Kibble was the first to point out that these objects could have formed naturally during a symmetry breaking phase transition in the early Universe. In the framework of Grand Unifies Theories (GUTs), cosmic strings might have been formed at a grand unification transition, or later. They first became very popular as a potential source for galaxy formation, but they were ruled out as the unique source by the first cosmic microwave background observations. A couple of years later, this field was revived in String Theory, where the formation of a superstring network is generic. In the simplest case, the strength of the gravitational interaction of cosmic strings is given in terms of the dimensionless quantity  $G\mu/c^2$ , with  $\mu$  the energy per unit length,  $G$  the Newton's constant and  $c$  the speed of light in vacuum. Strings are relativistic objects that typically move at a considerable fraction of the speed of light. Thus, the combinaison of a high energy scale and a relativistic speed evidently indicates that strings should be considered as a natural source of gravitational waves.

In this thesis we present the results of a search for transient signals of gravitational waves produced by cosmic strings using the LIGO-Virgo data. This search began in the LIGO/Virgo collaboration before this work, using data from the first generation of detectors. So far, no detection of cosmic strings has been achieved. Their non-detection has led to setting constraints on important parameters, such as  $G\mu/c^2$ , describing a network of cosmic strings.

This thesis manuscript begins with a brief overview of the framework of General Relativity in which gravitational waves are produced. Gravitational-wave properties and possible sources are presented. The detection principle of current interferometric gravitational-wave detectors is exposed in the second chapter, with the most important sources of noise which limit the current detector sensitivity. Then we present the Advanced LIGO and Advanced Virgo detectors and their first data taking. We conclude this chapter with a discussion on the methods used to study the quality of the data. The next chapter is devoted to cosmic strings. After introducing the standard cosmological model, we present simple models leading to the formation of strings, in order to understand the Kibble mechanism of topological string formation. Next, we give the equations of motion for strings in the limit of zero thickness, and discuss about their dynamic. In particular, we give the definition of two special points produced on strings: cusps and kinks. Finally, this chapter ends with a description of the observational signatures of cosmic strings, in particular the expected gravitational-wave signal produced by cusp/kink features. In the fourth chapter, we give a full description of the dedicated cosmic string burst pipeline. Then, we present the analysis performed to search for gravitational-wave bursts produced by cosmic strings, using the data from the first and second observing run of Advanced LIGO and

Advanced Virgo. In the absence of a detection, in the last chapter, we derive the upper limits on the cosmic string parameters obtained with the burst and stochastic search for different cosmic string models. We subsequently discuss the implications of a new type of burst produced when two kinks collide on the burst and stochastic search.

# Chapter 1

## Gravitational waves

The Einstein equations are complicated to be solved in full generality, only restrictive conditions or approximations allow to obtain a solution. Less than one year after the first paper on General Relativity [1], Einstein found a solution that predicts three kind of waves [2, 3]. The existence of gravitational waves was expected in a field theory of gravitation by analogy to the electromagnetic case. However, this result has been criticized by several researchers and even Einstein had doubts about it [4]. By 1922 the astrophysician Arthur Eddington showed that two of the three waves found by Einstein are mathematical artifacts produced by the coordinate system and thus are only fictitious waves [5]. But any objections was found about the third wave, and Eddington proved that this last wave type propagates at the speed of light in all coordinates system. More than a decade after, in 1936, Einstein and his young student, Nathan Rosen tried to publish an article in the *Physical Review* journal that claims that gravitational waves do not exist. One of the reviewer of this article was the mathematician Howard Percy Robertson who revealed an error in the proof and warned Einstein about it, without real feedback. Months later, a new student of Einstein, Leopold Infled confirmed with Robertson the error in the Einstein and Rosen manuscript. This time, Einstein reacted and corrected the proof, however he kept for a while, a linger skepticism toward the existence of gravitational waves. In this chapter we give a rapid overview of the General Relativity material which is relevant for this thesis. In the first section [1.1] General Relativity is introduced culminating in the Einstein equations. The second section [1.2] gives the linearized equations, then we provide an overview of gravitational waves in the Sec. [1.3] and Sec. [1.4]. Finally, the last section [1.5] is dedicated to the gravitational waves sources.

## 1.1 General Relativity

### 1.1.1 Geometry in General Relativity

The theory of General Relativity developed by Einstein is a geometric framework which brings together special relativity and gravitation. The general material below follows the presentation of [6], with some inputs from other sources [7, 8, 9, 10, 11, 12, 13, 14, 15, 16, 17]. In contrast to Galilean mechanics, General Relativity claims that time and space are interwoven into a single continuum known as “space-time“. A “point-event“ is a point in space, given by its three coordinates at an instant  $t$  in time. In this description time and space variables must be expressed in the same unity. It is therefore necessary to introduce a conversion factor that has the dimension of a speed: it is the constant  $c$ , the speed of light. Throughout the speed of light will be set to  $c = 1$ . A point in space-time is then described by a four component vector,

$$\vec{x} = \begin{pmatrix} x^0 \\ x^1 \\ x^2 \\ x^3 \end{pmatrix} = \begin{pmatrix} t \\ x \\ y \\ z \end{pmatrix}. \quad (1.1)$$

It will be convenient to use a different notation, and write this vector as  $x^\mu$ , where  $\mu$  is an index running from 0 to 3.

The geometry of space is described by the metric, which defines the concept of distance between two points. In Euclidean geometry where the metric is given by the scalar product defined as positive, the square of the distance  $dl$  between two infinitesimally close points can be written

$$dl^2 = g_{ij} dx^i dx^j, \quad (1.2)$$

where the Einstein summation convention is used, and  $g_{ij}$  is the metric given by

$$g_{ij} = \text{diag}(1, 1, 1), \quad (1.3)$$

of signature  $(+, +, +)$ . In a similar way, the space-time interval in General Relativity geometry is given by

$$ds^2 = g_{\alpha\beta} dx^\alpha dx^\beta, \quad (1.4)$$

where the metric  $\mathbf{g} = g_{\alpha\beta}(\vec{e}_\alpha, \vec{e}_\beta)$ , in a given basis  $(\vec{e}_0, \vec{e}_1, \vec{e}_2, \vec{e}_3)$ , is a bilinear form, symmetrical and not degenerated. We choose to work with the signature  $(-, +, +, +)$ . These properties of the metric allow to define the inverse metric as,

$$g^{\alpha\sigma} g_{\sigma\beta} = \delta_\beta^\alpha, \quad (1.5)$$

where  $\delta_\beta^\alpha$  is the Kronecker delta relating to the indices  $\alpha$  and  $\beta$ :  $\delta_\beta^\alpha = 1$  if  $\alpha = \beta$  and 0 if not. The metric for an infinite empty space without gravitation is the flat

Minkowski metric  $\eta_{\alpha\beta}$  whose expression in the usual time-space  $(t, x, y, z)$  is given by the matrix:

$$\eta_{\alpha\beta} = \eta^{\alpha\beta} = \begin{pmatrix} -1 & 0 & 0 & 0 \\ 0 & 1 & 0 & 0 \\ 0 & 0 & 1 & 0 \\ 0 & 0 & 0 & 1 \end{pmatrix} \quad (1.6)$$

The scalar product of a 4-vector with itself can a priori have any sign, unlike the classical scalar product in the Euclidean space. A 4-vector  $\vec{x}$  is said to be light-like if  $\mathbf{g}(\vec{x}, \vec{x}) = 0$ , time-like if  $\mathbf{g}(\vec{x}, \vec{x}) < 0$  and space-like if  $\mathbf{g}(\vec{x}, \vec{x}) > 0$ . The curves describing the photons must be of the light type ( $ds^2 = 0$ ), this is the generalization of the invariance of light-speed in special relativity. A material point (particle) in classical mechanics becomes a curve in relativistic space-time, corresponding to all "successive positions" occupied by the material point. The curve representing a point material or worldline must be of time type, i.e. such that any vector tangent to the curve is timelike (this property reflects the impossibility for particles to travel faster than light). The figure 1.1 allows to visualize the difference between these type of 4-vector. Lastly, we define the proper time interval  $\Delta\tau$  between two events along a

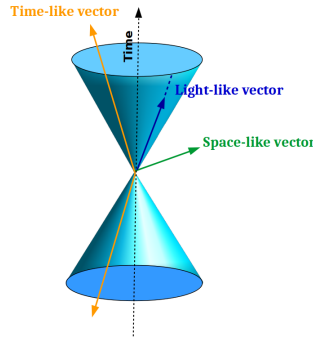


Figure 1.1: Light cone in 2D space plus a time dimension centered at each event in Minkowski Spacetime. It separates time-like vectors from space-like vectors: the former are located inside the cone, the latter outside.

time-like path  $\mathcal{P}$  by:

$$\Delta\tau = \int_{\mathcal{P}} d\tau = \int_{\mathcal{P}} \sqrt{g_{\alpha\beta} dx^{\alpha} dx^{\beta}}, \quad (1.7)$$

that allows us to construct the 4-velocity which is the tangent 4-vector of a time-like world line. In terms of components in respect of a coordinate system the 4-velocity is given by:

$$u^{\alpha} = \frac{dx^{\alpha}}{d\tau} \quad \text{with} \quad g_{\alpha\beta} u^{\alpha} u^{\beta} = -1. \quad (1.8)$$

### 1.1.2 The Einstein equations

The properties of the gravitational field are encoded in the metric. More precisely, the Einstein equations are the fundamental equations in General Relativity, which

determine the metric in function of the stress-energy distribution in space-time, being given by

$$G_{\alpha\beta} = \kappa T_{\alpha\beta}, \quad (1.9)$$

where  $G_{\alpha\beta}$  is called the Einstein tensor,  $\kappa$  is the Einstein's gravitational constant and  $T_{\alpha\beta}$  is the stress-energy tensor. In order to understand the first term we need to introduce a mathematical tool, the affine connection. In the Euclidean space, differentiation of vector fields is obtained by derivating the coordinates functions, since one has a constant basis. This is no longer true in space-time. The affine connection is a geometric object which connects nearby tangent spaces, and so allows tangent vector fields to be differentiated. For a given metric  $g_{\alpha\beta}$ , one can show that the affine connexion is fixed, having for coefficient the Christoffel symbols of the metric,

$$\Gamma_{\mu\nu}^{\alpha} = \frac{1}{2}g^{\alpha\sigma} \left( \frac{\partial g_{\sigma\nu}}{\partial x^{\mu}} + \frac{\partial g_{\mu\sigma}}{\partial x^{\nu}} - \frac{\partial g_{\mu\nu}}{\partial x^{\sigma}} \right). \quad (1.10)$$

From that, it is straightforward to calculate the variation of a vector field between two points, even if in general the result depends on the choice of path, or in other words on the curvature of the affine connexion, see Figure 1.2. The curvature of

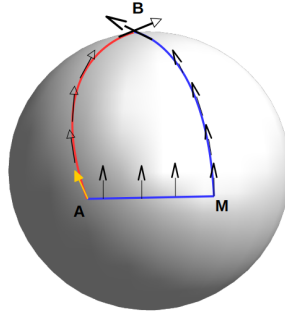


Figure 1.2: Transport of a vector (yellow) from A to B parallel to itself following two different paths on the surface of a sphere:  $A \mapsto B$  or  $A \mapsto M$  and  $M \mapsto B$ . The vector at the arrival point depends on the path followed. This is due to the curvature of the sphere.

space-time is then expressed through derivatives of Christoffel symbols, but in a much more "pleasant" form of a tensor called the Riemann tensor,

$$R_{\beta\mu\nu}^{\alpha} = \frac{\partial \Gamma_{\beta\nu}^{\alpha}}{\partial x^{\mu}} - \frac{\partial \Gamma_{\beta\mu}^{\alpha}}{\partial x^{\nu}} + \Gamma_{\sigma\mu}^{\alpha} \Gamma_{\beta\nu}^{\sigma} - \Gamma_{\sigma\nu}^{\alpha} \Gamma_{\beta\mu}^{\sigma}. \quad (1.11)$$

From this definition it comes two useful quantities that play an essential role in the formulation of the Einstein's equations, the Ricci tensor  $R_{\alpha\beta}$  defines as:

$$R_{\alpha\beta} = R_{\alpha\sigma\beta}^{\sigma}, \quad (1.12)$$

and the trace of the Ricci tensor, also called the Ricci scalar  $R$ :

$$R = g^{\alpha\beta} R_{\alpha\beta}. \quad (1.13)$$

By using these definitions, the Einstein tensor is given by:

$$G_{\alpha\beta} = R_{\alpha\beta} - \frac{1}{2} R g_{\alpha\beta}, \quad (1.14)$$

we understand now that the left side of the Einstein equations describe the geometry of space-time.

In General Relativity, it is the matter that curves space-time, we deduce then that the right side of the Einstein equations should describe the content in matter of space-time. The stress-energy tensor,  $T_{\alpha\beta}$ , is a symmetrical tensor which contains the informations about the content in mass-energy and momentum density in space-time. For example, in the case of a perfect fluid in thermodynamic equilibrium, the stress-energy tensor takes on a particularly form:

$$T_{\alpha\beta} = (\rho + p) u_\alpha u_\beta + p g_{\alpha\beta}, \quad (1.15)$$

where  $\rho$  is the energy density,  $p$  the hydrostatic pressure and  $u_\alpha$  the 4-velocity of the fluid. The divergence of the stress-energy tensor vanish:

$$\nabla_\beta T^{\alpha\beta} \equiv \eta^{\alpha\beta} \frac{\partial T_{\alpha\beta}}{\partial x^\alpha} + \Gamma_{\sigma\beta}^\alpha T^{\sigma\beta} + \Gamma_{\sigma\beta}^\beta T^{\alpha\sigma} = 0, \quad (1.16)$$

which is translated into conservation laws: energy, momentum, angular momentum, etc.

There is still a term which need to be clarified in the Einstein equations: the  $\kappa$  quantity. Being General Relativity an extension of Newtonian gravity, the Einstein equations should in a classical system reduce to Newton's equations of gravity. When we look in classical theory, the distribution of matter of density  $\rho$  gives rise to a gravitational potential  $\Phi$  which satisfies Poisson's equation:

$$\nabla^2 \Phi = 4\pi G \rho, \quad (1.17)$$

where  $G$  is Newton's constant. For a perfect fluid of density  $\rho$  at rest with nul pressure, we can show that the stress-energy tensor would have only one non-zero component  $T_{00} = \rho$  and that Einstein's equations reduce to

$$2\nabla^2 \Phi = \kappa \rho. \quad (1.18)$$

By identifying Eq. [1.18](#) with Eq. [1.17](#) we set

$$\kappa = 8\pi G, \quad (1.19)$$

and find that General Relativity thus passes an important test, in agreeing with Newtonian gravity, in the classical limit. The Einstein equations become:

$$G_{\alpha\beta} = 8\pi GT_{\alpha\beta}. \quad (1.20)$$

Later, in 1917 Einstein introduced the cosmological constant  $\Lambda$  in order to allow a consistent model of a universe that was assumed to be static:

$$G_{\alpha\beta} + \Lambda g_{\alpha\beta} = 8\pi GT_{\alpha\beta}. \quad (1.21)$$

If  $\Lambda = 0$ , then an absence of matter ( $T_{\alpha\beta} = 0$ ) leads to an absence of spacetime curvature, but if  $\Lambda \neq 0$  we have gravity associated with the vacuum. Today the cosmological constant is a key part of the standard cosmological model. The meaning of this constant will be detailed in the third chapter.

## 1.2 Linearized General Relativity

The Einstein equations are non linear which make them difficult to solve exactly. It is natural to consider the conditions and approximations where these equations become linear. This is the case in the weak-field limit, which is only valid far away from the source. From now we will consider a near-flat-space metric:

$$g_{\alpha\beta} = \eta_{\alpha\beta} + h_{\alpha\beta} \quad \text{with} \quad \|h_{\alpha\beta}\| \ll 1, \quad (1.22)$$

which is the sum of the Minkowski metric  $\eta_{\alpha\beta}$  and a perturbation  $h_{\alpha\beta}$  from flat space-time. By replacing the new metric in the Einstein equations and ignoring all terms of order higher than one in the perturbation we get the general form of the Einstein linearized equations:

$$\square \bar{h}_{\alpha\beta} + \eta_{\alpha\beta} \partial_\rho \partial_\sigma \bar{h}^{\rho\sigma} - \partial_\beta \partial_\rho \bar{h}_\alpha^\rho - \partial_\alpha \partial_\rho \bar{h}_\beta^\rho = -16\pi GT_{\alpha\beta}, \quad (1.23)$$

where we have defined the trace-reversed perturbation metric  $\bar{h}$  as

$$\bar{h}_{\alpha\beta} = h_{\alpha\beta} - \frac{1}{2} h \eta_{\alpha\beta}, \quad (1.24)$$

which has a trace  $\bar{h} = -h$ , with  $h \equiv \eta^{\alpha\beta} h_{\alpha\beta}$  the trace of the perturbation metric.

We can continue to simplify the Einstein equations. At this point it is useful to choose a specific gauge, or in other words to choose a new coordinate system. In order to do so we consider an infinitesimal coordinates transformation,

$$x'^\alpha = x^\alpha + \xi_\alpha \quad \text{with} \quad \|\xi_\alpha\| \ll 1. \quad (1.25)$$

In terms of the new coordinates, the perturbation metric transforms at the first order in  $\xi^\alpha$  and  $h_{\alpha\beta}$  as,

$$h'_{\alpha\beta} = h_{\alpha\beta} - \partial_\beta \xi_\alpha - \partial_\alpha \xi_\beta. \quad (1.26)$$

It is always possible to choose the  $\xi_\alpha$  in a way that

$$\partial_\alpha \bar{h}_\beta^\alpha = 0, \quad (1.27)$$

one say that the trace-reversed perturbation metric satisfy to the Lorenz gauge. Finally, the linearized Einstein equations take the elegant form of a wave equation for the perturbation  $h_{\alpha\beta}$  with a source term:

$$\square \bar{h}_{\alpha\beta} = -16\pi G T_{\alpha\beta}. \quad (1.28)$$

this is the theoretical prediction of wave solutions to the Einstein equations or simply gravitational waves.

## 1.3 Gravitational waves in vacuum

### 1.3.1 Generalities

In the vacuum, the stress-energy tensor is zero and then the wave equation becomes

$$\square \bar{h}_{\alpha\beta} = 0. \quad (1.29)$$

The general solution of this equation can be written as a superposition of monochromatic progressive plane waves,

$$\bar{h}_{\alpha\beta}(x^\mu) = A_{\alpha\beta} \times \exp(ik_\mu x^\mu), \quad (1.30)$$

where  $A_{\alpha\beta}$  represents the amplitude wave, a constant and symmetrical matrix of dimension  $4 \times 4$ ,  $k_\mu = (-\omega, k_x, k_y, k_z)$  represents the wavevector and  $\omega$  is the angular frequency. Note that the amplitude matrix contains only 10 independent components, due to the symmetrical properties. The wavevector determines the propagation direction of the wave and its frequency. This two quantities cannot be chosen arbitrarily as they must satisfy some conditions. By using the weak-field Einstein's equations in vacuum (see Eq. 1.29) one obtain a first condition,

$$k^\alpha k_\alpha = 0 \Leftrightarrow -\omega^2 + \|\vec{k}\|^2 = 0 \quad (1.31)$$

this relation is called dispersion relation. It indicates that gravitational waves in vacuum move at the speed of light, as we remember that  $c = 1$ . The second condition is given by the Lorenz gauge Eq. 1.27,

$$k_\alpha A^{\alpha\beta} = 0. \quad (1.32)$$

This condition reveals that the effect of a gravitational wave is orthogonal to its direction of propagation. It can be written as four equations that impose four conditions on the components of the amplitude matrix  $A_{\alpha\beta}$ . Instead of having 10 independent components, the amplitude matrix has only 6 independent ones. Due

to the gauge freedom, an appropriate choice of gauge can reduce the number of independent components of  $A_{\alpha\beta}$  even more. Indeed, one can also find a choice of a system of infinitesimal coordinates which satisfies the Lorenz gauge (see Eq. 1.27) and cancel some components of the amplitude matrix  $A_{\alpha\beta}$ . This choice is commonly known as the transverse-traceless gauge or TT gauge,

$$\begin{cases} \bar{h}_{0\alpha} = 0 & \Rightarrow \text{transverse} \\ \bar{h} = 0 & \Rightarrow \text{traceless} \end{cases} \quad (1.33)$$

and since we have seen before that the trace of  $\bar{h}_{\alpha\beta}$  and the trace of  $h_{\alpha\beta}$  are linked by the relation  $\bar{h} = -h$ , we have  $h = 0$ . Thus the TT gauge equations can be rewritten by replacing  $\bar{h}$  by  $h$ . Using the Eq. 1.30, we can also write these equations as

$$\begin{cases} A_{0\alpha} = 0 & \Rightarrow \text{transverse} \\ A_{\alpha}^{\alpha} = 0 & \Rightarrow \text{traceless} \end{cases} \quad (1.34)$$

which consequently add 4 constraints on the amplitude components, 1 from the traceless condition and only 3 from the transverse condition, since there is a redundancy with one of the constraints from the Lorenz gauge condition (see Eq. 1.27). We have now reduced the independent degrees of freedom of the amplitude matrix  $A_{\alpha\beta}$  to only 2.

### 1.3.2 Example

In order to make it more clear, we provide an example here. We consider a gravitational wave with angular frequency  $\omega$  that propagates along the z-axis. The wavevector is given by

$$k_{\beta} = (-\omega, 0, 0, +\omega). \quad (1.35)$$

To impose constraints on the amplitude matrix  $A_{\alpha\beta}$  we use the gauge equations. The Lorenz gauge (see Eq. 1.27) implies that

$$\omega(A_{\alpha 0} - A_{\alpha z}) = 0, \quad (1.36)$$

and the transverse condition in the TT gauge fixes

$$A_{\alpha 0} = 0. \quad (1.37)$$

Since the amplitude matrix is symmetrical, the only non-zero terms for  $A_{\alpha\beta}$  are:  $A_{xx}$ ,  $A_{xy} = -A_{yx}$  and  $A_{yy}$ . In addition, the traceless condition of the TT gauge gives us an other constraint,

$$A_{xx} + A_{yy} = 0. \quad (1.38)$$

This results in a wave amplitude matrix with only two independent components:

$$A_{\alpha\beta} = \begin{pmatrix} 0 & 0 & 0 & 0 \\ 0 & A_{xx} & A_{xy} & 0 \\ 0 & A_{xy} & -A_{xx} & 0 \\ 0 & 0 & 0 & 0 \end{pmatrix} \quad (1.39)$$

The wave is a linear combination of two independent types of waves, called polarizations of the gravitational wave. We introduce the notation

$$A_{xx} = A_+ \quad A_{xy} = A_\times, \quad (1.40)$$

the wave amplitude matrix is rewritten as a sum of two matrices

$$A_{\alpha\beta} = A_+ \begin{pmatrix} 0 & 0 & 0 & 0 \\ 0 & 1 & 0 & 0 \\ 0 & 0 & -1 & 0 \\ 0 & 0 & 0 & 0 \end{pmatrix} + A_\times \begin{pmatrix} 0 & 0 & 0 & 0 \\ 0 & 0 & 1 & 0 \\ 0 & 1 & 0 & 0 \\ 0 & 0 & 0 & 0 \end{pmatrix} \quad (1.41)$$

where the polarization states are commonly referred to as “plus“ and “cross“ polarization. In that example, the solution to the Einstein equations in the weak-field approximation and in the absence of matter (vacuum) is written:

$$h_{\alpha\beta} = \begin{pmatrix} 0 & 0 & 0 & 0 \\ 0 & h_+ & h_\times & 0 \\ 0 & h_\times & -h_+ & 0 \\ 0 & 0 & 0 & 0 \end{pmatrix} \quad (1.42)$$

with

$$\begin{cases} h_+ &= A_+ \exp[i\omega(t - z)] \\ h_\times &= A_\times \exp[i\omega(t - z)]. \end{cases} \quad (1.43)$$

### 1.3.3 Gravitational-wave effects on matter

After peeking at how gravitational waves are generated the next question to answer is what are their effects on an observer located on Earth. The simplest physical system we may consider is two test masses A and B, moving freely, which is to say they are not subject to any forces (except gravity), and a gravitational wave that propagates along the z-axis. We use the perturbation metric which satisfies the traceless-transverse gauge condition. The distance between the two test masses is given by:

$$ds^2 = g_{\alpha\beta} dx^\alpha dx^\beta = -dt^2 + (\delta_{ij} + h_{ij}) dx^i dx^j, \quad (1.44)$$

where the  $\delta_{ij}$  represents the Kronecker symbol. If we consider a coordinate system where the mass A is at the initial position  $(t, 0, 0, 0)$  and the mass B is at the position  $(t, x_B, y_B, z_B)$  and  $L_0$  the initial distance between A and B, then the distance L, at any time, between the two masses is:

$$L^2 = (\delta_{ij} + h_{ij}) x_B^i x_B^j, \quad (1.45)$$

we introduce  $\vec{n}$  a unitary spatial vector that joins A to B and therefore

$$\begin{cases} x_B^i &= L_0 n^i, \\ L_0^2 &= \delta_{ij} x_B^i x_B^j, \end{cases} \quad (1.46)$$

using these definitions and the unitary property, we rewrite  $L$  under the form,

$$L = L_0[1 + h_{ij}n^i n^j]^{1/2}. \quad (1.47)$$

which becomes at first order in  $h$ :

$$L = L_0[1 + \frac{1}{2}h_{ij}n^i n^j]. \quad (1.48)$$

Thus, the relative variation of the distance  $L$  to the passage of a gravitational wave is given at the first order by

$$\frac{\delta L}{L} = \frac{1}{2}h_{ij}n^i n^j, \quad (1.49)$$

which shows that the relative change in distance is proportional to the amplitude of the wave  $h$ , also called strain amplitude. To visualize this effect we choose a new coordinate system defined by the transformation,

$$\begin{cases} \hat{x}^0 &= x^0 \\ \hat{x}^i(t) &= x^i + \frac{1}{2}h_{ij}(t, 0)x^j. \end{cases} \quad (1.50)$$

where  $h_{ij}(t, 0)$  represents the value of the field at  $x^\alpha = (t, 0, 0, 0)$ . For a gravitational wave that propagates along the z-axis we gave the  $h_{ij}$  components in Eq. [1.42](#) and we have

$$\begin{aligned} \hat{x}(t) &= x_0 + \frac{1}{2}[A_+x_0 + A_\times y_0]e^{i\omega t}, \\ \hat{y}(t) &= y_0 + \frac{1}{2}[A_\times x_0 - A_+y_0]e^{i\omega t}, \\ \hat{z}(t) &= z_0. \end{aligned} \quad (1.51)$$

We represent the deformation of a ring of test masses in the plan  $z = 0$  for both polarizations in Fig. [1.3](#). Qualitatively, a gravitational wave that is propagating perpendicularly to the plane of a ring of test particles will cause the ring to deform into an ellipse, first along one axis and then along the other, oscillating between these two configurations as a function of time.

## 1.4 Gravitational-wave generation

To study the generation of gravitational waves, it is necessary to return to the linearized Einstein equations with source. When the gravitational field is strong there are a number of nonlinear effects that influence the generation and propagation of gravitational waves. The analytic description of such a dynamically changing in spacetime is complicated. However under some assumptions that simplify the equation of gravitational waves in presence of a source, it is possible to understand the generation of gravitational waves by a source.

We focus on **(i)** the gravitational field produced by a “weak“ localized source of characteristic size  $R$ , that is, a source where the energy content is small enough to

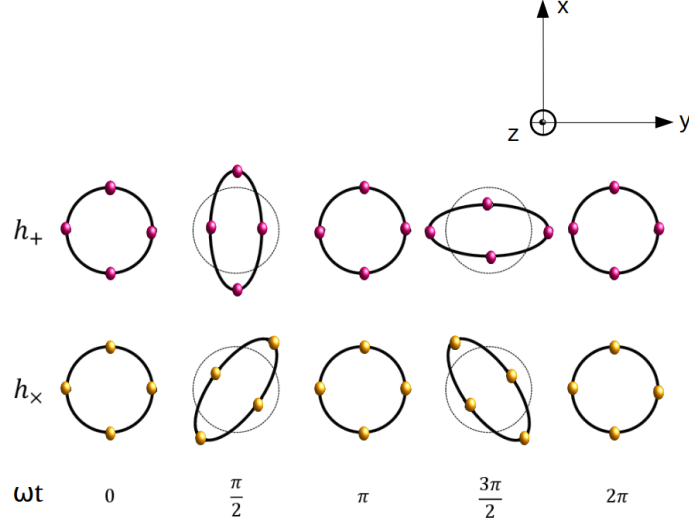


Figure 1.3: Effect of a passing gravitational wave propagating in the  $z=0$  plan, with plus polarization (top) and cross polarization (bottom) on a ring of freely-falling particles.

produce only small deformations of the flat space-time ( $|h_{\alpha\beta}| \ll 1$ ). The source is centered at the origin and we denote by  $\vec{y}$  the vector pointing to a particular point in the source, see Fig. 1.4. The observer is localized by its spatial position  $\vec{x}$  and we define:

$$r \equiv |\vec{x}| \quad \text{and} \quad \hat{n} \equiv \frac{\vec{x}}{r}. \quad (1.52)$$

In addition we assume that **(ii)** the observer is located at a great distance from the source, i.e.  $r \gg |\vec{y}|$  and we consider that **(iii)** the region where the source is confined of radius  $R$ , is much smaller than the wavelength of the emitted gravitational waves, which gives the condition

$$v = R\omega \ll c, \quad (1.53)$$

this approximation is often called the slow motion approximation. The general solution of the linearized Einstein is closely analogous to the classical retarded potential solution seen in electromagnetism (in the multipole radiation expansion):

$$\begin{aligned} \bar{h}_{\alpha\beta}(t, \vec{x}) &= \frac{4G}{c^4} \int \frac{T_{\alpha\beta}(t - \frac{1}{c}|\vec{x} - \vec{y}|, \vec{y})}{|\vec{x} - \vec{y}|} d^3\vec{y} \\ &\simeq \frac{4G}{c^4 r} \int T_{\alpha\beta} \left( t - \frac{r}{c} + \frac{\hat{n} \cdot \vec{y}}{c}, \vec{y} \right) d^3\vec{y} \\ &\simeq \frac{4G}{c^4 r} \int T_{\alpha\beta} \left( t - \frac{r}{c}, \vec{y} \right) d^3\vec{y}, \end{aligned} \quad (1.54)$$

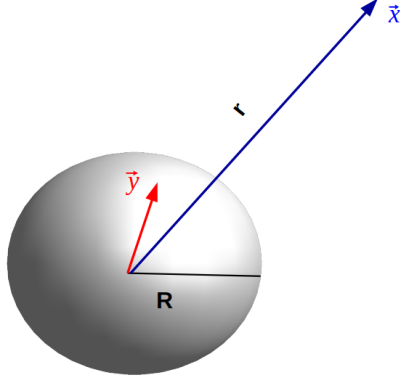


Figure 1.4: Source confined within a radius  $R$ , centered at the origin and  $\vec{y}$  is a vector pointing to a particular point of the source. The observer is localized at a large distance from the source by  $\vec{x}$ .

to pass from the first equation to the second we use the assumption that the observer is at a large distance from the source (ii), which leads to

$$|\vec{x} - \vec{y}| \simeq r \left( 1 - \frac{\hat{n} \cdot \vec{y}}{r} \right) \quad (1.55)$$

and we neglect the term  $\hat{n} \cdot \vec{y}$  in front of  $r$ , to obtain the last equation.

In the slow motion approximation, the stress-energy tensor,  $T_{\mu\nu}$ , varies slowly (the motion of the source is dominated by non-gravitational forces). Thus the conservation of the energy given (Eq. 1.16) becomes  $\eta^{\mu\nu} \partial_\nu T_{\alpha\mu} = 0$ . And the time-time component of the stress-energy tensor is dominated by the rest mass density  $T_{00} \simeq \rho c^2$ . From that one can show that the integral term in Eq. 1.54 is given by:

$$2 \int T_{ij} \left( t - \frac{r}{c}, \vec{y} \right) d^3 \vec{y} = \ddot{I}_{ij} \left( t - \frac{r}{c} \right), \quad (1.56)$$

where  $I_{ij}$  is the mass quadrupole moment of the source defined as

$$I_{ij}(t) = \int_{source} \rho(t, \vec{y}) y^i y^j d^3 \vec{y}, \quad (1.57)$$

which gives:

$$\bar{h}_{\alpha\beta}(t, \vec{x}) = \frac{2G}{c^4 r} \ddot{I}_{ij} \left( t - \frac{r}{c} \right). \quad (1.58)$$

We observe that even if the motion of the source is dominated by non-gravitational forces, the results depends only on the source motion. To obtain the metric perturbation in the transverse-traceless gauge, we take the transverse and without trace part of this result. To do this we introduce two quantities, the reduced quadrupolar mass moment of the source  $Q_{ij}$  given by

$$Q_{ij}(t) = \int_{source} \rho(t, \vec{y}) \left( y^i y^j - \frac{1}{3} \vec{y} \cdot \vec{y} \delta_{ij} \right) d^3 \vec{y}, \quad (1.59)$$

which is the traceless part of the quadrupolar mass moment  $I_{ij}$ . And we define the transverse projection operator

$$\Pi_{ij}(\vec{x}) = \delta_{ij} - \hat{n}_i \hat{n}_j \quad (1.60)$$

where  $\hat{n}_i = x_i/r$  is the unit vector normal to the wavefront. This operator projects a vector onto the plane orthogonal to the direction of  $\hat{n}_i$ . The metric perturbation in the transverse-traceless gauge is then given by the quadrupole formula:

$$h_{ij}^{TT}(t, \vec{x}) = \left[ \Pi_i^k \Pi_j^\ell - \frac{1}{2} \Pi_{ij} \Pi^{k\ell} \right] \ddot{Q}_{ij}(t - \frac{r}{c}). \quad (1.61)$$

In electromagnetism, the monopole radiation is zero, because the electromagnetic monopole moment is proportional to the total charge, which does not change with time (it is a conserved quantity for an isolated charge). Therefore the electromagnetic radiation consists of firstly the electric dipole radiation. Then comes the magnetic dipole. Similarly, the gravitational monopole produced by a source is proportional to the total mass, which does not change with time (it is a conserved quantity for an isolated source). Also, the rate of change of the mass dipole moment is proportional to the momentum of the system, which is a conserved quantity, and therefore there cannot be any gravitational dipole radiation. Indeed, by analogy with the dipole moment of accelerated charges particles, we define for an isolated system of masses a gravitational dipole moment  $\vec{d} = \sum_i m_i \vec{r}_i$  which satisfies the conservation law of the total momentum:

$$\dot{\vec{d}} = \sum_i \vec{p}_i \quad \text{and} \quad \ddot{\vec{d}} = 0. \quad (1.62)$$

The next term of the gravitational radiation multipole is proportional to the angular momentum of the system, which is also conserved for an isolated source. It follows that gravitational radiations are of quadrupolar nature. Finally, for a spherical or axisymmetric distribution of matter the quadrupole moment Eq. [1.59](#) is a constant. Thus a spherical or axisymmetric source does not emit gravitational waves.

Considering a metric perturbation, it is interesting to know how much energy it carries, in order to be able to estimate the maximum amplitude that can be generated by a source. Without demonstration, the flux of energy  $F$  transported by a gravitational wave and averaged over several wavelengths, is given by [\[6\]](#):

$$F = \frac{c^3}{16\pi G} \langle \dot{h}_+^2 + \dot{h}_\times^2 \rangle, \quad (1.63)$$

where the  $c$  factor has been made explicit. For a monochromatic wave of amplitude  $h$  and frequency  $f$  we can show that:

$$F = \frac{\pi c^3}{4G} f^2 h^2, \quad (1.64)$$

Let's take  $f = 10^2$  Hz and  $h = 10^{-21}$  we find  $F \simeq 0.003 \text{ W.m}^{-2}$ , so a gravitational wave of very small amplitude still carries an appreciable amount of energy.

The total amount of energy emitted per unit of time,  $L$ , also called luminosity, is [6]:

$$L = \frac{1}{5} \frac{G}{c^5} \left\langle \ddot{Q}_{ij} \ddot{Q}^{ij} \right\rangle. \quad (1.65)$$

In order to estimate an order of magnitude of the luminosity we can perform a dimensional analysis. We consider a source of mass  $M$ , confined in a radius  $R$  and described by a reduced quadrupolar moment of norm  $Q$  approximated to  $Q \sim sMR^2$ , where  $s$  is a mass distribution asymmetry:  $s = 0$  for a for an object with spherical symmetry. In that case, the luminosity is approximated to:

$$L \sim \frac{G}{c^5 \tau^6} s^2 M^2 R^4, \quad (1.66)$$

where  $\tau$  is a characteristic time scale. By substituting in this equation, the mass of the source in function of its Schwarzschild radius  $M = c^2 R_s / (2G)$  ( $R_s$  corresponds to the radius defining the boundary below which events cannot affect any outside observer (event horizon) of a Schwarzschild black hole) and the time scale in function of the characteristic speed of the source  $v = R/\tau$  we obtain:

$$L \sim \frac{c^5}{G} s^2 \left( \frac{R_s}{R} \right)^2 \cdot \left( \frac{v}{c} \right)^6, \quad (1.67)$$

From this equation, we derive the conditions for a source to produce large amounts of gravitational waves (where  $L \sim 1$ ):

- $s \sim 1$  a strongly asymmetric source,
- $v \sim c$  a relativistic motion,
- $R \sim R_s$  a compact source.

## 1.5 Gravitational waves sources

As we have seen, due to the fact that gravitational waves present quadrupolar radiation, the efficiency in converting mechanical energy in a system into gravitational radiation will be very low, making the signal produced by accelerating systems to be very weak. In practical terms, this means that the main sources of gravitational waves that are likely to be detected will be coming from astrophysical objects, as neutron stars or black holes, due to their potentially huge masses accelerating very strongly.

When we look at the spectrum of possible gravitational wave sources in the observable wave band, we see a range spanning over many orders of magnitude in frequency. We are mainly interested in the sources that emit gravitational waves powerful enough

to be detected by ground-based interferometric detectors as Advanced LIGO and Advanced Virgo, i.e. aiming to detect signals from sources radiating in the high frequency band between 10 Hz and  $10^4$  Hz.

Besides this constraint in frequency, a good source of gravitational waves is expected to be *asymmetric*, *compact* and *relativistic*. The emitted power of the source is not the only decisive parameter while evaluating possible good sources, two additional aspects have to be taken into account. The first is the distance of the source from the Earth, meaning that as the distance increases, the louder an event needs to be in order to be detected. The second is the rate at which the event occurs, regarding its impact on the detection probability.

Once we have considered these different aspects, we can go all along to consider in more detail the possible sources of gravitational waves in which we shall be interested. These potential sources are usually classified by their signal morphology. The typical categories are the following: continuous-waves signals, which are signals generated by sources that involve periodic motion that hold a roughly constant frequency over a long timescales. Another class of continuous sources is the stochastic background of gravitational waves, that is produced by the incoherent superposition of gravitational waves emitted by countless individual sources. The gravitational-wave burst signals are short duration signal corresponding to particular cataclysmic events. Such signals are divided into signals from sources that can be well modelled by theory or numerical simulations, and those that cannot be modelled. This classification is convenient in that it categorized the sources in the same way as the data analysis method that we use to search for sources.

### 1.5.1 Continuous waves

Continuous sources of gravitational waves are considered to be constantly emitting quasi-monochromatic gravitational waves. The primary expected sources of continuous gravitational waves in the high-frequency band are rotating neutron stars with an asymmetric mass distribution caused for example by stress induced by internal magnetic fields. The gravitational radiation from rotating neutrons stars occurs at a frequency proportional to the frequency of rotation.

Pulsars are a particular type of neutron stars, whose magnetic and rotational axis are not aligned. Consequently, the electromagnetic radiation (usually in radio wavelengths) is not symmetric around the rotation axis and the observed electromagnetic flux changes periodically as the star rotates. This allows a precise measurement of the rotation frequency. A typical example is the Crab pulsar and the Vela pulsar, which are young enough to rotate rapidly (without losing angular momentum due to gravitational radiation). The neutron star maybe be isolated or in binary systems with companions (star, white dwarf, neutron star), and an example is Scorpius X-1 which is a neutron star accreting matter from a donor star.

The mechanisms at the origin of the emission of gravitational waves are multiple. If the neutron star is not axisymmetric then it will produce gravitational waves at a frequency equal to twice the rotational frequency. If the neutron star is axisymmetric,

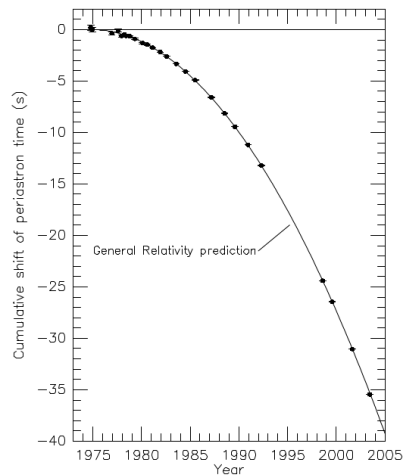


Figure 1.5: Plot of cumulative shift of the periastron time from 1975-2007 [18]. The point are observation data with measurement error bars (which are too small to be easily see) and the curve is the General Relativity prediction.

but the axis of symmetry is different from the rotational axis, it will emit gravitational waves at both the rotational frequency and twice the rotational frequency. Another mechanism for the production of gravitational waves from rotating neutrons star are fluid oscillation modes that may become instable.

The search for continuous wave signals from rotating neutron stars is divided into two populations, according to whether the star has already been observed or not. In the targeted searches for known pulsars the gravitational waveform is well modeled since we have access to several informations (frequency of rotation, sky position, ...). However such waves are not expected to be as loud as the gravitational waves generated from more violent events.

The pulsar PSR 1913+16 has been discovered by Hulse and Taylor in 1974 and it forms a close binary system with another compact object [19]. The orbital period was measured through precise radio observations. Over time a decrease in this period has been observed equal to the one predicted from energy loss by gravitational radiation [18]. The figure 1.5 shows that the shift in periastron time predicted by General Relativity is in perfect agreement with the observed one. This was the first indirect detection of gravitational-waves.

### 1.5.2 Gravitational wave bursts

This predicted population of signals contains the gravitational waves transients, or bursts, emissions that have only a short duration compared to the observation time. In addition to the amplitude of the burst, the expected rate is also crucial. Compact binary coalescence signals are the primary source target of gravitational wave burst searches for ground-based detectors. These systems are binaries composed of two

neutron stars (BNSs), two black holes (BBHs) or a neutron star together with a black hole (NSBH). They represent an ideal source for ground based gravitational wave detectors, as their compactness allows them to have an orbital separation increasingly small until their merge, leading to emission of gravitational waves throughout all the process. The gravitational wave signal will depend on the physical parameters of the binary system: masses, spins and eccentricity, and it presents three main parts, where the first is the inspiral, which increases in frequency and amplitude as the compact objects move closer, together with the energy and angular momentum being carried away in gravitational waves. When the motion is not too relativistic, this phase is described by post-Newtonian theory. The second phase is the merger phase when the black holes or neutron stars collide, this phase is explored with numerical relativity. The final object produces ringdown radiation. The duration of the gravitational radiation depends on the mass of the objects. The coalescence of black holes produces short gravitational waves on the order of fractions of a second, whereas neutron stars which are less massive than black holes, generate signals several tens of seconds long. The burst search includes transient lasting from seconds to minutes. The gravitational radiation produced during the merger and ringdown phase of black holes allows to observe strong-field effects of gravitation, and to test General Relativity in the strong-field regime. Even if our understanding of binary coalescence is incomplete, the gravitational waveform is well predicted in several cases. However search for signals of unknown form offers an opportunity for great discovery.

Apart from compact binary coalescence, there are many possible sources of transient gravitational waves. Without being exhaustive, we can also mention some sources usually considered. For example, stars with large masses are believed to produce an iron core during their evolution [20]. When this core collapses with a motion that is not spherically symmetric it can generate large amounts of gravitational radiation. The ejected matter during the core collapse produces an optical brightening called supernova, classified according to their optical spectra (type I, type II). A small fraction of core collapses are associated to emission of powerful and brief flashes of electromagnetic radiation with typical photon energies  $E \sim 100$  keV called gamma ray burst. Another case, more speculative refer to gravitational-waves emitted by cosmic strings, that is the subject of the third chapter.

### 1.5.3 Stochastic gravitational wave background

The stochastic background of gravitational waves may be produced by the superposition of weak individually unresolvable cosmological and astrophysical sources. Cosmological sources include quantum vacuum fluctuations during the inflationary epoch of the Universe, electro-weak phase transitions, pre-big bang scenario in the context of string theory and cosmic strings. While astrophysical sources can be compact binary coalescence, supernovae, pulsars and many others. Keeping in line with traditional cosmological definitions, the stochastic gravitational-wave background is

described by the gravitational-wave energy density defined as

$$\Omega_{GW}(f) = \frac{f}{\rho_c} \frac{d\rho_{GW}}{df}, \quad (1.68)$$

where  $\rho_c$  is the critical energy density of the universe and  $d\rho_{GW}$  is the gravitational-wave energy density contained in the frequency ranged  $f$  to  $f + df$ .

# Chapter 2

## Gravitational Wave Detectors

### 2.1 History

Einstein's theory of General Relativity, published in November 1915, led to the prediction of the existence of gravitational waves. Einstein wondered if they could ever be discovered. As we will see, the interest in the detection of gravitational waves began at a meeting which took place in Chapel Hill, North Carolina in 1957. This meeting would not have been possible without the funding of an eccentric American millionaire named Roger W. Babson. Babson was obsessed with finding a way to control the force of gravity. To that end, he founded first, the Gravity Research Foundation (GRF) which still exists today. A short essay competition on gravitation was organized each year, with an award of \$1000 offered to the best essay. It is a work that criticizes the idea that it is possible to control gravity that won the award, in 1953. The author was a young physicist, Bryce DeWitt. Later, Babson decided to create the Institute of Field Physics whose purpose would be pure research about the gravitational fields. Bryce DeWitt led the new institute, whose main office was established in Chapel Hill. In what follows we summarize very briefly the complicated story of gravitational waves, following mainly the work in [4] with some input from other sources [21, 22, 23]. Note that only a tiny part of the physicists that have contributed to the research of gravitational waves are mentioned here.

#### 2.1.1 The Role of the 1957 Chapel Hill Conference

The Chapel Hill conference in 1957 was of an immense historical significance for the study of gravity. It was the first conference of a series of "GR meetings", constituting the principal international meetings for scientists working in all areas of relativity and gravitation. This event provided a much-needed boost to gravitational research at a time when it was at a state of neglect. On January 18-23, 1957, a group of 40 physicists from several countries met at the University of North Carolina to discuss the role of gravitation in physics. The conference was driven by the younger generation of physicists. During six days, discussions focused on various topics:

unquantized and quantized General Relativity, its experimental tests, unified field theory, the dynamic of the universe, cosmological questions and gravitational waves. At that time, the debate over the existence and detectability of gravitational waves was still open. Technical discussions were initiated in order to answer the question about the effect a gravitational pulse would have on a particle when passing by. One of the major questions was to understand if a gravitational wave contains energy. During his presentation, the theoretical physicist Felix Pirani demonstrated that the relative acceleration of particles pairs can be associated to the Riemann tensor. This result was previously published in the article *On the physical significance of the Riemann tensor* [24]. It is a thought experiment from Richard Feynman, inspired by Pirani's article, that convinced most of the audience that gravitational waves carry energy and that it could be detected. Feynman's reasoning can be described briefly as follows: two rings of beads are placed on a bar and can move freely along it, as presented in the Fig 2.1. If a gravitational wave propagates perpendicular to the bar, the wave will generate tidal forces with respect to the midpoint of the bar. Because the bead rings can slide freely on the bar and in response to the tidal force, the bead rings will move with respect to each other. Hence it rubs the stick, and generates heat. This heating implies clearly that energy was transmitted to the bar by the gravitational wave. Feynman's argument was enough clear and efficient to plant a slightly fantastic idea in the mind of the young engineer Joseph Weber: to design a device that could detect gravitational waves.

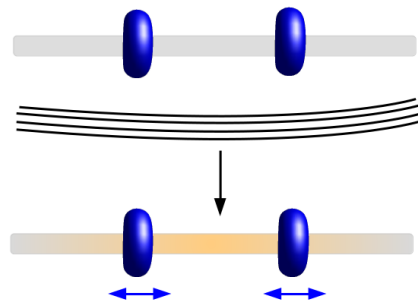


Figure 2.1: Sketch of the “Feynman’s sticky bead argument”

### 2.1.2 The first gravitational wave detectors: Weber bars

In 1960 Joseph Weber published an article that describes an experiment aiming at detecting gravitational waves. It took his team six years to build the device. In 1966, the first gravitational wave detector is constructed. Weber designed and built an aluminium cylinder about 66 cm in diameter and 153 cm in length, weighing 3 tons. A gravitational wave passing by the Weber's bar would compress and then tend the bar. He chose the size of the bar to reveal a gravitational wave frequency of about 1660 Hz, because at this time it was thought that this frequency is swept through during the emission in a supernova collapse which was one of the main

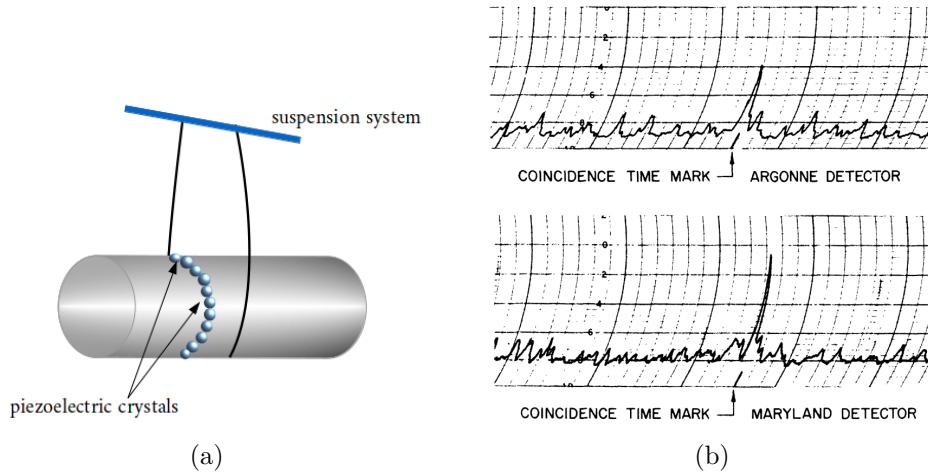


Figure 2.2: (a) Sketch of Weber’s bar cylinder and (b) Argonne National Laboratory and University of Maryland detector coincidence. The coincident signal was interpreted by Weber as the result of a gravitational wave [25]

sources studied at that time. The cylinder was suspended by a steel wire from a support built to isolate vibrations from its environment where the whole was placed inside a vacuum chamber. To complete the instrument, piezoelectric crystals were placed around the cylinder, see Fig 2.2. Piezoelectric crystals turned the mechanical signal into an electric signal. Weber built two similar detectors, one was at the University of Maryland and the other situated 950 km further, in Argonne National Laboratory. The data (radiofrequency output) from both detectors was sent by a telephone line. The idea of having two detectors separated by a large distance allowed Weber to discriminate spurious local signals that could mimic a gravitational wave signal. If a signal was not recorded “simultaneously” in both laboratories, then this signal would be considered as the result of a local disturbance. One of the main difficulties of the experiment was to isolate the detectors from the local sources of disturbances (spurious vibrations, local earthquakes, electromagnetic interferences, etc). In 1969 Weber published his results [25] announcing the first detection of gravitational waves, emanating from the center of our Galaxy. Thereafter Weber reported several significant gravitational wave detections and showed that these events imply that a lot of stellar mass became energy in the form of gravitational waves. Weber’s measurements indicate that  $\sim 1000M_{\odot}c^2$  in energy per year is being converted into gravitational waves [4]. Theoretical discussions began to try to determine what mechanism could make Weber’s result possible and it soon became evident that these experimental results were wrong. What is more, the strength and frequency of Weber’s gravitational waves signals, if real, would have required the sky to be filled with nearby astrophysical events on the scale of supernovae emitting gravitational waves. In 1972, several similar upgraded detectors were built and operated without Weber’s results being confirmed, leading to the invalidation of these results.

Finally some time later, the Russian physicist Vladimir Borisovich Braginsky showed that resonant bar detectors were severely affected by the uncertainty principle [26], which means that the quantum fluctuations were much larger than gravitational wave signals. By the late 1970s, everyone but Weber agreed that his claimed detections were spurious. Despite the mistake made, Weber has the merit for kick-starting the search for gravitational waves. With almost no funding, Weber continued to work on his devices until he died in 2000 [27].

## 2.2 Interferometric gravitational-wave detectors

### 2.2.1 Detection principle

In the previous chapter, we have shown that the effect of a passing gravitational wave is a relative change in distance between free-falling masses. At the first order, this relative variation in distance is proportional to the amplitude of the wave (see Eq. 1.49). The Michelson interferometer is the ideal system to detect such differential effect. It is a device that produces interference between two beams of light. The basic configuration of a Michelson interferometer is shown in Fig 2.3. The operation of the interferometer is as follows. Light from a laser source is split into two parts by a beam splitter mirror, which allows half of the radiation to be transmitted to one of the end of arms mirror. The other half of the radiation is reflected at  $90^\circ$  from the first and is transmitted to the other mirror. Then, both mirrors reflect the beams back toward the beam splitter. The two resulting beams are brought together to interfere. The merged beam is sent to a photodetector, a device which measures the brightness of the interference pattern.

From the principle of superposition, when two waves propagate, the resultant electric field at any point in that region is the vector sum of the electric field of each wave. The field at the photodetector is determined by the optical path difference  $\Delta L$  at the photodetector or by a related quantity, the phase difference:

$$\Delta\phi = \frac{2\pi}{\lambda} \Delta L, \quad (2.1)$$

with  $\lambda$  being the laser wavelength used as input beam. We can express this formula using Eq. 1.49<sup>1</sup>:

$$\Delta\phi = \frac{2\pi}{\lambda} [2L_0 h], \quad (2.2)$$

which shows that the phase shift is a fraction  $h$  of the total phase progression of the light in the round-trip arm. To understand the principle of detection we choose the coordinates system where the origin is on the beam-splitter and the  $x$  and  $y$  axes along the two arms. We assume that the beam-splitter and the end mirrors are suspended, only subject to gravity and fixed, this allows us to work in the traceless-transverse gauge (see Eq 1.33). We consider a gravitational wave normaly

---

<sup>1</sup>We are still in the long-wavelength approximation, i.e. the gravitational wave wavelength is much larger than the the arm length  $L_0$  of the interferometer.

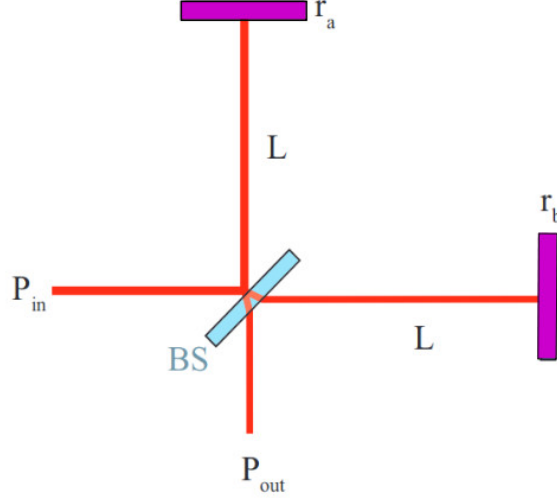


Figure 2.3: Scheme of a basic Michelson Interferometer. In purple the arm end mirrors, in blue the beam splitter mirror and in red the laser beam.

propagating to the detector's plane ( $z$  direction) characterized by a plus polarization. Thus, working with the perturbation metric given by Eq. [1.43](#), the equations for light propagation are given by:

$$\begin{aligned}
 0 = ds^2 &= (\eta_{\alpha\beta} + h_{\alpha\beta})dx^\alpha dx^\beta \\
 &= -dt^2 + (1 + h_+(t))dx^2 \quad \text{for the arm along the x axis,} \\
 &= -dt^2 + (1 - h_+(t))dy^2 \quad \text{for the arm along the y axis.}
 \end{aligned} \tag{2.3}$$

where the space-time interval  $ds$  between two neighboring points connected by a light ray remains null. We can now integrate these relations over the arm length  $L_0$ , which is assumed to be identical for both arms to not overload the calculations:

$$\begin{aligned}
 L_x &= \int dt = \int_0^{L_0} \sqrt{1 + h_+(t-x)} dx \\
 L_y &= \int dt = \int_0^{L_0} \sqrt{1 - h_+(t-y)} dy
 \end{aligned} \tag{2.4}$$

with  $L_x$  and  $L_y$  the optical path in the arms along the  $\mathbf{x}$  and  $\mathbf{y}$  direction respectively, and since we are working in the weak-field limit ( $h \ll 1$ ) we get:

$$\begin{aligned}
 L_x &\simeq \int_0^{L_0} [1 + \frac{1}{2}h_+(t-x)] dx \\
 L_y &\simeq \int_0^{L_0} [1 - \frac{1}{2}h_+(t-y)] dy.
 \end{aligned} \tag{2.5}$$

In our case, it can be assumed that the propagation time of the laser beam in the arms of the interferometer ( $x/c \leq L_0/c$ ) is negligible in front of the period of the

gravitational wave we are looking for. Or similarly that  $\lambda_{GW} \gg L_0$ , where  $\lambda_{GW}$  is the wavelength of the gravitational wave, this is the long-wavelength approximation. Hence we make the approximation that  $h_+(t)$  does not vary during the light travel of the photon:  $h_+(t-x) \simeq h_+(t)$ . This leads to:

$$\begin{aligned} L_x &\simeq L_0 + \frac{1}{2}L_0 h_+(t) \\ L_y &\simeq L_0 - \frac{1}{2}L_0 h_+(t). \end{aligned} \quad (2.6)$$

The phase shift (Eq. 2.2) induced by a passing gravitational waves is thus approximated by

$$\begin{aligned} \Delta\phi(t) &= \frac{2\pi}{\lambda}(2L_x - 2L_y) \\ &\simeq \frac{2\pi}{\lambda}(2L_0 h_+(t)), \end{aligned} \quad (2.7)$$

where the factor of 2 takes into account the round trip in the two arms. This shows that a measure of the phase-shift is a direct measure of the gravitational wave strain amplitude. By inverting this equation we define in our particular case a gravitational wave signal as

$$h(t) = h_+(t) = \frac{\lambda}{4\pi L_0} \Delta\phi(t), \quad (2.8)$$

For a Michelson interferometer, the power arriving to the detection photodiode,  $P_{out}$ , is given by [28]:

$$P_{out} = \frac{1}{2}P_{in} \frac{r_a^2 + r_b^2}{2} [1 + C \cdot \cos(\alpha + \Delta\phi)], \quad (2.9)$$

with  $P_{in}$  the input power and we assume that the interferometer is tuned to constant phase offset between arms given by  $\pi + \alpha + \Delta\phi(t)$ , where  $\alpha$  must be chosen, and  $r_a$  and  $r_b$  are the amplitude reflectivities of the ends mirrors of the Michelson interferometer.  $C$  is the contrast and it is defined as:

$$C = \frac{2r_a r_b}{r_a^2 + r_b^2}. \quad (2.10)$$

For perfectly reflecting mirrors  $r_a = r_b = 1$ . In the current detectors the mirrors are almost perfect and so the output power  $P_{out}$  becomes:

$$P_{out}(t) \simeq P_{in} \sin^2 \left[ \frac{\alpha + \Delta\phi(t)}{2} \right]. \quad (2.11)$$

The interferences are destructive if  $\alpha = 0(2\pi)$  and it is usually said that the interferometer is “on the dark fringe”. For a small shift phase one has:

$$P_{out}(t) \simeq P_{in} \left[ \sin^2 \frac{\alpha}{2} + \frac{1}{2} \Delta\phi(t) \sin \alpha \right] \quad \text{where} \quad \Delta\phi \ll 1. \quad (2.12)$$

Thus at the output of the interferometer a gravitational wave is detected as a power change, proportional to a variation in the phase-shift  $\Delta\phi(t)$ , which gives a direct measure of the the gravitational wave strain amplitude  $h(t)$ .

## 2.2.2 Angular response

So far we have only considered the case of a linearly polarized gravitational wave ( $h = h_+$  and  $h_\times = 0$ ) that propagates perpendicular to the detector plan. We consider now the general case of a gravitational wave with arbitrary direction and polarization, to understand the direction dependence of the response of the interferometer to the gravitational wave. A gravitational wave is coming from a direction given by the usual spherical coordinates  $(\Theta, \Phi)$ , relative to the detector's axes. The polarization of the gravitational wave is a combination of a plus and cross polarization, that are rotated with an angle  $\psi$  in the plan of the sky (the polarization axis are specified by  $\Psi$ ). The position of the source relative to the detector, that is in the  $xy$  plane with arms along the axes, is shown in Fig 2.4. The detector can

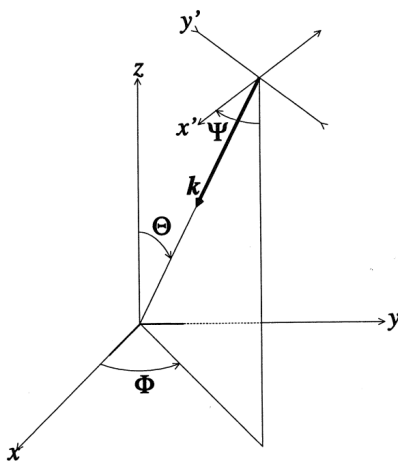


Figure 2.4: Detector frame  $(x, y, z)$  and Source frame  $(x', y', z')$  representations. The angle  $\Theta$  and  $\Phi$  are the usual polar coordinates of the wave's direction of travel as measured in the detector's frame. The angle  $\Psi$  is a measure of the polarization angle of the wave and represents a rotation about the  $z'$  axis. Figure taken from [29].

be assimilated to an “antenna” (and not a telescope) because its size ( $L_0$ , length of the arms) is small compared to the wavelengths ( $\lambda_{GW}$ ) it is meant to detect. The response of the detector depends on the sky localisation angle of the source and the gravitational wave polarization. By performing different projections [30], the response of the interferometer (for which the angle between the arms is  $\pi/2$ ) can be written as:

$$h(t) = F_+(\Theta, \Phi, \Psi)h_+(t) + F_\times(\Theta, \Phi, \Psi)h_\times(t), \quad (2.13)$$

where  $F_+$  and  $F_\times$  are the antenna pattern functions for the two polarizations. These functions describe the response of the detector to the two gravitational wave polarizations and define the region of space around the earth within which a source

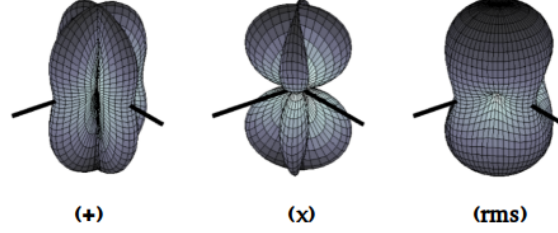


Figure 2.5: Antenna response pattern for a Michelson interferometer in the long-wavelength approximation ( $\lambda_{GW} \gg L_0$ ). The interferometer is located at the center of each pattern. The thick black lines indicate the orientation of the interferometer arms. The distance from a point of the plot surface to the center of the pattern is a measure of the gravitational wave “sensitivity” in this direction. The pattern on the left is for plus polarization (+), the middle pattern is for cross polarization ( $\times$ ), and the right-most one is for the root mean square (rms). Figure taken from [31].

should be detected. Using the geometry in Fig 2.4 one can show that:

$$\begin{aligned} F_+(\Theta, \Phi, \Psi) &= \frac{1}{2}(1 + \cos^2 \Theta) \cos 2\Phi \cos 2\Psi - \cos \Theta \sin 2\Phi \sin 2\Psi \\ F_\times(\Theta, \Phi, \Psi) &= \frac{1}{2}(1 + \cos^2 \Theta) \cos 2\Phi \sin 2\Psi + \cos \Theta \sin 2\Phi \cos 2\Psi. \end{aligned} \quad (2.14)$$

The maximum value of both  $F_+$  and  $F_\times$  is 1. The directional function for unpolarized gravitational waves  $F_{un}$  can be found by taking the quadratic sum of antenna pattern functions for the two polarizations:

$$F_{un} = \sqrt{F_+^2 + F_\times^2}. \quad (2.15)$$

Figure 2.5 illustrates the antenna-pattern functions for the plus polarization (+), the cross polarization ( $\times$ ), and for a combination of the polarization (rms). The interferometer is most sensitive to the gravitational propagating in a direction orthogonal (z-direction) to the detector plane with the polarization axes along the two arms. The interferometer does not produce any signal for a gravitational wave along the z-axis with the polarization axes  $45^\circ$  off the two arms of the interferometer. The beam patterns for the plus and cross polarization are different, that reflects the fact that it is possible to distinguish tensor polarization modes by means of typical two-arms interferometer. We also observe that the angular response for a combination of the two types of polarization is almost uniform for all sky direction, except the bisectors. Figure 2.6 shows that the angular response is nul for sources localized along the bisectors of the arms of the interferometers. That means that an interferometer is “blind” to some sky localisation. Thus we understand one of the interest to use a network of interferometers that fill in each other’s directional “holes”, increasing the overall detection volume.

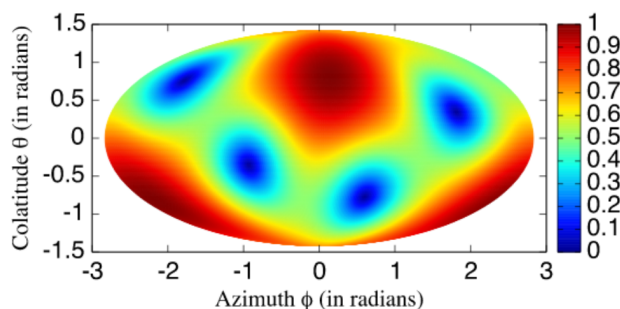


Figure 2.6: L-shape detector angle-average sky maps (Advanced Virgo interferometer). The color scale shows the distribution of the root mean square of the antenna pattern volume-averaged over the polarization ( $\Psi$ ) and the sky localisation angles ( $\Theta$ ,  $\Phi$ ). Figure taken from [32].

## 2.3 Fundamental noise sources

The detector output  $s(t)$  is a single time series which includes the gravitational-wave signal:

$$s(t) = n(t) + h(t), \quad (2.16)$$

where  $h(t)$  contains all the gravitational-wave informations and  $n(t)$  is the detector noise. Ideally, the noise time series  $n(t)$  is well defined by a sum of contribution described by an autocorrelated Gaussian process (colored noise). In most cases these contributions can be considered as independent. A good quantity that characterizes the noise of the detector is the single-sided power spectral density  $P_s(f)$  defined in Chap. 4.  $P_s(f)$  is a measure of the amount of time variation in the time series  $n(t)$  that occurs with frequency  $f$ . A better quantity to work with is the amplitude spectral density  $A_n(f)$  defined as the square root of the power spectral density. The amplitude spectral density  $A_n(f)$  is expressed in  $1/\sqrt{\text{Hz}}$ . The advantage of this object is that it is linear in the amplitude of the noise. As we will see in Chap. 4 a relevant figure of merit in comparing a gravitational-wave signal with noise is the signal to noise ratio (SNR). This quantity is proportional to the strain signal and the SNR is a perfect figure of merit for the signal strength if the detector noise is a Gaussian noise, which is clearly not the case in general.

A Michelson interferometer is designed to detect a phase difference  $\Delta\phi$ . Using Eq. 2.7, we estimate the phase shift produced by a passing gravitational wave to be of order  $\Delta\phi \sim 10^{-11}$  rad of a fringe, for typical wave amplitude of  $h \simeq 10^{-21}$ , a length arms of  $L_0 = 3$  km and a reference laser wavelength of  $\lambda = 1064$  nm. Thus we understand that the interferometer must be isolated from a host of harmful noise sources that could perturb the measure. In this section, we focus our attention on understanding the principal contributions of the fundamental noise sources to the total noise  $n(t)$ . These are sources of noise which come from intrinsic limits to the

detector. As we shall see, each of these terms dominates at a certain frequency range.

### 2.3.1 Shot noise

One of the fundamental noise for an interferometric detector is related to the quantum nature of light. It has two faces where either one of may dominate depending on the circumstances. We have seen that gravitational waves induce a phase difference  $\Delta\phi$  between the two interferometer arms. What is measured by the photodetector is the output light power  $P_{out}$ . So the phase shift can be determined by a careful measurement of the output light power and a first limit comes from the precision with which we can measure this power. To see why, recall that measuring  $P_{out}$  is equivalent to determining the number of photons of a certain energy arriving during a measurement interval.

We model the light flux at the photodetector as a set of discrete photons whose arrival times at the photodetector are statistically independent. Each photon carries an energy:

$$E_\gamma = \frac{2\pi\hbar c}{\lambda} \quad (2.17)$$

where  $\hbar$  is the reduced Planck constant. The mean number of photons  $\langle N \rangle$  arriving during a time  $\tau$  is given by:

$$\langle N \rangle = \frac{P_0\tau\lambda}{2\pi\hbar c}. \quad (2.18)$$

with  $P_{out} \equiv P_0$ . The mean number of photons  $\langle N \rangle$  is described by a Poisson distribution, which implies the uncertainty  $\sigma_N = \sqrt{\langle N \rangle}$ . Thus the power measured is a random variable described by its mean  $\langle P \rangle = P_0$  and by its standard deviation:

$$\begin{aligned} \sigma_P &= P_0 \frac{\sigma_N}{\langle N \rangle} \\ &= \sqrt{\frac{P_0 2\pi\hbar c}{\tau\lambda}}. \end{aligned} \quad (2.19)$$

we can interpret such statistical power fluctuations as equivalent to phase shift fluctuations:

$$\begin{aligned} \sigma_\phi &= \frac{\sigma_P}{P_{in} \times \frac{1}{2} \sin \alpha} \\ &= \frac{1}{\cos(\frac{\alpha}{2})} \sqrt{\frac{2\pi\hbar c}{\tau\lambda P_{in}}}, \end{aligned} \quad (2.20)$$

where we used Eq. [2.11](#) in case of no gravitational waves are present ( $\Delta\phi = 0$ ). The fluctuations on the phase shift is inversely proportional to  $\cos(\frac{\alpha}{2})$ , one of the first interesting results. By choosing  $\alpha = 0$ , we minimize the phase fluctuations. It is then more convenient to work on the dark fringe. In terms of the strain sensitivity  $h$  the photon shot noise is described by an amplitude spectral density of magnitude,

see [29]:

$$h_{shot} = \frac{1}{L_0} \sqrt{\frac{c\hbar\lambda}{4\pi P_{in}}} \quad 1/\sqrt{\text{Hz}}. \quad (2.21)$$

For a  $L_0 = 3$  km kilometer long Michelson interferometer with a laser input power  $P_{in} = 50$  W and a laser wavelength  $\lambda = 1064$  nm, the order of magnitude of the strain amplitude is

$$h_{shot} \simeq 6 \times 10^{-21} \quad 1/\sqrt{\text{Hz}}, \quad (2.22)$$

which is of the same order of magnitude of the amplitude expected for a gravitational wave.

Then if we want to be able to confidently detect and study a gravitational wave signal we need to decrease the shot noise. There are three parameters on which we could play. The photon shot noise depends on the length of the arm  $L_0$ , the input light power  $P_{int}$  and the laser frequency  $f = c/\lambda$ . As a matter of common sense, we realize that the length of the arms cannot extend for hundreds of kilometres. However it is possible to increase the photon path if they take many trips back and forth before reaching the photodetector. This is done by using Fabry-Perot cavities in the arms. The basic idea consists in adding two input mirrors and forming Fabry-Perot cavities with the end mirrors of the Michelson, where the light travels between parallel mirrors. To increase the light power, another mirror is added between the laser source and the beam splitter. This is the power recycling mirror which “recycles” the light in the interferometer. Since the interferometer is working on a dark fringe, that means that the two output beams that recombine at the beam splitter are in destructive interference. Thus no light should arrive to the detection photodiode, the power ends up coming back towards the laser. By adding this mirror the light power is thus recycled in order to be used. The shot noise is the dominant contribution to the noise detector at high frequency<sup>2</sup>.

### 2.3.2 Radiation pressure noise

We have treated so far the limit that a quantized world set on the precision of a measurement. We continue with a discussion on how the measurement process disturbs the system under measurement. Radiation pressure occurs in interferometers because photons transfer momentum to the end of arms mirrors when they are reflected. The difference between the radiation pressure in the two arms can cause a change in phase, which can mimic a gravitational-wave signal. If we consider the simplest Michelson interferometer and we assume that the beam splitter mirror is much more massive than the two end of arms mirrors (test masses), it can be shown in expressing the momentum imparted to a single test mass and by using the Eq. [2.18]

<sup>2</sup>Considering a more realistic case, the expression of  $h_{shot}$  is modified. A Fabry-Perot cavity acts as a low-pass filter of high frequency cut-off  $f_c$ . The expression of  $h_{shot}$  is multiplied by a factor  $\sqrt{1 + \left(\frac{f_{GW}}{f_c}\right)^2}$  [17] to take into account this effect.

that the radiation pressure noise is given by [29]:

$$h_{rp}(f) = \frac{1}{mf^2 L_0} \sqrt{\frac{\hbar P_{in}}{2\pi^3 c \lambda}}, \quad (2.23)$$

where  $m$  is the mass of the end of arms mirrors. This noise is reduced by increasing the mass of the mirrors. The radiation pressure noise dominates at low frequencies.

There is a counterplay between these two sources of noise associated with the quantum nature of light. Indeed the radiation pressure noise has opposite scaling with the shot noise with the light power. There is an optimal power laser which minimizes the total quantum noise at a particular frequency. Using this optimal power results in the minimum achievable quantum noise for an interferometer, called the “standard quantum limit”. This quantum limit can be sidestep by the use of squeezed states of light that can show sub-Poissonian counting statistic. Indeed, for squeezed states of light the probability of detecting a photon decreases with the more photons that are already detected in the same time interval. Thus the photons do not individually appear randomly upon detection. There are quantum correlations between the photons.

### 2.3.3 Seismic noise

Seismic noise is generated by large-scale motion of the Earth from seismic waves, earthquakes, ocean waves on continental coastlines, and human activity [3]. This noise causes motion on the test masses, and is managed through the use of pendulum. To isolate a mass we can suspend it by mean of spring. From the point of view of its mechanical response the system acts as an harmonic oscillator with a resonant frequency  $f_0$ . If we consider a mass  $m$  attached with a spring of constant  $k$  to the ground, and look at the one dimensional problem, with  $x_g$  the position of the ground and  $x$  the position of the mass, the equation of motion is:

$$m \frac{d^2 x}{dt^2} = -k(x - x_g), \quad (2.24)$$

where we have neglected the fluid friction or the damping from internal friction in order to not complicate the calculations unnecessarily [4]. In the frequency domain the transfer function is given by:

$$\left| \frac{x}{x_g} \right| = \frac{f_0^2}{f_0^2 - f^2}, \quad (2.25)$$

at low frequency, the spring is rigid  $x/x_g \simeq 1$ . In the high frequency limit we get:

$$\left| \frac{x}{x_g} \right| \simeq \frac{f_0^2}{f^2}, \quad (2.26)$$

---

<sup>3</sup>Also called anthropogenic noise.

<sup>4</sup>The purpose of this section being simply to clarify the reader’s understanding of the physical principle behind a complex isolation system.

thus, at large frequencies compared to  $f_0$  the motion in response to the spring is negligible, causing the mass to be isolated from the outside world. The ground motion is finally concentrated around the resonant frequency  $f_0$ . The vibration isolation system of the pendulum that suspends the mass is suspended again by a chain of many pendulums. Since a set of many oscillators, all with resonant frequency  $f_0$ , gives an identical function that can be approximated in the high frequency domain to:

$$\frac{x}{x_g} \simeq \left( \frac{f_0^2}{f^2} \right)^N, \quad (2.27)$$

in order to filter the ground motion by repeatedly applying this factor to all degree of freedom. We will see later how this principle is used in practice in current detectors.

### 2.3.4 Thermal noise

Dissipation which produces random displacements in mechanical systems, called thermal noise. It has different origins. The first one is due to dissipation in the wires used to suspend the test masses; this is called the suspension thermal noise. The second one is due to dissipation processes inside the test masses themselves which leads to a deformation of the mirror surface, this is the mirror thermal noise.

These noises dominate in the mid frequency range. The fluctuations are well described by modeling the system as an ideal oscillator and using the fluctuation-dissipation theorem. It has been shown that they can be minimized by using mirrors of large mass and working at low temperature. Moreover the mirrors are characterized by a mechanical factor of quality, the  $Q$ -factor, which measures the internal losses in a system or how long it takes a resonator to decay in amplitude. The higher the  $Q$ -factor the lower the internal dissipations. We understand now the interest to find and use high- $Q$  materials (fused silica, sapphire or silicon) that offer the opportunity to reduce the thermal noise within the detection band.

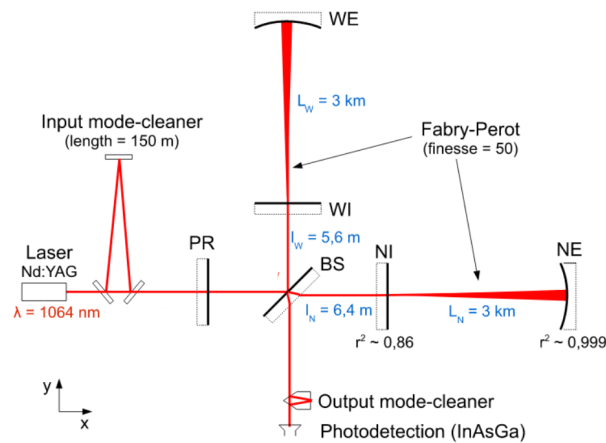
## 2.4 Current ground-based detectors network

### 2.4.1 Virgo and Advanced Virgo

The construction of the Virgo gravitational wave detector was decided in 1993-1994 by France and Italy and was finished building in 2003. It is located in Cascina, near Pisa in Italy. Virgo gets its name from the Virgo galaxy cluster for which the detector was supposed to be sensitive enough to detect a signal. Figure 2.7 shows an aerial view of the Virgo interferometer, we notice the two 3 km long arms of the Michelson, oriented towards north and west. In order to better understand how an interferometer used to search for gravitational waves works, an optical shema of Virgo's initial configuration is presented in the Fig 2.7. Virgo is a Michelson laser interferometer with three main optical elements: the two end of arms mirrors noted WE (west-end) and NE (north-end) on the figure, and the beam-splitter mirror (BS), which is placed at 45 degrees to divide the incident beam into two beams. The



(a)



(b)

Figure 2.7: (a) Aerial view of the gravitational wave detector Virgo. (b) Optical scheme of Virgo during the second science run (VSR2), figure taken from [33].

laser is a solid-state laser which uses a crystal Nd:YAG (neodymium-doped yttrium aluminum garnet) as active laser medium. It typically emits light with a wavelength of  $\lambda = 1064$  nm, in the infrared. The input power of the laser was  $P_{in} \sim 20$  W. The end of arms mirrors have a mass of  $m \sim 20$  kg and a diameter of 35 cm. The large mass of the mirrors allows to minimize the thermal noise and the radiation pressure noise, see Sec. 2.3. They are made of high quality fused silica and coated with reflective deposit (at 1064 nm), reflecting almost all the incident light (reflectivity of  $r \simeq 1$ ). In addition, a polishing is applied in order to reduce to a minimum the roughnesses present on the surface of the mirrors (below the angstrom). One of the advantage is to minimize the laser power losses. Two input mirrors (WI and NI) form Fabry-Perot cavities of 3 km long with the end mirrors, whose role is to increase the optical path. The finesse of the cavities which is a quantity that depends on

the reflectivities of the mirrors was  $F = 50$  [33]. The beam makes an average of  $2F/\pi \approx 30$  [28] round trips in Virgo's cavities, which amplifies the phase-shift (see Eq. 2.7) to:

$$\Delta\phi(t) = \frac{4\pi}{\lambda} L_0 h(t) \cdot \frac{2F}{\pi}. \quad (2.28)$$

The laser operates so that the light that recombines at the beam splitter (BS) returns to the laser, yielding to a dark fringe. An other mirror that is partially reflective, called power recycling mirror (PR), is added between the laser source and the beam splitter (BS). This ensures that the light returning from the interferometer and reflected by this mirror is in phase with the incident light. This is made to enhance the circulating power inside the interferometer. Between the laser and the PR mirror, the emerging beam is filtered thanks to three mirrors which form a triangular cavity, called the Input Mode Cleaner (IMC). The main purpose of the input mode cleaner is to stabilize the frequency of the laser. The Output Mode Cleaner (OMC) is another cavity used to reject unwanted spatial and frequency components of the light, before the signal is detected by the main photodetector. We have seen that one of the fundamental noise is seismic noise, consequently to achieve a good sensitivity it becomes necessary to provide both vertical and horizontal isolation from seismic noise to the mirrors of the interferometer. This need is met in Virgo by a vibration isolation stack. The Virgo Super-Attenuator was built to provide a nearly isotropic isolation. It is composed by an inverted pendulum that consists of a three 6m-long aluminium legs each fixed to the ground, and a series of wires and mechanical filters attached to the top of the inverted pendulum. Moreover, since near the resonant frequency, the seismic noise is amplified by the resonance modes of the isolation stages, an active control of the super-attenuator is needed. This is done by the use of actuators<sup>5</sup>. The net effect of this mechanic is to reduce the ground motion by 14 orders of magnitude in the sensitive band at a frequency  $f > 10$  Hz. The final suspension stage at the test masses uses low-dissipation suspension components to minimize the thermal noise. Finally, to limit fluctuations in the air index that result in fluctuations in laser power, the whole interferometer is located in ultra-high vacuum. Moreover, the vacuum isolates the test masses from external acoustic noise and temperature fluctuations. The pressure is of order  $10^{-7}$  mbar, which makes Virgo the largest ultra-high vacuum installation in Europe.

Between 2003 and 2007, Virgo went through a commissioning phase to reach the design sensitivity of  $10^{-21}/\sqrt{\text{Hz}}$  with a frequency band that extends from 10 Hz to 10 kHz. Virgo started science runs in May 2007 and no gravitational wave signal was detected. Virgo continued commissioning through late 2011.

Advanced Virgo [34] is an upgrade of the Virgo detector. It was designed to have a sensitivity an order of magnitude better than that of initial Virgo, which translates in three orders of magnitude in terms of volume of observable Universe. For this

---

<sup>5</sup>An actuator is a component of a machine that is responsible for moving and controlling a mechanism or system.

reason it is called second generation detector. The installation of the Advanced Virgo equipment started in mid 2012 and was completed in 2016. Most of the sub-systems was improved. The finesse of the arm cavities increased a lot, up to  $F \simeq 450$ . Advanced Virgo use the Virgo laser, capable of providing up to 60 W. However, for technical reason less than 20 W was really used. As seen before, a gain in power leads to an increase of the radiation pressure noise. To counterbalance this effect heavier mirrors ( $m \simeq 42$  kg) have been installed, this also has the advantage to reduce further the thermal noise. The mirrors have been also better polished to reach a better flatness in the central area of the test masses, in order to decrease the scattering of light. A new coating of mirrors is used to limit as far as possible the mechanical losses that limit the sensitivity of the detector due to the associated mirror thermal noise. On the other hand, this allows to reduce again the absorption of light in the coating that induces a limit in the amount of laser power that can be stored in the detector. In order to limit phase noise caused by part of the light being back-scattered into the interferometer, baffles designed to absorb this light are suspended around the mirrors. The laser beam was also increased on the test masses. In order to accommodate this larger beam the vacuum pipes had to be replaced with larger ones. The Super-Attenuators have been also modified to include a better active control in high seismicity conditions. Four magnets, controlled by coils, are attached to each mirrors, then the position of the mirrors is controlled by acting on the current sent to the coils. Figure 2.8 shows the gain in sensitivity between Virgo and Advanced Virgo.

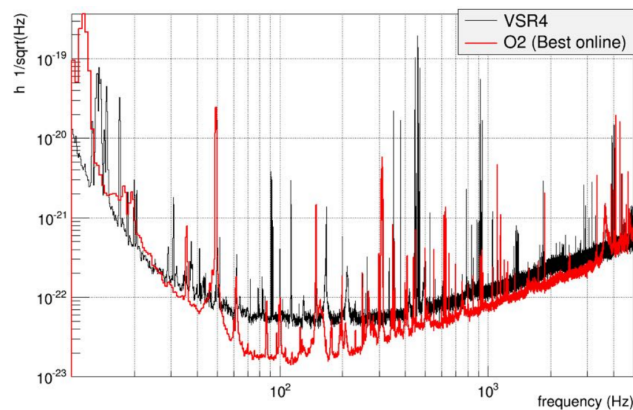


Figure 2.8: Best Advanced Virgo sensitivity in 2017 (O2) compared to the best Virgo sensitivity in 2011 (VSR4).

Most of the efforts in bringing an interferometer to best sensitivity is dealing with the reduction of noise sources that are not fundamental. Advanced Virgo is continuously monitored by several sensors placed in key points around the detectors, e.g. seismometers, magnetometers monitoring the magnetic field, acoustic probes used to measure a pressure change in the acoustic frequency band, thermometers, pressure and humidity probes or lightning detectors to detect radiofrequency disturbances

caused by close storms. Then data collected by the monitoring system are recorded together with the interferometer output and studying in order to try to discriminate noise from gravitational-wave signal. In parallel, a commissioning activity is required and of paramount importance to understand the observed noise in Advanced Virgo. Noise sources can be classified according to their origin, there are three main categories of noise in addition to the fundamental noises.

### Technical noises

Those noises are coming from the actual implementation of the detector. We give two examples of the most critical noise sources. Very small imperfections arising in the production and polishing of the mirrors can produce scattered light inside the interferometer. There are several scattered light sources. It is generated from scattering of the light beam by molecules or from diffraction from the edges of some optics. This light can redirect a small fraction of the laser light towards the walls or other components of the instruments. If this light recombines with the main beam it will generate a spurious signal in the readout photodetectors. The solution adopted is to operate the long arms at ultra high vacuum, and to place baffles and diaphragms inside the vacuum chamber [34]. Another typical technical noise is produced by fluctuations in the intensity and frequency of the laser, which can result from some imperfections in the optics, for example the mirrors reflectivity. To reduce this noise, a control system is implemented [35].

### Environmental noises

Environmental noise is as its name suggests, an external noise to the detector. These noises are multiple and they are often difficult to predict and to model. Even if the detector is well isolated from the environment (suspended mirrors and optical benches seismic, in-vacuum beams, etc) it is not enough. Acoustic noise produced by planes or thunder are part of the environmental noises. Magnetic noise also belongs to this category. The external magnetic field interferes with some part of the detector, for instance the mirrors through the magnets attached on their surface which are part of the actuator system used to exert control forces on the test masses. The current detectors are continuously monitored by several environmental sensors placed in key points around the detectors. We will see later how these probes are used to discriminate a real gravitational wave signal from a noise.

### Control noises

The different subsystems of Advanced Virgo are constantly controlled in order to maintain a correct operating point of the detector needed to reach the best sensitivity. Noises can be introduced in the subsystems or amplified by this control, for example by the actuators used to control the position of the mirrors. Another example is given by noises present in the error signals used to calculate the correction that

should be provided to the optics to bring them to their operating point.

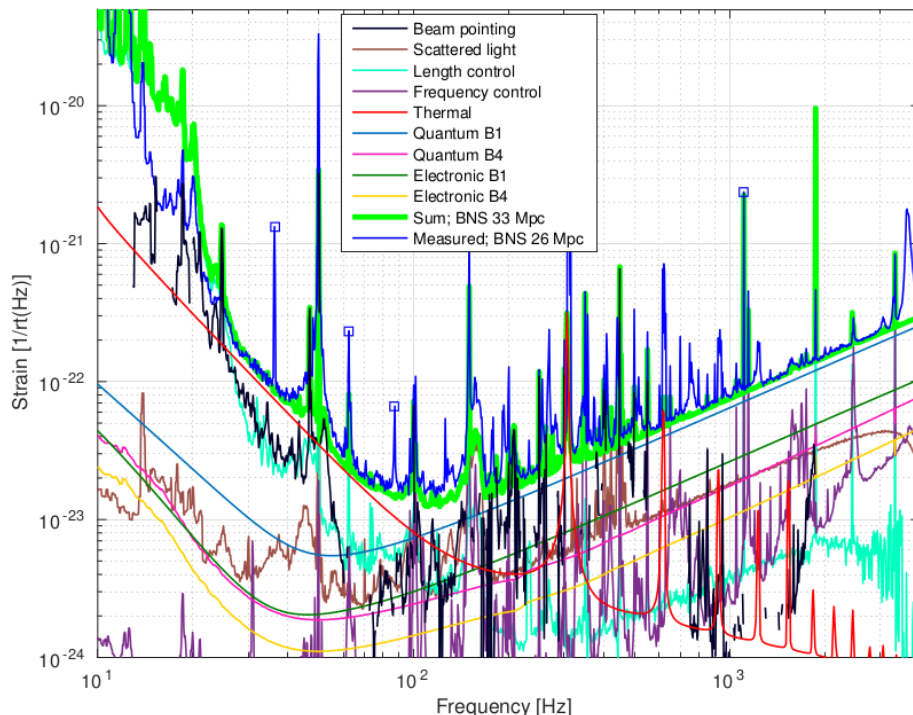


Figure 2.9: Summary of Advanced Virgo noise budget during O2. The measured sensitivity is shown in blue, and the sum of all the understood noise sources is shown in light green. Only the main contribution to the noise are shown. The difference between the measured sensitivity and the sum of known noises shows that most of the noise detector is understood and well modeled

Finally to understand the noise in Advanced Virgo, we should consider all the noises described above to estimate the total detector noise  $n(t)$ . This is done by modelling or measuring each contribution to the detector noise with an auxiliary sensor. By combining all the noise level estimations we derive an expected noise budget for Advanced Virgo. That is the decomposition of the amplitude spectral density of the total detector noise  $n(t)$  into different contributions. Figure 2.9 presents the noise budget for Advanced Virgo in August 2017. At high frequency, above 200 Hz it is the computed shot noise that dominates (magenta and blue curve) through the photodiodes that monitor the interferometer<sup>6</sup><sup>7</sup>. In addition, the photodiode electronic noise contributes also (yellow and dark green). We notice the pollution

<sup>6</sup>photodiode B1: power at the detection port, that measures directly the gravitational wave signal.

<sup>7</sup>photodiode B4: power reflected in the power recycling cavity, that is used as an error signal for frequency stabilization.

produced by scattered light inside the interferometer by the presence of large number of bumps and lines at high frequency (brown curve). We also observe the presence of large bumps originating from the laser frequency noise (purple curve). In the middle frequency range between 30 Hz and 600 Hz several features are the results of unstable pointing performance of the input laser (black curve), The thermal noise of the steel wires used to suspend the optics dominate between 25 Hz and 100 Hz (red curve). Finally, one of the control noise is the largest contribution below 25 Hz (cyan curve). The seismic noise contribution is negligible at the considered frequencies, it is why it is not presented on this figure.

## 2.4.2 LIGO and Advanced LIGO

From 2002 to 2007, the Laser Interferometer Gravitational-wave Observatory (LIGO) operated kilometer-scale Michelson interferometers [31]: one 4-km interferometer (H1) and one 2-km interferometer (H2) in Hanford (Washington) and another 4-km interferometer (L1) in Livingston (Louisiana). The two interferometers at Hanford was in the same vacuum chamber which was a considerable source of noise, for this reason H2 has been removed. Another major difference with Virgo is the seismic isolation of the lightest end of arms mirrors ( $m \simeq 10$  kg) which used a four stage single pendulum. From 2010 to 2015, the LIGO detectors collected no data, instead undergoing a series of upgrades to become Advanced LIGO.

The Advanced LIGO detectors [36] have undergone several changes, and were designed to be 10 times more sensitive than initial LIGO, and promised to increase the volume of the observable universe by a factor of  $10^3$ . By comparison with Advanced Virgo (during O2), a signal recycling mirror was added between the beam splitter mirror and the photodetector. This has the advantage to influence the detector bandwidth in order to optimize its response to expected astrophysical signals<sup>8</sup>, while the position of this mirror changes the frequency of the maximal sensitivity. The seismic isolation of the test masses became a quadruple pendulum system [37]. In each suspension system there are two chains (each chains contains four masses) of suspended masses: the main chain and the reaction chain, this last chain is used to apply forces onto the optics . To reduce the thermal noise, fused silica is used to suspend the lower two stages of the isolation system, since its level of internal friction is roughly about  $10^3$  times lower than steelwires used in initial LIGO. The laser is capable of producing up to 180 W (much more than the laser used in Advance Virgo), but only 22 W [35] were used in the first observing run, then it increases up to 30 W [38], during the second observing run. Finally, to reduce the quantum noise squeezed states of light was introduced [39, 40, 41]. The Advanced LIGO detectors started their first data taking in September 2015.

---

<sup>8</sup>Today signal recycling allows the resonance of the interferometer as a whole to be altered to boost signals from coalescing black hole and neutron star systems.

### 2.4.3 Observing Runs

During an observing run the detector is in optimal conditions to take data useful for physics analyses. However keeping the detectors in optimal conditions is complex and a variety of disturbances interfere with this process, for example seismic difficulties such as earthquakes, or high-speed winds. A useful quantity to define the sensitivity of a detector is given by the binary-neutron-star (BNS) inspiral horizon. It gives the distance at which a single detector could observe a pair of  $1.4M_{\odot}$  neutron stars optimally oriented, with a SNR of 8. The BNS range is the average horizon for

Run	Start time	End time	BNS range H1 (Mpc)	BNS range L1 (Mpc)
S4	February, 2005	March 23, 2005	8	7
S5	September, 2007	July 7, 2009	16	16
S6	July, 2009	October, 2010	21	20
O1	September, 2015	January 19, 2016	82	75
O2	November, 2016	August 26, 2017	82	100

Table 2.1: Observation runs for LIGO and Advanced LIGO. We give the maximum average BNS range value reached during the run. The data are taken from [42] [35] [38].

Run	Start time	End time	BNS range (Mpc)
VSR1	May, 2007	October, 2007	4
VSR2	July, 2009	January, 2010	9.5
VSR3	August, 2010	October, 2010	7.3
VSR4	June, 2011	August, 2011	11
O2	August 01, 2017	August 26, 2017	28

Table 2.2: Observation runs for Virgo and Advanced Virgo. We give the maximum average BNS range value reached during the run. The data are taken from [43] [42]

an uniform distribution of source in the sky with an averaged orientation. The horizon is about  $\sim 2.6$  the BNS range. During an observing run the range of each detector varies significantly on hourly time-scales, sometimes by few percent. This is mainly due to the noise variations. Table 2.1 and Tab 2.2 summarize the observation run periods for Virgo/Advanced Virgo and LIGO/Advanced LIGO, in addition the corresponding BNS range is indicated for each detector. We focus on the first two run of Advanced LIGO and Advanced Virgo.

The first observing run of Advanced LIGO is called O1. It started on September 12, 2015 and finished on January 19, 2016 [35]. The duty cycle of each detector defines the amount of science quality data taken over a period of observing time. The average duty cycle for H1 and L1 was respectively of 59% and 51%. The total coincident analysis time is 51.5 days. It is only a fraction of the total run duration and it is explained by the fact that data are analyzed only when both detectors are operating in their nominal state. Even if not yet operating at design sensitivity,

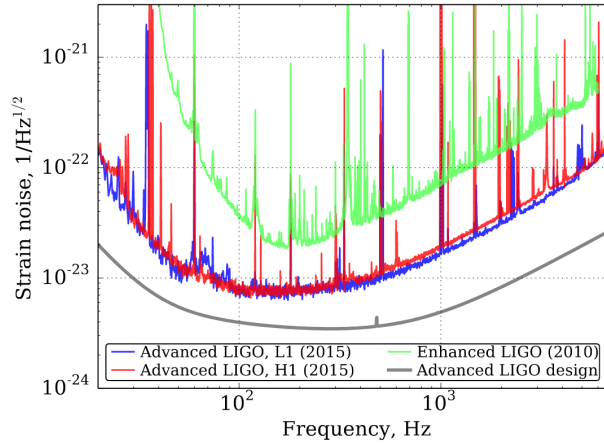


Figure 2.10: The strain sensitivity for the LIGO Livingston detector (L1) and the LIGO Hanford detector (H1) during O1. Also shown is the noise level for the Advanced LIGO design (gray curve) and the sensitivity during the final run in 2010 (S6) of the initial LIGO detectors. Figure taken from [35].

both detectors H1 and L1 reached an instrument noise 3-4 times lower than in the first generation detectors in their most sensitive frequency band: 100 Hz for H1 and 300 Hz for L1. Around 100 Hz, the strain sensitivity was  $8 \times 10^{-24} / \sqrt{\text{Hz}}$  for both detectors, as seen in Fig 2.10. Another figure of merit for Advanced LIGO detectors is their BNS range shown in Fig 2.11. By comparison with the initial LIGO detectors the average BNS range increased respectively by a factor 4 for L1 and 3.5 for L1. This gain in sensitivity improved significantly the observable volume of space that can be observed by a factor roughly 70 for L1 and 40 for H1. This enabled Advanced LIGO to detect for the first time a gravitational wave signal.

The second observing run (O2) started on November 30, 2016 to August 25, 2017. For technical reasons, 8 more months was needed by Advanced Virgo to reach a sufficient sensitivity and to join the Advanced LIGO detectors. The monolithic suspensions broke which resulted in a considerable delay. After months of investigation, the cause of this accident was finally understood: the silica fibers of the suspension have been weakened by grains of dust, causing kinds of fractures. The best solution was to fall back to steel wires. In addition, Advanced Virgo had an intense period of commissioning where noise investigation was crucial to gain in sensitivity. Finally, Advanced Virgo officially joined the O2 data taking period on August 1st, 2017 at 10:00 UTC. The average duty cycle was about 85%, which was higher than for Advanced LIGO detectors. It is due in part to the fact that Advanced Virgo was taking data during the summer where the environmental conditions are optimal. We often find in the winter months the duty cycle of the detectors to be less compared to the summer months. Indeed bad weather conditions (storms, strong winds, rough seas ...) can significantly prevent the detector from operating properly. This is what happened in Virgo, in August 11 and 12 where strong microseismic activity was

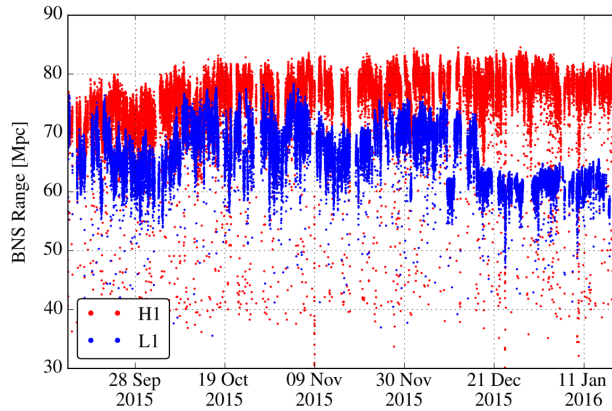


Figure 2.11: Time evolution of Advanced LIGO detectors BNS range over the O1 run. The sensitivity drop in the L1 interferometer at the end of the run was caused by electronics noise at one of the end stations. Figure taken from [35].

present due to bad weather. The evolution of the BNS range achieved by Advanced Virgo during the O2 data taking period is shown in Fig 2.12. We notice that the BNS range is stable over time with an average of 26 Mpc. In Advanced LIGO, the L1

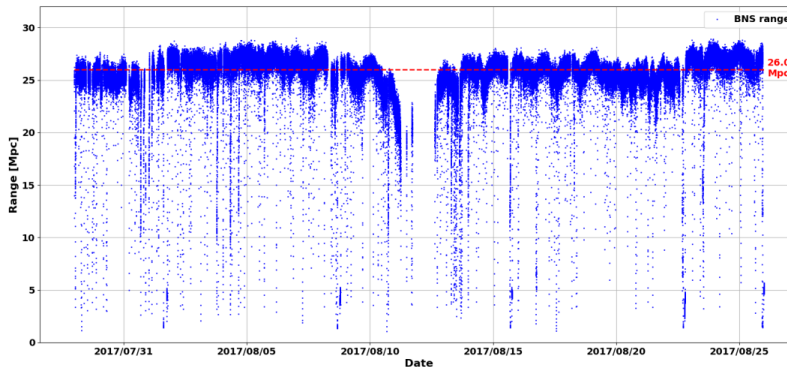


Figure 2.12: Evolution of the Advanced Virgo detector BNS range during O2 data taking period, including the engineering run 12 which started on July 28

detector starts O2 observing around a BNS range of 85 Mpc, and becomes steadily more sensitive as O2 progresses, reaching 100 Mpc at the end of the run. The H1 detector’s sensitivity is around 75 Mpc at the start of the observing run, but the sensitivity was highly affected by a sudden drop in sensitivity in July 2017 after an earthquake in Montana, finishing the run around 65 Mpc. Figure 2.13 shows the representative amplitude spectral density of the strain noise for each detector and the BNS range during O2. Table 2.14 summarizes the duty cycle of each of the detectors during O2, in addition we give the coincident duty cycle in both Advanced LIGO detectors and in the configuration with three detectors. Between O1 and O2

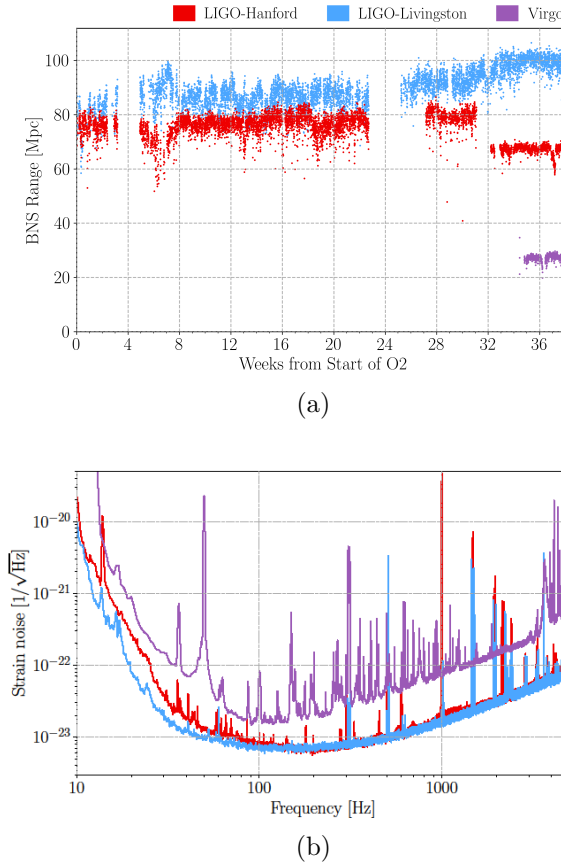


Figure 2.13: (a) BNS range for each detectors during O2. The holes in the BNS range of Advanced LIGO detectors are due to two scheduled breaks. At week 31, we observe a drop in the H1 sensitivity due to the Montana earthquake. (b) Amplitude spectral density of the total strain noise of each detectors. Figure taken from [38].

the duty cycle of L1 significantly increased, whereas the duty cycle of H1 remained roughly the same.

IFO	Duty cycle during O2
H1	59%
L1	58%
V1	85%
H1-L1	44%
H1-L1-V1	63%

Figure 2.14: Duty cycle for the Advanced LIGO detectors and Advanced Virgo during the second observing run (O2).

### 2.4.4 Detections

As we have seen, major upgrades to first generation detectors have resulted in increased sensitivity. This gain in sensitivity allowed the first direct detection of a gravitational-wave signal from a stellar-mass binary black hole (BBH) during the first observation run (O1) in 2015: GW150914 [44]. During this run Advanced LIGO made a total of 3 detections all from BBH [38]. During the second observing run, for the first time Advanced Virgo made its first detection of a BBH merger: GW170814 [45]. Virgo's contribution has made it possible to greatly improve the sky localization of the source. Shortly after, for the first time, a gravitational-wave signal from a binary neutron star inspiral was observed: GW170817 [46]. In addition during O2 there were a total of 7 detections from BBH [38]. Here we only summarize the two historical detections.

#### GW150914

On September 14, 2015 at 09:50:45 UTC just before the start of the O1 run, the Advanced LIGO detectors made the first direct detection of a gravitational-wave signal, called GW150914 [44]. The signal was produced by the inspiral, merger, and ringdown of a black hole binary system with masses respectively of  $36_{-4}^{+5}M_{\odot}$  and  $29_{-4}^{+4}M_{\odot}$ . The mass of the final black hole was  $62_{-4}^{+4}M_{\odot}$  and so a colossal amount of total energy of  $3.0_{-0.5}^{+0.5}M_{\odot}c^2$  was emitted in gravitational waves. The signal lasted for a few tens of milliseconds and has a typical chirp waveform, which increases in frequency from 35-250 Hz and reaches a maximum strain amplitude of  $1.0 \times 10^{-21}$ . The predictions of General Relativity are in agreement with the measurements made in the data of Advanced LIGO. Figure 2.15 shows the signal observed and the reconstructed waveform. Additional tests of General Relativity were performed and no evidence for breach of General Relativity were found [47]. The overall binary black hole merger rate was estimated to be between  $2\text{-}600 \text{ Gpc}^{-3}\text{yr}^{-1}$  [48]. The astrophysical implications of the detection of GW150914 and its estimated parameters have been discussed in [49], in particular the binary mechanisms of black hole formation.

#### GW170817

The blossoming field of joint gravitational-wave and electromagnetic astronomy began on August 17th. At 12:41:04 UTC an event is identified by a low-latency compact binary search in the Advanced LIGO-Hanford detector. However nothing is seen in Advanced LIGO-Livingston, which was not expected because its sensitivity was better than that of other detectors at the time of the detection. It is a visual inspection of the data at the time of the event that reveals a typical long-duration chirp signal in the data of the Advanced LIGO-Livingston detector. A glitch with a high SNR, which subsequently will be subtracted from the data, disrupted the search algorithms in Advanced LIGO-Livingston. The event is seen in time coincidence in Advanced LIGO-Livingston detector with a  $\text{SNR} = 26.4$  with Advanced LIGO-

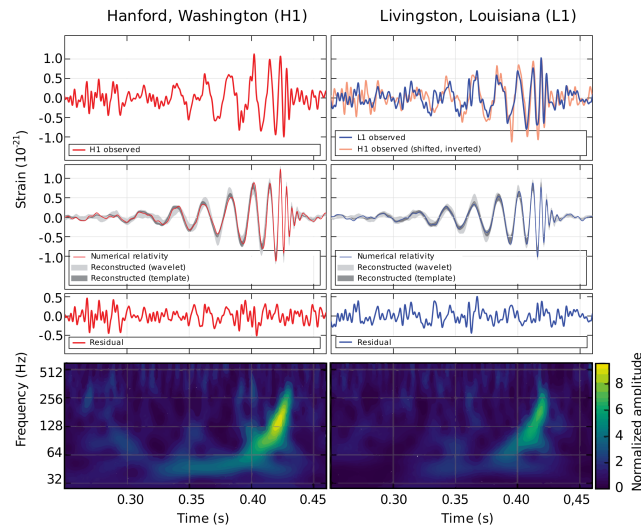


Figure 2.15: GW150914, as detected by the H1 (left column) and the L1 (right column) Advanced LIGO detectors. Times shown are relative to 09:50:45 UTC on September 14, 2015. Top row: detector whitened strain time-series. Middle row: computed waveforms, using numerical relativity (in red). In addition, a sine-Gaussian wavelet reconstruction is also plotted (light grey), and a black hole binary template (grey). Just below this row is presented the residual difference between the computed signal and the reconstructed signal. Bottom row: time-frequency plots of the strain data which clearly illustrates the “chirp” signature of the waveform.

Hanford detector ( $\text{SNR} = 18.8$ ). This detection corresponds to a low mass binary system with component mass very close to neutron star [46]. This event was not detected in Advanced Virgo data, the low value of the reconstructed  $\text{SNR} = 2.0$  indicates that the position of the source is located near a blind point of the detector. At almost the same time, The Fermi-GBM telescope detects an electromagnetic event (short gamma-ray burst GRB 170817A) 1.7s after the gravitational-wave merger [50]. This is the first confirmation of binary neutron star merger being the progenitor of an electromagnetic event [51]. The Advanced LIGO detectors localize the source in a sky region of  $190\text{deg}^2$ . As the source was situated near one of the blind spots of the Advanced Virgo detector, the source was localized much more accurately than with only two detectors, in a region of  $31\text{deg}^2$ , see Fig 2.16. Realizing the importance of the discovery, within 30 minutes after the detection an alert is sent to find an electromagnetic counterpart and a complete observation campaign is launched on the whole electromagnetic spectrum [52]. Thanks to a three-detector source localization, few hours later a first electromagnetic emission was found in the direction of the galaxy NGC4993 (at  $\sim 40$  Mpc) situated in the Hydra constellation. In addition, the follow-up of this signal made it possible to find an emission signal characteristic

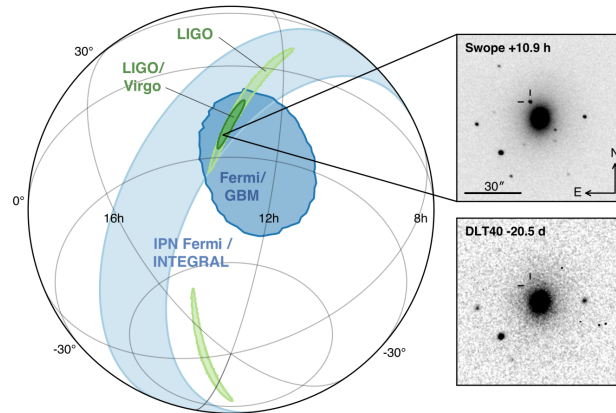


Figure 2.16: Skymap reconstructed for GW170817 from a Hanford-Livingston (light green contours) and Hanford-Livingston-Virgo (dark green contours) analysis. The LIGO only skymap is reduced from  $190\text{deg}^2$  to  $31\text{deg}^2$  when Advanced Virgo data are used. The insets show the location of the apparent host galaxy NGC4993 seen by Swope telescope 10.9 hours after GW170817 and an image of the same sky region taken by DLT40 20.5 days before. Figure taken from [52].

of a kilonova<sup>9</sup> (also called macronova) emission [53, 54, 55, 56, 57, 58, 59, 60, 61]. This detection had an impact on several additional fundamental topics. GW170817 provides a new way to study the extreme state of nuclear matter inside a star. The determination of the position of the source is used to measure the Hubble constant  $H_0$ , the expansion rate of the universe. This is done independently of the measurement made with CMB Planck [62] and the supernovae type Ia [63]. The combination of informations from electromagnetic observations and the gravitational wave provides an estimate of  $H_0 = 70_{-8}^{+12} \text{kms}^{-1}$  [64, 65]. This value is consistent with the other experiments mentioned above.

## 2.5 Data Quality

Detecting a signal in the presence of noise is subject to several difficulties. In many cases the detector noise is described by a stationary and Gaussian contribution to which is added a large number of non-Gaussian transient noises. The data of gravitational-wave interferometers is contaminated by these transient noises, often called glitches. The presence of glitches degrade the sensitivity of searches for gravitational-wave signals in the strain data, specially burst searches (see Sec. 1.5) because of the similarity between glitches and a generic burst signal. That is why it becomes necessary to describe, to understand and if possible to mitigate glitches.

<sup>9</sup>A transient event that emits short gamma-ray bursts and strong electromagnetic radiation. It is a source for nucleosynthesis of heavy elements.

### 2.5.1 Glitches

A glitch can be as short as 1 ms or last for several seconds, it can be well localized in frequency or wide band. Transient noises can originate from a lot of sources as detector malfunctions, technical or environmental sources. Understanding glitches relies on a complete monitoring of the instrument and its environment. For that purpose, the detector is monitored by a thousand of probes as thermometers, microphones, seismometers, magnetometers and many more. These probes collect data that are measurements of the detector's environment. Each probe is associated with an auxiliary channel. An auxiliary channel is any channel except the gravitational-wave channel often called strain channel. To supplement it, other auxiliary channels are used to sense and control the detector, for instances some record the signal of photodiodes used to control the state of the interferometer. It is the study of the relation between a glitch and the auxiliary channels that usually gives a hint about the origin. The glitch investigation may requires months of hunting, it takes a lot of patience, regularity and strong understanding of how the whole detector works. Many efforts are done permanently by the noise hunting teams to improve the quality of the data. Sometimes depending on the characteristics of the glitches (amplitude, duration, frequency, shape ...) they can be classified in families. In particular, transient events must be searched for in thousands of channels data in order to identify correlations with the detector's output data and understand coupling mechanisms leading to glitches. The ultimate goal is to be able to correct the cause that generates this kind of noise or in a less optimistic case to find a criteria to apply to the data in order to remove these glitches.

The primary focus of the investigation is the identification and classification of glitches. For this purpose, the main tool used is a search algorithm called **Omicron** [66] which is able to detect and characterize detector glitches with a very good efficiency and accuracy in all auxiliary data of gravitational-wave detectors. **Omicron** was designed to process hundreds of auxiliary channels required to study coupling in the detectors. The data is processed using a particular transform which consists of decomposing the signal time serie  $x(t)$  onto a generic basis of complex-valued sinusoidal Gaussian functions centered on time  $\tau$  and frequency  $\phi$ :

$$X(\tau, \phi, Q) = \int_{-\infty}^{+\infty} x(t) \frac{\sqrt{4\pi}\phi W}{Q} \exp \left[ -2\pi\phi \frac{(t - \tau)}{Q} \right]^2 e^{-2i\pi\phi t} dt, \quad (2.29)$$

such that the time-frequency plane is covered by tiles (time-frequency regions) of constant quality factor  $Q$ . The noise of the input signal is whitened, i.e. normalized by the local noise power spectrum density. This is done by the normalization factor  $W$  which includes an estimate of the local stationary noise. The parameter space  $(\tau, \phi, Q)$  is tiled in a set of time-frequency planes with a fixed  $Q$  value called  $Q$  plane. Then whitened data are projected onto tiling structure. This procedure allows to express the signal-to-noise-ratio (SNR). For whitened data it can be shown that  $\text{SNR}^2 = |X|^2 - 2$ . Finally a glitch in the data is detected by **Omicron** as a collection of tiles with a SNR value above a given treshold. **Omicron** offers a two-dimensional

representation in the frequency-time plane. The SNR distribution of tiles is plotted on this representation in one or several  $Q$  planes. Figure 2.17 displays a representation of a typical glitch measured by Omicron.

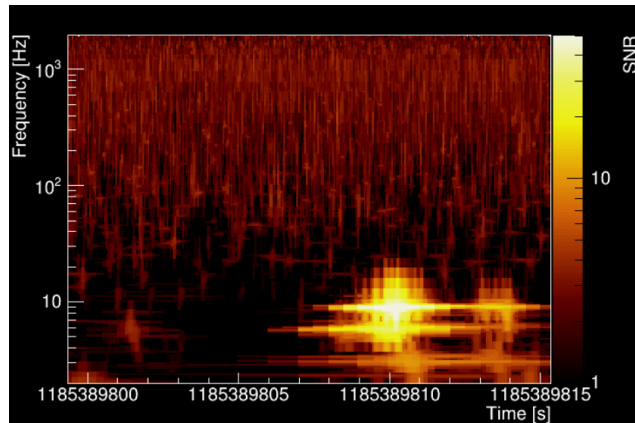


Figure 2.17: Time-frequency representation of a glitch detected by Omicron. The color scale indicates the SNR of the glitch. The shape is characteristic of a glitch resulting from light scattered by optics, justifying its name: scattered-light glitch.

The strain data of Advanced Virgo are analyzed using the Omicron algorithm, to characterize the transient noise in the detector. An example of the distribution of glitches obtained with Omicron in the time-frequency plane over one week of data in Advanced Virgo is shown in Fig 2.18. There are three main families of glitches

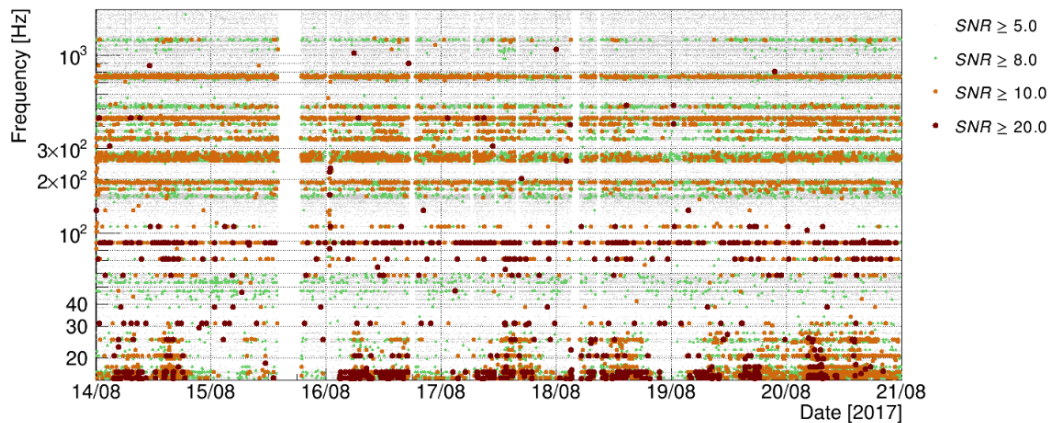


Figure 2.18: Time-frequency distribution of transient noise events (represented by coloured dots) detected by Omicron in Advanced Virgo strain data between August 14 and August 21, 2017.

depending on their origin: technical, environmental and control glitches. Some

examples of common transient noises encountered in Advanced Virgo and Advanced LIGO are given to clarify these denominations a little bit. Typical technical glitches are the alignment glitches which result from light scattered by vibrating optics. These glitches are distributed at specific frequencies above 100 Hz and forms several lines in Fig 2.18. Another example of technical glitches is photodiode glitches which are short duration, and appear after a relock of the interferometer. These glitches are visible on August 16 right after midnight, between 100 Hz and 300 Hz in Fig 2.18 (see the red points localized on a vertical line). The origin of these glitches comes from one of the photodiodes installed in the detection system to measure the dark fringe signal. However these glitches do not occur systematically and the cause of why they appear is not well understood yet, a time-frequency representation of a typical photodiode glitch is given by Fig 2.19. At low frequency, the presence of an excess of glitches is

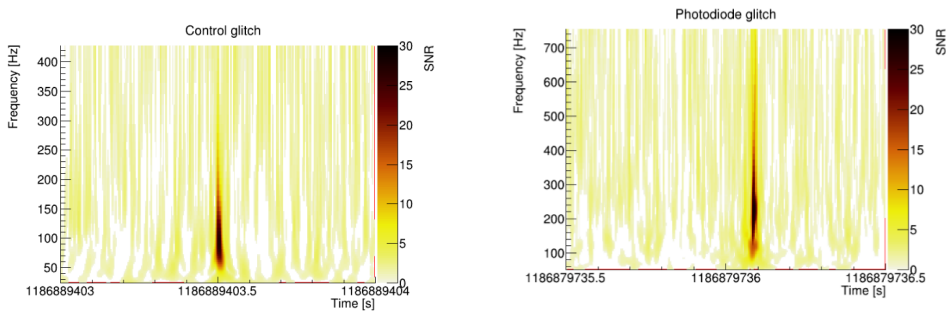


Figure 2.19: (a) Time-frequency representation of a typical control glitch. (b) Time-frequency representation of a typical photodiode glitch.

associated with microseismic activity, which is part of environmental noise. Human seismic activity is clearly visible on the distribution of glitches during a week, since it is at the origin of high SNR glitches of frequency below 30 Hz (red points at very low frequency in Fig 2.18). The distribution of anthropogenic glitches is not homogeneous over a week, for example on August 15 there is much less glitches, it is because this day is a holiday in Italy. In Advanced Virgo, short duration glitches with high SNR, called control glitches are produced with a high rate, see Fig 2.19. These are localized between 60 Hz and 100 Hz. They are associated to missing samples in the signal used to control the mirrors. These glitches are removed when reconstructing the gravitational-wave strain signal  $h(t)$ . However some of these glitches are still present in the analyzed data. In Advanced LIGO, the worst contributors to the background of transient gravitational-wave searches are blip glitches. These are very short duration transients, with a large frequency band [67]. It is not evident to identify clearly blip glitches and to separate them into sub-families. However, the current classification [68] is based on four different categories of blip glitches:

blip, repeated blips, tomte<sup>[10]</sup> and koi fish<sup>[11]</sup>. A time-frequency representation of typical blip glitches is shown in Fig 2.20. Investigations have shown that there are several sources of blip glitches. For example, it has been observed that the blip glitches rate increases when the relative humidity falls below a reference value in the Advanced LIGO detectors localized in Hanford (H1). The cause of this behaviour is still being investigated. Other correlations have been found and are still not well understood today. Despite the efforts made, less than 10% of blip glitches have shown a correlation with one of the thousands of auxiliary channels that constantly monitor the Advanced LIGO detectors. By comparison, in Advanced Virgo, there are much less blip glitches and those were quite well understood during O2. For example the photodiode glitches and control glitches are included in the category of blip glitches.

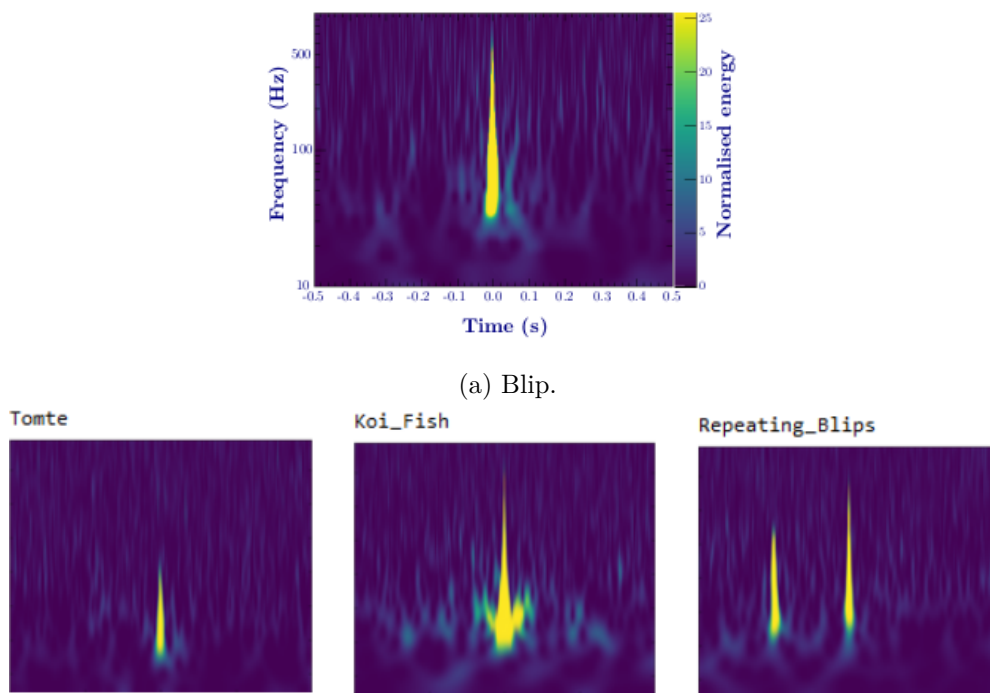


Figure 2.20: Current classification of blip glitches. Figure taken from [67] and [68].

## 2.5.2 Vetoes

Several factors can affect the quality of the data to make it unsuitable for data analysis. For instance the strain channel,  $h(t)$ , is too much glitchy, or data are

<sup>10</sup>This name is given in reference to the conical hat worn by a tomte, a mythological creature of Nordic folklore not more than 90 cm high.

<sup>11</sup>A fish from the carp family. The koi fish is a symbol of luck in Japan.

corrupted due to a severe problem that occurs while the detector is taking data. Time stretches in which the data quality is too low, can be flagged and eliminated from the analysis. For instance periods of time where  $h(t)$  is too glitchy or  $h(t)$  is few order of magnitudes larger than the usual values, are flagged. Once the source of the problem is well established and understood, a data quality (DQ) flag is developed. A DQ flag is a list of time segments where the data is qualified as noisy. The DQ flags are classified in categories [69] that inform on the severity of the problem and provide a prescription on how to use the flags in the analyses. For that purpose flags are organized into four categories (CAT). Table 2.3 provides a definition for each category. To give an example of the significance of the impact of DQ flags on

Categories	Definition
CAT1	Indicate that the data have been severely impacted by noise and should not be analyzed at any stage of a gravitational-wave search.
CAT2	Indicate time that demonstrates excess noise and should be treated with caution. Triggers should be removed if flagged by a CAT2.
CAT3	Indicate time where the noisy period is not well understood. This category should be applied with an extrem caution.
CAT4	Indicate time where simulated gravitational-wave signals are injected in the detector (hardware injection). CAT4 time periods should be removed for any search analysis.

Table 2.3: Definition of the categories used to classify the DQ flags.

data quality, Fig 2.21 shows the same distribution of glitches found in Advanced Virgo strain data (see Fig 2.18) after applying a list of DQ flags. We observe that the DQ flags removed most of the glitches with a high SNR. The DQ flag used was built following a noise investigation which is a long process. In particular it requires a lot of expertise from the people involved in the detector characterization group (DetChar) of Advanced Virgo. The study of the correlation between a glitch and the auxiliary channels is used to generate vetoes which remove triggers that occur at the time of the glitch. For this purpose, a systematic study of time coincidences between events in the strain channel and all the auxiliary channels is performed, in order to identify which auxiliary channels have a statistically significant correlation with the strain channel. It is also important to note that the work of characterizing the noise of a detector is a continuous work. Indeed the noise in the detector is changing all the time, therefore a veto is valid only for a limited time. Finally, once the segment list of a veto is generated, its performance need to be studied. This is discussed at the end of Sec. 2.5.3.

### 2.5.3 Data quality tools

Many tools were developed in order to track the noise in the detector and to understand the coupling with the gravitational-wave channel. We introduce briefly the main tools used for the work of this thesis.

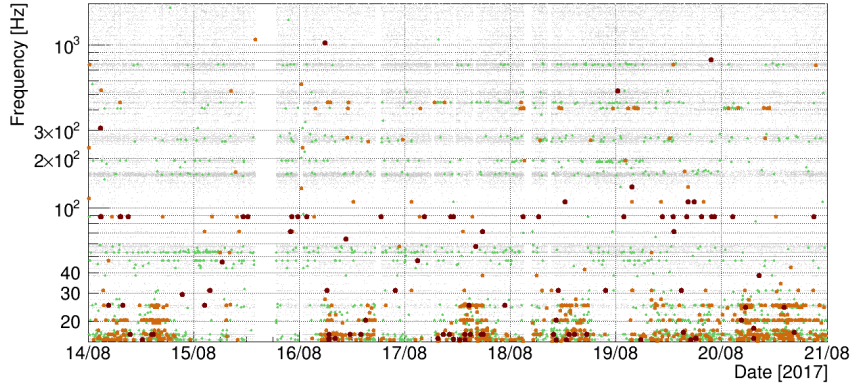


Figure 2.21: Distribution of glitches seen in Fig 2.18 after applying a list of DQ flags designed to reject glitches resulting from a noise coupling which is understood. Most of the glitches with a high SNR are vetoed by the list of DQ flags.

### UPV algorithm

UPV [70] is an algorithm standing for used-percentage veto. UPV is used to find statistical correlations between transient noise in the gravitational-wave channel and in auxiliary channels. The code finds time-coincident events between the gravitational wave channel and the auxiliary channels. A use-percentage value is used to characterize the coupling between these two channels, defined as:

$$\text{use percentage} \equiv \frac{N_{\text{coinc}}^{\text{aux}}}{N_{\text{total}}^{\text{aux}}}, \quad (2.30)$$

where  $N_{\text{coinc}}^{\text{aux}}$  is the number of the auxiliary channel events coincident with the gravitational-wave channel and  $N_{\text{total}}^{\text{aux}}$  is the total number of events present in the auxiliary channel. Typically, if the use-percentage is higher than 50%, the coupling is said to be real, by opposition to accidental coincidence. If this requirement is fulfilled the channel is selected to produce a veto for a category of glitches. Such a channel selection insures that the coupling between the auxiliary channels and the strain channel is founded. The use-percentage is computed as an increasing function of the SNR. Moreover a glitch family is often characterized by a given frequency. It is why in addition the use-percentage is computed in bins of frequency of the auxiliary channel. If the use-percentage is found to be above a given threshold (e.g. 50%), a SNR threshold for the set of events seen in the auxiliary channel is defined. Since the use-percentage is computed for multiple frequency bins, the SNR threshold is a function of the frequency. This threshold is used to define a veto. Any events from an auxiliary channel with a SNR above the threshold is considered to be coupled to the gravitational-wave channel. Figure 2.22 shows an example of histogramm produced by UPV.

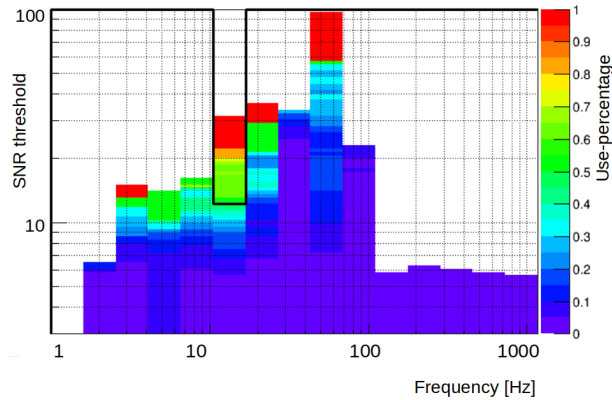


Figure 2.22: UPV tuning histogram for an auxiliary channel. The use-percentage is represented by the color scale. We observe that the use-percentage increases with the SNR, which is expected. The threshold is indicated by the thick black line. When the black line is at the very top of the plot, the threshold is considered as infinite. The final SNR threshold is set when the use-percentage is above 50% (green region). Some frequency bins are excluded even when the use-percentage is measured to be above 50%. This is because there is not enough statistic in these bins. In this example only events between 10 Hz and 20 Hz are involved in the coupling, and so the coupling between the auxiliary channel and the gravitational wave channel is weak.

## VetoPerf

**Vetoperf** is an algorithm that applies a veto on a set of triggers and measures its performance. The veto performance is characterized by several quantities:

- the dead-time ( $d$ ), defined as the fraction of time rejected by the veto.
- the efficiency ( $\epsilon$ ) which is the fraction of triggers that are vetoed. Usually the efficiency is estimated as a function of SNR.

**Vetoperf** measures the numbers presented above. It also generates plots with trigger distributions, before and after applying the veto. This tool is very useful for data analysis because it provides the quantities used to estimate the quality of a veto. Indeed, it is important to check that the vetoes do not discard good quality data periods because they could contain a genuine signal. A good veto should have a large use percentage, however this criteria is not sufficient, for example the use percentage can be high only because the dead time is large. It needs to be completed by another quantity: the ratio efficiency over dead-time ( $\epsilon/d$ ). Its value gives us the fraction of triggers vetoed over the fraction of time vetoed. If  $\epsilon/d = 1$  the flagging is random while  $\epsilon/d > 1$  means that the flaggings starts to be effective and if  $\epsilon/d \gg 1$  the veto can be considered as “excellent”. By using a veto there is always a risk to remove a

real gravitational wave trigger and so its use must be well justified.

Several other tools exist, such as the Virgo Interferometer Monitor (VIM) [71] which provides informations on each sub-system of Advanced Virgo. Periodically various plots are generated and archived on a daily basis. These plots inform about the state of each sub-sytem, the online processings and the online DetChar analyses. The whole information is displayed in a well structured page. An other example is the DataDisplay which is an interactive tool that allows also to visualize the data, but in a more flexible way. These tools will be used during the cosmic burst analysis, presented in Chap. 4.

# Chapter 3

## Cosmic Strings

The basic ingredients in cosmology are General Relativity and the choice of a metric. The Friedmann-Lemaitre-Robertson-Walker (FLRW) model, known as the hot Big Bang model is a homogeneous and isotropic solution of Einstein's equations (Sec. 3.1). However this model has several outstanding enigmas. Cosmic strings have been introduced to explain a variety of these enigmas. These are linear topological defects that are expected to be form during some phase transitions in the Universe (Sec. 3.2). Cosmic strings have several astrophysical signatures (Sec. 3.4.1), in particular they can emit gravitational waves (Sec. 3.3).

### 3.1 The standard cosmological model

#### 3.1.1 The cosmological principle

The cosmological principle is the notion that the Universe is spatially homogeneous and spatially isotropic when viewed on a large enough scale. While these two properties appear similar, they describe very different features of the Universe. Figure 3.1 illustrates the difference between these two terms. The Universe is isotropic if we see no difference in the structure of the Universe as we look in different directions. Homogeneity implies that the average density of matter is about the same in all places in the Universe. This means there is no preferred observing position in the Universe. Notice that this is clearly true for the Universe only on very large scales, of ten millions of light-years in size.

#### 3.1.2 The FLRW metric

It can be shown [6] that a space-time spatially homogeneous and isotropic is described by the Friedmann-Lemaitre-Roberston-Walker (FLRW) metric:

$$ds^2 = g_{\alpha\beta}dx^\alpha dx^\beta = -dt^2 + a^2(t) \left[ \frac{dr^2}{1 - kr^2} + r^2(d\theta^2 + \sin^2\theta d\phi^2) \right] \quad (3.1)$$

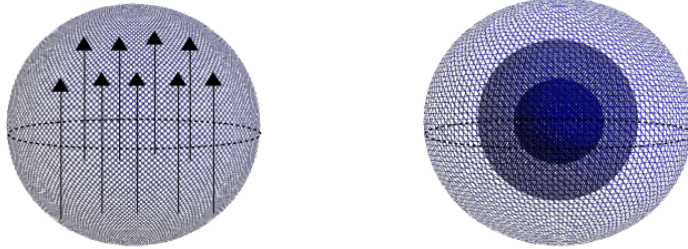


Figure 3.1: Illustration of how homogeneity and isotropy are not equivalent. On the left, a unique direction is picked out, but translation invariance is maintained. On the right, all direction are the same (rotation invariance) but a radial gradient exists.

where  $(r, \theta, \phi)$  are the spherical coordinates, this choice is used to make the symmetry of space manifest. The quantity  $a(t) > 0$  is called the scale factor which has the dimension of a length. It can be noted that the metric remains unchanged if we rescale simultaneously  $a(t)$ ,  $r$  and  $k$ . This freedom is used to set the scale factor to unity today  $a_0 \equiv a(t_0) \equiv 1$ . The parameter  $k$  is the spatial curvature and it can only takes three values:

$$k = \begin{cases} 0 & \text{flat space} \\ 1 & \text{elliptical space} \\ -1 & \text{hyperbolic space} \end{cases} \quad (3.2)$$

We note that there is no cross terms between time and space coordinates in the metric, so that there is no privileged direction: the FLRW metric describes well an isotropic Universe. It also describes a homogeneous Universe because of the hyperspherical  $\square$  symmetry. In the following, the time dependence will be implicit such as  $a(t) \equiv a$ .

### 3.1.3 The Friedmann equations

To derive the general dynamic equations of a homogeneous and isotropic Universe we need to specify the stress-energy tensor. A perfect fluid is general enough to describe a wide variety of cosmological fluids. The stress-energy tensor  $T^{\alpha\beta}$  of a perfect fluid given by Eq. [1.15](#), can be written in a matrix form:

$$T^{\alpha\beta} = \begin{pmatrix} \rho & 0 & 0 & 0 \\ 0 & P & 0 & 0 \\ 0 & 0 & P & 0 \\ 0 & 0 & 0 & P \end{pmatrix} \quad (3.3)$$

---

<sup>1</sup>Generalization of the ordinary sphere to spaces of arbitrary dimension.

where  $\rho$  and  $P$  are respectively the energy density and pressure in the rest-frame of the fluid. The Einstein equations given by Eq. 1.9 reduce to the form:

$$\begin{cases} \left(\frac{\dot{a}}{a}\right)^2 + \frac{k}{a^2} = \frac{8\pi G}{3}\rho + \frac{\Lambda}{3} \\ \ddot{a} = -\frac{4\pi G}{3}(\rho + 3P) + \frac{\Lambda}{3}. \end{cases} \quad (3.4)$$

These are known as the Friedmann equations. Usually the first one is simply called “the Friedmann equation”, while the second is explicitly referred to as the “the second Friedmann equation”<sup>2</sup>. These are a system of two differential equations for the functions of time:  $a(t)$ ,  $\rho(t)$  and  $P(t)$ . To have a closed system, these equations have to be complemented with an equation of state, which relates  $P$  and  $\rho$ . We use the equation of state of a barotropic fluid, which is a fluid whose density is a function of pressure only:

$$P = w\rho, \quad (3.5)$$

where the value of  $w$  depends a priori on the age of the Universe. By differentiating the (first) Friedmann equation and using this equation of state we obtain an evolution equation for the density  $\rho$ . By integrating this equation for  $w = cte$ , we get:

$$\rho(t) = \rho_0 \left[ \frac{a_0}{a(t)} \right]^{3(1+w)}, \quad (3.6)$$

where we use subscripts “0” to denote quantities evaluated today, at  $t = t_0$ . Since the Universe is filled with a mixture of different matter components, we classify the different sources by their contribution to the pressure:

- **Matter.** The term “matter“ used here is large. It refers to all forms of matter for which the pressure is much smaller than the energy density  $P \ll \rho$  (gas of non-relativistic particles). Setting  $P = 0$  ( and so  $w = 0$ ), the equation of the evolution of the density gives

$$\rho_m(t) \propto a^{-3}(t), \quad (3.7)$$

where the dilution of the energy density reflects the expansion of the volume of the Universe  $V \propto a^3$ . Most of the matter in the Universe is in the form of invisible dark matter. The rest is ordinary matter, often called baryonic matter.

- **Radiation.** The radiation term denotes anything for which the pressure is about a third of the energy density,  $P = \rho/3$  (gas of relativistic particles). The density dilution is then given by

$$\rho_r(t) \propto a^{-4}(t). \quad (3.8)$$

For example the early Universe was dominated by photons. Being massless, they are always relativistic. Moreover for most of the history of the Universe, neutrinos behaved like radiation. It is only recently that their small masses have become relevant and they have begun to behave like matter.

<sup>2</sup>This equation is also called the acceleration equation.

- **Dark Energy.** the Universe today seems to be dominated by a mysterious negative pressure component  $P = -\rho$ , the dark energy. The density of the dark energy does not evolve,

$$\rho_\Lambda(t) \propto \text{cst.} \quad (3.9)$$

It is convenient to rewrite the Friedmann equation in another form, for that purpose we introduce the Hubble function defined as:

$$H(t) \equiv \frac{\dot{a}}{a}, \quad (3.10)$$

which has the dimension of the inverse of a time. Today, in case of flat space ( $k = 0$ ) with  $\Lambda = 0$ , Eq [3.4](#) becomes:

$$H_0^2 = \frac{8\pi G}{3}\rho, \quad (3.11)$$

and by inverting this equation we obtain the critical energy

$$\rho_c = \frac{3H_0^2}{8\pi G}. \quad (3.12)$$

It is the density which makes the Universe flat. The critical density allows us to define the dimensionless density energy parameters:

$$\Omega_i = \frac{\rho_i}{\rho_c}. \quad (3.13)$$

Finally, by using these notations we rewrite the Friedmann equation under the form

$$H^2(a) = H_0^2 \left[ \Omega_{r,0} \left( \frac{a_0}{a} \right)^4 + \Omega_{m,0} \left( \frac{a_0}{a} \right)^3 + \Omega_{k,0} \left( \frac{a_0}{a} \right)^2 + \Omega_{\Lambda,0} \right], \quad (3.14)$$

where we have defined a “curvature” density parameter  $\Omega_{k,0} \equiv -\frac{k}{(a_0 H_0)^2}$ , with  $H_0$  the Hubble constant which is the Hubble parameter measured today at  $t = t_0$ . Usually the subscript “0” is dropped such that the equation is much “prettier” and since we have chosen the scalar factor to be  $a(t_0) \equiv a_0 = 1$  today we get:

$$H^2(a) = H^2 \left[ \Omega_r a^{-4} + \Omega_m a^{-3} + \Omega_k a^{-2} + \Omega_\Lambda \right]. \quad (3.15)$$

For a flat, single-component Universe, by integrating this last equation, we obtain the time dependence of the scale factor  $a(t)$ . This is summarized in Tab. [3.1](#). Since radiation density decreases the fastest with time it must increase fastest on going back in time and so radiation must dominate early in the Universe. The radiation-dominated era is followed by the matter-dominated era. Finally, as the density of other forms of matter drops with time, the dark energy ultimately dominates the energy density of the Universe. Currently, the simplest cosmological model that fits the experimental observations is called the Lambda cold dark matter model or  $\Lambda$ CDM model. The cosmological parameters of our Universe, whose geometry is assumed

	w	$\rho(a)$	a(t)
Radiation domination	1/3	$a^{-4}$	$t^{1/2}$
Matter domination	0	$a^{-3}$	$t^{2/3}$
$\Lambda$ domination	-1	<i>cst</i>	$e^{Ht}$

Table 3.1: FLRW solutions for a flat single-component Universe.

to be well modelled by the FLRW metric, have been measured with an increasing precision over the last decades. We use Planck-2015 fiducial parameters [62]:

$$H_0 = 67.74 \pm 0.46 \text{ km/s/Mpc}^3, \quad (3.16)$$

with the *concordance set* of cosmological parameters:

$$\Omega_{r,0} = 9.1476 \times 10^{-5} \quad \Omega_{m,0} = 0.308 \pm 0.0062 \quad \Omega_{\Lambda} = 0.6911 \pm 0.0062, \quad (3.17)$$

where

$$\Omega_{tot} \equiv \Omega_r + \Omega_m + \Omega_{\Lambda} \simeq 1, \quad (3.18)$$

indicating that it is consistent with a flat Universe.

The FLRW space have a particle horizon; it is only possible at at time  $t$  to have received light signals from particles lying within a radial distance:

$$d_H = a(t) \int_0^t \frac{dt'}{a(t')}, \quad (3.19)$$

this quantity is often called the horizon distance. In the radiation dominated era for a flat Universe, the horizon size is  $d_H = 2t$ , while in the matter dominated era  $d_H = 3t$ .

The main characteristic of the FLRW model is the non-stationarity of the Universe introduced through the scale factor. One of the consequences is the expansion of the Universe. This was observed first by Hubble [72] with the displacement of the spectrum of astronomical objects toward longer (red) wavelengths called redshift. Indeed we show [12] that the metric in Eq. 3.1 introduces a Doppler effect in the propagation of light by means of the scale factor  $a(t)$ . The redshift is then defined as:

$$z \equiv \frac{\lambda_{obsv}}{\lambda_{em}} - 1 = \frac{a(t_{obs})}{a(t_{em})} - 1, \quad (3.20)$$

where the photon is emitted at a time  $t_{em}$  with a wavelength  $\lambda_{em}$  and is received by an observer at a time  $t_{obs}$  with a different wavelength  $\lambda_{obs}$ . In the FLRW metric, the redshift of cosmological objects is explained by the expansion of the Universe: the

<sup>3</sup>Often written as  $H_0 = h \times 100 \text{ km/s/Mpc}$  with  $h = 0.6774$ .

scale factor is an increasing function of time.

In the following we express the Hubble rate at redshift  $z$  by:

$$H(z) = H_0 \mathcal{H}(z) \quad \text{with} \quad \mathcal{H}(z) = \sqrt{\Omega_\Lambda + \Omega_M(1+z)^3 + \Omega_R \mathcal{G}(z)(1+z)^4}. \quad (3.21)$$

In the standard model, entropy is assumed to be conserved and it is shared approximately among each of the relativistic species present. The higher the temperature, the greater the number of species present. As the Universe cools down, species become non-relativistic and release their entropy to the relativistic species that are still in thermal equilibrium. In the radiation era, this is described by the function  $\mathcal{G}(z)$  defined as [73]:

$$\mathcal{G}(z) \equiv \frac{g_*(z)g_S^{4/3}(0)}{g_*(0)g_S^{4/3}(z)} = \begin{cases} 1 & \text{for } z < 10^9 \\ 0.83 & \text{for } 10^9 < z < 2 \times 10^{12} \\ 0.39 & \text{for } z > 2 \times 10^{12}, \end{cases} \quad (3.22)$$

where  $g_*(z)$  is the total effective number of degrees of freedom of all relativistic particle in thermal equilibrium at redshift  $z$  and  $g_S(z)$  is the effective number of entropic degrees of freedom. The two breaks above correspond to the quark-hadron phase transition ( $T \geq 200$  Mev) and to the electron-positron annihilation ( $T \geq 200$  kev). The cosmic time is expressed using the interpolation function  $\varphi_t(z)$ :

$$t(z) = \frac{\varphi_t(z)}{H_0} \quad \text{with} \quad \varphi_t(z) = \int_z^{+\infty} \frac{dz}{\mathcal{H}(z)(1+z)}. \quad (3.23)$$

The proper distance  $r(z)$  at redshift  $z$  is expressed as:

$$r(z) = \frac{\varphi_r(z)}{H_0} \quad \text{with} \quad \varphi_r(z) \equiv \int_0^z \frac{dz}{\mathcal{H}(z)}, \quad (3.24)$$

and the proper volume element  $dV(z)$  is:

$$dV(z) = \frac{\varphi_V(z)}{H_0^3} dz \quad \text{with} \quad \varphi_V(z) = \frac{4\pi\varphi_r^2(z)}{(1+z)^3\mathcal{H}(z)}. \quad (3.25)$$

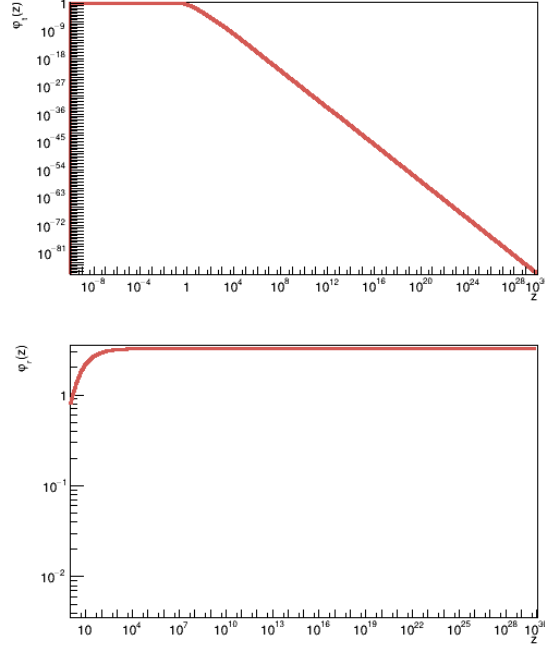
The analytical calculation gives an asymptotic approximation for  $\varphi_t(z)$ :

$$\begin{cases} \varphi_t(z) \approx 0.9566 & \text{for } z \ll 1 \\ \varphi_t(z) \approx \frac{1}{2z^2\sqrt{\Omega_R\mathcal{G}(z)}} & \text{for } z \gg 1, \end{cases} \quad (3.26)$$

and for  $\varphi_r(z)$ :

$$\begin{cases} \varphi_r(z) \approx z & \text{for } z \ll 1 \\ \varphi_r(z) \approx 3.2086 & \text{for } z \gg 1. \end{cases} \quad (3.27)$$

The interpolation functions are computed using numerical calculations where  $5 \times 10^6$  points are distributed logarithmically between  $z = 10^{-10}$  and  $z = 10^{30}$ . Figure. 3.2 shows the results.


 Figure 3.2: Interpolating functions  $\varphi_t(z)$  and  $\varphi_r(z)$ .

### 3.1.4 A brief history of the Universe

Let us close this section with a very brief history of our Universe, as inferred in the  $\Lambda$ CDM framework. First of all, following the dynamics given by the Friedmann equations backwards in time shows that a singularity, namely  $a = 0$ , occurs in a finite-time past. This is the so-called Big Bang singularity which is taken as the origin of cosmic time and then today corresponds to  $t_0 = 13.81$  Gyr. At the time of the Big Bang, the Universe was a very hot and dense particle soup in thermal equilibrium. Thanks to this assumption, the description of the Universe depends only on the temperature  $T$ . At the Planck epoch  $t \sim 10^{-35}$  s the temperature was about  $T \sim 10^{19}$  GeV<sup>4</sup>. This refers to the period in the history of the Universe during which the four fundamental interactions (electromagnetism, weak interaction, strong interaction and gravitation) were unified. Because of expansion the Universe is diluted and therefore cools down. Particle species lose their energy and “freeze-out”, i.e. decouple from thermal equilibrium. This decoupling occurs when a particle’s interaction rate  $\Gamma$  becomes comparable to the rate of expansion  $\Gamma \approx H$ . As the Universe cooled down it went through at least three phase-transitions:

- At  $\mathbf{T} \sim 10^{15}$  GeV: the Grand unification transition occurs between  $t = 10^{-37}$  s and  $t = 10^{-35}$  s after the Big Bang. The Grand Unification Theories (GUTs)

<sup>4</sup>The orders of magnitude listed here are provided just to give an idea of the energy scales involved. Values often vary in the literature.

predict that at very high-energy scales the electroweak-nuclear and strong-nuclear forces are unified into one force, but gravity has become distinct. It is when the symmetry of these forces is broken that a phase transition takes place. The strong force separates from the other fundamental forces.

- At  $\mathbf{T} \sim 100$  Gev: the electroweak transition occurs around  $t = 10^{-11}$  s after the Big Bang and causes the electroweak symmetry breaking. The electroweak symmetry unified electromagnetism and the weak interaction.
- At  $\mathbf{T} \sim 200$  Mev: the quark-hadron transition at  $t = 10^{-6}$  s after the Big Bang causes the plasma of free quarks and gluons to convert into hadrons (baryons and mesons).

Around  $t \sim 3$  min and  $T \sim 150$  MeV to 50 keV, the quarks combine into baryons (protons, neutrons) and mesons (pions), followed by light atomic nuclei formation (essentially deuterium, helium and lithium). This process is called the Big Bang nucleosynthesis (BBN). At the end of this period, the expansion dynamics is still dominated by radiation. However, as seen in Tab [3.1](#), the energy density of radiation decreases faster than the one of nonrelativistic matter, and both contributions become comparable  $\Omega_r \sim \Omega_m$  for:

$$z_{eq} = \frac{\Omega_{m,0}}{\Omega_{r,0}} \approx 3400. \quad (3.28)$$

Later, neutral hydrogen forms through the reaction  $e^- + p^+ \rightarrow H + \gamma$  this is the recombination period. Before recombination the strongest coupling between the photons and the rest of the plasma is through Thomson scattering,  $e^- + \gamma \rightarrow e^- + \gamma$ . The drop in the free electron density after recombination implies that this reaction becomes inefficient and the photons decouple from matter. Photons are spreading freely for the first time in the history of the Universe. The photon last scattering occurred at temperature and redshift:

$$T_{rec} \simeq 3000K \quad z_{rec} \simeq 1090 \quad (3.29)$$

when the age of the Universe was about 380000 years. It was at this point that the Universe went from being totally opaque, to transparent. This is the earliest possible light that we can observe. This light is the so-called cosmic microwave background or CMB, a nearly-uniform and isotropic radiation. The frequency spectrum of the CMB radiation was measured to high accuracy in the early nineties and it was shown that it is that of a perfect black-body spectrum at a temperature of  $2.72K$ .

After recombination, the Universe remains neutral for a few hundreds of millions of years (the dark ages), during which structures form via gravitational accretion. On small scales, some matter clumps collapse and get hot enough to activate the fusion of hydrogen into helium, giving birth to the first stars. The next billions of years are then characterised by the formation and evolution of galaxies on small scales; and by the apparition of a large-scale cosmic web where voids are separated by walls and filaments.

## 3.2 Cosmic strings

The standard model of cosmology successfully explains the cosmological redshift, the origin of the cosmic background radiation, and the synthesis of light elements. However, there are questions, which mainly concern the initial conditions, to which the hot Big Bang model is unable to provide an answer. We can mention for example, the *flatness problem*. The density of our Universe is  $\Omega_{tot} \sim 1$  for a critical energy  $\rho_c$ . However the critical density is a point of unstable equilibrium, and deviations from its value grow in time. If  $\Omega_{tot}$  in the early Universe was slightly different from 1 we would not observe our Universe. Numerically it means that  $\Omega_{tot}$  at the Planck time had to be fine-tuned to within an incredible accuracy. Another example is given by the *horizon problem*. This problem stems from the large-scale homogeneity and isotropy of the Universe, and in particular, for the CMB. The CMB is uniform at  $T \sim 10^{-5}$  K, in standard cosmology a mechanism to establish this uniformity would need to transmit energy and information much faster than the speed of light. A last notable example includes the *structure formation*. The presence of galaxies and cluster of galaxies is interpreted as the result of gravitational instabilities (Jeans instabilities) from small density fluctuations in the early Universe. To address the question of the origin of the initial density inhomogeneities, one needs to add more ingredients to the cosmological model. To deal with these issues, inflation was proposed [74, 75]. Inflation essentially consists of a phase of accelerated expansion, corresponding to repulsive gravity characterized by a negative pressure. Although several of inflationary models have been proposed and tested against observations, the most popular ones involve a single scalar field (the inflaton), whose slight inhomogeneities, due to quantum fluctuations, have been the seeds of the structures that we observe today. For almost two decades, cosmic strings have been also considered for describing the formation of large-scale structure in the Universe [76]. However the characteristics of the CMB anisotropies and the statistical properties of the CMB have made it possible to discriminate among models. Today, cosmic strings are ruled out as the unique source of the structure formation by the CMB measurements. However, many particle physics models admit solutions which correspond to cosmic strings and cosmic strings can be included as a sub-dominant partner of inflation. Thus, the effort to detect cosmic strings is still ongoing.

In this section we will review the properties of cosmic strings. We first discuss the formation of cosmic strings using simple models, then we introduce the framework to describe kinematics of cosmic strings. Next, we present the Kibble mechanism of cosmic string formation. We also introduce two basic structures which arise on cosmic strings due to their dynamic behaviour: cusps and kinks.

### 3.2.1 Spontaneous symmetry breaking

The Universe has steadily cooled down since the Planck time, leading to a series of phase transitions. Topological defects can occur when the field symmetries are broken. This means that the ground state of the theory does not exhibit the same

symmetry as the full theory. The symmetry is then said to be spontaneously broken. As a consequence, energy can get trapped in specific regions of space and it is the topological structure of this trapped energy which determines the nature of the defect. A line-like structure is called a cosmic string. In this section we present two models to illustrate the formation of cosmic strings. The general material below follows the presentation of [77, 78], with input from other sources [79, 80, 76, 81].

### Goldstone model

The simplest model that can be studied to understand the concept of spontaneous symmetry breaking is the Goldstone model defined by the classical Lagrangian density:

$$\mathcal{L} = \partial_\mu \phi^* \partial^\mu \phi - V(\phi), \quad (3.30)$$

where  $\phi$  is a complex scalar field sometimes called a Higgs field and  $V(\phi)$  a potential given by:

$$V(\phi) = \frac{1}{4} \lambda (\phi^* \phi - \eta^2)^2. \quad (3.31)$$

The self-interaction term is denoted by  $\lambda$ , it states how strongly two scalar particles interact and  $\eta$  is the mass term. These two terms are real positive constants. This potential is the *Mexican-hat* potential illustrated in Fig 3.3. By looking at Fig 3.3

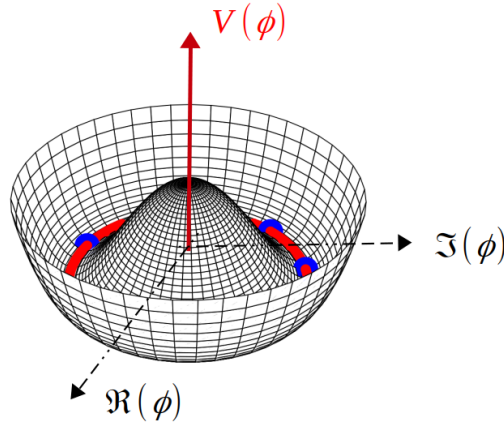


Figure 3.3: The *Mexican-hat* potential for a broken U(1) symmetry showing a circle of minima. The vacuum state  $|\phi| = \eta$  is represented in red and some of the possible choices of the phase are in blue. The state of unbroken symmetry with  $|\phi| = 0$  corresponds to a maximum of  $V(\phi)$ . Figure taken from [79].

it can be seen that the Lagrangian has a rotational symmetry: the shape of the potential does not change, no matter in what direction you look at the horizontal plane. The Goldstone model is then invariant under the U(1) group of global phase transformations:

$$\phi(x) \rightarrow e^{i\alpha} \phi(x) \quad (3.32)$$

where  $\alpha$  is a real constant. The term “global” refers to the fact that the symmetry transformation involves rotating every point in the field by the same constant. We want to show that the fundamental state of the theory, i.e. the minimum energy configuration, does not exhibit the full symmetry of the Hamiltonian defined by:

$$H = \int d^3x \mathcal{H} \quad (3.33)$$

where the Hamiltonian density  $\mathcal{H}$  is given by the Legendre transformation of the Goldstone Lagrangian:

$$\mathcal{H} = \pi \partial_0 \phi + \pi^* \partial_0 \phi^* - \mathcal{L} \quad (3.34)$$

with

$$\pi \equiv \frac{\delta \mathcal{L}}{\delta(\partial_0 \phi)} = \partial_0 \phi^*. \quad (3.35)$$

By injecting the expression of  $\pi$  in the Hamiltonian density we get:

$$\mathcal{H} = |\partial_0 \phi|^2 + \sum_{i=1}^3 |\partial_i \phi|^2 + V(\phi), \quad (3.36)$$

we deduce that the ground state of the theory or the vacuum state corresponds to a constant scalar field which minimizes the potential  $V(\phi)$ . The vacuum state of the theory is characterised by a nonzero expectation value given by:

$$\phi = \eta e^{i\theta}, \quad (3.37)$$

where  $\theta$  can take arbitrary values: there is thus an infinity of solutions. Any phase of the field describes a vacuum state. The vacuum state is not invariant under the phase transformation given by Eq. 3.32, while the theory is invariant under this transformation. When the system goes to one of those vacuum solutions, the symmetry is said to be spontaneously broken.

We want now to describe the properties of the vacuum state. To do this, we consider small fluctuations around the ground state. Since each vacuum state is equivalent we can choose a particular value, for example  $\theta = 0$ . The scalar field can be rewritten as:

$$\phi = \eta + \frac{(\phi_1 + i\phi_2)}{\sqrt{2}} \quad (3.38)$$

where  $\phi_1$  and  $\phi_2$  are real scalar field such that  $\phi_1 \ll \eta$  and  $\phi_2 \ll \eta$ . By substituting this expression into the Goldstone Lagrangian (Eq. 3.30) we obtain:

$$\mathcal{L} = \frac{1}{2}(\partial_\mu \phi_1^* \partial^\mu \phi_1) + \frac{1}{2}(\partial_\mu \phi_2^* \partial^\mu \phi_2) - \frac{1}{2}\lambda\eta^2\phi_1^2 + \mathcal{L}_{int}. \quad (3.39)$$

The last term,  $\mathcal{L}_{int}$ , is an interaction term which includes cubic and higher order terms in the real scalar fields  $\phi_1$  and  $\phi_2$ . The scalar field  $\phi_1$  corresponds to a scalar massive particle with mass  $\sqrt{\lambda}\eta$ . The scalar field  $\phi_2$  corresponds to a scalar massless particle called the Goldstone boson.

### The abelian-Higgs model

For the moment we have only considered the case of a global symmetry. We are now interested by a local transformation which allows the scalar field in each point to vary by a different angle. A theory that is invariant under local transformation, is referred to as a Gauge theory. This symmetry is present in the abelian-Higgs model described by its Lagrangian density:

$$\mathcal{L} = (D_\mu \phi)^*(D^\mu \phi) - \frac{1}{4}F_{\mu\nu}F^{\mu\nu} - V(\phi). \quad (3.40)$$

where  $\phi$  is complex scalar field and  $V(\phi)$  is the potential expressed by Eq. 3.31. The covariant derivative  $D_\mu$  is given by:

$$D_\mu = \partial_\mu - ieA_\mu, \quad (3.41)$$

with  $A_\mu$  a gauge vector field and  $e$  the gauge coupling. The term  $F_{\mu\nu}$  represents the electromagnetic tensor:

$$F_{\mu\nu} = \partial_\mu A_\nu - \partial_\nu A_\mu. \quad (3.42)$$

The abelian-Higgs Lagrangian density is invariant under the U(1) group of local transformations:

$$\begin{cases} \phi(x) & \rightarrow e^{i\alpha(x)}\phi(x) \\ A_\mu(x) & \rightarrow A_\mu(x) + \frac{1}{2}\partial_\mu\alpha(x). \end{cases} \quad (3.43)$$

where  $\alpha(x)$  is a real single-valued function which depends now on the position in space-time  $x$ . By analogy with what was done previously, the Hamiltonian density can be calculated using Eq. 3.34 and we show that the vacuum state corresponds to:

$$\begin{cases} A_\mu(x) = 0 \\ \phi(x) = \eta e^{i\theta}. \end{cases} \quad (3.44)$$

Once again the vacuum state is no longer invariant under the U(1) gauge transformations and the field acquires a non-zero vacuum expectation value  $\eta$ . Consequently, the symmetry is spontaneously broken by choosing a value of the phase  $\theta$ .

To study the properties of the vacuum state for the abelian-Higgs model we choose to represent the field  $\phi$  by:

$$\phi(x) = \left( \eta + \frac{\rho(x)}{\sqrt{2}} \right) \exp\left( \frac{i\psi(x)}{\eta} \right). \quad (3.45)$$

Since all vacuum states are equivalent, we choose to work once again in the particular case where the scalar field  $\phi(x)$  is real:

$$\phi(x) = \eta + \frac{\rho(x)}{\sqrt{2}}. \quad (3.46)$$

We consider small fluctuations around  $\phi(x) = \eta$  such that  $\rho(x) \ll \eta$ . Then in these conditions, the Lagrangian density given by Eq. 3.40 is written:

$$\mathcal{L} = \frac{1}{2}(\partial_\mu \rho)^2 - \frac{1}{2}\lambda\eta^2\rho^2 - \frac{1}{4}F_{\mu\nu}F^{\mu\nu} + \frac{1}{2}(\sqrt{2}e\eta)^2 A_\mu A^\mu + \mathcal{L}_{int}. \quad (3.47)$$

The scalar field  $\rho$  corresponds to a scalar massive particle with mass  $m_h = \sqrt{\lambda}\eta$ . The vector field (gauge boson)  $A^\mu$  has gained a mass  $m_b = e\eta$  after the symmetry breaking that is proportional to  $\eta$ , the vacuum expectation value of the Higgs scalar field. These two models containing the symmetry of the U(1) group are sufficient to illustrate the general mechanism of cosmic string formation. However, it is possible to construct models incorporating the spontaneous breaking of much more complex symmetry groups [77, 82].

### 3.2.2 The Nielsen-Olesen string formation

In this section we consider the case of linear topological defects, generally called cosmic strings. We take the example of the formation of such defects during the spontaneous symmetry breaking of the abelian-Higgs model.

The vacuum manifold  $\mathcal{M}$  is formed by the fundamental states accessible to the Higgs field  $\phi$ . In the abelian-Higgs model, the vacuum expectation values of the theory lie on a circle of fixed radius  $|\phi| = \eta$ . The vacuum variety can be written as:

$$\mathcal{M} = \left\{ \phi \mid \phi = \eta e^{i\theta}, \theta \in [0, 2\pi] \right\}, \quad (3.48)$$

which is isomorphic to the circle. Going around an oriented closed path  $\Gamma$  that wraps around this circle, the phase  $\theta$  varies by a factor of  $2\pi$  for each round. For  $n$  rounds the phase varies by a factor of  $2n\pi$  and so  $n$  represents the winding number. This quantity is more rigorously defined as:

$$n(\Gamma) = \frac{1}{2\pi} \oint_{\Gamma} \vec{\nabla} \theta \cdot d\vec{l}. \quad (3.49)$$

The phase being a continuous function,  $n(\Gamma)$  characterizes the algebraic number of rotations that  $\theta$  does on the oriented curve  $\Gamma$  before returning to its initial value. It is therefore an integer:  $n(\Gamma) \in \mathbb{Z}$ . If we assume  $n \neq 0$ , then by continuity the Higgs field  $\phi$  must necessarily pass through zero at least once inside the closed path  $\Gamma$ . In this point, the field is at the local maximum of the potential. Figure 3.4 illustrates this formation mechanism. By translation in the transverse direction to the plane that contains  $\Gamma$ , the field can be cancelled many times and thus forming a linear structure where its value is  $\phi = 0$  along this direction. This linear structure is a one dimensional topological defect called cosmic string. A string must be either a closed loop or an infinitely long string, since otherwise one could deform the closed path  $\Gamma$  and avoid to cross a string.

We consider the abelian-Higgs Lagrangian given in Eq. 3.40. To solve the equations of motion we look for a static solution with cylindrical symmetry, which corresponds to strings along the  $z$ -axis. The position of the center of the string, i.e. all the points where the Higgs field cancels out, is then identified by  $r = 0$ . The solution is invariant by translation on the  $z$ -axis. In that case the Higgs scalar field

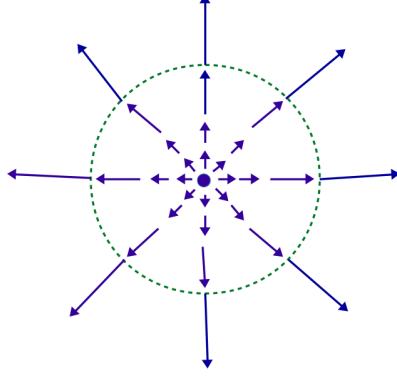


Figure 3.4: Configuration for the Higgs field  $\phi$  for  $n = 1$ . The field  $\phi$  is described by the arrows: the direction represents the phase of the field and the length indicates the norm. On the external contour (green circle):  $|\phi| = \eta$  and the phase  $\theta$  of the field varies from 0 to  $2\pi$ . By continuity, the Higgs field  $\phi$  must necessarily pass through zero at least once inside the closed path. This is represented by the center of the drawing. Figure adapted from [78].

and the gauge field reduce to the form:

$$\phi(r, \theta) = \varphi(r)e^{in\theta}, \quad A_\theta = A_\theta(r), \quad A_0 = A_r = A_z = 0, \quad (3.50)$$

where we used the gauge freedom to choose  $A_0 = 0$ . This solution is known as the Nielsen-Olesen strings (1973) [83]. For convenience we work with the quantities defined as [79]:

$$X \equiv \frac{\varphi}{\eta}, \quad Q \equiv n + eA_\theta, \quad \rho \equiv m_h r, \quad (3.51)$$

with  $m_h = \sqrt{\lambda}\eta$  the Higgs boson mass determined in Sec. 3.2.1. The equations of motion are then expressed in the form of a differential equation system [79]:

$$\begin{aligned} \frac{d^2 X}{d\rho^2} + \frac{1}{\rho} \frac{dX}{d\rho} &= \frac{XQ^2}{\rho^2} + \frac{1}{2}X(X^2 - 1) \\ \frac{d^2 Q}{d\rho^2} - \frac{1}{\rho} \frac{dQ}{d\rho} &= \frac{m_b^2}{m_h^2} X^2 Q, \end{aligned} \quad (3.52)$$

with  $m_b = e\eta$  the gauge boson mass. Although no analytical solution to these equations is known, it is possible to determine them numerically for different values of the winding number  $n$  [81, 84]. The solution associated with a cosmic string corresponds to the boundary conditions:

$$\begin{cases} \lim_{r \rightarrow 0} X(r) = 0 \\ \lim_{r \rightarrow 0} Q(r) = n \end{cases} \quad \text{and} \quad \begin{cases} \lim_{r \rightarrow \infty} X(r) = 1 \\ \lim_{r \rightarrow \infty} Q(r) = 0. \end{cases} \quad (3.53)$$

The Higgs field vanishes in the center of the string identified by  $r = 0$ , whereas far from the string the field returns to its average value in the vacuum  $|\varphi| = \eta$ . The solution far from the string minimizes the energy, and this is verified if the spatial part of the covariant derivative  $D_\mu\phi \propto Q(r)\phi$  is cancelled [82].

The physical width of the string  $\delta$  is determined by the distance scale over which the fields  $(\phi, A_\theta)$  tend to their limit far from the string ( $r \rightarrow \infty$ ). The study of the asymptotic behavior of the Nielsen-Olesen string solutions show that two regimes exist depending on the value of the factor [85]:

$$\beta \equiv \frac{\lambda}{e^2} = \frac{m_b^2}{m_h^2}, \quad (3.54)$$

which measures the mass ratio of the Higgs field and the gauge field. In this case the typical diameter of the string is given by:

$$\begin{cases} \delta \sim \frac{1}{m_b} & \text{for } \beta > 4 \\ \delta \sim \frac{1}{m_h} & \text{for } \beta \leq 4. \end{cases} \quad (3.55)$$

Therefore the typical diameter of the string is roughly given by the largest Compton wavelength of the Higgs and gauge bosons.

One of the most important parameters for describing a cosmic string is the energy per unit length  $\mu$ . The numerical resolution of the equations of motion shows that [86]:

$$\mu = 2\pi f(\beta) \times \eta^2, \quad (3.56)$$

for the lowest energy string configuration where the winding number is unity ( $n = \pm 1$ ). The function  $f$  varies rather slowly growing as  $\log(\beta)$  for  $\beta > 1$  [87, 88, 81] and is of the order of the unit for  $f(1) = 1$  [86]. In the following we will keep in mind the relation between the energy per unit length and the vacuum expectation value of the Higgs field:

$$\mu \sim \eta^2. \quad (3.57)$$

This result can also be obtained analytically by making some approximations [77, 78]. We will see in the next section that this energy is determined by the energy scale of the symmetry breaking.

We end this section by presenting an argument to justify the stability of such strings and thus to clarify their potential existence. The local string contains a tube of magnetic flux through a horizontal surface to the z-direction. We may write the general cylindrically symmetric solution for the gauge field as:

$$A_\theta = -\frac{n g(r)}{e r} \quad \text{with} \quad \begin{cases} \lim_{r \rightarrow 0} g(r) = 0 & \text{so that } A_\theta \text{ does not diverge in } 0 \\ \lim_{r \rightarrow \infty} g(r) = 1. \end{cases} \quad (3.58)$$

The magnetic flux through a horizontal surface that rests on a closed contour of infinite radius centered on the string is given by the Kelvin-Stokes theorem:

$$F \equiv \oint \vec{B} \cdot d\vec{S} = \oint \vec{A} \cdot d\vec{l}. \quad (3.59)$$

We deduce that:

$$F = \oint \vec{A} \cdot d\vec{l} = \int_0^{2\pi} -\frac{n}{e} \frac{1}{r} r d\theta = n \frac{2\pi}{e} \quad \text{with } n \in \mathbb{Z}, \quad (3.60)$$

the magnetic field is then quantized. This is a consequence of the quantization of the winding number  $n$ . Because the phase of  $\phi$  must change by an integer multiple of  $2\pi$ , the flux is quantized. We have seen that the description of cosmic strings in the abelian-Higgs model revealed a single parameter  $\beta$  on which the structure of the strings depends. We distinguish 3 cases depending on the winding number value:

$$\begin{cases} \beta < 1 & \text{and } n \in \mathbb{Z} & \text{stable - type I} \\ \beta > 1 & \text{and } |n| > 1 & \text{unstable} \\ \beta > 1 & \text{and } |n| = 1 & \text{stable - type II.} \end{cases} \quad (3.61)$$

For the type I regime, a string with a winding number  $n$  is more stable than  $n$  strings with a winding number 1, and the stability of the strings increases with their number of windings [86, 87]. For the second case, the magnetic flux is  $F = 2\pi n/e$  with  $n > 1$  and this configuration is unstable because it can be divided into  $n$  strings carrying the elementary unit of flux  $2\pi/e$  [81]. Finally, in general when discussing the cosmological properties of cosmic strings, the strings being considered are those of the type II regime. In this regime, local strings are stable [89]. The result of the interaction of such strings will be discussed later in this chapter.

### 3.2.3 Phase transition

We are now focusing on the formation of cosmic strings during the evolution of the Universe. As the Universe cools down, it passes through a succession of at least three phase transitions as we have seen in Sec. 3.1.4. All these phase transitions occurred at a given temperature  $T_c$ . The main idea is that at very high temperature, symmetry breaking is not present and only occurs during these phase transitions. To connect the whole description of spontaneous symmetry breaking with cosmology, we need then to include the temperature in the abelian-Higgs Lagrangian. The main effect of adding the temperature is to change the expression of the potential [90, 77]. In particular we add thermal corrections to the *Mexican-hat* potential  $V(\phi)$ . The effective potential can be written as:

$$V_{eff}(\phi, T) = V(\phi) + \Delta V(\phi, T). \quad (3.62)$$

The evolution of the effective potential as a function of the temperature  $T$  will govern the phase transition.

We consider the abelian-Higgs model with the following expression for the effective potential at high temperature [77]:

$$V_{eff}(\phi, T) = V(\phi) + \frac{\lambda + 3e^2}{12} T^2 |\phi|^2 - \frac{2\pi^2}{45} T^4. \quad (3.63)$$

For clarity's sake, we set  $e = 0$  which is equivalent to considering the Goldstone model [77]. This potential can then be written as:

$$V_{eff}(\phi, T) = m^2(T) |\phi|^2 + \frac{\lambda}{4} |\phi|^4 \quad \text{with} \quad m^2(T) = \frac{\lambda}{12} (T^2 - 6\eta^2), \quad (3.64)$$

where  $m(T)$  is the effective mass of the Higgs field in the symmetric state  $|\phi| = 0$ . The effective mass-squared vanishes at the critical temperature:

$$T_c \equiv \sqrt{6\eta}. \quad (3.65)$$

In the high temperature regime  $T > T_c$ , the effective square mass is positive, the minimum of  $V_{eff}$  is at  $\phi = 0$ : the theory is symmetric. Figure 3.5 illustrates the shape of  $V_{eff}$ . When the temperature drops below the critical temperature  $T < T_c$ ,

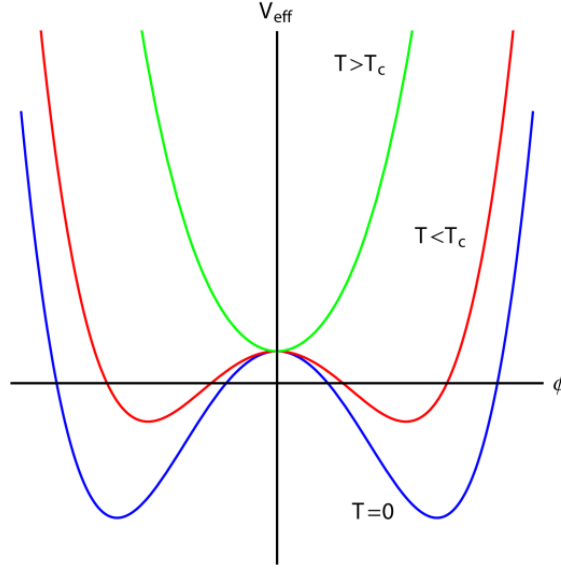


Figure 3.5: The temperature-dependant effective potential  $V_{eff}(\phi, T)$  for a second order phase transition near the critical temperature  $T_c$  for  $\phi \in \mathbb{R}$ .

the effective square mass becomes negative and the symmetric state becomes unstable, i.e. maximazing  $V_{eff}$ . In addition, the potential develops a new minimum given by:

$$|\phi| = \sqrt{\frac{(T_c^2 - T^2)}{6}}, \quad (3.66)$$

and so the Higgs field acquires a non-zero expectation value: the symmetry is broken. There was a phase transition. This transition is called second-order because the value of  $\phi$  varies continuously with the temperature  $T$ . The general behaviour is the same if we consider the abelian-Higgs effective potential. The relationship between the phase transition temperature  $T_c$  and the symmetry breaking energy scale  $\eta$  obtained with the Goldstone model is typical of second-order phase transitions:

$$\eta \sim T_c. \quad (3.67)$$

Thus we can estimate the string energy per unit length  $\mu$  using Eq. 3.57:

$$\mu \sim T_c^2. \quad (3.68)$$

For GUT scale strings with  $\eta \sim 10^{15}$  GeV, this corresponds to a string energy per unit length of  $\mu \sim 10^{22}$  kg/m located in a diameter smaller than that of the hydrogen atom <sup>5</sup>

To conclude this section, it is important to mention some of the implications of symmetry breaking at a cosmological phase transition. It was first studied by Kibble in 1976 [91, 92]. The non-zero expectation value of the Higgs field in Eq. 3.66 has a fixed norm while the choice of the phase  $\theta$  remains free. This choice will depend on random fluctuation in  $\theta$  which can be expected to differ in different region of space [93]. This statement is based on the argument that distant regions in space may not communicate with each other. This is a consequence of the fact that correlations cannot be established faster than the speed of light. The typical scale beyond which fluctuations in  $\theta$  are uncorrelated is set by the correlation length  $\xi(t)$  and an upper limit is given by the causal horizon  $d_H$ :

$$\xi(t) < d_H. \quad (3.69)$$

Above the correlation length  $\xi(t)$ , the vacuum expectation values of the field  $\phi(t)$  at two points of the Universe are uncorrelated. The correlation length  $\xi(t)$  is well described by the Zurek-Kibble mechanism that takes into account the duration of the phase transition named *quench timescale* and the time of relaxation, which is the time it takes correlations to establish on the length scale  $\xi(t)$  [94]. Near the transition it was shown that  $\xi(t)$  diverges, in the Zurek-Kibble mechanism it is counterbalanced by the fact that the relaxation timescale also diverges.

### 3.2.4 The Nambu-Goto action

The Nielson-Olesen strings considered until now are straight and static. We want now to study a more realistic case of a moving and curved string. The equations of motion presented in Eq. 3.52 are complicated to solve analytically, and so to give a description of these objects we have to simplify the study. We consider the string as

---

<sup>5</sup>It corresponds to  $G\mu/c^2 = 10^{-6}$ .

a one-dimensional object, i.e. an infinitely thin string. This means that the radius of curvature of the string  $R$  is much greater than the string diameter  $\delta$ . When  $t$  varies, the movement of the string sweeps out a two-dimensional surface often called the worldsheet. On a curved worldsheet each point of the string is parameterized by:

$$x^\mu(\zeta^\mu) = x^\mu(\zeta^0, \zeta^1), \quad (3.70)$$

where the worldsheet coordinate  $\zeta^0$  is chosen to be timelike, while the other,  $\zeta^1$  is spacelike. From the action of the abelian-Higgs model in a general spacetime we want to construct an appropriate local string action called the Nambu Goto action. The action for the abelian-Higgs model in a general spacetime described by a metric  $g_{\mu\nu}$  is:

$$S = \int d^4y \sqrt{-g} \times \mathcal{L}_{\mathcal{H}} \quad (3.71)$$

where we define  $g$  to be the determinant of the metric and  $\mathcal{L}_{\mathcal{H}}$  the abelian-Higgs Lagrangian density given by Eq. 3.40. In this way, the spacetime interval between two nearby points on the worldsheet is:

$$ds^2 \equiv g_{\mu\nu} dx^\mu dx^\nu = g_{\mu\nu} x_{,a}^\mu x_{,b}^\nu d\zeta^a d\zeta^b \quad \text{with} \quad x_{,a}^\mu \equiv \frac{\partial x^\mu}{\partial \zeta^a}, \quad (3.72)$$

where at each point of the worldsheet, there are two tangent vectors  $x_{,a}^\mu$  with  $a = 0$  or 1. Hence the two-dimensional induced metric on the worldsheet is given by:

$$\gamma_{ab} = g_{\mu\nu} x_{,a}^\mu x_{,b}^\nu. \quad (3.73)$$

Since an infinitely thin string is invariant with respect to a Lorentz boost, one has to consider only transverse motions of the string. We can construct an approximate solution around each point  $x^\mu(\zeta^\mu)$  using the Nielsen-Olesen ansatz (Eq. 3.50). From our first assumption, within the limit  $R \gg \delta$  we can show that an integration over the transverse coordinates of the abelian-Higgs Lagrangian reduced to the energy per unit length  $\mu$  [77]. Another way to find this result is to use a more qualitative argument. As there is no long-range interaction between different string segments, it is possible to derive the equations of motion of the string from a local action  $S$ . Taking the general form of a local action:

$$S = \mathcal{L} \int d^2\zeta \sqrt{-\gamma}. \quad (3.74)$$

we have to find a Lagrangian which is invariant under general spacetime transformations  $\delta x^\mu$  and under arbitrary reparametrizations of the worldsheet  $\delta \zeta^a$ . Moreover, a dimensional analysis reveals that this Lagrangian should have the dimension of a square mass. Thus, there are only two quantities left that meet these conditions: the energy per unit length  $\mu$  and geometric quantities [77]. Finally, the local action which describes the motion of a curved and dynamic string is the action of Nambu Goto [95, 96]:

$$S_{NG} = -\mu \int d^2\zeta \sqrt{-\gamma}. \quad (3.75)$$

This quantity is proportional to the area of the worldsheet which the string traces as it travels through spacetime.

Lastly, we have seen that the general Lagrangian  $\mathcal{L}$  in Eq. 3.74 may also depend on geometric quantities, such as the the tensor curvature of the string denoted by  $\kappa_{ab} \propto \frac{1}{R^2}$  <sup>6</sup>. In this way we can write at the first order:

$$\mathcal{L} = -\mu + \alpha\kappa. \quad (3.76)$$

Since the string diameter is  $\delta \sim \frac{1}{m_h}$  (Eq. 3.55) with  $m_h = \frac{1}{\sqrt{\lambda}\eta}$  and the energy per unit length is  $\mu \sim \eta^2$ , the string thickness is approximated by  $\delta \geq \frac{1}{\sqrt{\mu}}$ . Recalling our first assumption that can be rewritten as  $R \gg \delta$ , we find that the curvature term  $\kappa$  can be neglected in front of the energy per unit length  $\kappa \ll \mu$ . Thus the general local action in Eq. 3.74 is well reduced to the action of Nambu-Goto in the case of an infinitely thin string. If the string curvature is small but not negligible, one may consider an expansion in powers of the curvature to correct the Nambu-Goto action <sup>97</sup>.

### 3.2.5 String dynamic

We are interested here in studying the dynamics of strings. In the previous part, a process of dimensional reduction led to Nambu Goto's action  $S_{NG}$ . In a general spacetime described by a metric  $g_{\mu\nu}$ , the equations of motion can be derived by varying this action  $S_{NG}$  with respect to the  $x^\mu(\zeta^a)$ :

$$\frac{1}{\sqrt{-\gamma}} \partial_a \left( \sqrt{-\gamma} \gamma^{ab} x_{,b}^\mu \right) + \Gamma_{\nu\sigma}^\mu \gamma^{ab} x_{,a}^\nu x_{,b}^\sigma = 0, \quad (3.77)$$

where we recall that  $\gamma$  is the determinant of the worldsheet metric and  $\Gamma_{\nu\sigma}^\mu$  represents the Christoffel symbols corresponding to the metric  $g_{\mu\nu}$  expressed in Eq. 1.10. For the purpose of this thesis, it is sufficient to discuss the case of a flat space. On Minkowski spacetime in the standard coordinates, the Christoffel symbols are all zero and the equations of motion reduced to:

$$\partial_a \left( \sqrt{-\gamma} \gamma^{ab} x_{,b}^\mu \right) = 0. \quad (3.78)$$

We saw two transformations that leave the Nambu-Goto action invariant: general spacetime coordinate transformation and arbitrary reparametrizations of the worldsheet. It is useful to choose a specific gauge where the equations of motion get simplified. One way to fix the gauge in our case is to fix the two-dimensional metric  $\gamma$ . A common choice of gauge is to require that the  $2 \times 2$  metric matrix  $\gamma$  is diagonal and traceless:

$$\gamma_{01} = 0 \quad \text{and} \quad \gamma_{00} + \gamma_{11} = 0. \quad (3.79)$$

---

<sup>6</sup>The world sheet is two-dimensional, hence the square.

This is the conformal gauge. This transformation preserves the form of an object but not its size, it is why we call it “conformal”, indeed this metric is derived from the Minkowski’s metric by multiplying by a simple factor:

$$\gamma_{ab} = \sqrt{-\gamma}\eta_{ab}. \quad (3.80)$$

Given the expression of the metric in Eq. 3.73, these conditions are rewritten as:

$$\begin{cases} \dot{x}^\mu \cdot x^{\mu'} = 0 \\ (\dot{x}^\mu)^2 + (x^{\mu'})^2 = 0, \end{cases} \quad (3.81)$$

where the dots and primes stand for derivatives with respect to  $\zeta^0$  (time) and  $\zeta^1$  (space) respectively. The point “.” represents here the scalar product defined by the flat spacetime metric  $\eta_{\mu\nu}$ . The equations of motion in Eq. 3.78 take the form of a 2 dimensional wave equation:

$$\ddot{x}^\mu - x^{\mu''} = 0. \quad (3.82)$$

The gauge is not yet completely fixed. We can use the freedom given by the invariance under reparametrizations of the worldsheet to choose:

$$\zeta^0 = x^0 \equiv t, \quad (3.83)$$

which verifies the wave equation. In such a gauge, the string trajectory is described by a 3-vector with  $\underline{\mathbf{x}}(\zeta, t)$  where  $\zeta \equiv \zeta^1$ , the spacelike component. Thus the conditions of conformal gauge in Eq. 3.81 are written in the form:

$$\begin{cases} \dot{\underline{\mathbf{x}}} \cdot \underline{\mathbf{x}}' = 0 \\ \dot{\underline{\mathbf{x}}}^2 + \underline{\mathbf{x}}'^2 = 1. \end{cases} \quad (3.84)$$

The first condition tells us that the string moves perpendiculary to itself since the velocity of the string  $\dot{\underline{\mathbf{x}}}$  is perpendicular to the string. Thus, the gauge in Eq. 3.83 is called transverse gauge. By inverting the second condition it comes  $d\zeta = (1 - \dot{\underline{\mathbf{x}}}^2)^{-1/2} dl$  with  $dl \equiv |d\underline{\mathbf{x}}|$ . The energy of the string is thus:

$$\mathcal{E} \equiv \mu \int (1 - \dot{\underline{\mathbf{x}}}^2)^{-1/2} |d\underline{\mathbf{x}}| = \mu \int d\zeta. \quad (3.85)$$

Thus, this last condition is a choice of normalization which fixes the curvilinear abscissa  $\zeta$  as proportional to the energy of the string. Finally, with these conditions the wave equation Eq 3.82 is:

$$\ddot{\underline{\mathbf{x}}} - \underline{\mathbf{x}}'' = 0. \quad (3.86)$$

The first term  $\ddot{\underline{\mathbf{x}}}$  represents the acceleration of a string element. To understand the meaning of the second term we can use an example. We consider an arc defined by a function  $f$ . For a straight arc, the tangent vector at each point is the same and  $f' = 0$ , while for an arc with a non-zero curvature we notice that the tangent vector at all points varies. Intuitively, we see that the more curved the arc is, the faster the

derivative varies. We can thus link the curvature to the variation of the derivative  $f'$ , and therefore to the second derivative  $f''$ . We deduce then that the term  $\underline{\mathbf{x}}''$  is directly linked to the local curvature radius  $R$ . We can rewrite it as  $|\underline{d^2\mathbf{x}}/d\zeta^2| \propto R^{-1}$ . Therefore, the wave equation tell us that the acceleration of a string element in its local rest frame ( $\underline{\dot{\mathbf{x}}} = 0$  transverse velocity) is inversely proportional to the local curvature radius  $R$ . The direction of  $\underline{\ddot{\mathbf{x}}}$  is such that the curved strings tends to straighten. The string begins to oscillate at each point around the equilibrium position where the string is straight. The general solution of the wave equation is a superposition of two waves traveling at the speed of light in opposite directions:

$$\underline{\mathbf{x}}(t, \zeta) = \frac{1}{2} [\underline{\mathbf{a}}(\zeta - t) + \underline{\mathbf{b}}(\zeta + t)]. \quad (3.87)$$

where  $\underline{\mathbf{a}}(\zeta - t)$  and  $\underline{\mathbf{b}}(\zeta + t)$  are two continuous arbitrary functions. However, the conformal gauge conditions in Eq. 3.84 require that:

$$\underline{\mathbf{a}}'^2 = \underline{\mathbf{b}}'^2 = 1. \quad (3.88)$$

We will see later that when strings interact with each other they form loops. Thus it is interesting to describe the dynamics of such a closed loop. We can use the results obtained just above for an infinite string because the Nambu-Goto action from which we derived the equations of motion is a local action. In that case  $\zeta$  varies in a closed interval:

$$0 \leq \zeta < L, \quad (3.89)$$

where  $L$  is the invariant length of the loop defined as:

$$L \equiv \frac{\mathcal{E}}{\mu}, \quad (3.90)$$

with  $\mathcal{E}$  the energy of the string and  $\mu$  the energy per unit length. For the loop to be close, the propagation of a perturbation must be periodic

$$\underline{\mathbf{x}}(\zeta + L, t) = \underline{\mathbf{x}}(\zeta, t) \quad , \quad \forall t. \quad (3.91)$$

We want to show that  $\underline{\mathbf{a}}$  and  $\underline{\mathbf{b}}$  are two periodic functions. By injecting this condition into the general solution, given by Eq. 3.87 we get:

$$\underline{\mathbf{b}}(\zeta + t + L) - \underline{\mathbf{b}}(\zeta + t) = -\underline{\mathbf{a}}(\zeta - t + L) + \underline{\mathbf{a}}(\zeta - t) \equiv \underline{\Delta}, \quad (3.92)$$

where the vector  $\underline{\Delta}$  must be a constant and so it should not depend on the value of  $\zeta$ . The string momentum is defined by 77:

$$\underline{\mathbf{P}} = \mu \int d\zeta \underline{\dot{\mathbf{x}}}(\zeta, t), \quad (3.93)$$

that can be written using Eq. 3.87 as:

$$\underline{\mathbf{P}} = \frac{\mu}{2} \int_0^L d\zeta (\underline{\mathbf{b}}' - \underline{\mathbf{a}}') = \frac{\mu}{2} \times 2\underline{\Delta}, \quad (3.94)$$

where primes stand for derivatives with respect to  $\zeta$ . In the centre-of-mass frame the momentum is zero thus  $\underline{\Delta} = 0$ . Therefore  $\underline{\mathbf{a}}$  and  $\underline{\mathbf{b}}$  are periodic functions:

$$\underline{\mathbf{a}}(\zeta + L) = \underline{\mathbf{a}}(\zeta) \quad \underline{\mathbf{b}}(\zeta + L) = \underline{\mathbf{b}}(\zeta). \quad (3.95)$$

Using the spatial periodicity of the perturbation we show that the closed loop oscillates in time with a period of  $L/2$ :

$$\begin{aligned} \underline{\mathbf{x}}\left(\zeta + \frac{L}{2}, t + \frac{L}{2}\right) &= \frac{1}{2} \left[ \underline{\mathbf{a}}\left(\zeta + \frac{L}{2} - t - \frac{L}{2}\right) + \underline{\mathbf{b}}\left(\zeta + \frac{L}{2} + t + \frac{L}{2}\right) \right] \\ &= \frac{1}{2} [\underline{\mathbf{a}}(\zeta - t) + \underline{\mathbf{b}}(\zeta + L + t)] \\ &= \frac{1}{2} [\underline{\mathbf{a}}(\zeta - t) + \underline{\mathbf{b}}(\zeta + t)] \\ &= \underline{\mathbf{x}}(\zeta, t). \end{aligned} \quad (3.96)$$

The fact that the timescale of the oscillations is comparable to the loop length  $L$  indicates then that the motion of the loop is relativistic [77]. Indeed, the quadratic velocity over a loop period is given by

$$\langle v^2 \rangle = \int_0^T \frac{dt}{T} \int_0^L \frac{d\zeta}{L} \dot{\underline{\mathbf{x}}}^2, \quad (3.97)$$

and we can show using the previous results that:

$$\langle v^2 \rangle = \frac{1}{2}. \quad (3.98)$$

Finally, the internal structure of the string is meaningless when we deal with scales much larger than the string width. We can show [77] for a straight string lying along the  $z$ -axis, that the effective energy-momentum tensor is:

$$T_\nu^\mu(x, y) = \mu \delta(x) \delta(y) \times \text{diag}(1, 0, 0, 1). \quad (3.99)$$

The tension for a Nambu-Goto string is huge, equal to its energy per unity length  $\mu$  and forces any cosmic string which is not completely straight to move relativistically. It is very usual in literature to refer to the dimensionless quantity  $G\mu/c^2$  as the string tension.

### 3.2.6 Intercommutation

To understand the mechanism of loop formation, it is necessary to describe the interaction between strings. We consider strings formed in Abelian models. When two strings intersect there are two possible issues: either the strings simply pass through each other or they intercommute i.e. they exchange partner [78]. The probability of intercommutation  $p$  is an important parameter to describe the cosmological evolution of a string network. Numerical simulations performed to solve the field equations given in Eq. 3.52 indicated that a string invariably “exchange partner” when it

interacts with itself or with another string. The probability of intercommutation for Nielsen-Olesen strings found by the simulations is [98] <sup>7</sup>:

$$p \simeq 1 \tag{3.100}$$

and in the following of this thesis we will consider:

$$p = 1. \tag{3.101}$$

The intersection of a string with itself leads to the formation of a closed loop and an infinite string, as represented on Fig 3.6. Whereas when a string intercommute with another string, a closed loop is formed made up of the segments of each string. A

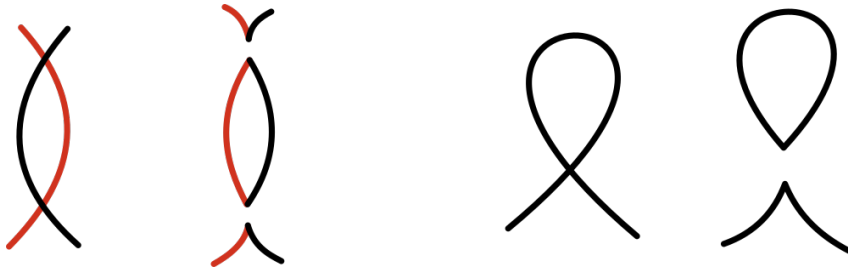


Figure 3.6: Cosmic string loop formation. A loop forms when two strings interact in two separates points or when a string cross itself.

major consequence of the intercommutation mechanism is the ongoing formation of cosmic string loops.

In certain field theories, strings networks can also have junctions namely points at which three strings meet, see Fig 3.7. For example, junctions occur in the abelian-

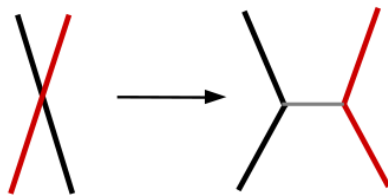


Figure 3.7: In certain field theories, when two strings intersect, a new strand can be created. This one joins the original strings into two vertices called junctions.

Higgs model for type I strings briefly described in Sec. 3.2.2. In this regime the strings are always stable, regardless of the winding number  $n$  and the stability increases with  $n$ . For  $n = 1$  and under certain conditions it is shown that two strings tend to form junctions instead of merging to form a string with  $n = 2$  [101]. Junctions

---

<sup>7</sup>This result is no longer valid at very high incoming velocities between strings [99, 100]

can also occur in more complicated models in which non-abelian symmetries are broken [102, 103].

Development in String Theory suggest that fundamental strings may be stretched to macroscopic sizes and play the cosmological role of cosmic superstrings. There are important differences between cosmic superstrings and topological strings. When superstrings meet they reconnect with probability  $p$  that can be less than unity. This is partly due to the fact that fundamental strings of String Theory interact probabilistically. Furthermore, these models have extra spatial dimensions so that even though two strings may meet in 3 dimensions, they miss each other in the extra dimensions. These two effects result in values of  $p$  in the range  $10^{-3} \leq p \leq 1$  [104].

### 3.2.7 Cusps and Kinks

As we will see later, the long strings lose energy into loop production, and the loops decay by emission of gravitational waves. Two objects propagating on cosmic string loops are expected to emit bursts of gravitational waves: cusps and kinks. Thus, for the rest of this thesis it is relevant to introduce the formation of such objects.

#### Cusps

A cusp is a point on the worldsheet where the string moves at the speed of light:

$$\dot{\mathbf{x}} = 1. \quad (3.102)$$

From the conditions of conformal gauge in Eq. 3.84 this implies that the string tangent vector vanishes:  $\mathbf{x}'(\zeta, t) = 0$ . Thus, there should be a couple of point  $(\zeta_a, \zeta_b)$  such that:

$$\mathbf{a}'(\zeta_a) = -\mathbf{b}'(\zeta_b). \quad (3.103)$$

From the condition in Eq. 3.88 it follows that the vector functions  $\mathbf{a}'(\zeta_a)$  and  $-\mathbf{b}'(\zeta_b)$  describe curves on a unit sphere<sup>8</sup> as  $\zeta$  runs from 0 to 1. In addition, the periodicity of these functions requires that:

$$\int_0^L \mathbf{a}' d\zeta = \int_0^L \mathbf{b}' d\zeta = 0, \quad (3.104)$$

but are otherwise arbitrary, thus these curves may intersect since nothing prevent them to lie in one hemisphere of the unit sphere. These points of intersection wich reach the velocity of light are called cusps. Figure 3.8 illustrates the cusp formation.

We are now interested in the shape of the string in the vicinity of a cusp. It is convenient to choose the parametrization of the string such that the cusp occurs at

---

<sup>8</sup>Often called the Kibble-Turok sphere [105].

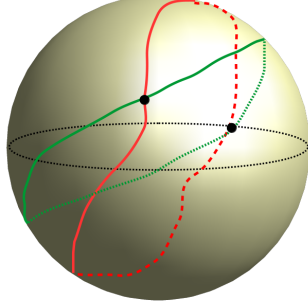


Figure 3.8: A cusp is produced if the closed curves described by the functions  $\underline{\mathbf{a}}'$  and  $\underline{\mathbf{b}}'$  intersect on the unit sphere. In this picture shows two cusps (black points).

$t = \zeta = 0$ . In this way we can expand the perturbation functions around the cusp in 0:

$$\begin{aligned}\underline{\mathbf{a}}(\zeta) &\simeq \underline{\mathbf{a}}'_0 \zeta + \frac{1}{2} \underline{\mathbf{a}}''_0 \zeta^2 + \frac{1}{6} \underline{\mathbf{a}}'''_0 \zeta^3 \\ \underline{\mathbf{b}}(\zeta) &\simeq \underline{\mathbf{b}}'_0 \zeta + \frac{1}{2} \underline{\mathbf{b}}''_0 \zeta^2 + \frac{1}{6} \underline{\mathbf{b}}'''_0 \zeta^3\end{aligned}\quad (3.105)$$

where the subscript 0 denotes quantities at the cusp. From Eq. [3.103](#) at a cusp  $\underline{\mathbf{a}}'_0 = -\underline{\mathbf{b}}'_0$  and so the shape of the string at  $t=0$  is given by:

$$\begin{aligned}\underline{\mathbf{x}}(\zeta, t = 0) &= \frac{1}{2} [\underline{\mathbf{a}}(\zeta, t = 0) + \underline{\mathbf{b}}(\zeta, t = 0)] \\ &\simeq \frac{1}{2} \left[ \underline{\mathbf{a}}'_0 \zeta + \underline{\mathbf{b}}'_0 \zeta + \frac{1}{2} \underline{\mathbf{a}}''_0 \zeta^2 + \frac{1}{2} \underline{\mathbf{b}}''_0 \zeta^2 + \frac{1}{6} \underline{\mathbf{a}}'''_0 \zeta^3 + \frac{1}{6} \underline{\mathbf{b}}'''_0 \zeta^3 \right] \\ &\simeq \frac{1}{4} (\underline{\mathbf{a}}''_0 + \underline{\mathbf{b}}''_0) \zeta^2 + \frac{1}{12} (\underline{\mathbf{a}}'''_0 + \underline{\mathbf{b}}'''_0) \zeta^3,\end{aligned}\quad (3.106)$$

which can be rewritten as:

$$\underline{\mathbf{x}}(\zeta, t = 0) \simeq \underline{\mathbf{x}}''_0 \frac{\zeta^2}{2} + \underline{\mathbf{x}}'''_0 \frac{\zeta^3}{6},\quad (3.107)$$

so if  $\underline{\mathbf{x}}''_0 \neq 0$  the string momentarily develops a cusp and  $\underline{\mathbf{x}}''_0 \equiv \underline{\mathbf{a}}''_0 + \underline{\mathbf{b}}''_0$  gives the direction of the cusp. Moreover from Eq. [3.88](#) it follows:

$$\begin{aligned}(i) \quad &|\underline{\mathbf{a}}'_0| = |\underline{\mathbf{b}}'_0| = 1 \\ (ii) \quad &\underline{\mathbf{a}}'_0 \cdot \underline{\mathbf{a}}''_0 = \underline{\mathbf{b}}'_0 \cdot \underline{\mathbf{b}}''_0 = 0,\end{aligned}\quad (3.108)$$

where (i) implies that the cusp velocity is:

$$\dot{\underline{\mathbf{x}}}(\zeta = 0, t = 0) \equiv \dot{\underline{\mathbf{x}}}_0 = \frac{1}{2} (\underline{\mathbf{a}}'_0 + \underline{\mathbf{b}}'_0) = \underline{\mathbf{a}}'_0 = -\underline{\mathbf{b}}'_0.\quad (3.109)$$

Therefore, it follows from (ii) that the the direction of the cusp  $\underline{\mathbf{x}}''_0 \equiv \underline{\mathbf{a}}''_0 + \underline{\mathbf{b}}''_0$  is orthogonal to that of the cusp velocity  $\dot{\underline{\mathbf{x}}}_0$ . The shape of the string near a cusp is shown in Fig [3.9](#).

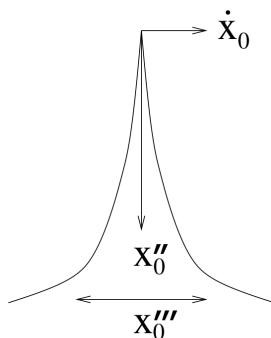


Figure 3.9: Generic shape of a string segment when a cusp forms. The cusp moves at the speed of light in the direction  $\dot{\mathbf{x}}_0$ , the direction of the string near the cusp is given by  $\mathbf{x}''_0$  and the spreading of the strings is in the direction  $\mathbf{x}'''_0$

### Kinks

Another type of discontinuity appears when strings intercommute. The string newly-connected points in different directions and moves with different velocities. The conservation of momentum imposes that at the moment of the intercommutation  $t_0$  and around the point of intersection, the velocity  $\dot{\mathbf{x}}(\zeta, t_0)$  and the shape  $\mathbf{x}'(\zeta, t_0)$  of the new string must change very quickly. For Nambu-Goto strings these functions are considered as discontinuous. These discontinuities, which resembles a “corner” on the string loop are the kinks. Since the motion of the string at each point is described by the superposition of two perturbations that propagate in opposite direction  $\mathbf{a}'(\zeta - t)$  and  $\mathbf{b}'(\zeta + t)$ , we deduce that at least one of these functions is discontinuous at a kink. If both,  $\mathbf{a}'$  and  $\mathbf{b}'$  are discontinuous then we can interpret this as two kinks running along the string at the speed of light in opposite directions [77]. Therefore, because kinks are formed during strings intersection, they are created in pairs and each “kinky” loop is expected to have an equal number of left- and right-moving kinks at formation.

Simulations show that loops just formed from a long string network have many kinks [106]. Kinks may affect the form of the loop by giving it a wiggly shape. On the other hand, as we will see later, kinks are expected to emit bursts of gravitational waves and a significant fraction of the loop length is lost in this process. This may have the effect to smooth the loop, i.e reducing the number of kinks on the loop [107]. Moreover, we have seen that the perturbation functions can be considered as paths on the Kibble-Turok sphere of unit vectors. In general, these paths intersect and the point of intersection is called a cusp. However, loops which have kinks are more likely to avoid cusps, since there are gaps (discontinuities) in the two curves on the unit sphere, see Fig 3.8. Therefore, kinks render the appearance of cusps less likely [108].

### 3.3 Gravitational waves emitted by cosmic strings

In the previous part we saw that the interaction between cosmic strings leads to the formation of loops. The mechanism involved is called intercommutation. Two features can then be produced on the oscillating loops. Cusps where the string instantaneously reaches the speed of light and kinks considered as discontinuities on the tangent vector of a string. In this section we present the results obtained by Damour and Vilenkin (2001) [109, 110] concerning the emission of gravitational wave bursts by cusps and kinks. The calculation of the waveform is quite technical, so we refer the reader back to the original paper which will find a clear demonstration. However, all the knowledge needed to calculate the waveform has been presented earlier in this chapter and in Chap. 1. First, we present the results obtained for an asymptotically flat space. Then we will see how these results are modified to take into account the effect of the propagation of the gravitational waves in a curved FLRW Universe.

#### 3.3.1 Waveform from cusps and kinks

Before introducing the results of Damour and Vilenkin [109, 110], we clarify the underlying assumptions that are considered in the calculations. We focus on the gravitational-wave bursts emitted by a cusp or a kink as seen by an observer located at a distance  $r$  from the source in the “local wave zone”, i.e. at a distance large compared to the gravitational wavelength but small compared to the cosmological scale. This condition is then written:

$$r \gg \lambda_{GW} \quad \text{and} \quad r \ll \frac{1}{H_0}, \quad (3.110)$$

with  $\lambda_{GW}$  the gravitational-wave wavelength and  $1/H_0$  the Hubble radius. For this purpose, we work in a near-flat-space which is characterized by its local metric  $g_{\mu\nu} = \eta_{\mu\nu} + h_{\mu\nu}$ , with  $\eta_{\mu\nu}$  the Minkowski metric and  $h_{\mu\nu} \ll 1$  the metric perturbation generated by the source, see Sec. 1.2. In this case, we have shown that the loop dynamic is governed by the Nambu-Goto action. The closed loop oscillates in time with a fundamental period  $T_\ell = \ell/2$ , where  $\ell$  is the invariant loop length. The frequency of the harmonics of the fundamental mode is denoted by:

$$w_m \equiv m \frac{2\pi}{T_\ell} = m \frac{4\pi}{\ell} \quad \text{with} \quad m \in \mathbb{Z}^* \quad (3.111)$$

and we consider only the asymptotic behavior when  $m \rightarrow \infty$ , i.e. a frequency domain much larger than the frequency of the fundamental mode of the string. Cusps and kinks are expected to contribute to the harmonic  $m \gg 1$  of the loop oscillations. Under these conditions, it is shown that the frequency-domain waveform is:

$$h(\ell, f) = A_q(\ell) f^{-q} \Theta(f_h - f) \Theta(f - f_\ell) \quad \text{where} \quad \begin{cases} q = 4/3 & \text{for cusps} \\ q = 5/3 & \text{for kinks.} \end{cases} \quad (3.112)$$

In addition, it is also proven that the gravitational-wave waveform is linearly polarized. The signal amplitude  $A_q$  produced by a cusp/kink propagating on a loop of size  $\ell$  is given by:

$$A_q = g_1 \frac{G\mu\ell^{2-q}}{r}, \quad (3.113)$$

where  $r$  denotes the distance to the source. Here  $g_1$  is an ignorance factor that absorbs different uncertainties which enter into the calculation of the cusp and kink waveform [111]. If loops are not too wiggly, this factor is expected to be of  $O(1)$ , the analytically calculated values [109] are given in Tab. 3.2. The amplitude of the signal emitted by a cusp is higher than that emitted by a kink.

	q	$g_1$	$g_2$
Cusp	4/3	0.85	1/2.31
Kink	5/3	0.3	1/2.31
Kink-kink collision	2	0.1	1/2.31

Table 3.2: Numerical factors taken from [109] depending on the feature considered.

The emission direction of the gravitational wave is identified by the vector  $\mathbf{n}$ . We note  $\mathbf{n}_c$  the direction of the cusp which is given by the intersection of the curves  $\mathbf{a}'(\zeta_a) = -\mathbf{b}'(\zeta_b)$ . The cusp waveform is only valid in the case where the angle between the line of sight and the cusp is small, i.e.  $\theta \equiv \arccos(\mathbf{n} \cdot \mathbf{n}_c)$  satisfies:

$$\theta \lesssim \theta_m \ll 1 \quad \text{with} \quad \theta_m \equiv \frac{1}{(g_2 f \ell)^{1/3}}. \quad (3.114)$$

Here  $\theta_m$  is the maximal gravitational-wave beam opening angle. The second inequality comes from the fact that the waveform has been derived in the high frequency regime:  $f\ell = 2m \gg 1$  (see Eq. 3.111). Thus a loop with a cusp emits a gravitational wave burst in a cone of solid angle  $d\Omega \sim \pi\theta_m^2$  around the exact direction of the cusp. The same validity condition is imposed for the kinks waveform, by replacing  $\mathbf{n}_c$  by  $\mathbf{n}_k$ : the direction of the kink. The gravitational-wave burst is emitted in a fan-shaped set of directions by the moving kink, contained within an angle  $d\Omega \sim 2\pi\theta_m$ . Here  $g_2 = 1/2.31$  is a constant factor which once again absorbs several uncertainties in the derivation of the waveform. [109].

Finally, let us justify the presence of the step functions (1 if  $x > 0$ ; 0 if  $x < 0$ ). Because of the condition in Eq. 3.114, there is a maximum observable frequency  $f_h$ . The value of  $f_h$  is obtained by inverting the expression of the beaming angle  $\theta_m$ . The lowest frequency we can observe  $f_\ell$  is in practice given by the lower end of the gravitational-wave detector's sensitive band as we will see in Chap. 4.

Another source of gravitational-wave emission corresponds to the collision of two kinks moving in opposite directions. The gravitational-wave emission at a kink-kink collision is isotropic, see Tab. 3.2.

### 3.3.2 Propagation in an expanding space

Here we present how the waveform in Eq. 3.112 is modified by taking into account the expansion of the Universe. We consider the case of a spatially flat FLRW Universe, the cosmology used is developed in Sec. 3.1. There are two terms to correct in the waveform. We have the usual frequency redshifting:

$$f \rightarrow f(1+z), \quad (3.115)$$

with  $z$  the cosmological redshift. A gravitational-wave burst emitted at redshift  $z$  travels over a physical distance  $r(z)$ , and so it is also necessary to replace the distance  $r$  that appears in the amplitude expression by the proper distance:

$$r \rightarrow r(z) \equiv \frac{\varphi_r(z)}{H_0} \quad \text{with} \quad \varphi_r(z) \equiv \int_0^z \frac{dz}{\mathcal{H}(z)}. \quad (3.116)$$

The frequency waveform is thus rewritten in the form:

$$h(\ell, z, f) = A_q(\ell) f^{-q} \Theta(f_h - f) \Theta(f - f_\ell) \quad \text{with} \quad A_q(\ell, z) = g_1 \frac{G\mu\ell^{2-q}}{(1+z)^{q-1} r(z)}, \quad (3.117)$$

where the angle between the direction of emission and the cusp/kink satisfies:

$$\theta \lesssim \theta_m \equiv (g_2(1+z)f\ell)^{-1/3}. \quad (3.118)$$

### 3.3.3 Radiation power from a loop

In this section, we estimate the energy loss of a loop in the form of gravitational waves. In the hypothesis where gravitational radiation is the main energy-loss mechanism for local U(1) strings, the radiated power is the quantity which determines the lifetime of non-intersecting loop. For smooth loops, i. e. without structures on length scales smaller than the size of the loops  $\ell$ , we show that the power can be expressed as  $P = \Gamma G\mu^2$  where  $\Gamma$  is a numerical constant [77].

The total energy radiated in the form of gravitational waves per unit of time can be roughly estimated using Eq. 1.65. We neglect the tensor structure of the quadrupole moment  $Q$  and we use simple dimensional considerations as in Eq. 1.66 to write:

$$\dot{E} \equiv P \sim G \left( \frac{d^3 Q}{dt^3} \right)^2 \quad \text{with} \quad Q \sim M\ell^2, \quad (3.119)$$

with  $M = \mu\ell$  the total mass of the string. The factor  $\propto t^6$  is substituted by the only quantity that has the dimension of a time: the fundamental period of oscillation of

the loop  $T_\ell = \ell/2 \propto \ell$ . Thus we obtain:

$$P \sim G\mu^2, \quad (3.120)$$

that we rewrite:

$$P = \Gamma G\mu^2, \quad (3.121)$$

where  $\Gamma$  is a constant that absorbs all numerical factors missing from previous estimates. This quantity is the radiative efficiency coefficient, a dimensionless quantity which defines how effective the gravitational-wave emission mechanism is. As we see from Eq. [3.121](#) the more massive the string is, the faster it decays through gravitational-wave emission. Clearly,  $\Gamma$  does not depend on the size of the loops. But as the quadrupolar moment is obtained by integration on the source and depends on the motion of the source (see Eq. [1.58](#) and Eq. [1.59](#)), we will assume that  $\Gamma$  depends on the shape (more or less smooth, i.e. with more or less kinks) and the trajectory of the loop. The lifetime of the loop is then:

$$\tau \sim \frac{M}{\dot{E}} \sim \frac{\ell}{\Gamma G\mu}, \quad (3.122)$$

in the following we will note:

$$\gamma_d \equiv \Gamma G\mu. \quad (3.123)$$

The quadrupole formula is derived in the slow motion approximation, i.e.  $v \ll c$ , with  $v$  the velocity of the source, see Sec. [1.4](#). However, we have shown that strings move at relativistic velocities, in particular in the vicinity of cusps. Therefore, the validity of the estimations made by using the quadrupole formula can be doubted, and it is necessary to go through a more rigorous calculation.

A full relativistic formalism was developed using the power  $P$  in gravitational radiation from an isolated and periodic source given by the Weinberg formula (cf Chap.10 from [\[12\]](#), or [\[77\]](#)). For some families of loop trajectories, the expression of  $P$  can be derived analytically [\[112\]](#). Other methods are also used [\[113\]](#) and the result is that the power in gravitational radiation for quite smooth loops is still given by Eq. [3.121](#). Calculations were numerically performed for different classes of cosmic string loops (e.g. without kinks or with kinks [\[114\]](#)) to determine the value of  $\Gamma$ . The different works [\[115, 116, 117, 118\]](#) produce quite similar results with an average value:

$$\Gamma \sim 50. \quad (3.124)$$

### 3.4 Other observational signatures of cosmic strings

Cosmic strings are linked with a variety of other different observational signatures. In this section we will briefly describe two of the most important.

### 3.4.1 Gravitational properties of cosmic strings

The gravitational properties of cosmic strings are radically different from those of non-relativistic matter. This can be seen by adopting two major simplifications to describe a gravitating string. First we continue to consider a string in the zero-width approximation. Second the gravitational field of the string is assumed to be sufficiently weak, i.e.  $G\mu \ll 1$ , to linearize the Einstein Equations. We can quickly justify this last hypothesis, by remembering the planck mass definition  $m_p = \sqrt{\hbar c/G}$  with  $\hbar = c = 1$  we get:

$$G \sim \frac{1}{m_p^2}, \quad (3.125)$$

from Eq. [3.57](#) we estimate the magnitude of  $G\mu$  to be:

$$G\mu \sim \left( \frac{\eta}{m_p} \right)^2. \quad (3.126)$$

So for strings with  $\eta \ll m_p$ , which is verified for strings that have formed in most phase transitions, linearized gravity is applicable almost everywhere except in small regions affected by cusps or kinks.

In such conditions we show that a cosmic string will produce no gravitational force on surrounding matter, despite its huge mass. The line element around a static straight string lying along the  $z$ -axis can be written in cylindrical coordinates as [\[77\]](#):

$$ds^2 = dt^2 - dz^2 - dr^2 - r^2 d\theta^2 \quad \text{with} \quad 0 \leq \theta < 2\pi \times (1 - 4G\mu), \quad (3.127)$$

this is the Minkowskian metric of flat spacetime, but with the angular coordinate not allowed to vary up to  $2\pi$ . Therefore, the spacetime around a straight cosmic string is locally flat, but globally conical in shape, with a wedge removed from the  $\theta$ -plane. The flat solution implies no gravitational force due to cosmic strings. Indeed in General Relativity tension is a negative source of gravity and, since tension equals energy per unit length for the strings of infinite thickness, their effects cancel. The angular dimension of the wedge removed from the  $\theta$ -plane is called the deficit angle

$$\Delta = 8\pi G\mu, \quad (3.128)$$

implying that the surface of constant  $t$  and  $z$  has the geometry of a cone rather than that of a plane. The effect of such a geometry is given by the trajectories of two test particles moving in parallel toward a cosmic string which is perpendicular to their motion plane as shown in Fig [3.10](#). Before reaching the cosmic string, nothing changes in their trajectories since the cosmic string does not gravitate. When they pass it however, they follow the geodesics of the conical spacetime around the string and converge, acquiring an extra velocity component. A more realistic model needs to take into account a wiggly structure for the cosmic string, i.e. strings with cusps and kinks. In that case the deficit angle is larger [\[77\]](#). The gravitational properties of cosmic strings are responsible for two of their observational signatures, gravitational lensing and CMB anisotropies, to which we dedicate the two following sections.

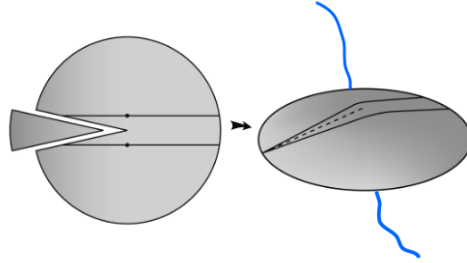


Figure 3.10: Spacetime around a straight cosmic string with  $\eta \ll m_p$  with the cosmic string's axis passing through the tip of the cone. A cosmic string changes the geometry of spacetime around it globally, giving it a conical shape. This is visualised by a circular surface from which a wedge is removed and the two sides are identified. Spacetime geometry however remains locally flat. The trajectories of two set of particles as they move perpendicular to the cosmic string are also shown. Figure taken from [77].

### 3.4.2 Gravitational lensing

The form of the metric around a cosmic string can result in characteristic lensing patterns of distant light sources [19]. As seen before, near the string the space is

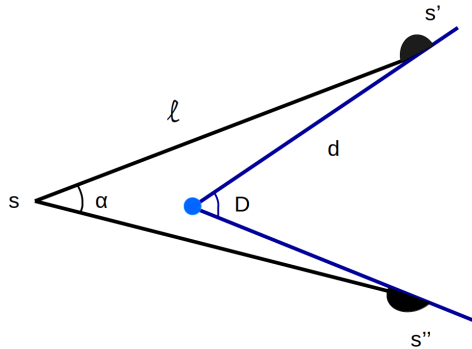


Figure 3.11: Gravitational lensing by a cosmic string, a double images of sources ( $s'$  and  $s''$ ) is created behind the string (blue point).

cone-shaped with an angle deficit  $\Delta = 8\pi G\mu$ . If a cosmic string crosses the line of sight connecting the observer with a distant source, a double image of the source is expected to be seen in the opposite sides of the string, as in Fig 3.11. Thus the string acts as a cylindrical gravitational lens. In Fig 3.11,  $\ell$  is the distance from the source ( $s$ ) to the images of the source ( $s'$  and  $s''$ ) and  $d$  is the distance from the string (blue point) to the images, and  $\theta$  is the angle between the string and the line

of sight, then the angular separation  $\alpha$  between the two lensed images is:

$$\alpha = D \frac{\ell}{d + \ell} \sin \theta, \quad (3.129)$$

where the string is assumed to be at rest with respect to the source. The lensing effects of cosmic strings is particular because they do not cause any deformation of the original image, while usual lensing sources (e.g. galaxies) produce inhomogeneous gravitational fields which always distort the multiple images [120]. We have seen that generally the strings are not either straight or static, and several effects may complicate this picture. For example this formula can be generalized for a moving string since we know now that strings are expected to move at relativistic speeds. In addition the presence of cusps or kinks will also change the result by changing the value of the deficit angle predicted in Eq 3.128.

We can mention that in 2003 the discovery of the gravitational lensing object CSL-1 [121] was considered as a good candidate for cosmic string, since it exhibited exactly the properties expected: two undistorted identical image of a galaxy. Unfortunately, it was realized that the event was a rare close pair of two very similar and isolated giant elliptical galaxies. Since other searches for gravitational lensing events by cosmic strings were performed with no detection.

### 3.4.3 CMB anisotropies

Spatial variations in the CMB temperature at recombination are seen as temperature anisotropy by the observer today. The first detection of the anisotropies of the CMB was done in 1992 by the COBE instrument [122]. These corresponded to variations of order  $\Delta T/T \simeq 10^{-5}$  in the sky. If we consider a statistically isotropic and Gaussian random temperature, the description in Fourier space is more efficient. The CMB anisotropies can be expanded in a series of spherical harmonic  $Y_{\ell m}(\theta, \varphi)$ . The spherical harmonic expansion of the CMB temperature anisotropies, as a function of angular position  $\hat{\mathbf{n}} \equiv (\theta, \varphi)$ , is given by:

$$\Theta(\hat{\mathbf{n}}) = \sum_{\ell=2}^{\ell_{max}} \sum_{m=-\ell}^{m=\ell} a_{\ell m} Y_{\ell m}(\hat{\mathbf{n}}) \quad (3.130)$$

where  $a_{\ell m}$  represents the expansion coefficients. The sum in equation 3.130 start at  $\ell = 2$  and go to a given  $\ell_{max}$  which is dictated by the resolution of the data obtained by an experiment. The monopole ( $\ell = 0$ ) is excluded because it is the average temperature  $T_0 \simeq 2.725K$  over the whole sky and it does not provide informations about the fluctuations. The dipole term ( $\ell = 1$ ) is affected by our own motion across space, but it is always possible to find a frame where the CMB dipole would be zero, thus this term is also removed. For statistically isotropic fluctuations, the ensemble average of the temperature fluctuations are described by the angular power spectrum:

$$\mathcal{C}_\ell = \frac{1}{2\ell + 1} \sum_{m=-\ell}^{\ell} |a_{\ell m}|^2. \quad (3.131)$$

In addition to the temperature fluctuations of the CMB, it appears that the CMB is also polarized.

The formation of CMB anisotropies by a network of cosmic strings is known as

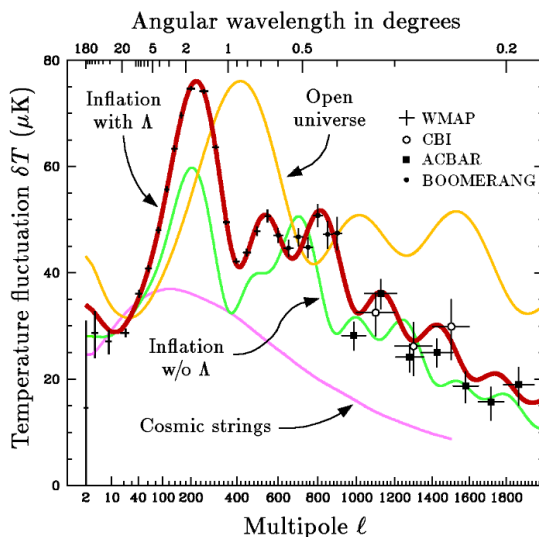


Figure 3.12: CMB power spectrum from WMAP including 7 years of data represented by the black crosses. The power spectrum predicted by the theory with the only source of cosmic strings is represented by the pink curve. Figure taken from [123].

the Kaiser-Stebbins effect [124]. We have seen that the peculiar shape of a cosmic string at rest induces lensing. If now the string is moving with a velocity  $\mathbf{v}$  in a direction transverse to the direction of the string, then photons passing on different sides of the string are measured with a different frequency, due to Doppler effect. This frequency change is discontinuous because of the negligible width of the string. If a network of cosmic strings exists, then we should expect that such effects must be observable in the CMB, manifesting as discontinuous temperature changes of linear shape. The temperature fluctuations can be calculated directly from the Doppler formula and are given by [77]:

$$\frac{\Delta T}{T} = 8\pi G\gamma_L \hat{\mathbf{n}} \cdot (\mathbf{v} \times \hat{\mathbf{s}}), \quad (3.132)$$

where  $\hat{\mathbf{n}}$  is the unit vector along the line of sight,  $\hat{\mathbf{s}}$  a unit vector tangential to the cosmic string and  $\gamma_L = (1 - v^2)^{-1/2}$  is the Lorentz factor with  $\mathbf{v}$  the cosmic string velocity.

The possibility of cosmic strings being the dominant contribution in the CMB anisotropies was ruled out since the first CMB measurements, see Fig 3.12. However, cosmic strings are still considered as possible source for CMB anisotropies with few percent ( $< 10\%$ ) contribution [125]. In addition to this, cosmic strings are also expected to induce B-mode polarisation signatures in the CMB, providing an

additional method for their detection [126].

Besides the observational signatures discussed above, cosmic strings are connected with a variety of others. For example, cosmic strings are expected to create anisotropies in the 21-cm power spectrum just as in the CMB [127, 128]. In addition there are several other types of strings that have not been introduced here. The global strings resulting from the breaking of a U(1) global symmetry which decay through radiating Nambu-Goldstone bosons. Also, cosmic strings which carry electric currents called superconducting strings can form, leading to interesting astrophysical signatures in the cosmological context. These are expected to be source of high energy gamma ray bursts, cosmic rays, neutrino emission. And many others types of strings can form depending on the topology and coupling to other fields.

# Chapter 4

## Cosmic String analysis for O1/O2

The goal of an analysis is to isolate a characteristic gravitational waveform  $h(t)$  buried in a noisy signal  $n(t)$ . The output signal  $s(t)$  of the detector is given by:

$$s(t) = n(t) + h(t). \quad (4.1)$$

If we consider that the detector noise is a random process, the problem of extracting the signal from the noise is a statistical one. The presence of a signal  $h(t)$  changes the statistical characteristics of the data  $s(t)$  and the analysis technique used depends on the signal  $h(t)$  you are looking for. In Chap 3, we have seen that gravitational-wave bursts are emitted by cusps and kinks on cosmic string loops and the frequency-domain waveform is:

$$h(\ell, z, f) = A_q(\ell, z) f^{-q} \Theta(f_h - f) \Theta(f - f_l), \quad (4.2)$$

where  $q = 4/3$  for cusps,  $q = 5/3$  for kinks, and  $A_q(\ell, z)$  is the signal amplitude produced by a cusp/kink propagating on a loop of size  $\ell$  at redshift  $z$ . This waveform is linearly polarized and is only valid if the beaming angle is:

$$\theta_m(\ell, z, f) = (g_2 f (1+z) \ell)^{-1/3} < 1. \quad (4.3)$$

The waveforms are cut off at low and high frequencies. To be able to detect a signal, the angle between the direction of observation and the cusp/kink must be smaller than  $\theta_m$ . This condition determines the high-frequency cutoff  $f_h$ . The low-frequency cutoff  $f_l$  is determined in practice by the lower end of the gravitational-wave's detector sensitive band<sup>1</sup>. The gravitational-wave signal produced by cosmic string features is then well modeled.

The cosmic string burst pipeline<sup>2</sup> is based on an analysis technique utilized in the case of a known signal waveform called matched-filter analysis described in Sec. 4.2.

<sup>1</sup> The sensitivity curve of current detectors is cutoff at 10 Hz and so  $f_l$  must be higher. The value used in the analyses is  $f_l = 16$  Hz.

<sup>2</sup>A data analysis pipeline is a sequence of operations/instructions used to process the data.

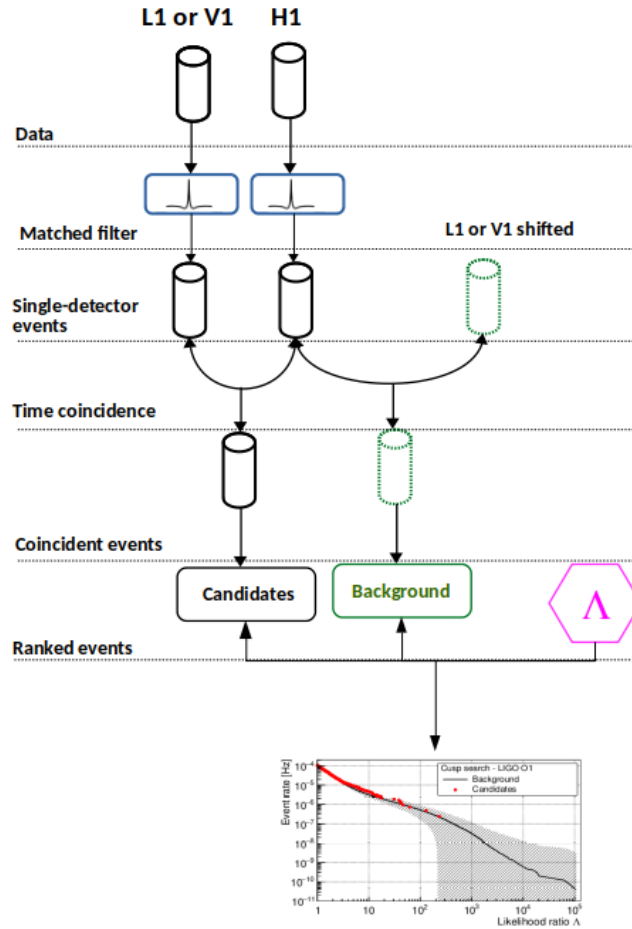


Figure 4.1: Cosmic Strings pipeline workflow.

It uses a discrete waveform template banks to cover the targeted parameter space, see Sec. 4.4. Candidate events are then extracted separately from each detector, cf. Sec. 4.5. To remove transients noise that can mimic a cosmic string signal we require a simultaneous detection between single-detector events from each detector, cf. Sec. 4.6. In addition, a likelihood ratio  $\Lambda$  is constructed which increases monotonically with signal probability, cf. Sec. 4.7. This function is used to rank the coincident events. To estimate the background of coincident events of the search we perform a time-shifted analysis using single-detector events, see Sec. 4.6. All such random coincidences are recorded and assigned a ranking statistic value  $\Lambda$ . An event is considered to be a gravitational wave signal if it differs significantly from the noise distribution. In the absence of detection, the search sensitivity is determined by injecting a population of cosmic string waveform in the data, cf. Sec. 4.7. Schematically, the pipeline used look like Fig 4.1. We present the results from the cosmic string burst analysis using

O1<sup>3</sup> and O2<sup>4</sup> data respectively in Sec. 4.9 and in Sec. 4.10.

## 4.1 O1 and O2 data set

The second generation of Advanced LIGO detectors [129] consist of two 4-km-long interferometers: H1 in Hanford, Washington and L1 in Livingston, Louisiana. The first observing run of Advanced LIGO, called O1, started on September 12, 2015 and finished on January 19, 2016. At this time, Advanced Virgo was not operating yet. We searched the Advanced LIGO O1 data for individual bursts of gravitational waves from cusps and kinks. The O1 run of Advanced LIGO was described in more detail in Chap. 2.

The pipeline uses the last version of calibrated data<sup>5</sup> [130, 131]  $h(t)$  from both detectors called C02. The O1 data are divided in two time chunks to perform the analysis. The chunk boundary is positioned at a significant maintenance break of the detectors. Performing the analysis in chunks allows to take into account fluctuating noise levels of the detectors over the duration of the observing run. Time segments flagged by CAT1 and CAT4 data quality flags are excluded, due to respectively the malfunctions of the detector (data missing, calibration failure, interferometer losing control, ...) and hardware injections performed, see Sec. 2.5.2 for more details. The total coincident time of observation where Advanced LIGO detectors are operating simultaneously is about 49 days, cf. Tab. 4.1.

	Start time	End time	H1L1 [days]
chunk 1	Sep 12, 2015	Nov 17, 2015	26
chunk 2	Nov 17, 2015	Jan 19, 2016	23

Table 4.1: The O1 data are divided in two chunks. The coincident livetime is provided after applying the DQ flags CAT1 and CAT4. It is defined as the livetime where the Advanced LIGO Hanford (H1) detector and the Advanced LIGO Livingston (L1) are operating simultaneously in stable conditions.

The O2 period spanned approximately 268 calendar days. The Advanced LIGO detectors participated in the observing run over this entire period from November 30, 2016 to August 25, 2017. The Advanced Virgo detector joined the LIGO detectors during this period and began its first observing run on August 1, 2017. Advanced Virgo joining for the last 25 days with a BNS range around 30 Mpc. There were two breaks during this period, at the end of 2016 and a few weeks in May 2017, which permitted improvements to be made to each of the LIGO detectors. The Livingston detector starts O2 observing around 85 Mpc, and becomes more sensitive at the end

---

<sup>3</sup>First observing run of Advanced LIGO

<sup>4</sup>Second observing run of Advanced LIGO and Advanced Virgo.

<sup>5</sup>The main purpose of the calibration is to allow to reconstruct the amplitude  $h(t)$  of the gravitational wave strain from the interferometer data.

of the run, reaching 100 Mpc. The Hanford detector’s sensitivity is around 75 Mpc at the beginning of the observing run and finished the run with a lower sensitivity, around 65 Mpc due to an earthquake. The coincident duty cycle is about 44% for H1L1 and about 63% for H1L1V1, the difference is explained by the large duty cycle of Advanced Virgo (85%).

Chunks numerotation	Start time	End time	H1L1 [days]	H1L1V1 [days]
1	Nov 30, 2016	Dec 23, 2017	6.2	N/A
2	Jan 04, 2016	Feb 08, 2017	12.1	N/A
3	Feb 08, 2017	May 09, 2017	55.6	N/A
4	May 26, 2017	Jul 07, 2017	16.0	N/A
5	Jul 07, 2017	Aug 01, 2017	9.0	N/A
6	Aug 01, 2017	Aug 26, 2017	17.0	15.0

Table 4.2: O2 data division for the cusp analysis. The two last columns provide the coincident livetime between detectors.

The data are divided into 6 time chunks to perform the analysis, see Tab. 4.2. The boundaries are positioned in a way that takes into account the period of commissioning or the large environmental disturbances. Figure 4.2 shows the chunk division of the O2 period analyzed depending on the evolution of the BNS range and the scheduled breaks. A preliminary analysis was performed with the first calibrated strain data  $h(t)$  (C00) of Advanced LIGO detectors. For the first time in Advanced LIGO, methods to subtract some well identified sources of noise from the data are used. Thanks to that, Hanford’s sensitivity increased by 10%. The final analysis is conducted with these cleaned final calibrated data (C02). The first analysis conducted with Advanced Virgo data use the online reconstructed strain data  $h(t)$ . The final analysis use the second reconstruction process to reprocess the data (V1O2Repro2A). Time segments flagged by category 1 and category 4 DQ flags were excluded, see Sec. 2.5.2. Thereafter, we illustrate the burst analysis using O1 data.

## 4.2 Detecting gravitational-wave with matched filter

The problem of detecting a cosmic string signal  $h(t)$  in noise  $n(t)$  can be set as a statistical hypothesis testing problem. There are two hypothesis [132]:

- $\mathcal{H}_N$ :  $s(t) = n(t)$  (the strain data  $s(t)$  do not contain signal  $h(t)$ );
- $\mathcal{H}_S$ :  $s(t) = n(t) + h(t)$ .

A hypothesis test is used to make a decision between these two hypotheses. There are two kinds of errors that we can make:

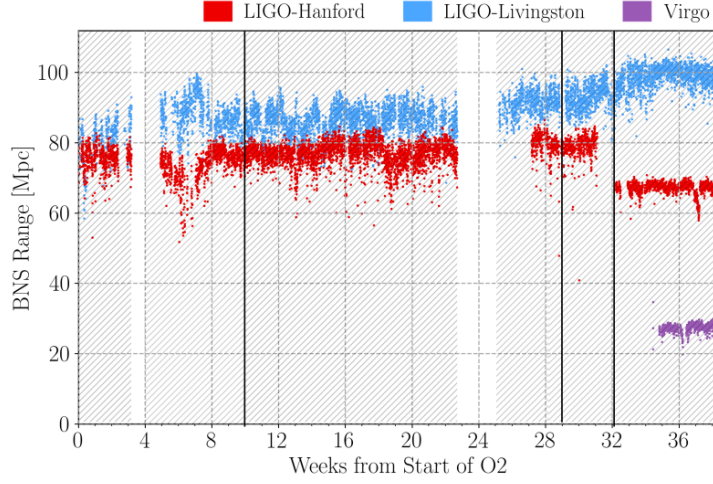


Figure 4.2: BNS range for each detector during O2. The holes in the BNS range of Advanced LIGO detectors are due to two scheduled breaks. At week 31, we observe a drop in the H1 sensitivity due to the Montana earthquake. The orange blocks represent the analyzed data chunk.

- type I error: choosing hypothesis  $\mathcal{H}_S$  when  $\mathcal{H}_N$  is true;
- type II error: choosing hypothesis  $\mathcal{H}_N$  when  $\mathcal{H}_S$  is true.

The probability of type I error is called false alarm probability (FAP) and is denoted by  $\alpha_R$ . The type II error is called false dismissal probability. The detection probability is denoted by  $\beta_R = 1 - \text{false dismissal probability}$ . We wish to find an optimal test to distinguish between these two hypothesis. There are several approaches to find such a test. In the cases of a gravitational-wave detection, we need a test that does not depend on making assumptions about the a priori probability of each hypothesis. The Neyman-Pearson criterion says that we should construct our test to have maximum probability of detection  $\beta_R$  while not allowing the probability of FAP to exceed a certain value  $\alpha_R$ . In this framework there is just one subjective parameter  $\alpha_R$ . Suppose one is performing a hypothesis test using the likelihood ratio test with threshold  $k_\alpha$  which reject  $\mathcal{H}_N$  in favor of  $\mathcal{H}_S$  at a significance level  $\alpha_R$ :

$$p[\Lambda(\mathcal{H}_S|s(t)) \geq k_\alpha] = \alpha_R, \quad (4.4)$$

where the likelihood ratio is defined by:

$$\Lambda(\mathcal{H}_S|s(t)) = \frac{P(s(t)|\mathcal{H}_S)}{P(s(t)|\mathcal{H}_N)}, \quad (4.5)$$

and  $P(s(t)|\mathcal{H}_S)$  is the probability that we observe the data  $s(t)$  given that hypothesis  $\mathcal{H}_S$  is true. The Neyman-Pearson lemma states that  $\Lambda(\mathcal{H}_S|s(t))$  is the most powerful test at significance level  $\alpha_R$  [132]. Since the exact form of a cosmic string signal

is known and assuming that the statistical properties of the noise are also known, we will construct from  $\Lambda(\mathcal{H}_S|s(t))$  an optimal detection statistic called the matched filter. This quantity expresses the value of the probability that the data contain a cosmic string signal. The calculations are derived from different references [132, 133, 134, 111].

In the following we define the Fourier transform of a time serie signal  $x(t)$  by:

$$\tilde{x}(f) = \int_{-\infty}^{+\infty} x(t)e^{-i2\pi ft} dt, \quad (4.6)$$

with the identity relation given by

$$\int_{-\infty}^{+\infty} e^{i2\pi f(t-t')} df = \delta(t - t'). \quad (4.7)$$

The auto-correlation function of the noise signal  $n(t)$  with itself is defined as:

$$(n \star n)(\tau) = \int_{-\infty}^{+\infty} n(t)n(t + \tau) dt. \quad (4.8)$$

For instance, the autocorrelation of a periodic function will have maxima at multiples of the period. In Chap 2 we introduced one definition of the power spectral density of the noise time serie  $n(t)$ . To obtain the expression of the matched-filter, we will use two other equivalent definitions. The noise power spectral density can also be interpreted as the Fourier transform of the autocorrelation function of the noise time serie:

$$P_s(f) \equiv \int_{-\infty}^{+\infty} (n \star n)(t)e^{-i2\pi ft} dt \quad (4.9)$$

It is usual in experiment to work with the single-sided power spectral density of the noise only defined in term of positive frequencies

$$S_n(f) \equiv \begin{cases} 2P_s(f) & \text{if } f \geq 0 \\ 0 & \text{else.} \end{cases} \quad (4.10)$$

We can also define the single-sided noise power spectral density by considering the expectation value of the frequency component  $\tilde{n}(f)$ :

$$\begin{aligned} E[\tilde{n}(f)\tilde{n}^*(f')] &\equiv \left\langle \int_{-\infty}^{+\infty} n(t)e^{-i2\pi ft} dt \int_{-\infty}^{+\infty} n(t')e^{i2\pi f't'} dt' \right\rangle \\ &= \frac{1}{2}\delta(f - f')S_n(f), \end{aligned} \quad (4.11)$$

where we perform the change of variable  $t = t' + \tau$  and we used the equivalent of Eq. (4.7) reexpressed in the frequency domain to pass from the first line to the second. We consider that the noise detector  $n(t)$  is a continuous function of time described by a Gaussian process (which is also stationary) with a zero-mean. Using the general

discrete probability density of a Gaussian process and Eq. (4.11), the continuum probability density of the noise is expressed by:

$$p_n[n(t)] \propto \exp \left\{ -\frac{1}{2} * 2 * 2 \int_0^{+\infty} df \frac{|\tilde{n}(f)|^2}{S_n(f)} \right\}, \quad (4.12)$$

this formula holds for a white noise ( $S_n(f)$  does not depend on the frequency) and a coloured noise ( $S_n(f)$  depends on the frequency). We can reexpress this equation in a more condensed form by introducing a “noise-weighted“ scalar product of two time series:

$$\begin{aligned} (x|y) &\equiv 4\Re \int_0^{+\infty} \frac{\tilde{x}(f)\tilde{y}^*(f)}{S_n(f)} df \\ &= 2 \int_{-\infty}^{+\infty} \frac{\tilde{x}(f)\tilde{y}^*(f)}{S_n(|f|)} df \\ &= \int_{-\infty}^{+\infty} \frac{\tilde{x}(f)\tilde{y}^*(f) + \tilde{x}^*(f)\tilde{y}(f)}{S_n(|f|)} df, \end{aligned} \quad (4.13)$$

where the reality of  $x(t)$  implies  $\tilde{x}(-f) = \tilde{x}^*(f)$ , similarly with  $y$ . With this scalar product the probability density for a stationary Gaussian noise process takes the form of:

$$p_n[n(t)] \propto e^{-(n|n)/2}. \quad (4.14)$$

We compute the probability densities under the hypothesis  $\mathcal{H}_N$  ( $n(t) = s(t)$ ) and the hypothesis  $\mathcal{H}_S$  ( $n(t) = s(t) - h(t)$ ) to express the numerator and denominator of the likelihood ratio in Eq.(4.5):

$$\begin{aligned} p(s|\mathcal{H}_N) &= p_n[s(t)] \propto e^{-(s|s)/2} \\ p(s|\mathcal{H}_S) &= p_n[s(t) - h(t)] \propto e^{-(s-h|s-h)/2}, \end{aligned} \quad (4.15)$$

and so the likelihood ratio is now written (assuming that the factors are the same in front of the exponentials):

$$\Lambda(\mathcal{H}_S|s(t)) = \frac{e^{-(s-h|s-h)/2}}{e^{-(s|s)/2}} = e^{(s|h)} e^{-(h|h)/2}, \quad (4.16)$$

where we used the last relation given by Eq (4.13) to obtain the second equality. The likelihood ratio  $\Lambda(\mathcal{H}_S|s(t))$  is a monotonically increasing function of the scalar product  $(s|h)$ , which is the only term that depends on the data  $s(t)$ . Thus any choice of a threshold<sup>6</sup> on the likelihood ratio for accepting the hypothesis  $\mathcal{H}_N$  can be translated to a threshold on the value of  $(s|h)$ . Therefore we can use as optimal detection statistic<sup>7</sup> the scalar product:

$$(s|h) \equiv 4\Re \int_0^{+\infty} \frac{\tilde{s}(f)\tilde{h}^*(f)}{S_n(f)} df, \quad (4.17)$$

---

<sup>6</sup> $k_\alpha$  in Eq.(4.4)

<sup>7</sup>Which is the optimal test found to distinguish the hypothesis  $\mathcal{H}_N$  and  $\mathcal{H}_S$ .

which is called “matched-filter” because it is a noise-weighted correlation of the expected signal  $h(t)$  with the data  $s(t)$ . The matched filter is the optimal filter for detecting a known waveform in stationary Gaussian noise.

### 4.3 Power spectral density estimation

We have seen that matched filter involves weighting the data by the detector’s noise one sided power spectral density. An incorrect estimate of the power spectral density can attenuate a signal or amplify a noise, degrading the sensitivity of the analysis. The difficulty, in the case of interferometric detectors, is due to the non-Gaussian and non-stationary nature of the data. In the cosmic string pipeline the power spectral density of the data is estimated with the median-mean average method. The median is more robust than the mean because it is less sensible to the extreme values of the detector data due to glitches. The detector data  $s(t)$  are sampled at some sampling frequency  $f_s$ <sup>8</sup>:

$$s[j] = s(j/f_s). \quad (4.18)$$

In the analysis the data are sampled at a lower rate (downsampled) of 8192 Hz and high-passed above 16 Hz, since frequencies below this value are not of big interest as the sensitivity at low frequencies in the detector is poor. The segment list of data is broken into smaller segments to estimate the power spectral density in order to take into account the non-stationarities of the data. The power spectral density is then

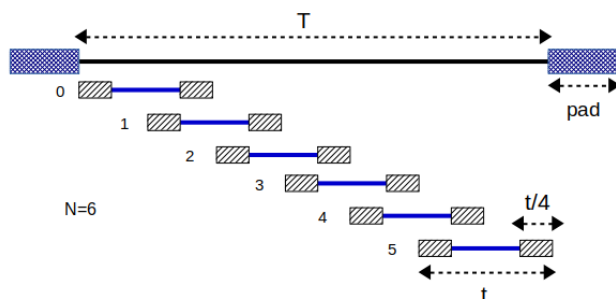


Figure 4.3: Illustration of the segmentation used by the pipeline. In this example the inner chunk have a total length of  $T + 2\text{pad}$ . It is divided into  $N=6$  short segments of length  $t$  with overlap by 50%.

estimated for each chunk of duration  $T$ . Moreover  $T$  must be large enough to have sufficient statistics to estimate a reliable noise power spectral density. The first and last quarters of each chunk, called “pad”, is thrown out. This ensures that the whole time window is covered with contiguous inner parts of blocks that do not overlap. Each segment is divided into  $N$ <sup>9</sup> overlapping sub-segments as shown in the figure 4.3

<sup>8</sup>The sampling frequency is  $f_s = 16384$  Hz for Advanced LIGO and  $f_s = 20$  kHz for Advanced Virgo

<sup>9</sup> $N$  is an even integer.

with an example. The data of each sub-segment are multiplied by a Hann window. This allows to reduce spectral leakage<sup>10</sup> due to data sampling. The sub-segments are overlapped by 50% in order to avoid losing data when windowing. The total length of a segment is  $T + 2\text{pad}$  divided in short sub-segments of total length  $t$ . The analyzed segment is covered with 336 s blocks, starting  $\text{pad} = 4$  s before the start of the time window, overlapped by 8 s and ending at least 4 s after the end of the time window. Note that:

$$\frac{Nt}{2} = (T + 2\text{pad}) - \frac{t}{2}. \quad (4.19)$$

Each segment is searched for bursts from cosmic string cusp and kink features.

## 4.4 Searching for cosmic strings with templates

### 4.4.1 Search with one template

In the frequency domain, the waveforms for bursts of gravitational radiation from cosmic strings are given by Eq. 4.2. Since we search for signals of known form we use the matched-filter technique. The waveform in the time domain is put on the form:

$$h(t) = A\tau(t), \quad (4.20)$$

where  $A$  is the unknown amplitude of the signal. The function  $\tau(t)$  which is proportional to the anticipated signal is known as a filter template. We define the scalar product  $x \equiv (s|\tau)$  which is proportional to the matched-filter  $(s|h)$ , given in Eq. 4.17. If no signal is present in the strain data so that  $s(t) = n(t)$  is purely noise, which we assume has zero mean,  $\langle x \rangle = 0$ , then

$$\begin{aligned} \text{Var}(x) &\equiv \langle x^2 \rangle - \langle x \rangle^2 \\ &= \left\langle \left( 2 \int_{-\infty}^{+\infty} \frac{\tilde{n}(f)\tilde{\tau}^*(f)}{S_n(|f|)} df \right) \left( 2 \int_{-\infty}^{+\infty} \frac{\tilde{n}^*(f')\tilde{\tau}(f')}{S_n(|f'|)} df' \right) \right\rangle \\ &= 4 \int_{-\infty}^{+\infty} df \int_{-\infty}^{+\infty} df' \frac{\langle \tilde{n}^*(f')\tilde{n}(f) \rangle \tilde{\tau}^*(f)\tilde{\tau}(f')}{S_n(|f|)S_n(|f'|)} \\ &= (\tau|\tau) \end{aligned} \quad (4.21)$$

the last equality is derived by using the equation Eq. 4.11. Therefore, the variance  $\sigma^2 \equiv \text{Var}(x)$  of the matched filter is  $\sigma^2 = (\tau|\tau)$ . So when no signal is present, the matched filter is a zero-mean Gaussian random variable with variance  $\sigma^2 = (\tau|\tau)$ . The signal-to-noise ratio (SNR) is defined as a normalized matched filter:

$$\rho \equiv \frac{(s|\tau)}{\sigma} = (s|\hat{\tau}), \quad (4.22)$$

---

<sup>10</sup>For example the sampling of a periodic signal may add new frequency components when the signal is Fourier transformed. This effect is referred as to spectral leakage.

where

$$\hat{\tau}(t) = \frac{\tau(t)}{\sigma} \quad \text{and} \quad (\hat{\tau}|\hat{\tau}) = 1. \quad (4.23)$$

When Gaussian noise alone is present, the SNR is a normally distributed random variable with zero mean and unit variance:

$$\langle \rho \rangle = 0 \quad \text{and} \quad \text{Var}(\rho) = 1. \quad (4.24)$$

When a signal  $h(t)$  is present in the data:

$$\langle \rho \rangle = A\sigma \quad \text{and} \quad \text{Var}(\rho) = 1, \quad (4.25)$$

since

$$\begin{aligned} \text{Var}(\rho) &\equiv \langle \rho^2 \rangle - \langle \rho \rangle^2 \\ &= \left\langle \frac{(s|\tau)^2}{\sigma^2} \right\rangle - \left\langle \frac{(s|\tau)}{\sigma} \right\rangle^2 \\ &= \frac{1}{\sigma^2} [\langle [(n|\tau) + (h|\tau)]^2 \rangle - \langle (n|\tau) + (h|\tau) \rangle^2] \\ &= \frac{1}{\sigma^2} [\sigma^2 + 2 \times 0 + A^2\sigma^4 - 0 - A^2\sigma^4] = 1. \end{aligned} \quad (4.26)$$

The measured SNR increases linearly with the amplitude of the signal:

$$\tilde{\rho} = A\sigma \pm 1. \quad (4.27)$$

The measured amplitude  $\tilde{A}$  that we assign the event depends on the template normalization

$$\tilde{A} = A \pm \frac{1}{\sigma}. \quad (4.28)$$

It implies that in the presence of Gaussian noise, the relative difference  $\Delta A$  between the “real” amplitude  $A$  and the measured amplitude  $\tilde{A}$  is proportional to the inverse of the SNR:

$$\frac{\Delta A}{A} = \pm \frac{1}{\langle \rho \rangle}. \quad (4.29)$$

Consequently, if a SNR threshold  $\rho_{min}$  is chosen for the search, on average only events with amplitude  $A_{min}$ :

$$A_{min} \geq \frac{\rho_{min}}{\sigma}, \quad (4.30)$$

will be detected. Therefore the quantity  $\sigma$  set a scale for the sensitivity search.

The cosmic string waveforms have 3 unknown parameters: the amplitude  $A$ , the high frequency cutoff  $f_h$  and the signal time arrival. The amplitude simply sets a scale for the matched filter output and is unimportant for a template. To be clear we consider a fixed high frequency cutoff  $f_h$  for the moment. To take in account the arrival time at the detector,  $t_0$ , we modify Eq. [4.20](#):

$$h(t) = A\tau(t - t_0). \quad (4.31)$$

The matched filter becomes by using Eq [4.17](#):

$$x(t_0) \equiv 4 \int_0^{+\infty} \frac{\tilde{s}(f)\tilde{\tau}^*(f)}{S_n(f)} e^{i2\pi ft_0} df, \quad (4.32)$$

a time serie that represents the application of the matched filter at different possible arrival time  $t_0$ . The SNR time serie for a template with a fixed high frequency cutoff  $f_h$  is:

$$\rho_{f_h} = \frac{x(t)}{\sigma}. \quad (4.33)$$

#### 4.4.2 Search with a set of templates

If the form of the template is identical to that of the signal, the signal-to-noise ratio  $\langle\rho\rangle$  is the highest possible. In practice, however, the template waveforms will differ somewhat from the signals. In order to minimize SNR losses it is necessary to cover the parameter space with several templates. In the cosmic string search only one parameter is necessary to construct a set of matched-filter templates. This parameter is the high frequency cutoff  $f_h$ . The set of templates used is often called a template bank.

The minimum high frequency cutoff used in the analysis is  $f_{h,min} = 30$  Hz. The high frequency cutoff can take in principle arbitrary large value, but as we have seen in [Sec. 4.1](#) the data are sampled at 8192 Hz. The largest distinguishable high frequency cutoff is equal to the Nyquist frequency  $\mathcal{F}_N$  <sup>[11](#)</sup> which is half the sampling frequency  $f_{h,max} = 4096$  Hz.

We introduce an index  $i = 1, 2, \dots, N$ , labeling the particular waveform template  $\tau_i(f)$  in the bank of  $N$  waveform templates specified by a collection of high frequency cutoff  $\{f_{h,i}\}$ . The template bank is iteratively constructed. If we choose to ordering the template so that  $f_{h,i} > f_{h,i+1}$ , the first template  $\tau_1$  is normalized (using [Eq. 4.13](#)) such that:

$$\sigma_1^2 = (\tau_1|\tau_1) = 4\Re \int_{f_i}^{\mathcal{F}_N} df \frac{|\tau(f)|^2}{S_n(f)}. \quad (4.34)$$

where we recall that  $f_i$  is the low frequency cutoff which must be higher than the frequency at which the sensitivity of the detector is cut off. In practice we choose  $f_i = 16$  Hz. This template is the one with the largest  $\sigma$ , and thus the largest possible mean SNR value  $\langle\rho\rangle$  at fixed amplitude. The high frequency cutoff  $f_h$  describing the search templates vary continuously, however the set of templates is discrete. Therefore even if a gravitational wave signal were to lie within the template space it would not correspond to any template. The maximum mismatch  $\epsilon$  between a template and the signal is the central quantity which governs template spacing. It informs about the maximum fractional SNR loss we choose to tolerate, due to mismatch between a template and the signal. The fitting factor between two adjacents templates  $\tau_i$  and

---

<sup>11</sup>The Nyquist frequency is the maximum frequency that a signal must contain to allow its unambiguous description while it is sampled at regular intervals.

$\tau_{i+1}$  specified by high frequency cutoff  $f_i$  and  $f_{i+1}$  is:

$$F \equiv \frac{(\tau_i|\tau_{i+1})}{\sqrt{(\tau_i|\tau_i)(\tau_{i+1}|\tau_{i+1})}} = 1 - \epsilon. \quad (4.35)$$

It describes quantitatively the ‘‘closeness’’ of the template in term of the reduction of the SNR. All the template have the same lower frequency  $f_l$  and so:

$$(\tau_i|\tau_{i+1}) = (\tau_{i+1}|\tau_{i+1}), \quad (4.36)$$

the maximal mismatch is then obtained from Eq. [4.35](#):

$$\epsilon = 1 - \sqrt{\frac{(\tau_{i+1}|\tau_{i+1})}{(\tau_i|\tau_i)}} = 1 - \frac{\sigma_{i+1}}{\sigma_i}. \quad (4.37)$$

In the analysis the maximal mismatch between two consecutive templates is  $\epsilon = 0.1\%$ , we will see later the interest in choosing such a low value. From this equation we notice that the high frequency cutoff  $f_{h,i+1}$  is iteratively determined using  $f_{h,i}$ .

The template bank contains 31 templates, spanning over the high frequency cutoff  $f_h$ . We use the same template bank in the matched-filter for both Advanced LIGO detectors. The reason is given below in the chapter. We have seen that the matched filter depends on the estimation of the one-sided power spectral density  $S_n(f)$  and that this quantity evolves over time. As a result, the template bank should also change over time. However we use a fixed template bank. The figure [4.4](#) presents the distribution of the mismatch between two consecutive templates for H1 and L1 data during the first chunk of O1 data. It allows us to check that the mean mismatch is well 0.1%, despite the evolution of  $S_n(f)$ . We also note that the spacing between the cut-off frequencies increases with the frequency. This is because the SNR losses decreases with the frequency (see Eq. [4.29](#)).

### 4.4.3 $\chi^2$ consistency test

As we have seen, the matched filter is the optimal filter for detecting a known waveform in stationary Gaussian noise. In reality, many glitches, which are neither Gaussian nor stationary, are observed. Using the method in [\[135\]](#) a  $\chi^2$  parameter is computed to characterize the match between the event and the signal waveform in the time domain. This test is used to distinguish a real signal from a glitch. The basic idea of the test is to ‘‘break’’ the detector’s bandwidth in several smaller bands, and to see if the response in each band is consistent with what might be expected of the supposed signal. This method can only be used to discriminate signals for which the waveform is known, which is the case in our search. A large  $\chi^2$  means that a signal is probably the result of a transient noise.

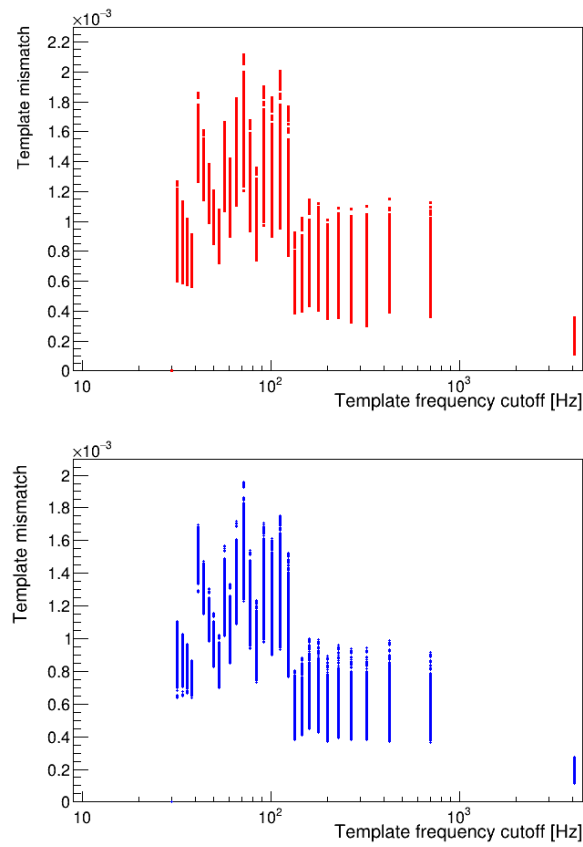


Figure 4.4: Distribution of the mismatch computed for every template with respect to the previous template as a function of the template high frequency cutoff  $f_h$ . In red the distribution for the single detector events in H1 and in blue the distribution in L1, for the first chunk of O1 data.

## 4.5 Trigger selection

After we apply the matched filter for each template, The SNR threshold is the first parameter in identifying candidate events or triggers. The choice of the threshold depends on two effects. It is necessary to maximize the threshold in order to reduce the number of triggers that are produced by noise artifacts. However, we will see later that the search is optimized for signals with low SNR and therefore the threshold must also maximize the sensitivity of the research. In the analysis an event is identified with  $\text{SNR} > 3.75$ . A signal with a high SNR may crossed for several data samples. Rather than record triggers for all samples, we cluster together triggers that lie in a time  $T_c$ . This time must be larger than the typical duration of a signal. If a trigger is within a time window  $T_c$  after an earlier trigger with a larger value of SNR, this trigger is discarded. Whereas if this trigger is within a time window  $T_c$  after an earlier trigger with a smaller SNR, the earlier trigger is discarded. The result is a set of remaining triggers that are separated by a time of at least  $T_c$ . In the analysis events are clustered over  $T_c = 0.1$  s timescale. Only the template with the largest SNR is kept when several templates are triggered at the same time. Finally a trigger is definitely described by a set of variables:

The figure [4.5](#) shows that the SNR distribution is clearly not Gaussian: a large

Trigger parameters	Definition
$\rho_j$	The maximum SNR of the cluster for the j-th template retained.
$A_{max}$	The amplitude of the trigger given by Eq. <a href="#">4.25</a> .
$t_{peak}$	The location in time of the maximum SNR.
$f_h$	The high frequency cutoff of the template retained.
$t_{start}$	The start time of the trigger, which is the time of the first trigger with SNR value above threshold in the cluster.
$\Delta t$	The duration of the trigger, which is the length of the cluster.
$\chi^2$	Statistical test used to discriminate true signals from transient noises.

Table 4.3: Single-detector trigger parameter in the Cosmic String analysis.

number of transient noise (glitches) excursions are present in the data. These glitches mimic the signal produced by a cosmic string and some of them are characterized by a very high  $\text{SNR} \geq 10^2$ . Thus, as mentioned in section [4.2](#), the matched-filter is not an optimal technique in the case where the noise of the detector is not Gaussian. We also observe that the SNR is higher in H1 detector than in L1 detector, which is in agreement with the fact that the H1 detector was noisier than L1 detector [\[35\]](#) during this period. In figure [4.6](#), the SNR over time distribution presents period with

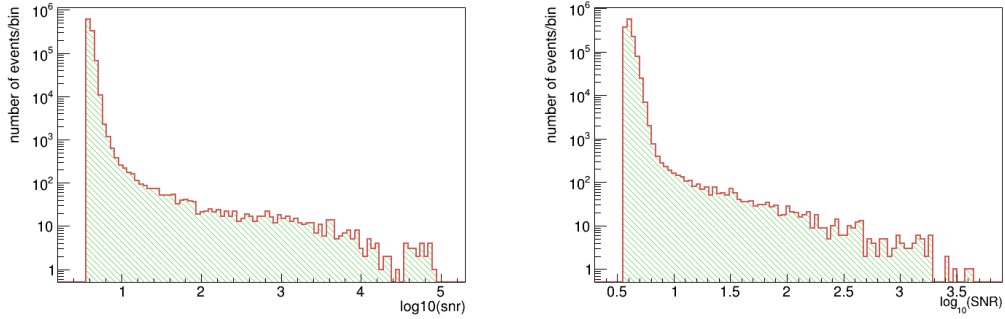


Figure 4.5: SNR distribution for the single-detector triggers in H1 and in L1 in the first chunk of O1 data.

localized excesses of single-detector triggers in both detectors. In comparison the figure shows the same distribution for the Omicron triggers. The two distributions are consistent. In the figure [4.7](#), the  $\chi^2$  versus SNR distribution in L1 detector

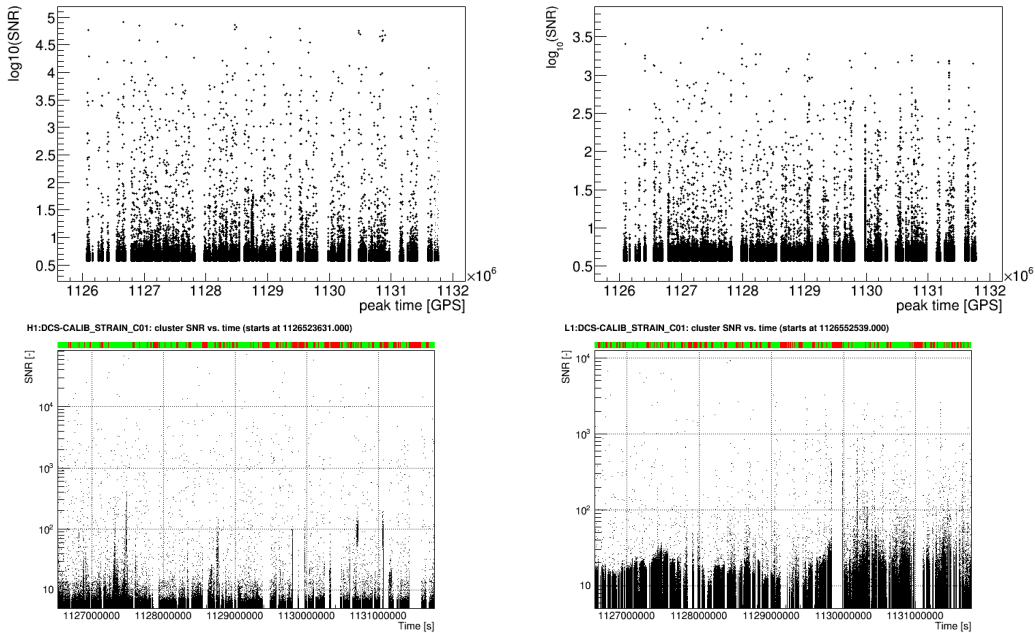


Figure 4.6: SNR over time distribution for the cosmic string single-detector triggers in H1 (top left) compared to the same distribution for the Omicron triggers (bottom left). SNR over time distribution for the cosmic string single-detector triggers in L1 (top right) compared to the same distribution for the Omicron triggers (bottom right). Results for the first chunk of O1 data.

exhibits a population of glitches well located (red box), which is present all over

O1. An investigation has shown that these triggers are vetoed by Hveto and UPV vetoes [12](#). The last two plots of the figure [4.8](#) represent the frequency template

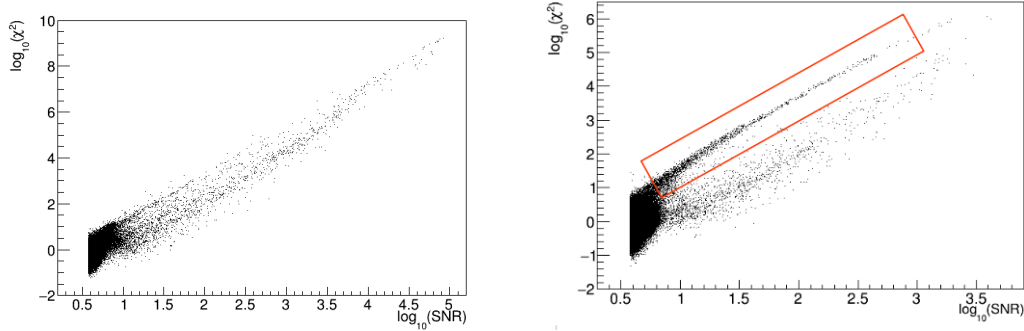


Figure 4.7:  $\chi^2$  versus SNR distributions for the cosmic string single-detector triggers in H1 (left) and in L1 (right). Results for the first chunk of O1 data.

distribution indexed by the high cutoff frequency. The excess of triggers observed in the first template is the result of all the low-frequency noises. The shape of the distribution is explained by the mismatch between templates in Fig. [4.4](#). The distribution is not flat across the bank of template. For example the mismatch is smaller at high frequencies ( $\epsilon \sim 3.5 \cdot 10^{-4}$ ) than at low frequencies ( $\epsilon \sim 1.25 \cdot 10^{-3}$ ), this is why high-frequency cutoff templates trigger more often. We choose to show only the parameter distribution for the single-detector events from the first chunk of O1. The same characteristics were observed in the second chunk of data. Whenever

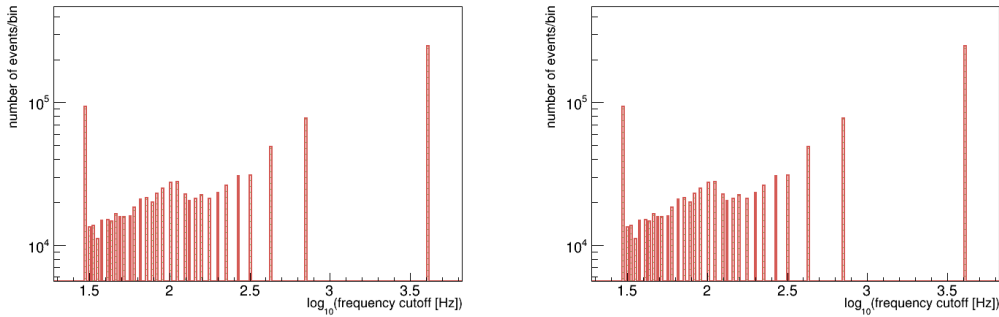


Figure 4.8: Template distribution indexed by the high frequency cutoff for the cosmic string single-detector triggers in H1 (left) and in L1 (right). Results for the first chunk of O1 data.

the distribution exhibits a particular behaviour that is not expected, we try to understand how these triggers are correlated in order to identify events with similar

<sup>12</sup>The vetoes are associated with OMC-PZT channel. OMC for output mode cleaner, an optical resonator which consist in four mirrors in Advanced LIGO. PZT for piezoelectric actuator used to change the position of the OMC mirrors

properties or families. Then, the idea is to find a way to remove these events from the list of single-detector triggers. A meticulous and often repetitive study is then undertaken, which will be illustrated later in the chapter.

## 4.6 Time coincidence between triggers

### 4.6.1 The zero-lag

Until now, our focus has been on the derivation of the matched filter under the assumption that the detector noise is stationary and Gaussian. In chapter 2 we have seen that the detector noise has often a non-Gaussian component of transient noise artefacts, often called glitches. These glitches can mimic a gravitational signal produced by cosmic strings. Consequently, the detection statistic used can misidentify glitches as gravitational wave events. This is exactly what we observed in the previous section: the distribution of the SNR of single-detector triggers presents a tail characterized by very high SNR value and these events are typically glitches. Therefore we must improve the detection statistic to reject spurious glitches that mock a gravitational event, while retaining true signals. In practice a network of gravitational wave detectors is operated and combining data from across a network of detectors allows good rejection of noise glitches. The basic principle is that a gravitational-wave signal is correlated in time across a network of detector, while noise is uncorrelated. In order to suppress transient noise we require temporal coincidence of detected burst events in at least a pair of detectors. Since a gravitational wave propagates at the “finite“ speed of light in vacuum, it takes a given time to reach the different detectors. Thus a time delay appears between the signal received by one detector and another. The table 4.4 provides light distance between all possible pairs of current detectors. The non-shifted data set of coincident events is called zero-lag data set.

Suppose a pair of detectors, the coincidence window must be sufficiently large to take

Pair of detectors	Light distance between detectors [ms]
H1L1	$\pm 10.00$
H1V1	$\pm 27.20$
L1V1	$\pm 26.39$

Table 4.4: Maximum travel time between the current terrestrial interferometer: LIGO Hanford (H1), LIGO Livingston (L1) and Virgo (V1).

into account the maximum travel time of the gravitational wave between detectors, the signal duration, and the timing uncertainty. Several types of uncertainties contribute to temporal uncertainty. For example, the reconstructed peak time (corresponding to the matched filter) have an uncertainty due to the sampling of the data. The timing error is given by the accuracy of the synchronization of the system that is used to record the signal in the detectors and a GPS clock [136]. The intrinsic time

delay within the instrument has to be accounted for by the phase calibration of the detector [136] (computer processing delay in the length-control loop, delay to drive the magnets and electrical coils, ...).

We need also to set a global false alarm rate (FAR) when searching for coincidences. If we denote by  $R_1$  and  $R_2$  the rate of glitches respectively in a first detector and second detector, and by  $\Delta t_{12}$  the time coincidence window considered, in a Poisson process the coincidence rate is expressed as:

$$R = R_1 R_2 \Delta t_{12}. \quad (4.38)$$

For example for  $R_1 = R_2 = 1/$  per hour and  $\Delta t_{12} = 20$  ms then the approximate rate of accidental coincidence is  $R \simeq 5.5 \cdot 10^{-6} \text{h}^{-1}$  or about once every 21 years. We conclude that coincidence between detectors considerably reduces the false alarm rate.

In the analysis, the central time of the single-detector events must lie within a time window  $\delta t = 18$  ms, which is sufficiently large to take into account the maximum light travel time between detectors, the signal duration, and the timing uncertainty. We parametrize a coincident-event by a vector  $\vec{x}$  characterized by a set of variables:

- $\Delta t_{H1L1} = t_{L1} - t_{H1}$ , the arrival time difference between detectors.
- $A_{H1}/A_{L1}$ , the ratio of the amplitude between detectors.
- $\Delta f_{h,H1H2} = (f_{h,H1} - f_{h,L1})/\frac{1}{2}(f_{h,H1} + f_{h,L1})$ , the frequency cutoff asymmetry between detectors.
- $\rho_{H1}$  and  $\rho_{L1}$ , the single-detector SNR.
- $\chi_{H1}^2$  and  $\chi_{L1}^2$ , the single-detector  $\chi^2$ .

These events constitute the zero-lag data set of the cosmic string search.

It is of interest to note that the assumption that the noise is not correlated between detectors is assumed to hold when detectors are far enough apart on the Earth's surface. Indeed, in this limit it seems reasonable that there are no common environmental disturbances consistent with the light-travel-time between the detector. This is not totally true since there are for example common known sources of noise between the LIGO Hanford and Livingston detectors. For example, a distant lightning would affect the electronics or magnets of both interferometers. On an even larger scale, another source of correlated noise arises from the electromagnetic fields on the Earth [137, 138]. This is known as Schumann resonances [139], which produce a noise correlation through the coupling with the magnets used in the interferometer system. In this case, correlations with magnetometers monitoring the detector environment are used to generate vetoes that can be used in searches to eliminate these noise events.

### 4.6.2 Background estimation

To estimate the significance of a gravitational-wave candidate, we need to characterize the statistical distribution of the accidental coincidences. To create this distribution, we apply unphysical delays between the detector data stream of the network, in order to remove all the possibly true cosmic string signals. For example, if we consider a pair-wise detector ( $d_1, d_2$ ) we time shift the trigger sets relative to one another and we look for “fortuitous” coincidence events. Figure 4.9 shows a shema of this technique. This method is called time slide background estimation. The triggers generated with

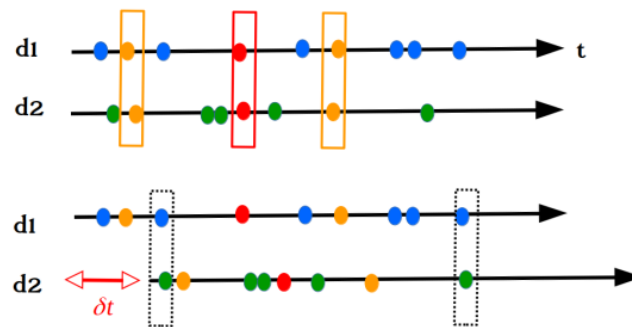


Figure 4.9: Time slide background estimation with a pair of detectors  $d_1$  and  $d_2$ . At the top: the single detector’s triggers are represented by circles. The coincident events in a time window (represented by the box width) form the zero-lag of the search. The zero-lag data set contains a gravitational-wave signal, represented by the red box. In addition, it includes fortuitous coincident events, represented by the orange box. At the bottom: the set of triggers found in the  $d_2$  detector is time shifted from  $\delta t$  with respect to  $d_1$ . Fortuitous coincidences represented by the black box are created. On the other hand, the gravitational-wave signal is no longer in coincidence in this new data set. By applying this technique again and again, we build a set of events that is “pure” noise: the background.

timeshifted data behave like an independent realization of the background called a lag or a timeslide [17]. The distribution of time shifted coincidence events or often called time-lag coincidence events should follow a Poisson distribution. Despite the fact that our dataset is limited, it is possible to increase its size, also called livetime by doing several time shifts on the data. Even if the background estimation accuracy cannot be increased indefinitely by performing more timeshifts [17], the gain in effective livetime can be considerable.

Again we assumed that there is no correlations between noise in the detector network. If the detectors are too close the assumption that noise between detectors is not correlated is no longer valid, the background estimation could be underestimated, therefore the timeslide method can not be used. The time shift must satisfy two conditions. First, it should be larger than the maximum duration of the signal model we consider and the maximum light travel time between detectors, to avoid correlated

events (which will not obey Poisson statistic). And the time shift should be shorter than the typical time scale over which the single detector rate varies significantly. This ensures that the number of events for different times shifts will follow a Poisson distribution for a quasi stationary process, and thus minimize dependence on any non-stationarity in the background event rate. The time shift process is repeated in order to gain a more accurate estimation of the background estimation. In a network of 3 detectors we have to be careful not to repeat the lags, since the set of triggers of two detectors are shifted with respect to the last one, a way to avoid this is to shift in opposite directions. The principal source of systematic errors in the background estimate is a bad choice of time-lag that could introduce a time dependency of the background rate.

In the analysis, the background sample was obtained by artificially time shifting the single-detector triggers from L1 with respect to H1. In a first analysis we performed 300 time shifts. This analysis is used for noise investigation. However, since the first detection of gravitational waves, we must consider the case where there would be a detection of cosmic string signal. Consequently we must estimate the most precisely the background of our search. For the final analysis we have increased the number of time slides to 6000. Another reason which justify the choice of repeating the analysis several times with different noise estimates is given later in the chapter. The reason is related to the choice of the statistical quantity used to rank candidates and its behavior when the number of time slide evolves. The double coincidence time offered by each background data set for the cusps and kinks search is given in the Tab. 4.5.

Finally, it should be noticed that another implicit assumption is made in this method.

Number of time slides	Time shift [s]	Total livetime [years]
300	3.54	39
6000	0.19	791

Table 4.5: This table shows the number of time slides used to estimate the background with the associated time shift for the O1 cusp/kink analysis. In addition we provide the total livetime rounded to the year.

True gravitational wave signals are considered so rare that their contribution to the background estimate through random coincidences is neglected. In fact a loud gravitational wave signal in one detector can appear in time shifted coincidence with a glitch in the other detector, as we have seen for GW150914. Hence the distribution of the estimated background can be relatively distorted, leading to a truly rare occurrence being ranked as only moderately rare. A solution to this problem of a loud signal contaminating its own background estimation is to exclude single-interferometer “foreground” triggers of a given zero-lag candidate from the set of shifted triggers used to estimate its own background. This solution have the problem that such exclusion could itself lead to a bias that overestimates the importance of a coincident candidate.

## 4.7 Ranking Statistic

### 4.7.1 Bayesian coincidence test

We have seen that the standard technique used to reject noise is to discard triggers that are not in coincidence in at least two detectors. We summarize here, an alternative coincidence test based on Bayesian statistical inference [140] used in the cosmic string analysis. It uses a set of simulated gravitational wave events  $S$  and a set of noise events  $N$  to statistically infer the probability for a coincident-event to be signal or noise. This technique is proven to be significantly more effective than the standard one, when the number of parameters  $n$  used to characterize an event is large ( $n > 10$ ). We consider a tuple of events in coincidence in a network of detectors. An event is described by a vector  $\vec{x}$  in the  $n$ -dimensional parameter space:

$$\vec{x} = (x_1, x_2, \dots, x_n). \quad (4.39)$$

We denote by  $T$  this tuple of events, by  $N$  a tuple of noise events and by  $S$  a tuple of gravitational-wave events. We have already discussed one of the techniques used to produce a “pure” noise data set. We will see later in this section how to produce a signal sample. The Bayes’s theorem [141] states that:

$$P(T \in S | \vec{x}) = \frac{P(\vec{x} | T \in S)P(T \in S)}{P(\vec{x})}, \quad (4.40)$$

and we want to know the probability that the tuple of events  $T$  described by the parameter  $\vec{x}$  is the result of a gravitational wave, ie the quantity  $P(T \in S | \vec{x})$ . So that there is no ambiguity, it should be remembered that on the right-hand side, in the numerator, we have the probability of observing the parameter  $\vec{x}$  in a tuple of events  $T$  known to be the result of a gravitational wave multiplying the probability that any tuple is a gravitational wave and in the denominator, we have the probability of observing the parameter  $\vec{x}$  in any kind of events. Because each tuple of events is either the result of noise or of a gravitational wave we have:

$$P(T \in N) = 1 - P(T \in S). \quad (4.41)$$

The probability of observing the parameter  $\vec{x}$  is given by:

$$\begin{aligned} P(\vec{x}) &= P(\vec{x} | T \in S)P(T \in S) + P(\vec{x} | T \in N)P(T \in N) \\ &= P(\vec{x} | T \in N) + [P(\vec{x} | T \in S) - P(\vec{x} | T \in N)]P(T \in S) \\ &= P(\vec{x} | T \in N) + P(\vec{x} | T \in N) \left[ \frac{P(\vec{x} | T \in S)}{P(\vec{x} | T \in N)} - 1 \right] P(T \in S), \end{aligned} \quad (4.42)$$

where we used Eq. 4.41 to pass from the first line to the second, and the Baye’s theorem expressed in Eq. 4.40 to deduce the last line. By replacing  $P(\vec{x})$  by its expression from the Baye’s theorem we obtain:

$$P(T | S \in \vec{x}) = \frac{P(\vec{x} | T \in S)P(T \in S)}{P(\vec{x} | T \in N) + [P(\vec{x} | T \in S) - P(\vec{x} | T \in N)]P(T \in S)}. \quad (4.43)$$

From this last relation we define the likelihood ratio as:

$$\Lambda(\vec{x}) = \frac{P(\vec{x} | T \in S)}{P(\vec{x} | T \in N)}. \quad (4.44)$$

Equation 4.43 can be expressed as:

$$P(T \in S | \vec{x}) = \frac{\Lambda(\vec{x})P(T \in S)}{1 + [\Lambda(\vec{x}) - 1]P(T \in S)}, \quad (4.45)$$

and by differentiating this expression with respect to  $\Lambda(\vec{x})$  we show that the derivative is always positive. Thus  $P(T \in S | \vec{x})$  is a monotonically increasing function of the likelihood ratio. If the likelihood ratio is zero  $\Lambda(\vec{x}) = 0$ , the event described by  $\vec{x}$  is noise, whereas if  $\Lambda(\vec{x}) \gg 1$  the event is most likely the result of a gravitational wave. We then use the likelihood ratio  $\Lambda(\vec{x})$  to rank the events.

In the analysis, to discriminate true signals from background events, we apply this Bayesian technique. Given a set of parameters  $\vec{x}$  describing an event, the computed likelihood ratio is given by:

$$\Lambda(\vec{x}) \simeq \frac{P^S(\Delta t_{H1L1})}{P^N(\Delta t_{H1L1})} \times \frac{P^S(A_{H1}/A_{L1})}{P^N(A_{H1}/A_{L1})} \times \frac{P^S(\Delta f_{h,H1L1})}{P^N(\Delta f_{h,H1L1})} \times \frac{P^S(\chi_{H1,\rho H1}^2)}{P^N(\chi_{L1,\rho L1}^2)} \times \frac{P^S(\chi_{H1,\rho H1}^2)}{P^N(\chi_{L1,\rho L1}^2)} \quad (4.46)$$

where  $P^S(x_i)$  represents the probability of observing the parameter  $x_i$  in a tuple of events known to be the result of a gravitational wave (S) and  $P^N(x_i)$  is the probability of observing the parameter  $x_i$  in a noise tuple (N). The majority of parameters used to characterize a coincident event are nearly uncorrelated. And we assume in addition that there are independent<sup>13</sup>. This allows us to compute the likelihood ratio one variable at a time. However, we do not perform any factorization for SNR and  $\chi^2$  parameters because of the strong correlation between these two variables.

### 4.7.2 Signal sample

To construct the ranking statistic cosmic string simulated signals are injected into the data. The simulated signals (S) are randomly generated and injections are performed each 83.7 s. The choice of this value is influenced by several factors, to have sufficient statistics it is necessary to increase the number of injections, but at the same time it is important to have a reasonable spacing between injections to avoid two injections overlapping. The analysis is run 10 times to obtain more statistic and about  $515 \times 10^3$  signals are injected in the O1 analysis. These injections are done on a time-shifted data set. Indeed, the probability densities associated with injections show statistical fluctuations that could not estimate the likelihood with enough accuracy. This avoids constructing the likelihood on the same data set on which it is

---

<sup>13</sup>This is not systematically true, the only general case when lack of correlation implies independence is when the  $x_i$  are Gaussian.

	Cusp Search	Kink Search
Time step	83.7 s	83.7 s
High frequency cutoff	$f_h^{-5/3}$	$f_h^{-4/3}$
Amplitude min	$1 \times 10^{-22} \text{s}^{-1/3}$	$5 \times 10^{-22} \text{s}^{-2/3}$
Amplitude max	$1 \times 10^{-18} \text{s}^{-1/3}$	$1 \times 10^{-17} \text{s}^{-2/3}$
Frequency min	40 Hz	40 Hz
Frequency max	8192 Hz	8192 Hz
Number of injections	$515 \times 10^3$	$515 \times 10^3$
Injection-reweight-cutoff	$8 \times 10^{-22} \text{s}^{-1/3}$	$4 \times 10^{-21} \text{s}^{-2/3}$

Table 4.6: Injection parameters in the analysis of O1 data for the search for gravitational wave signals produced by cusps or kinks.

applied. The injections accounts for the physical properties of the population. These are uniformly distributed in volume and the distribution of frequency cutoffs  $f_h$  for cusp is  $dN \propto f^{-5/3} df$  between 40 Hz and 8192 Hz. The amplitude are distributed logarithmically between  $1.0 \times 10^{-22} \text{s}^{-1/3}$  and  $1.0 \times 10^{-18} \text{s}^{-1/3}$  spanning the range of detectability . We use astrophysically radial distribution and reweight the injection by a factor  $A^{-3}$ . The effect of doing so is to construct the ranking statistic on a weighted set of injections to favor low amplitude signals, which are more likely to be real. We can not allow weight assigned to arbitrarily low-amplitude injections to grow without bound. Therefore we crop the weight assigned to injections above  $8 \times 10^{-22} \text{s}^{-1/3}$ . Table 4.6 summarizes the injection parameters used in O1 search. The waveform used to compute the injections has an exponential cutoff at the high frequency cutoff:

$$h(l, z, f) = A_q(l, z) f^{-q} \Theta(f - f_l) \times \begin{cases} 1 & \text{if } f \leq f_h \\ e^{1-f/f_h} & \text{if } f > f_h. \end{cases} \quad (4.47)$$

An injection is found if its peak time lies between the start time and end time of a coincident event.

### 4.7.3 Probability density functions

To construct the likelihood ratio on the background and injection sample we use the probability density functions expressed in Eq. 4.46. The figure. 4.10 shows that the simulated events with  $\text{SNR} \geq 10$  are well differentiated from the noise. The figure. 4.11 shows that the  $\chi^2$  variable can discriminate the signal and the background for high SNR value ( $\sim \text{SNR} \geq 30$ ) in both detectors. The other probability distributions used to compute the likelihood ratio are presented in Fig. 4.12. The first point is that the background and injection distributions for each of parameter are different: these parameters are good quantities to discriminate signal from noise. But if for one parameter, the distribution density for the noise and injection sample would have

been more similar to one another than they are for others distributions it would not harm the search. Indeed, in the worst case where noise and injection distributions are identical this parameter will contribute by a factor of 1 to the total likelihood ratio. The training samples S and B are generated for each chunk of O1 data to account for the noise nonstationarities and the evolution of the detector sensitivities.

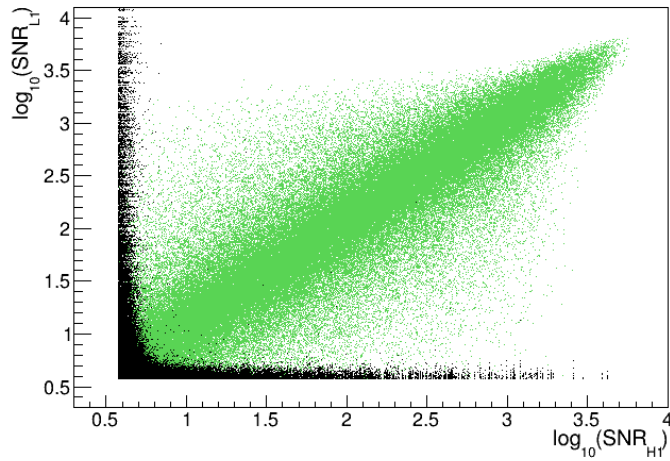
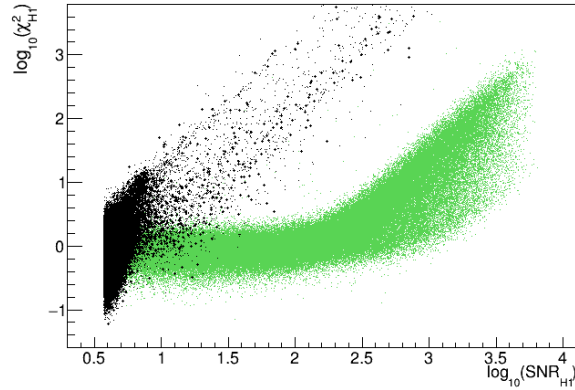
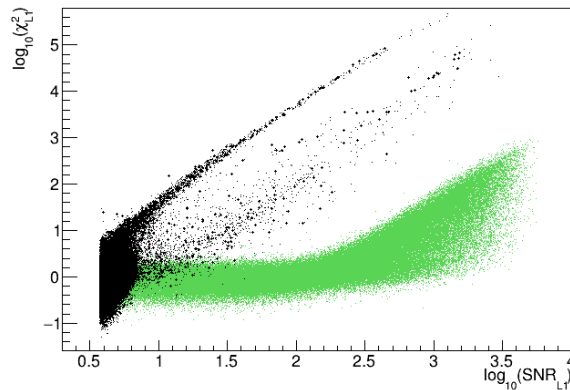


Figure 4.10: SNR distribution for the background coincident-events (black) and for the simulated signal coincident-events (green) in the first data chunk of O1. The simulated coincident-events are properly distinguished from the noise in the SNR distribution for a value of  $\text{SNR} \geq 10$ . Since both detectors have a similar sensitivity, we expect to measure roughly the same SNR for a gravitational-wave signal. This is not the case for noise. Moreover, when there is a glitch with high SNR in a detector, it is more likely that this one “triggers” with a low SNR glitch in the other detector. This justify the L-shaped shape of the noise distribution.

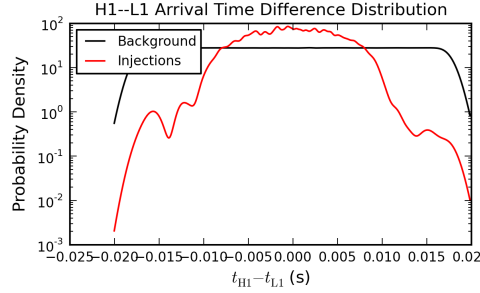


(a)  $\chi^2$  versus SNR distributions in H1.

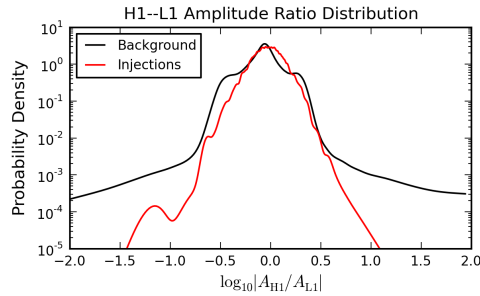


(b)  $\chi^2$  versus SNR distributions in L1.

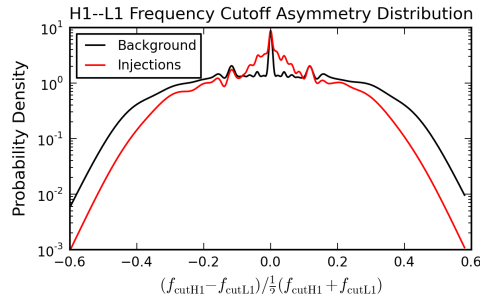
Figure 4.11: (a) and (b): distribution of SNR and  $\chi^2$  for the background coincident-events (black) and for the simulated signal coincident-events (green) in the first data chunk of O1. These two variables are strongly correlated, therefore we use the joint distribution probability to compute the ranking statistic  $\Lambda(\vec{x})$ . Signal events with a  $\text{SNR} \geq 30$  are well separated in this plane from background events. In theory one interferometer could be used to detect a sharp gravitational-wave signal.



(a) Arrival peak time distribution.



(b) Amplitude ratio distribution.



(c) High frequency cutoff asymmetry distribution.

Figure 4.12: The black curves show the distribution densities as observed in noise, and the red show them as observed in software injections. In all plots the vertical axis is the probability density. The symbols have the following meanings:  $t$  is the peak time of arrival,  $f_{cut}$  is the high frequency cutoff and  $A$  is the amplitude. The distribution densities for the noise and injection set are not similar to one another: these parameters are good to discriminate noise from injections. We note that there is no volumes of the parameter space in which injections can be found but no noise at all.

## 4.8 Data quality

A crucial part of the analysis is to understand the background of accidental triggers due to detector noise; this is important for preventing false identifications of noise

triggers as cosmic string candidates and for improving the overall sensitivity of the search. To each coincident background event is assigned a value of the ranking statistic  $\Lambda(\vec{x})$ . Figure. 4.13 shows the combined cumulative background event rate as a function of the likelihood ratio  $\Lambda(\vec{x})$ . The event rate is normalized by the background observation time given in Tab. 4.5. In presence of a Gaussian noise in the detector we expect a Gaussian distribution, this is clearly not the case. The purpose of data quality work is to understand the tail of the distribution and find a way to remove these events. In this section we present efforts made to improve the background distribution of the search.

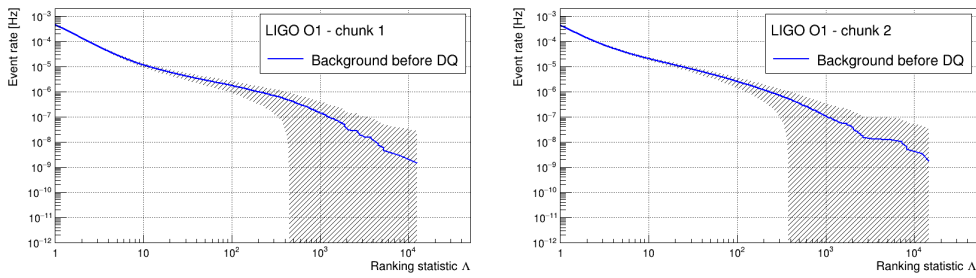


Figure 4.13: The blue line shows the expected background estimated with 300 time slides for the O1 cusp search for each chunk of data. The dashed hatched area corresponds to the  $1\sigma$  statistical error.

#### 4.8.1 The impact of data quality flags

As we have seen in chapter 2, data from the Advanced LIGO detector typically contain many non-Gaussian transient noises (glitches) due to instrumental and environmental conditions. These glitches are problematic for the search as they can mask or mimic a cosmic string signal. To minimize the contamination of the data with glitches, data quality (DQ) flags are created. A DQ flag consists of a list of time segments where the data is qualified as noisy. In general, it is built by the information provided by one or several of the auxiliary channels monitoring the detector. DQ flags from category 2 (CAT2) flag noisy periods where the coupling between the noise source and the gravitational-channel  $h(t)$  is well established. The first step to improve the background distribution is to evaluate the impact of these vetoes to remove the highest ranked coincident events. As seen in section. 4.6.2, the background is estimated initially with 300 time slides. We tested the impact of all the DQ flags on the background single detector triggers and we found two flags which improve the search, these are given in Tab. 4.7. In the final analysis we estimated the background using 6000 time slides. The likelihood functions are modified between these two analyses and so the ranking of the background events changed. As a result, we identified two additional DQ flags presented in Tab. 4.7. A quick definition of the channels is given. For example, a period with significantly elevated transient noise rate in the gravitational-channel  $h(t)$  is observed in H1. A correlation is found

IFOs	Name	Definition	deadtime (%)	efficiency (%)
H1	DCH-ASC_AS_B_RF36_GLITCHING	Severe glitching in DARM, which looks like RF45 noise.	0.39	1.60
H1	DCH-OMC_DCPD_A_SATURATION	Loud glitches can cause OMC DCPD <a href="#">[14]</a> saturations which push the instrument into a non-nominal operating condition.	0.45	1.70
H1	ODC-IMC_WFS_DOA4_PIT_HIGH	Flags indicating when angular alignment of IMC <a href="#">[15]</a> mirrors was fluctuating more than desired.	2.5	4.72
H1	ASC-AS_A_RF45_Q_PIT_OUT_DQ	Severe glitching due to the 45 MHz electro-optic modulator driver.	0.09	0.15

Table 4.7: The deadtime introduced by each veto in the O1 cusps analysis and the efficiency associated.

between these glitches and the behavior of the 45 MHz electro-optic modulator driver system used to generate optical cavity control feedback signals [\[142\]](#). The principal channel which best correlates with these glitches, monitors the part of the detector which deals with alignment sensing and mirror control. A DQ flag associated to this channel is applied as a category 1 to the search. However a part of these glitches is also observed in the 36 MHz driver system channel also, and the best channel correlated to these glitches is the H1\_DCH-ASC\_AS\_B\_RF36\_GLITCHING channel. We checked that the amount of data removed by a flag (deadtime) is reasonable i.e. that applying this flag as vetoes would not make us lose too much data. Most burst searches today use the same list of CAT2 flags [\[16\]](#). We choose to not use this list, in order to not remove period of time from the zero-lag data without having demonstrated advantageous effects on the background search. This has the advantage to minimize the risk of losing a cosmic string event. The vetoes applied to the search removed about 3.43% of the total of the zero-lag data. By comparison, the total period of time removed from the zero-lag using the general burst list of CAT2 flags would have been off  $\sim 4.9\%$ . The vetoes applied to the search are included in the general burst list of CAT2 flags. We have set a threshold on the efficiency/dead-time ratio of 2 to keep a DQ flag. Other factors influence the choice of vetoes. For example, a DQ flags with an efficiency/dead-time ratio of less than 2 remains interesting if it removes events characterized by a high likelihood. We also verified that each veto used does not remove the same events. None of the vetoes produced by HVeto and UPV had a significant impact on the search.

The figure [4.14](#) shows the limited impact of the two first flags presented in table [4.7](#)

<sup>16</sup>Burst category definer file.

on the background distribution estimated using 300 time slides. The background was

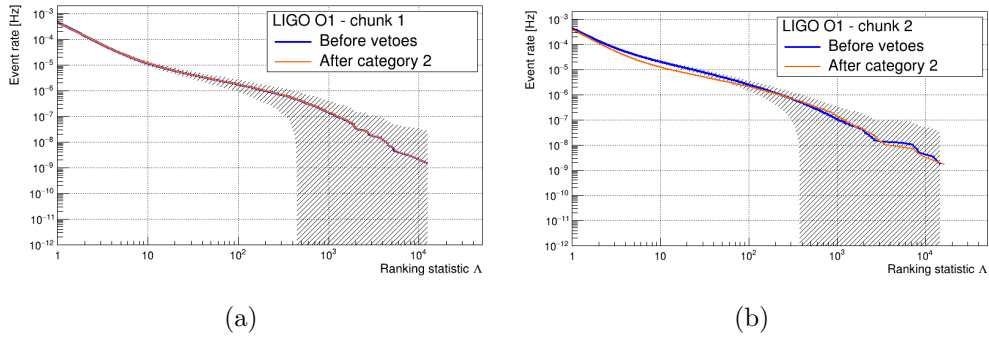


Figure 4.14: The blue lines show the expected background distribution estimated with 300 time slides before applying vetoes and the red lines show the background after applying the two first DQ flags given in Tab. 4.7.

estimated again with 6000 time slides. Since the background distribution changed, the likelihood ratio was constructed on a new sample of background events. Consequently the ranking of the events changed and new coincident events appear in the background distribution. The impact of the two last vetoes given in table 4.7 is shown in Fig. 4.15. The end of the distribution is very slightly improved by these vetoes.

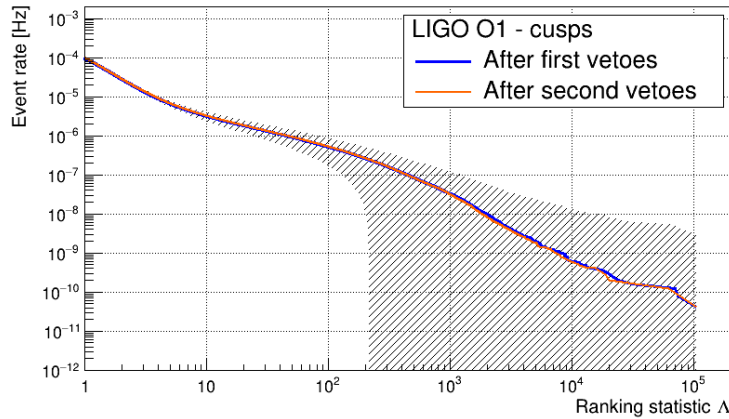


Figure 4.15: Expected background estimated with 6000 time slides for the O1 cusps analysis after applying the first vetoes (blue) and after the second vetoes (red).

### 4.8.2 Background event identification

Here we summarize efforts made to understand the origin of noise in the cosmic string cusp search. A typical method to visualize the data from a transient search perspective is by representing each detector's data using `Omicron`. It identifies excess power transient at a given central time, duration, bandwidth, SNR and Q-value. We used `Omicron` to build glitch families by grouping events according to their frequency, bandwidth, shape, arrival time and the period with which it arrive. For that we used a list of the  $\sim 200$  highest ranked background triggers in H1 and the  $\sim 200$  in L1, after applying the category 2 flags. We have produced the spectrogram for each of these events and we have grouped together glitches with similar shape, frequency, and bandwidth. The table 4.8 allows to visualize the typical shape of a glitch and its characteristics. The same work was done for L1 triggers and we did not find any families. These families may be two sub-families of blip glitches (tomte, and koi fish

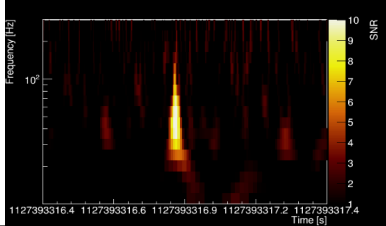
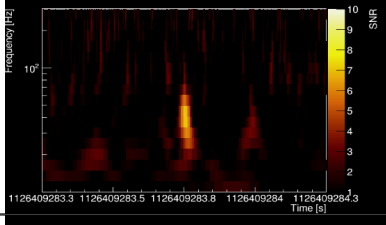
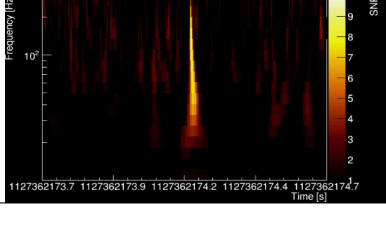
Omicron spectrogram	Frequency [Hz]	Number in %	Remarks
	45	26 %	1st, 2nd and 4th loudest events.
	37	14%	
	severals	16%	larger bandwidth than the two previous glitches.

Table 4.8: Classes of glitches in the investigation of  $\sim 200$  loudest triggers in H1 after applying category 2 flags. For each family, the spectrogram of a typical glitch is given, the central frequency, the number percentage contained in the list and some remarks.

see Fig 2.20), characterized by a very short duration,  $\sim 10$  ms with a large frequency bandwidth,  $\sim 100$  Hz. These glitches resemble the gravitational-wave signature of cosmic strings cusps or kinks. Hence, the sensitivity of the search is highly degraded

by the presence of these blip glitches. The occurrences of blip glitches in the data are not easily identifiable, but even if we couldn't build subfamilies with the list of L1 loudest triggers, the vast majority of the most significant events seen in L1 are blip glitches.

In addition, we tried to see if there were any time coincidences between these events and events seen in all the auxiliary channels. For that, we compared the spectrogram obtained for each event from the list (200 in H1, 200 in L1) with the spectrogram produced for all the auxiliary channels at the time of the event. We found no significant correlations with any safe auxiliary channel that could reveal the source of the noise.

### 4.8.3 UPV

In order to study possible sources of these noise transients called blip glitches we used UPV to repeat the previous work on a larger set of cosmic string triggers. UPV is utilized to find statistical correlations between transient noises in the gravitational-wave channel and in the auxiliary channels, cf Sec. 2.5.3. We utilized the hierarchical mode of UPV working with the full list of safe channels on Omicron  $h(t)$  triggers for H1 and L1. In the hierarchical mode, the most effective channel is determined after each round and all the triggers vetoed by this channel are removed from the initial list of triggers. This provides the advantage to not take in account the channels which veto the same triggers. Some channels provided a list of good vetoes with a high efficiency/dead-time ratio, see for example Fig. 4.16. However these vetoes have flagged very few events in the list of cosmic string triggers and so we can not prove that the coincidences we observe are not accidental.

Among the list of the highest ranked events in L1, we were able to identify 4 events in time coincidence with different magnetic channels. In addition, the detector and characterization group of Advanced LIGO had a clue about some blips correlated with magnetic channels. We run UPV on Omicron  $h(t)$  triggers for L1, using all the magnetic auxiliary channels to check if good vetoes are created. Instead of using the reference value of the user-percentage of 0.5, we utilized different number between 0.1 and 0.5 to find the optimal value to work with. Indeed, in general if the use-percentage is higher than 0.5, the coupling between the gravitational wave channel and an auxiliary channel is said to be real, by opposition to accidental coincidence. Reducing the threshold allows to be less strict and to find meaningful correlations with auxiliary channels that could provide either a way of vetoing those glitches. There were no major findings in such investigations and the vetoes produced did not have a significant impact on research.

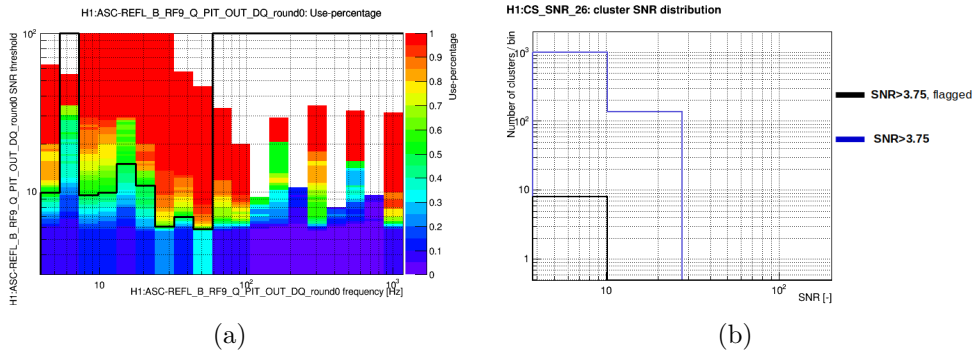


Figure 4.16: (a) UPV histogram for a given channel. Sources in the frequency range  $[7, 60]$  Hz are coupled to this channel (outside this frequency range the threshold is infinite and there is no real coupling). In addition the UPV report provides the ratio efficiency/dead-time  $\sim 29$  of the veto produced which tell us that this veto can be considered as good (see Chap. 2). (b) The SNR distribution for the  $2 \times 10^3$  highest ranked background events in H1, before (red) and after applying the veto (blue) produced by the hierarchical mode of UPV. The distribution is identical before and after we apply the veto: this veto is thus not effective to improve the search.

#### 4.8.4 Highest ranked background events

The final analysis is done using only the vetoes presented in Tab. 4.7. We investigate the five loudest events of the background distribution more rigorously to make sure they are not in coincidence with any of the auxiliary channels. The first highest ranked background event of the O1 cusp analysis is characterized by  $\Lambda \sim 1.06 \times 10^5$  with a  $\text{SNR}_{H1} = 6.6$  and  $\text{SNR}_{L1} = 8.5$ . The figure 4.17 gives the time-frequency representation of the first highest ranked events found in H1 and L1. We do not provide a scan of the first two events, because the SNR in H1 is too low to get a proper view at the event on the spectrogram. The characteristics of these coincident-events (frequency, bandwidth, duration, shape ...) in each detector reveals without surprise that both events are to be blip glitches.

The highest ranked background events found in the kink analysis are also identified as blip glitches. The templates used in cusp search are enough robust to be used in kink search [143], and so we deduce that the background events (which results from the matched-filer) have the same characteristics in both searches. From that, we can legitimately applied the same vetoes found in the cusp analysis to the kink analysis.

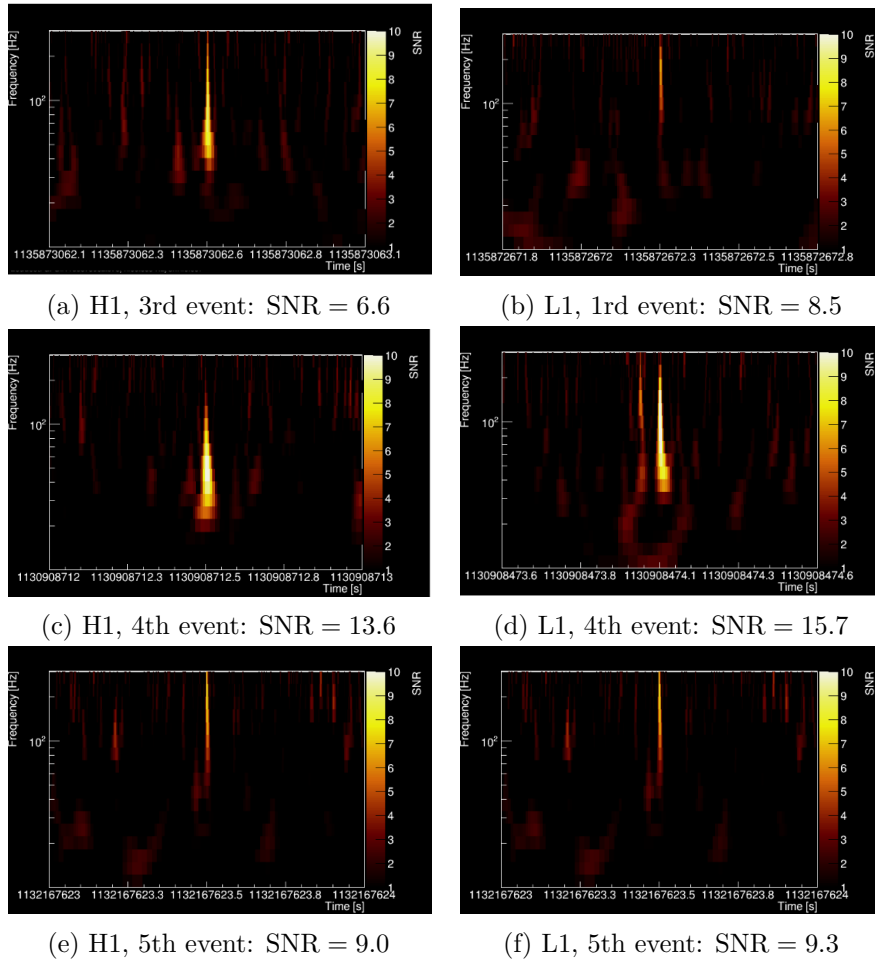


Figure 4.17: Time-frequency representation of the first the background highest ranked events found in the O1 cusp analysis.

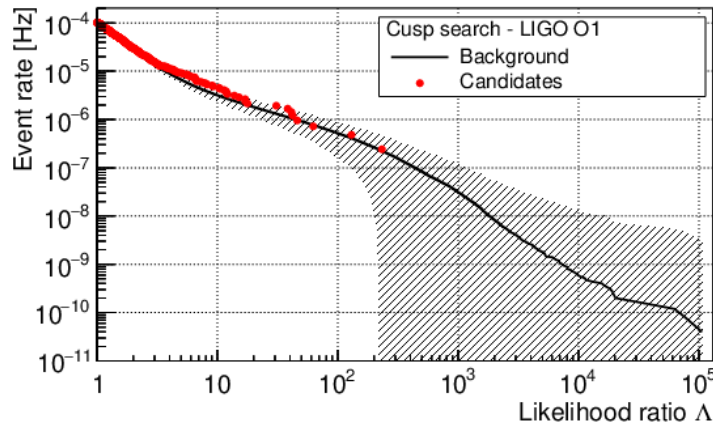
## 4.9 O1 results

Here we report on the results obtained to specifically search for gravitational-wave bursts from cosmic string cusps and kinks [144].

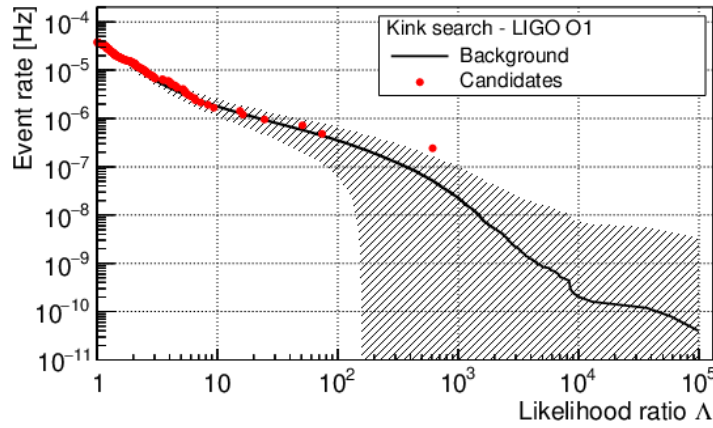
### 4.9.1 Cusp and kink search

Once the work of data quality on the background distribution is completed we then “open the box”, which means look at the real candidate of the search (the zero-lag). For both cusp and kink search, we compare the candidate ranking values with the expected background distribution. Figure 4.18 shows the cumulative event rate for the candidate events (zero-lag) as a function of the ranking statistic  $\Lambda(\vec{x})$ , as well as the average rate of events found in the time shifted data (background). The

shaded region corresponds to a  $1\sigma$  uncertainty computed from the variations in the number of events found in the time shifted data. For both searches there are no candidate events which deviate significantly from the background distribution. The highest-ranked event is measured with  $\Lambda_h \simeq 232$  for cusp search and  $\Lambda_h \simeq 611$  for kink search, associated to a false alarm rate  $\text{FAR}_{O1} = 1/T_{obs} = 2.40 \times 10^{-7}$  Hz, with  $T_{obs}$  the livetime of the zero-lag data. An investigation of these events shows that they seem to belong to the blip glitch family.



(a)



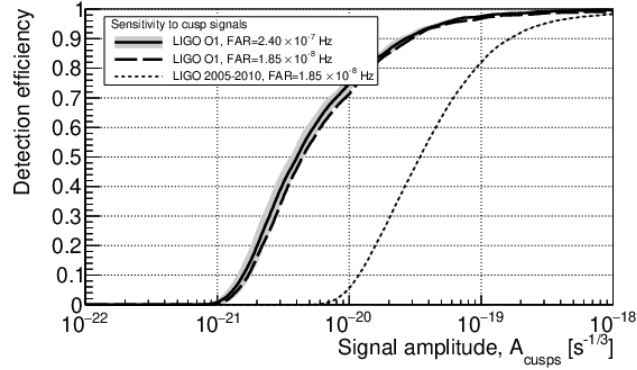
(b)

Figure 4.18: The red points show the measured cumulative (a) cusp and (b) kink gravitational-wave burst rate as a function of the likelihood ratio  $\Lambda$ . The black line shows the expected background of the search with the  $1\sigma$  statistical error represented by the hatched area.

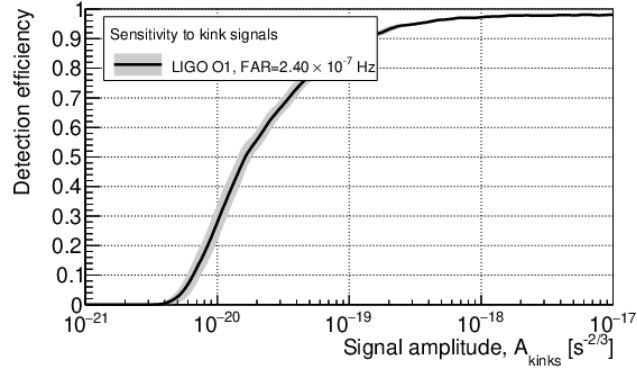
### 4.9.2 Search sensitivity

To measure the cusp or kink search sensitivity we injected over a total of  $515 \times 10^3$  simulated signals of known amplitude into a time-shifted data set and then we performed a search identical to the one described above. To avoid self-selection issues, we use a set of injections that is independent from the S sample used to construct the ranking statistic. The search sensitivity  $\epsilon_q$  is then defined as the fraction of simulated signals recovered with  $\Lambda > \Lambda_h$  where  $\Lambda_h$  is the highest-ranked candidate of the search.

Figure. [4.19a](#) shows the detection efficiency  $e_q$  as a function of the injected cusp signal amplitude  $A_q$ . The amplitude at which we recover half of our injections is  $A_{50\%} = 4.03 \times 10^{-21} \text{s}^{-1/3}$ . The uncertainties associated with the efficiency curve include three different effects. The first one is associated to binomial counting fluctuations since at each point the value of the efficiency is measured by counting a finite number of injections. There is an additional uncertainty in the amplitude to which a measurement of the efficiency should be assigned. Finally the last uncertainty is related to the calibration: the injections from which the efficiency is measured are performed at amplitudes different from what was planned. We also compare the cusp sensitivity curve to the one obtained in the previous analysis during the S5/S6 runs (2005-2010) for a same false alarm rate, see Fig. [4.19](#). The sensitivity to cosmic string signals is improved by a factor 10. This gain is explained by the significant sensitivity improvement at low frequencies of Advanced detectors.



(a)



(b)

Figure 4.19: The sensitivity of the search as a function of the cusp/kink signal amplitude. The uncertainties associated with the efficiency curve include binomial counting fluctuations, calibration uncertainties, and an amplitude binning uncertainty.

## 4.10 O2 analysis

This section describes the burst cosmic string analysis conducted with the data from the second observing run (O2). We used the same pipeline as described for O1 and the same input parameters. But there are some differences with the O1 analysis. The period of time analyzed is longer. Indeed the amount of coincident data analyzed between the two Advanced LIGO detectors is approximately  $\sim 115.9$  days. The LSC Algorithm Library Suite [145] (LALSuite) containing the pipeline has undergone several changes, therefore, the pipeline used during the O1 had to be restored in a way that was compatible with the new LALSuite. Two analyses were run in parallel, one with the pipeline used for the O1 analysis (IN2P3 computing centre, Lyon) and the other with the restored pipeline (LSC grid centre, Caltech). This work, which will not be discussed in this thesis, has considerably eased the review of the restored pipeline. For practical reasons we only conducted a search for cusps. In addition, we also performed a three-detector search using the data collected by Advanced Virgo

in August 2017 to conclude that the sensitivity of the Advanced Virgo detector was not sufficient to improve the detection efficiency of cosmic string signals.

#### 4.10.1 Results

Here, we report on the search for signals from cosmic string cusps in LIGO data. We kept the configuration used for the final O1 analysis (template bank, SNR threshold, number of time slides, injections ...). The distribution for the mismatch between templates is verified. For each chunk of data, we studied the single-detector parameter distributions. We observed an excess of triggers in H1 at the end of the analyzed period (chunk4), which is explained by a drop in sensitivity in July, 2017 after an earthquake in Montana. We have not found any other particular behaviour that could be studied more precisely here. In a similar way we also studied the parameter distributions used to compute the ranking statistic, and we have not identified any particular behaviour.

The background is estimated using 6000 time slides, see Tab. 4.5. We have considered all DQ flags and vetoes produced by UPV and Hveto. For each chunk of data, we look at the effectiveness of a veto which is defined to be the ratio of the fraction of glitches removed to the fraction of analyzable livetime removed by the veto. We select those for which that ratio is greater than 2. The selection of vetoes used for the final analysis is presented in Tab. 4.9. These vetoes removed about respectively a total of 2.4% in L1 and 1.8% in H1 of the zero-lag livetime. As in the O1 analysis, we found that the background highest ranked events are consistent with blip glitches. The detector and characterization group of LIGO found several origins to a few percent of blip during O2 [67]. The vetoes produced are not effective on the search. The blip glitches have several origins and therefore we are not sensitive to the particular blips for which a veto exists.

The cumulative event rate as a function of the ranking statistic  $\Lambda$  is displayed in the upper plot of Fig. 4.20. The highest-ranked event measured with  $\log(\Lambda) = 9.1$ <sup>17</sup> is consistent with the background distribution. Therefore we cannot argue this event to be the result of a gravitational-wave signal produced by cosmic string cusp. We examined this event and concluded that it belongs to the category of blip glitch noises. We also give the sensitivity curve combining O1 and O2 data, since the sensitivity of the O2 LIGO cusp search is comparable to the O1 LIGO one.

---

<sup>17</sup>This event is found with a SNR=9.4 in L1 and a SNR=3.8 in L1.

IFOs	Veto name	Definition	deadtime %	efficiency %
L1	DMT-ETMY_ESD_DAC_OVERFLOW	Saturation in the drive signal of one of the end test mirror producing glitches.	1.56	3.07
L1	DCH-EY_MIC_BLRMS_GT_200	Microphone 30-200Hz, created to capture thunder.	0.019	0.19
L1	DCH-CS_MIC_BLRMS_GT_250	Microphone 30-200Hz, created to capture thunder.	0.013	0.23
L1	DCH-EARTHQUAKE_CS_Z_BLRMS_GT_190	Earthquakes causing glitching in $h(t)$ .	0.14	1.6
H1	DCH-EARTHQUAKE_CS_Z_BLRMS_GT_320	Earthquakes causing glitching in $h(t)$ .	0.13	1.4
H1	DMT-ITMY_L2_DAC_OVERFLOW	Glitches produced by an overflow in the digital to analog converter used for one of the input test mirror.	0.2	0.8
H1	DCH-ETMX_L3_OPLEV_SUM_HIGH_BLRMS	Glitches caued by one of the end test mirror optical lever laser.	0.028	0.064
H1	DCH-ETMY_L3_OPLEV_BLRMS_GT65	Glitches caued by one of the end test mirror optical lever laser.	0.08	0.24
L1	L1_ASC_Y_TR_A_NSUM_OUT_DQ_OMICRON	Glitches correlated to the alignment angular control system (ASC).	0.23	1.38
H1	H1_ASC_Y_TR_A_NSUM_OUT_DQ_OMICRON	Glitches due to the ASC system.	0.55	1.72
L1	HVeto	see Sec 2.5.3	0.44	X
H1	HVeto	see Sec 2.5.3	0.85	X

Table 4.9: The deadtime (% of total coincidence time in the zero-lag) introduced by each veto in the O2 cusps analysis and the associated efficiency.

#### 4.10.2 Search using Advanced Virgo data

We also conducted a three-detector search using the data collected by Advanced Virgo in August 2017, corresponding to  $\sim 17$  days of data. By analogy with the two-detector search an event is represented by a total of 18+1 variables, see Eq. 4.46. Indeed an additional parameter is considered to account for the different sensitivity: the number of detectors involved in the event. The background is now estimated by shifting the data from L1 and from V1 by the same amount but in opposite direction with respect to H1 data. This ensures that all the lags are independant. Moreover, simulated signals are injected onto a lag of Virgo data to construct the signal sample.

Figure. 4.21 shows the combined cumulative background event rate as a function of the likelihood ratio  $\Lambda(\vec{x})$  without Virgo and with Virgo. We note the presence of

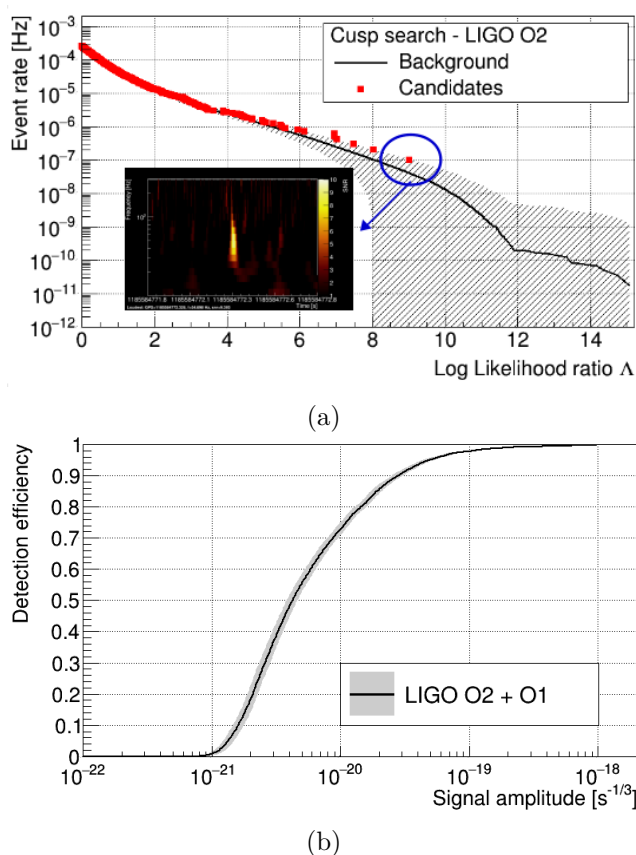


Figure 4.20: (a) Cumulative event rate for the cosmic string cusp search as a function of the ranking statistic  $\Lambda$  (red points). The black line shows the expected background distribution with a  $\pm 1\sigma$  statistical error represented by the hatched area. The highest-ranked coincident event is measured with  $\log(\Lambda) = 9.1$  and we give a time-frequency representation for this event in L1. (b) Search efficiency as a function of the cusp signal amplitude, when combining O1 and O2 Advanced LIGO data sets. This is measured by the fraction of simulated cusp events recovered with  $\Lambda > \Lambda_h$ .

events characterized by a higher likelihood ranking value using Virgo's data. These events are double coincident events HV or LV identified with a small SNR  $< 4$  in Virgo with a blip glitch in LIGO detector.

We performed data quality studies on Virgo data to reject glitches that may mimic the waveform from cosmic string cusps. We selected 4 data quality flags found to slightly improved the search. Blip glitches are well understood in Virgo as discussed in Sec. 2.5. Figure 4.22 shows the  $\chi^2$  versus SNR distribution used to compute the ranking statistic. We note the presence of a population of transient noises that is not easily distinguished from injections. These are known as control glitches and are part of blip glitch family in Virgo. A good veto exists to reject

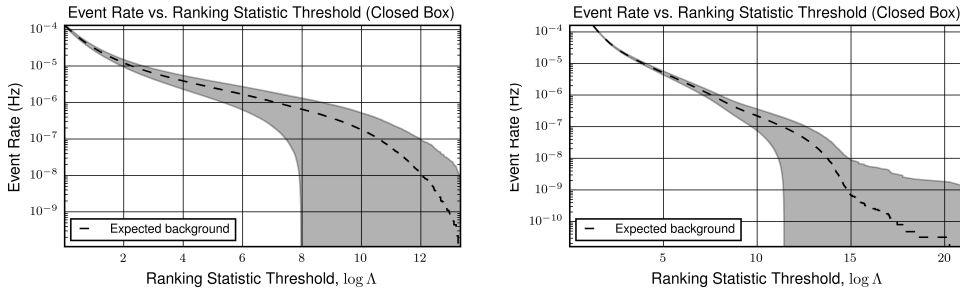


Figure 4.21: Background event rate for the last chunk of O2 data analyzed: (a) without Virgo and (b) with Virgo.

these glitches, however these are not the ones that limit the search in Virgo. We isolated another family of blip glitches called “photodiode glitches” see Fig. 4.23. These glitches are found in one of the photodiode that measures the dark fringe signal and the origin is not well understood. In addition we found two others vetoes that slightly improves the search.

Figure. 4.24 presents the sensitivity curve obtained by using or not Virgo data. We note that the search efficiency is slightly improved for the large amplitudes when applying the vetoes selected. However at low amplitudes the search efficiency is better when using only LIGO detectors. We conclude that Virgo has a limited impact and seems to slightly degrade the search sensitivity. This is due to the low sensitivity of Virgo compared to the one of LIGO detectors.

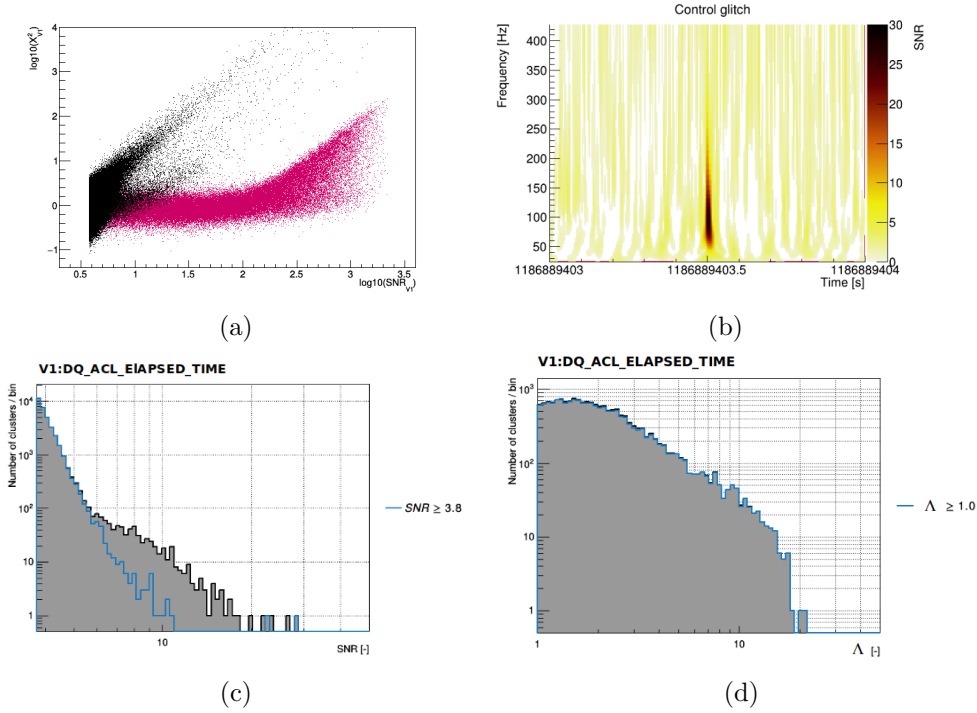


Figure 4.22: (a)  $\chi^2$  versus SNR distribution in V1. In black are represented the background coincident-events and in purple the simulated signal coincident-events. We note a well localized population in the background which is very close to the injection. This population belongs to a known category of transient noises called “control glitches”. (b) Time-frequency representation of a typical control glitch. These glitches appear to be of short duration and cover a large band of frequencies. They look similar to the cosmic string signal, this is why they are not well discriminated from the injections. A category 2 DQ flags (`V1:DQ_ACL_ELAPSED_TIME`) was created to remove a large part of these glitches. (c) The SNR distribution of the background coincident-events before (black) and after (blue) applying the veto. The veto removed the high SNR events. (d) The likelihood distribution of the background coincident-events before (black) and after (blue) applying the veto. This veto has no impact on the tail of the distribution.

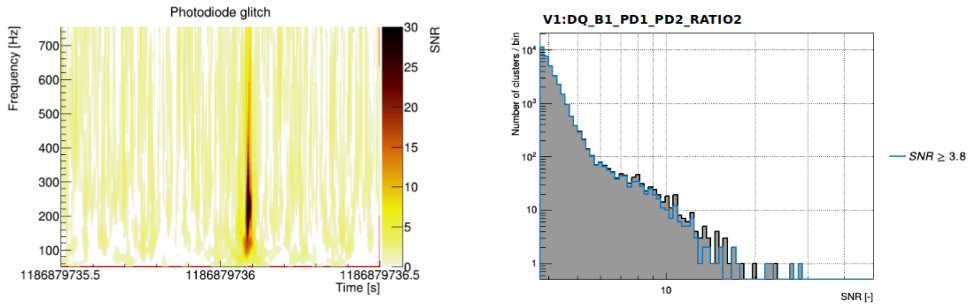


Figure 4.23: (a) Time-frequency representation of a typical photodiode glitch vetoed by a DQ flag (`V1:DQ_B1_PD1_PD2_RATIO2`). (b) The SNR distribution of the background coincident-events before (black) and after (blue) applying the veto. The veto removed the high SNR events.

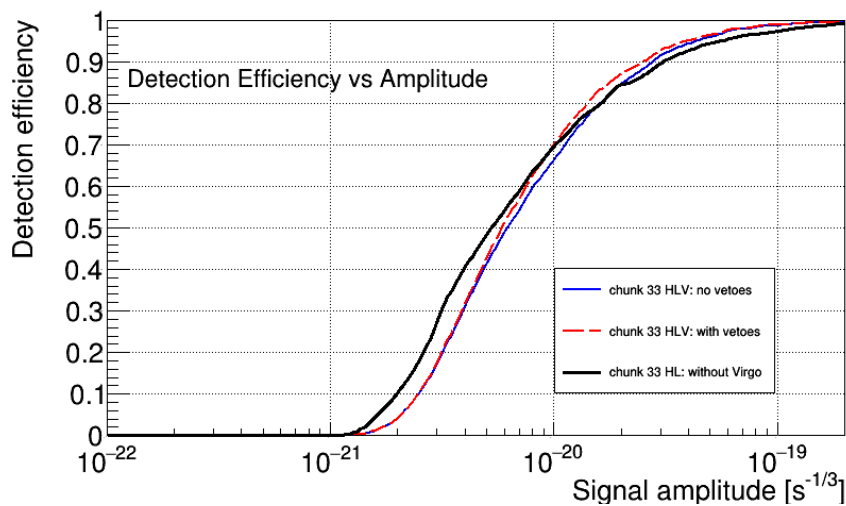


Figure 4.24: The sensitivity of the search (close-box) as a function of the cusp signal amplitude for a 3-detectors search before (blue) and after (red) data quality study. It is compared to the search sensitivity curve (black) obtained by using only LIGO detectors. The efficiency is measured at same false alarm rate  $10^{-8}$  Hz.

# Upper limits on cosmic string parameters

We have seen that a network of cosmic strings formed in the early Universe is firstly characterized by the dimensionless string tension  $G\mu$ . In addition, for topological strings we often assume that when strings collide, they always intercommute, i.e. they always “exchange partners” and reconnect after a collision. This is not longer true for superstrings, i.e. fundamental strings of String Theory stretched at cosmological scale. Thus, another parameter is the intercommutation probability (with  $p < 1$ ). In the absence of detection, we can use the results of Sec. 4.9 and Sec. 4.10 to constrain the parameter space  $(G\mu, p)$ . To do so, we need to derive the expression for the cosmological rate as a function of the strain amplitude, which is needed to evaluate the upper limits (Sec. 5.2). This rate is directly proportional to the number density of loops at all times, so we first review the three expressions for the loop number density which have been used in this work (Sec. 5.1). Furthermore, the incoherent superposition of many bursts from cusps and kinks<sup>1</sup> generates a gravitational-wave stochastic background which is searched for in Advanced LIGO-Virgo data (Sec. 5.3). We present the results obtained using the O1 and O2 data from Advanced LIGO-Virgo detector, published in [144, 146, 147] (Sec. 5.4.2). Finally, the last section of this chapter is dedicated to the continuation of the previous work, this time by looking at the contribution of a new type of burst. Indeed, when there is at least two kinks on a loop, they can meet and produce a gravitational-wave burst.

## 5.1 Loop distribution models

The purpose of this section is to briefly present the configuration of a cosmic string network at the time of its formation and how it evolves. Then we compare three loop distribution models used to constrain the cosmic string parameters.

---

<sup>1</sup>And from kink-kink collisions, however this is not included in this work.

### 5.1.1 String network in a FLRW Universe

As mentioned in Sec. 3.2.3 the mechanism of cosmic string formation was first pointed out by Kibble [91, 92] (1976). According to the Kibble’s mechanism, when the temperature of the Universe drops below a critical temperature  $T_c$ , the Higgs field  $\phi$  develops, at each point, a non-zero expectation value corresponding to some point in the manifold  $\mathcal{M}$  of the minima of the potential. If two points are separated by a distance greater than the correlation length  $\xi(t)$ , they can take different expectation values. The magnitude of  $\xi(t)$  depends on the phase transition considered. Then depending on the topological properties of the manifold  $\mathcal{M}$ , a network of cosmic strings will form with a characteristic length scale comparable to  $\xi(t)$ . Since correlations between different regions of space can not be established at speeds greater than the speed of light,  $\xi(t)$  can not exceed the causal horizon  $\xi \leq d_h(t) \sim t$ .

To determine the cosmological evolution of a cosmic string network in an expanding FLRW Universe, it is necessary to determine the initial characteristics of the network. For a second order transition, once the temperature is sufficiently low ( $T \ll T_c$ ), the Higgs field  $\phi$  can no longer change its value and the cosmic strings are “frozen”, cf. Sec. 3.2.3. The initial string distribution can be obtained by examining the statistical properties of the Higgs field values just after the phase transition responsible for string formation [77, 148], over distances greater than the correlation length  $\xi(t)$ . Numerical simulations to determine the initial configuration of a cosmic string network were conducted for the first time by Vachaspati and Vilenkin [149]. It is shown that the network preferably contains long strings at its formation (80%) with a lower proportion of strings in the form of loops (20 %).

From the initial string distribution, the evolution of the network will depend on the dynamics of each string. As in a flat space, the Nambu-Goto action allows to derive the equations of motion (cf. Eq. 3.77) applied to a FLRW space. From that, we can show that the total energy variation of a string is [77]:

$$\dot{\mathcal{E}} = \frac{\dot{a}}{a}(1 - \langle v^2 \rangle)\mathcal{E}, \quad (5.1)$$

where the dots stand for derivatives with respect to the conformal time  $\tau$  defined by  $d\tau = dt/a(t)$  and  $\langle v^2 \rangle$  is the average string velocity squared<sup>2</sup>. We see that the total energy  $\mathcal{E}$  of the string increases proportionally to the scale factor  $a(t)$ , as we could have expected intuitively. Thus, in an expanding Universe, the string gains energy by stretching. However, the term  $\langle v^2 \rangle$  aims to reduce this energy gain. So there are two contrasting effects, and the equations of motion show that there are two possible evolutions. For super-horizon strings ( $L > d_H$  with  $L$  a characteristic length which measures the average distance between strings), often called long strings<sup>3</sup>, the Universe expansion aims to damp the oscillations of the strings and therefore to

<sup>2</sup>For a closed loop of size  $\ell$  the average is made over a period of oscillation  $T = \ell/2$ .

<sup>3</sup>Or infinite strings.

reduce  $\langle v^2 \rangle$ : stretching dominates. In contrast, for smaller length scales the “damping” term in the equations of motion becomes progressively negligible. In particular for a subhorizon ( $\ell \ll d_h$ , with  $\ell$  the loop size) cosmic string loop,  $\langle v^2 \rangle = 1/2$ , and the energy of the loop remains conserved. In comparison with the result obtained in Sec. [3.2.5](#), we conclude that the evolution of sub-horizon cosmic string loop in a FLRW space is therefore reduced to that in a flat space.

In addition, it is also necessary to take into account the interactions between strings within the network. We have seen in Sec. [3.2.6](#) that in the simplest case of Nambu-Goto strings, when two strings interact they always intercommute, i.e. they exchanges partners. This mechanism leads to the continuous formation of cosmic string loops. These loops oscillates and dissipates their energy in the form of gravitational waves until they disappear<sup>4</sup>. Thus, the determination of the loop distribution at a time  $t$  is a major challenge in determining the network’s evolution. To summarize, the investigation of the evolution of a network of cosmic strings requires at least to solve the equation of motion for each string and to take into account intercommutation. This complex problem is solved by means of numerical simulations (cf [\[79\]](#) and section 9.4 in [\[77\]](#) for an introduction). The earliest simulations were produced around 1985 [\[152, 153, 154\]](#). The simulations of the evolution of the cosmic string network throughout the history of the Universe involve very large scales, ranging for example, from the distance between kinks to the horizon size. This is a technical challenge due to the limits on numerical resolution and computation times. Significant progress has been made in this area, however this is not enough and therefore there are still several questions about the evolution of a string network that remain open.

In particular, one of the characteristic behaviors of a cosmic string network is the existence of a scaling regime. The “scale-invariant” network evolution is the results of two competitive effects: the expansion of the Universe that stretches the strings is compensated by the dissipation of energy through the loop formation and the emission of gravitational waves. In this regime, the typical length scale of long strings is proportional to the horizon distance  $L(t) \sim d_H \sim t$ . The scaling nature of long strings is supported by subsequent simulations [\[152, 153, 154\]](#). In this case, the long string energy density remains a fixed fraction of the Universe energy density, this ensures that long strings never dominate the energy density of the Universe and remain compatible with cosmological observations [\[77\]](#). The expected cosmological distribution of loops has been subject to debate since the development of the first analytical model [\[155\]](#). Loops reach a scaling regime over a long time scale and therefore it is only recently that simulations have become enough robust to show the existence of a population of scaling loops [\[156, 157\]](#). In the following sections we present the three models used in the work of this thesis.

---

<sup>4</sup> The main energy dissipation mechanism for other classes of strings may be different (superconducting strings [\[150\]](#), global strings [\[151\]](#)).

These models use an analytical approach supplemented by Nambu-Goto simulations. Indeed, in Nambu-Goto simulations, the effect of gravitational-wave emission and the backreaction of gravitational waves onto the string are ignored. We define more precisely the loop distribution  $n(\ell, t)d\ell$  as the number of cosmic string loops per unit volume with invariant length between  $\ell$  and  $\ell + d\ell$  at cosmic time  $t$ . The three models differ in the loop distribution, and to determine the consequence of these differences on their gravitational wave signal, it is more convenient to work in unit of cosmic time. For this purpose, let us define a new dimensionless variable  $\gamma$ , the relative loop size, and a new dimensionless function  $\mathcal{F}$ , that we will refer as the loop distribution:

$$\gamma(\ell, t) \equiv \frac{\ell}{t} \quad \text{and} \quad \mathcal{F}(\gamma, t) \equiv n(\ell, t) \times t^4. \quad (5.2)$$

Superstrings may have an intercommutation probability  $p$  significantly smaller than unity. The effect of a reduced intercommutation probability on the loop distribution is still a matter of debate [158, 159]. Therefore we restrict ourselves to study the generally expected behaviour  $\mathcal{F}_{p<1} = \mathcal{F}/p$  [159], leading to an enhancement of the loop density. Note that here, we neglect different aspects of a realistic cosmic superstring network as the creation of junctions, see Sec. 3.2.6.

### 5.1.2 Model 1

The first analytical model we consider is often referred as the one-scale model, was initially developed by Kibble [155, 77]. Despite its simplicity, it catches various properties of the network evolution. In this model, the network is described using a unique scale, i.e. the typical distance between the strings  $L(t) \sim t$ , in scaling regime. Here, all loops chopped off in the infinite string network are formed with the same relative size  $\alpha$  at a fixed fraction of the horizon,

$$\ell = \alpha t \quad , \text{ at formation.} \quad (5.3)$$

These loops can self-intersect and fragment further but ultimately this process ceases and a non-intersecting population of loops remains [77]. We assume then that loops do not self-intersect once formed. Initially, it was considered that the size of loops is given by gravitational back-reaction [111]. The gravitational field produced by a moving loop acts back on the string and one expects that the small-scale structure on the loop are cut off by this back-reaction. It was then assumed that the typical size of loops  $\ell(t)$  is set by the scale of the smallest wiggles, which is in turn determined by damping due to gravitational emission and thus  $\alpha \sim \Gamma G\mu$ . Since the last few years, simulations suggest that loops are produced in a wide range of sizes, unrelated to the gravitational back-reaction scale [160, 161, 156]. The results indicate that most of the string length is going into relatively large loops of size comparable to the inter-string distance with  $\alpha \gg \Gamma G\mu$  [160]. In this work we assume that:

$$\alpha \simeq 0.1. \quad (5.4)$$

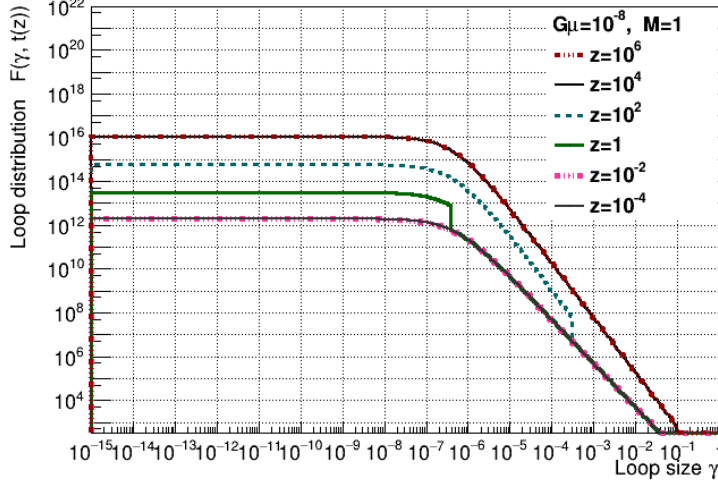


Figure 5.1: Loop size distributions predicted by model  $M=1$ . The loop distribution  $\mathcal{F}(\gamma, t(z))$ , is plotted for different redshift values and fixing  $G\mu = 10^{-8}$ .

Moreover to take into account the decay by gravitational-wave emission, we consider from section. [3.3.3](#) that loops formed at a time  $t_i$  with a size  $\ell_i = \alpha t_i$  shrink such that:

$$\ell(t) = \ell_i - \gamma_d(t - t_i) \quad \text{with} \quad \gamma_d \equiv \Gamma G\mu \quad , \quad \Gamma \simeq 50. \quad (5.5)$$

Then the loops decay at a time

$$t_f = \left( \frac{\alpha}{\gamma_d} + 1 \right) t_i. \quad (5.6)$$

Loops are long-lived when  $t_f \gg t_i$ , i.e. when  $\alpha \gg \gamma_d$ .

Under these assumptions, the scaling loop distribution in the radiation era is given by:

$$\mathcal{F}_{\text{rad}}^{(1)}(\gamma) = \frac{\mathcal{C}_{\text{rad}}}{(\gamma + \gamma_d)^{5/2}} \Theta(\alpha - \gamma) \quad , \quad \mathcal{C}_{\text{rad}} \simeq 1.6, \quad (5.7)$$

where the superscript (1) stands for model  $M=1$ . The constant  $\mathcal{C}_{\text{rad}}$  is fixed with numerical simulations of Nambu-Goto strings. The Heavside function  $\Theta$  ensures that no loops are formed with sizes larger than  $\alpha t$ . In the matter era, the scaling loop distribution has two components. On one hand, there are loops formed in the radiation era which survive into the matter era:

$$\mathcal{F}_{\text{mat}}^{(1),a}(\gamma, t) = \frac{\mathcal{C}_{\text{rad}}}{(\gamma + \gamma_d)^{5/2}} \left( \frac{t_{\text{eq}}}{t} \right)^{1/2} \Theta(-\gamma + \beta(t)). \quad (5.8)$$

Here,  $\beta(t)$  is determined using Eq. [5.6](#) by considering that the largest loops are formed in the radiation era with a length  $\ell = \alpha t_{\text{eq}}$ , but have since shrunk due to

gravitational wave emission:

$$\beta(t) = \alpha \frac{t_{eq}}{t} - \gamma_d \left(1 - \frac{t_{eq}}{t}\right). \quad (5.9)$$

Loops formed in the matter era have lengths distributed according to

$$\mathcal{F}_{\text{mat,b}}^{(1)}(\gamma, t) = \frac{\mathcal{C}_{\text{mat}}}{(\gamma + \gamma_d)^2} \Theta(\alpha - \gamma) \Theta(\gamma - \beta) \quad , \quad \mathcal{C}_{\text{mat}} \simeq 0.48. \quad (5.10)$$

The total loop distribution in the matter era is then given by the sum of both contributions.

Figure 5.1 shows the loop distribution for different redshift values and fixing  $G\mu$ . We observe that the largest contribution is given by smallest loops. At fixed redshift, the shape of the distribution is explained by the behaviour of  $\gamma$  with respect to  $\Gamma G\mu$ , see Fig. 5.2. For  $G\mu = 10^{-8}$  the distribution of loops is constant as long as  $\gamma \ll \gamma_d \simeq 5 \times 10^{-7}$ . During the radiation-to-matter transition, the distribution depends on the redshift as observed (green curves). A discontinuity, visible for low redshift values, results from the radiation-matter transition which is modeled by Heavside functions.

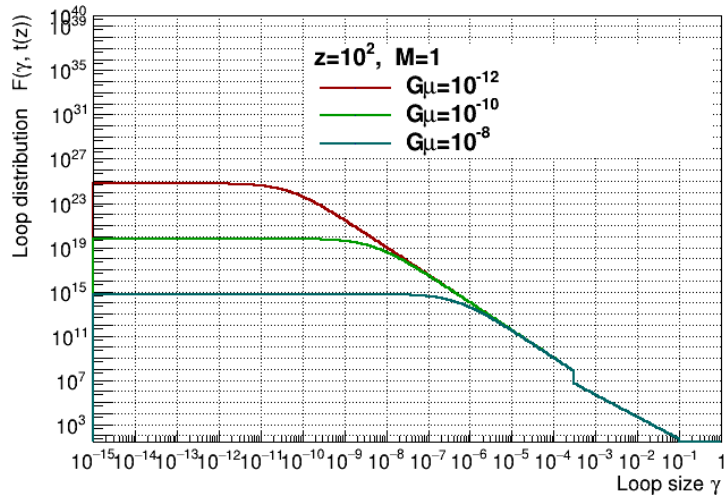


Figure 5.2: Loop size distributions predicted by model  $M=1$ . The loop distribution  $\mathcal{F}(\gamma, t(z))$ , is plotted for different values of  $G\mu$  and fixing the redshift  $z = 10^2$ .

### 5.1.3 Model 2

This loop distribution, taken from [157], is based on analytical modelling and numerical simulations [162, 163]. We focus on describing the significant differences with the first model. Here, we no longer consider that all loops are created with

a length equal to a fixed fraction of the horizon,  $\alpha$ . The loop production is given by simulations. This function depends on the time of loop production  $t$ , the loop size  $\ell$  and the loop momentum  $\mathbf{p}$ . In addition to the energy loss of the loops by gravitational wave emissions, the small loops lose energy by redshifting. Indeed, it can be shown that the loop momentum is redshifted like the momentum of a point particle in an expanding universe and decays as  $\mathbf{p} \propto a^{-1}$  [77]. However, in this model, the momentum dependence of the loop production function is considered weak and thus this function is integrated over  $p$ , to obtain the scaling number density distribution.

In the radiation era the scaling distribution is:

$$\mathcal{F}_{\text{rad}}^{(2)}(\gamma) = \frac{\mathcal{C}_{\text{rad}}^{(2)}}{(\gamma + \gamma_d)^{5/2}} \Theta(\alpha - \gamma) \quad , \quad \mathcal{C}_{\text{rad}}^{(2)} \simeq 0.18, \quad \alpha = 0.1 \quad (5.11)$$

where the superscript (2) stands for model M=2. The constant  $\mathcal{C}_{\text{rad}}^{(2)}$  is fixed by numerical simulations, with a cutoff at maximum size of a loop  $\alpha$ . In the matter era we have again two contributions, relic loops from the radiation era give:

$$\mathcal{F}_{\text{mat}}^{(2),a}(\gamma, t) = \frac{\mathcal{C}_{\text{rad}}^{(2)}}{(\gamma + \gamma_d)^{5/2}} \left( \frac{t_{\text{eq}}}{t} \right)^{1/2} \Theta(-\gamma + \beta(t)), \quad (5.12)$$

this is time-dependant, since it is not a scaling population. Loops produced during the matter era:

$$\mathcal{F}_{\text{mat}}^{(2),b}(\gamma) = \frac{\mathcal{C}_{\text{mat}}^{(2)}}{(\gamma + \gamma_d)^2} \Theta(\tilde{\alpha} - \gamma) \Theta(\gamma - \beta(t)) \quad , \quad \mathcal{C}_{\text{mat}}^{(2)} \simeq 0.27 - 0.45\gamma^{0.31}, \quad \tilde{\alpha} = 0.18, \quad (5.13)$$

for  $\gamma < 0.18$ . The loop distribution is plotted in Fig. 5.3. In the radiation era, the loop distribution takes the same power-law behaviour as for model 1, Eq. 5.7. However, this loop distribution is significantly reduced compared to model 1 due to the normalization factors where  $\mathcal{C}_{\text{rad}}^{(1)}/\mathcal{C}_{\text{rad}}^{(2)} \simeq 10$ . The functional form is different for the distribution of loops formed in the matter era in model 1. In the case  $\ell \ll t$ , the second term in the numerator can be ignored and the functional form agree with Eq. 5.10, with a reduction  $\sim 2$ . The authors of [157] attribute this reduction in the number of loops to two effects. First, only about only 10% of the power is radiated into large loops [164] and most of the energy leaving the long string goes into smaller loops. This energy is lost to redshifting.

### 5.1.4 Model 3

This analytical model is presented in [165] and is based in part on different numerical simulations [166] from model M=2. Furthermore, as opposed to model M=2, the loop production function is not the quantity inferred from the simulations: rather, authors of [165] extract directly the distribution of scaling loops from their simulations. Here again, the model is not fully described but only the main differences with previous

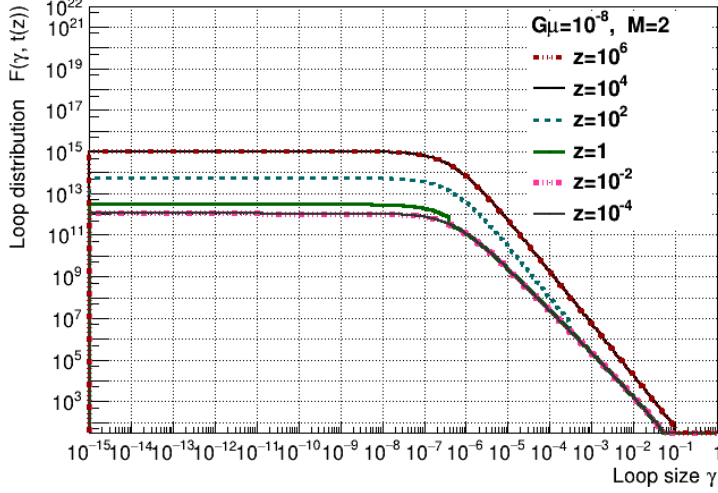


Figure 5.3: Loop size distributions predicted by model  $M=2$ . The loop distribution  $\mathcal{F}(\gamma, t(z))$ , is plotted for different redshift values and fixing  $G\mu = 10^{-8}$ .

models are highlighted. It uses the Polchinski-Rocha loop production function [167] which itself is theoretically derived. This loop production function is very different from the Dirac loop production function assumed in the one-scale model, where all loops are formed with the same size ( $\ell = \alpha t$ ). This is then adjusted to fit Nambu-Goto numerical simulations. In addition to the scale of gravitational decay  $\gamma_d$ , a new scale is introduced here. As seen before, the gravitational-wave emission back-reacts on the loops. This has the effect to render the string smoother and smoother on the smallest length scales (in particular for any kinks). Therefore loops cannot produce infinitely small loops: gravitational backreaction cuts off loop production below a certain scale  $\gamma_c$  such that [5]:

$$\gamma_c \ll \gamma_d. \quad (5.14)$$

The scale characteristic of gravitational backreaction was estimated [169] to be given by:

$$\gamma_c = \Upsilon(G\mu)^{1+2\chi} \quad \text{with} \quad \begin{cases} \Upsilon \sim 10 \\ \chi = 1 - \frac{P}{2} > 0. \end{cases} \quad (5.15)$$

where  $P$  is given by numerical simulations [166] in radiation and matter era, see Tab. 5.1. We note that very small scales on a string network can potentially be dependent on the value of  $\chi$  which is studied in [170]. In addition, we see that  $\gamma_c$  changes between radiation and matter era.

<sup>5</sup>The consequence of this process for the network and the loops are not well understood and are still being studied [168]

	Radiation	Matter
$P$	$1.6^{+0.21}_{-0.15}$	$1.41^{+0.08}_{-0.07}$
$\mathcal{C}_0$	$0.21^{+0.12}_{-0.13}$	$0.09^{+0.03}_{-0.03}$
$\mathcal{C}$	$\sim 0.08$	$\sim 0.016$

Table 5.1:  $P$ ,  $\mathcal{C}_0$  and  $\mathcal{C}$  factors for  $M=3$ , in the radiation and matter dominated epochs.

The loop distribution is defined on three different domains:

$$\left\{ \begin{array}{ll} \text{(i)} & \gamma \leq \gamma_c \\ \text{(ii)} & \gamma_c \leq \gamma \leq \gamma_d \\ \text{(iii)} & \gamma_d \leq \gamma \leq \gamma_{\max}. \end{array} \right. \quad (5.16)$$

For convenience, the distance to the horizon in term of cosmic time is expressed as:

$$d_h(t) = \frac{t}{1-\nu}, \quad (5.17)$$

where the scale factor is  $a(t) \propto t^\nu$  with  $\nu = 1/2$  in the radiation era and  $\nu = 2/3$  in the matter era. The current approach does not describe the superhorizon loop sizes which are not discernible from long strings. Hence, an upper bound on the accessible range of  $\gamma$  appears. From Eq. 5.17 we have:

$$\gamma_{\max} = \frac{1}{1-\nu}. \quad (5.18)$$

The exact distribution is given in [165]. However, we have worked with the analytic asymptotic loop distribution in the different regimes of loops length assuming the scaling regime is well established. For loops with length scale smaller than the gravitational back-reaction length scale  $\gamma_c$ :

$$\mathcal{F}^{(3)}(\gamma \ll \gamma_c \ll \gamma_d) \simeq \frac{\mathcal{C}(3\nu - 2\chi - 1)}{2 - 2\chi} \frac{1}{\gamma_d} \frac{1}{\gamma_c^P}, \quad (5.19)$$

which is independent of  $\gamma$ . For loops with length scale in the middle range:

$$\mathcal{F}^{(3)}(\gamma_c < \gamma \ll \gamma_d) \simeq \frac{\mathcal{C}(3\nu - 2\chi - 1)}{2 - 2\chi} \frac{1}{\gamma_d} \frac{1}{\gamma^P}. \quad (5.20)$$

And, for loop with length scale large compared to the scale of gravitational decay  $\gamma_d$ :

$$\mathcal{F}^{(3)}(\gamma_d \ll \gamma < \gamma_{\max}) \simeq \frac{\mathcal{C}}{(\gamma + \gamma_d)^{P+1}}. \quad (5.21)$$

Here  $\mathcal{C}$  is given by:

$$\mathcal{C} = \mathcal{C}_0(1 - \nu)^{3-P}. \quad (5.22)$$

Table 5.1 gives the numerical values of  $\mathcal{C}_0$  and  $\mathcal{C}$  for loops produced in radiation and matter era.

The loop distribution is plotted on Fig. 5.4 where we can distinguish the three regimes. We can distinguish the distribution in the matter era and radiation era.

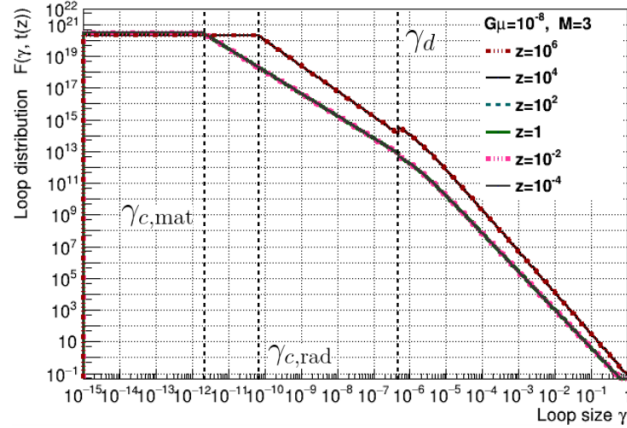


Figure 5.4: Loop size distributions predicted by model  $M=3$ . The loop distribution  $\mathcal{F}(\gamma, t(z))$ , is plotted for different redshift values and fixing  $G\mu = 10^{-8}$ .

For  $\gamma < \gamma_c$  the loop distribution is flat in each era, which reveals that the details on how backreaction smooths the strings is not relevant for the number of loops [165]. By comparison with the other two previous models, the most significant difference is in the very small loop regime ( $\gamma \ll \gamma_c$ ). This model contains many more small loops, due to the inverse power of the gravitational-wave backreaction scale  $\gamma_c$ , which is itself very small. The distributions of the three models can be compared in this regime. We compare the Eq. 5.19 in radiation era with Eq. 5.7 for model 1 and Eq. 5.11 for model 2, in the limit  $\gamma \ll \gamma_c \ll \gamma_d$ . The distribution ratio is then given by:

$$\left. \frac{\mathcal{F}^{(3)}}{\mathcal{F}^{(i)}} \right|_{\gamma \ll \gamma_c}^{i=1,2} \sim k^{(3,i)} \times (G\mu)^{-0.74} \quad \text{with} \quad \begin{cases} k^{(3,1)} \approx 2.2 \times 10^{-2} \\ k^{(3,2)} \approx 2.0 \times 10^{-1} \approx 10 \times k^{(3,1)}. \end{cases} \quad (5.23)$$

For example, if we take  $G\mu = 10^{-8}$ , there are  $\sim 2 \times 10^4$  more very small loops in the radiation era for model  $M=3$  than in model  $M=1$ . The number of very small loops increases even more when  $G\mu$  drops. For  $G\mu = 10^{-13}$ , there are  $\sim 10^8$  more very small loops in the radiation era for model  $M=3$  than in model  $M=1$ . In the next section, we will see that such a high number of small loops in model  $M=3$  will have important consequences in the rate of gravitational-wave events we can detect and on the amplitude of the stochastic gravitational wave background.

## 5.2 The rate of bursts

In this section we derive the expression for the cosmological rate of burst events generated by a cosmic string network [III]. The detection of gravitational waves from cosmic strings is conditioned by this rate, in addition it is also needed to evaluate the upper limits. In the O1 analysis, we set constraints on the string tension  $G\mu$  and the probability of intercommutation  $p$ , since as distinct from the topological strings, when superstrings meet they reconnect with probability  $p < 1$ . However, the dependence on  $p$  of the models is poorly known, so in the O2 analysis we only set upper limits on the string tension.

The rate of gravitational-wave events we expect to detect from a proper volume  $dV(z)$  at redshift  $z$  in an interval of amplitude  $dA_q$  is:

$$\frac{d^2 R_q^{(M)}}{dV(z)dA_q}(A_q, z, f) = \frac{1}{1+z} \nu_q^{(M)}(A_q, z) \Delta_q(A_q, z, f), \quad (5.24)$$

where  $\nu_q^{(M)}(A_q, z)$  represents the number of cusp/kink features per unit space-time volume which produce gravitational waves with amplitudes between  $A_q$  and  $A_q + dA_q$  at redshift  $z$ . The function  $\Delta_q(A_q, z, f)$  is the fraction of gravitational-wave events of amplitude  $A_q$  that are geometrically observable at frequency  $f$  and redshift  $z$ . We have seen that geometrically the radiation from cusps will be in a conic region with half opening angle  $\theta_m$ . The corresponding solid angle is  $\Omega \simeq \pi\theta_m^2$ . Thus the probability that the line of sight is within this solid angle is  $\Omega/4\pi \simeq \theta_m^2/4$ . In contrast, kinks radiate continuously, as kinks travel on a string loop they radiate in a fan-like pattern, therefore  $\Omega \simeq 2\pi\theta_m$ , and the probability of observing a radiation from a kink is then  $\Omega/4\pi \simeq \theta_m/2$ . We then combine the cutoff of large angles and beaming effects to express the fraction of gravitational-wave events that are observable as:

$$\Delta_q(\ell, z, f) \sim \left( \frac{\theta_m(\ell, z, f)}{2} \right)^{3(2-q)} \times \Theta(1 - \theta_m(z, \ell, f)). \quad (5.25)$$

The factor of  $(1+z)^{-1}$  translates the fact that burst coming from large redshift are spaced further apart in time.

We have seen in Sec. 3.2.5, that the fundamental period of oscillation of a loop of length  $\ell$  is  $T = \ell/2$ . We can write the number of cusp/kink features per unit space-time volume on loops with lengths in the interval  $d\ell$  at a redshift  $z$  as:

$$\nu_q^{(M)}(\ell, z)d\ell = \frac{2}{\ell} N_q n^{(M)}(\ell, t(z))d\ell, \quad (5.26)$$

where the superscript (M) stands for the loop distribution model  $M = \{1, 2, 3\}$  described above and we denote by  $N_q$  the number of cusp/kink features per oscillation. We would like to express this quantity in terms of the amplitude  $A_q$ . From the

definition of the amplitude in Eq. 3.117, the change of variables from  $\ell$  to  $A_q$  gives:

$$\ell(A_q, z) = \left( \frac{A_q(\ell, z)(1+z)^{q-1}r(z)}{g_1 G\mu} \right)^{1/2-q} \quad \text{and} \quad \frac{d\ell}{dA_q} = \frac{\ell}{(2-q)A_q}. \quad (5.27)$$

Then we rewrite:

$$\begin{aligned} \nu_q^{(M)}(A_q, z)dA_q &= \nu_q^{(M)}(\ell(A_q, z), z) \frac{d\ell}{dA_q} dA_q \\ &= \nu_q^{(M)}(\ell(A_q, z), z) \frac{\ell(A_q, z)}{(2-q)A_q} dA_q. \end{aligned} \quad (5.28)$$

Finally, the rate given in Eq. 5.24 is reexpressed as:

$$\frac{d^2 R_q^{(M)}}{dz dA_q}(A_q, z, f) = \frac{2N_q H_0^{-3} \varphi_V(z)}{(2-q)(1+z)A_q t^4(z)} \times \mathcal{F}^{(M)}\left(\frac{\ell(A_q, z)}{t(z)}, t(z)\right) \times \Delta_q(A_q, z, f), \quad (5.29)$$

where we injected the loop distribution  $\mathcal{F}^{(M)}$ . The proper volume is expressed as a function of the the interpolating function  $dV(z) = \varphi_V \times H_0^{-3} dz$  given in Eq. 3.25. Since the gravitational-wave detectors are sensible to the strain amplitude using the frequency-domain waveform in Eq. 3.117, the rate can also be written as:

$$\frac{d^2 R_q^{(M)}}{dz dh}(h, z, f) = \frac{2N_q H_0^{-3} \varphi_V(z)}{(2-q)(1+z)h t^4(z)} \times \mathcal{F}^{(M)}\left(\frac{\ell(h f^q, z)}{t(z)}, t(z)\right) \times \Delta_q(h f^q, z, f). \quad (5.30)$$

The rate of gravitational waves produced by cusps or kinks given in Eq. 5.30 is marginalized over the strain amplitude and the redshift. Therefore, we consider a wide enough  $(z, h)$  parameter space to ensure a full integration. We consider a range from  $z_{\min} = 10^{-12}$  to  $z_{\max} = 10^{32}$ , at which we reach the Planck scale. The gravitational-wave rate is limited by two physical conditions, which set the integration limits. The gravitational waves emitted by cusp/kink features are beamed and the maximal gravitational-wave beam opening angle must satisfy:  $\theta_m < 1$ , see Sec. 3.3. In addition, the relative size of cosmic string loops can not exceed a maximal value given for each loop distribution model:  $\gamma < \gamma_{\max}$ . By using Eq. 3.117 and Eq. 3.118 we turn these two constraints into conditions on the strain amplitude:

$$\begin{cases} \theta_m < 1 & \Rightarrow h(z) > h_{\min}(z) \equiv \frac{g_1}{(g_2)^{2-q}} \frac{G\mu H_0}{f^2(1+z)\varphi_r(z)} \\ \gamma < \gamma_{\max} & \Rightarrow h(z) < h_{\max}(z) \equiv g_1 \frac{G\mu(\gamma_{\max}\varphi_t(z))^{2-q}}{f^q(1+z)^{q-1}\varphi_r(z)H_0^{q+1}}. \end{cases} \quad (5.31)$$

Given these conditions, we perform the strain amplitude integration before the redshift integration:

$$R_q^M = \int_{z_{\min}}^{z_{\max}} dz \int_{h_{\min}(z)}^{h_{\max}(z)} dh \frac{d^2 R_q^M}{dz dh}(h, z, f). \quad (5.32)$$

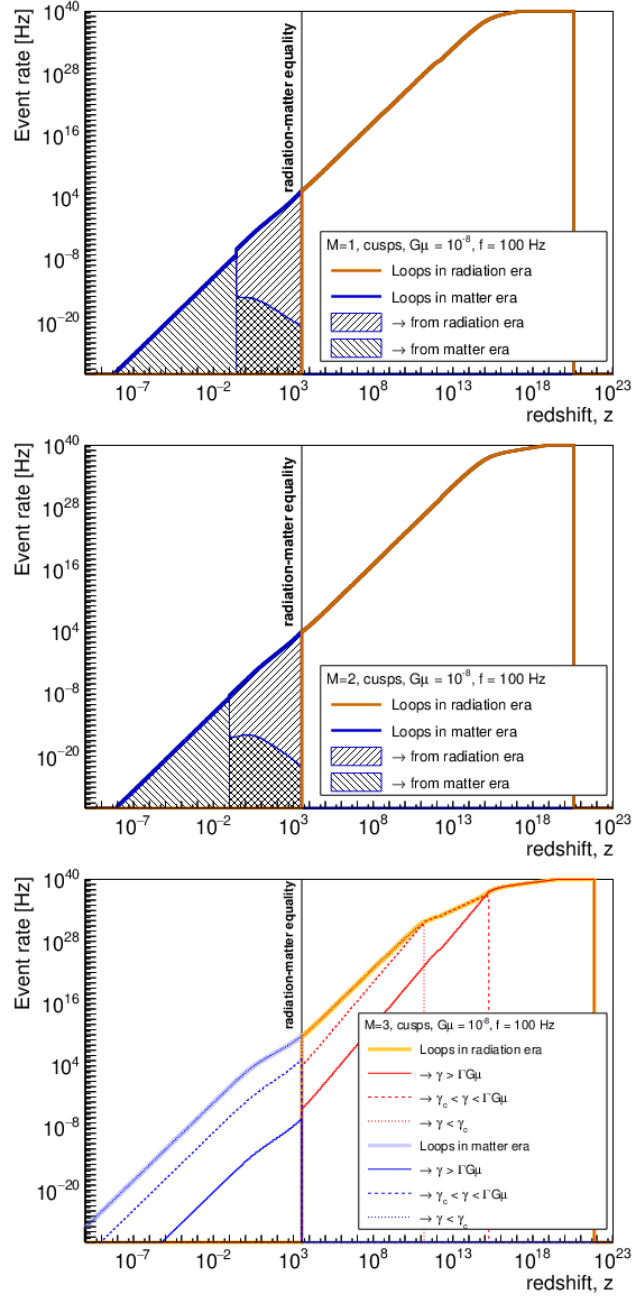


Figure 5.5: Gravitational-wave event rate from cusps  $R_{\text{cusps}}^{(M)}$  as a function of the redshift  $z$  given by Eq. 5.30, predicted by models  $M = 1$  (top row),  $M = 2$  (middle row) and  $M = 3$  (bottom row) for  $G\mu = 10^{-8}$  and  $f = 100$  Hz. For each model we show the contribution from loops in the radiation era and in the matter era. We separate the two contributions for loops in matter era for model  $M = 1$  and  $M = 2$ : relics of loops produced in radiation era and loops produced in matter era. The effect of the three loop size regimes presented in section 5.1.4 are also separated, for model  $M=3$ . Figure taken from [144].

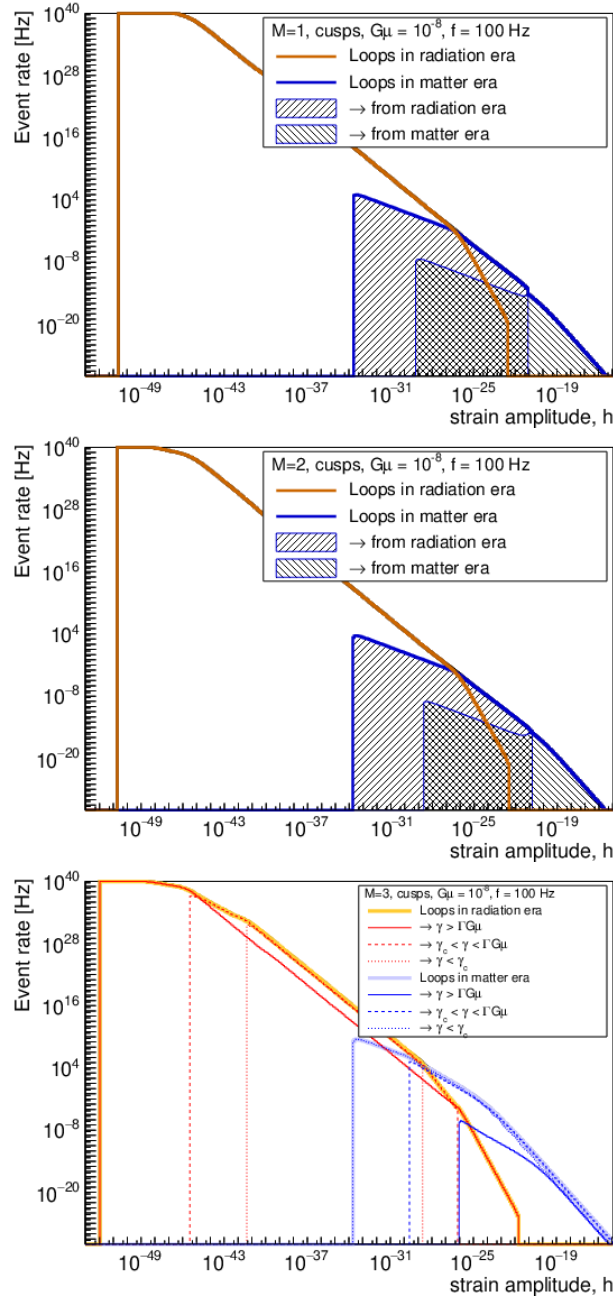


Figure 5.6: Gravitational-wave event rate from cusps  $R_{\text{cusps}}^{(M)}$  as a function of the strain amplitude  $h$  predicted by models  $M = 1$  (top row),  $M = 2$  (middle row) and  $M = 3$  (bottom row) for  $G\mu = 10^{-8}$  and  $f = 100$  Hz. For each model we show the contribution from loops in the radiation era and in the matter era. We separate the two contributions for loops in matter era for model  $M = 1$  and  $M = 2$ : relics of loops produced in radiation era and loops produced in matter era. The effect of the three loop size regimes presented in section. 5.1.4 are also separated, for model  $M=3$ . Figure taken from [144].

Since each integral cover a wide range of redshift and strain amplitude, we perform a logarithmic integral using 500 bins for each variable.

Figure 5.5 shows the gravitational-wave rate produced by one cusp ( $N_{\text{cusp}} = 1$ ), predicted for a loop distribution model  $M = \{1, 2, 3\}$ , marginalized over the strain amplitude  $h$ , in a ring of width  $\Delta_z(z)$  at redshift  $z$  (the redshift bin width) at a typical LIGO-Virgo frequency  $f = 100$  Hz, and fixing  $G\mu = 10^{-8}$ :

$$R_{\text{cusps}}^M(z) = \Delta_z(z) \int_{h_{\min}(z)}^{h_{\max}(z)} dh \frac{d^2 R_{\text{cusps}}^M}{dz dh}(h, z, f = 100 \text{ Hz}). \quad (5.33)$$

Similarly, Fig 5.6 shows the the gravitational-wave rate produced at strain amplitude  $h$ :

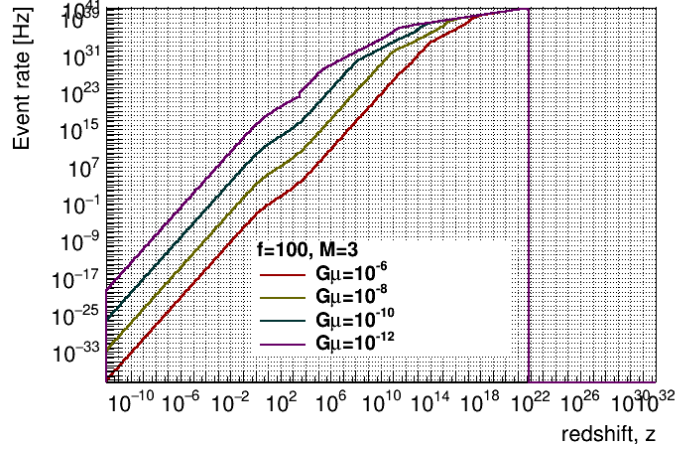
$$R_{\text{cusps}}^M(h) = \Delta_h(h) \int_{z_{\min}}^{z_{\max}} dz \frac{d^2 R_{\text{cusps}}^M}{dz dh}(h, z, f = 100 \text{ Hz}), \quad (5.34)$$

with  $\Delta_h(h)$  is the strain amplitude bin width at strain amplitude  $h$ .

We separate the contribution from loops in the matter era (blue) and in the radiation era (red/yellow). First observation, all models present the same general behaviour on redshift and strain amplitude. Gravitational waves with high amplitude are produced in the matter era with a low rate, while gravitational waves with low amplitude are produced in the radiation era with a high rate. The redshift cannot be arbitrarily large, and the strain amplitude arbitrarily small because the loop size is limited:  $\gamma < \gamma_{\max}$ . We also note the discontinuities due to the Heavside functions in the loop distributions for model 1 and 2. At  $f = 100$  Hz ground-based gravitational wave detectors are typically sensitive to strain amplitude  $h \sim 10^{-23}$ , where we see that the burst search is expected to be sensitive to loops in matter era but produced in radiation era. Indeed, the size of loops produced in the radiation era decreases over time and for small loops the beaming angle is larger, thus the probability detection increases. We can compare the rate given by Eq. 5.33 by fixing the strain amplitude:

$$\frac{R_{\text{cusps}}^1(h = 10^{-23})}{R_{\text{cusps}}^2(h = 10^{-23})} = \frac{1.1 \times 10^{-9}}{1.2 \times 10^{-10}} \approx 10 \quad \text{and} \quad \frac{R_{\text{cusps}}^3(h = 10^{-23})}{R_{\text{cusps}}^1(h = 10^{-23})} = \frac{1.0 \times 10^{-6}}{1.1 \times 10^{-9}} \approx 10^3. \quad (5.35)$$

For model 1 and model 2 the difference in the rate verifies the ratio between the normalization factors  $\mathcal{C}_{\text{rad}}^{(1)}/\mathcal{C}_{\text{rad}}^{(2)} \approx 10$ . While for model 3, the rate at this strain amplitude is dominated by small loops which are much more abundant than in the other two models. The gravitational-wave rate in Eq. 5.30 depends implicitly of the string tension in the loop distribution function  $\mathcal{F}$  and in the integration limits given by Eq. 5.31. Figure 5.7 shows the dependence on  $G\mu$  for the gravitational-wave rate for cusps for models  $M=3$ .


 Figure 5.7: Gravitational-wave event rate predicted by models  $M = 3$  for  $f = 100$  Hz.

### 5.3 Stochastic gravitational-wave background

A stochastic background of gravitational waves is a gravitational-wave signal produced by a large number of weak, independent, and unresolved sources, see Sec. [1.5](#). Cosmic strings produce a stochastic background of gravitational waves, whose spectrum is usually defined by the dimensionless quantity:

$$\Omega_{\text{GW}}(t_0, f) = \frac{f}{\rho_c} \frac{d\rho_{\text{GW}}}{df}(t_0, f). \quad (5.36)$$

Here,  $d\rho_{\text{GW}}$  is the energy density of gravitational waves in the frequency range  $f$  to  $f + df$  observed today at  $t = t_0$ , and  $\rho_c$  is the critical energy density of the Universe, i.e. the energy required for a spatially flat Universe. From [\[171, 172\]](#), the gravitational wave energy density is given by

$$\Omega_{\text{GW}}(f; G\mu, p) = \frac{4\pi^2}{3H_0^2} f^3 \int_0^{h^*} h^2 dh \times \int_0^{+\infty} dz \frac{d^2 R^{(M)}}{dz dh}(h, z, f; G\mu, p). \quad (5.37)$$

where it is computed for a specific choice of free parameters  $G\mu$  and  $p$ .

The stochastic background generated by a network of cosmic strings includes powerful events which occur infrequently, sometimes referred to as ‘‘popcorn-like’’ [\[173\]](#). These events are characterized by a rate of occurrence that is lower than the signal frequency. Since these events are observed as individually separable bursts they should not be counted within the computation of  $\Omega_{\text{GW}}(f)$  [\[109\]](#). Therefore, following [\[172\]](#), this condition on the rate can be implemented by a cutoff on the strain amplitude  $h^*$ , defined as:

$$\int_{h^*}^{\infty} dh \int_0^{+\infty} dz \frac{d^2 R^{(M)}}{dz dh}(h, z, f) = f. \quad (5.38)$$

This equation is solved for  $h^*$  and used to exclude rare events using the integration in Eq. [5.37](#). This procedure removes large amplitude events (those with strain  $h > h^*$ )

that occur at a rate smaller than  $f$ .

Figure 5.8 shows  $h^*$  as a function of the frequency, for the different loop distribution models considered. At a typical LIGO-Virgo frequency  $f = 100$  Hz, the spectrum originates from gravitational-waves with strain amplitude below  $h^* \sim 10^{-28}$ . In the

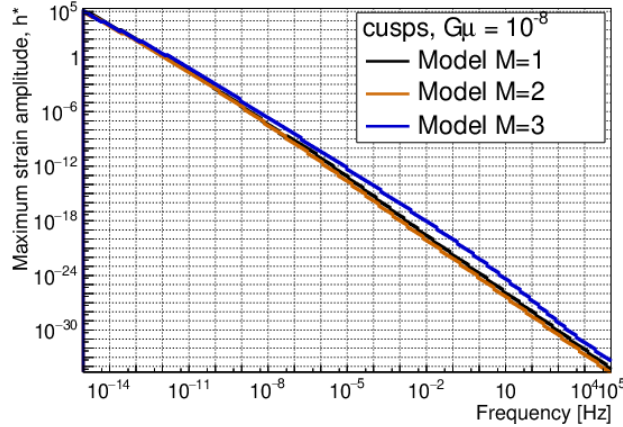


Figure 5.8: Maximum strain amplitude  $h^*$  used to compute the gravitational wave energy density  $\Omega_{GW}^{(M)}(f)$ .

frequency range of the LIGO-Virgo detector, the maximal strain amplitude  $h^*$  does not change a lot when varying  $G\mu$  as shown on Fig. 5.9 with for example model  $M=3$ . At low frequency the values of the strain amplitude  $h^*$  are not physical. However

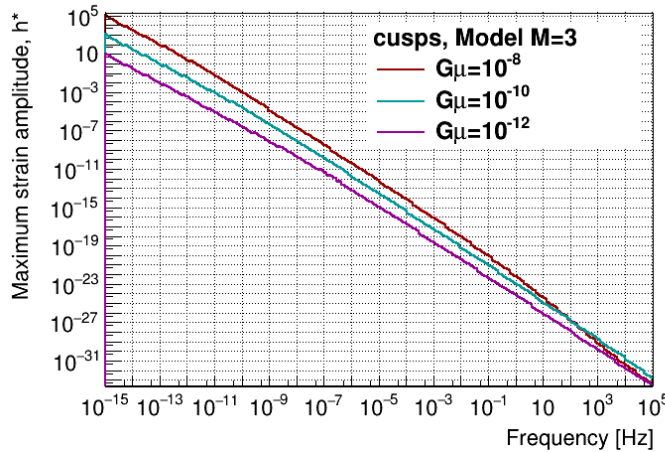


Figure 5.9: Maximum strain amplitude  $h^*$  used to compute the gravitational wave energy density  $\Omega_{GW}^{(M)}(f)$  for model  $M=3$  and for different values of  $G\mu$ .

we found that removing the rare burst has no significant effect on the predicted gravitational-wave energy density  $\Omega_{GW}^{(M)}(f)$  and so the integration could also be done

with  $h^* \rightarrow +\infty$ .

The total stochastic gravitational wave spectrum is given by the superposition of unresolved signals from cusps and kinks, and so the total energy density is given by adding both contributions. Figure 5.10 compares the spectrum for the three models, adding both the kink and the cusp contribution for  $G\mu = 10^{-8}$ . At very high fre-

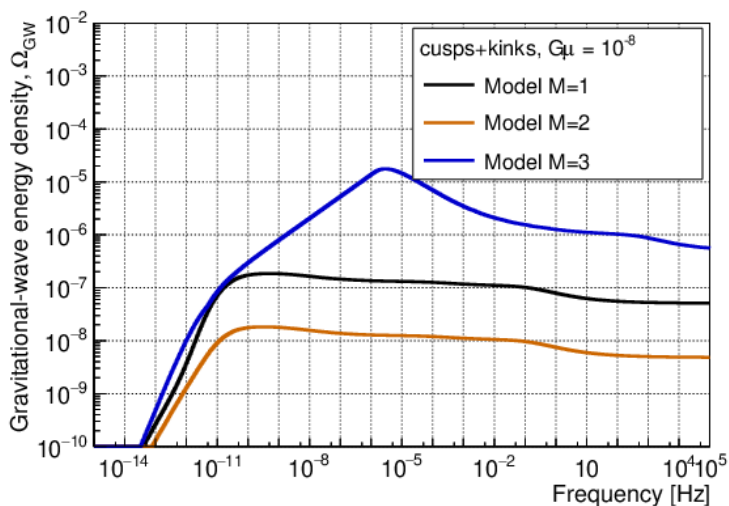


Figure 5.10: Gravitational wave energy density  $\Omega_{GW}^{(M)}(f)$  from cusps and kinks predicted by the three loop distribution models for  $G\mu = 10^{-8}$ .

quency, the gravitational wave energy density spectrum  $\Omega_{GW}^{(M)}(f)$  is flat, i.e. frequency independent for each model. For model M=1 and M=2 the value of the plateau only depends on two quantities: the string tension  $G\mu$  and the radiative efficiency coefficient  $\Gamma$  [174]. The bump in the spectrum is dominated by matter era loops, for the string tension considered  $G\mu = 10^{-8}$  [6]. Another feature observable here is the variation in the number of relativistic degrees of freedom described by the function  $\mathcal{G}(z)$  (see Sec. 3.3) in the radiation era, which produces smooth variations in the spectrum at high frequency [175, 174]. The spectrum predicted by the model M=3 has a different shape than those of models M=1 and M=2. The spectrum  $\Omega_{GW}^{(3)}(f)$  exhibits a knee followed by a maximum. These two features in the spectrum correspond to the change of behaviour of the loop distribution at  $\gamma = \gamma_d$  (knee) and  $\gamma = \gamma_c$  (peak) [175].

Comparing models M=1 and M=2, we note that the spectrum predicted by model M=2 is about 10 times weaker than that predicted by model M=1. Figure 5.11 presents the different contributions to the gravitational wave energy density spectrum  $\Omega_{GW}^{(M)}(f)$  predicted by model M=1. The distribution is clearly dominated by the contribution of loops in the radiation era for most of the frequency range. Therefore, the difference can be attributed to the ratio of the normalization factors  $\mathcal{C}_{\text{rad}}^{(1)}/\mathcal{C}_{\text{rad}}^{(2)} \simeq$

<sup>6</sup>This is no longer true when considering too small values of  $G\mu$  [175].

10, calculated in Sec. 5.1.3.

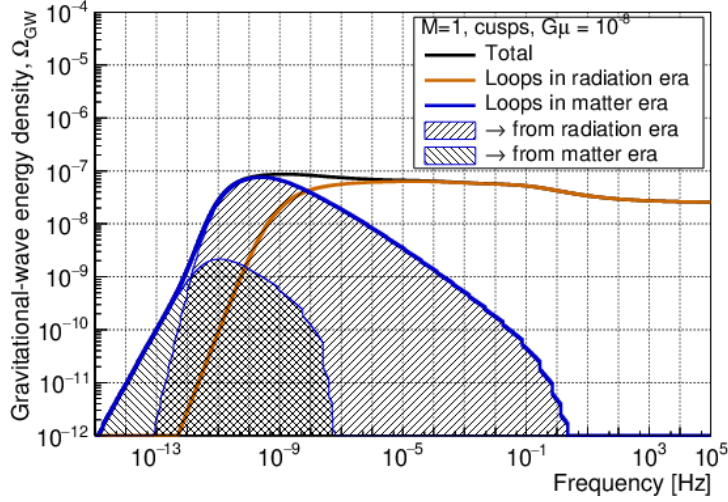


Figure 5.11: Gravitational wave energy density  $\Omega_{GW}^{(M)}(f)$  from cusps predicted by the loop distribution model  $M=1$  for  $G\mu = 10^{-8}$ . The contributions from loops in the radiation ( $z > 3366$ ) and matter ( $z < 3366$ ) eras are separated. In addition, we also show for loop in the matter era, the effect of loops produced in the matter era and the ones produced in the radiation era.

The spectrum predicted by model  $M=3$  is larger than those of models  $M=1$  and  $M=2$ . Figure 5.12 shows the contribution of the different loop length regime to the energy density  $\Omega_{GW}^{(M)}(f)$  in the radiation era and in the matter era, given by model  $M=3$ . In both cosmological epoch, the very small loops contribute significantly to the spectrum. This explains why this model predict the largest gravitational-wave energy density  $\Omega_{GW}^{(M)}(f)$ .

Burst and stochastic searches are sensitive to different types of loops. Stochastic search is sensitive to loops formed in the radiation era, while burst search is sensitive to loops formed in the material era. Thus these two searches are complementary, in the sense that they probe different parts of the redshift distribution. We will see in the next section, how these differences are reflected on the constraints of the parameter space.

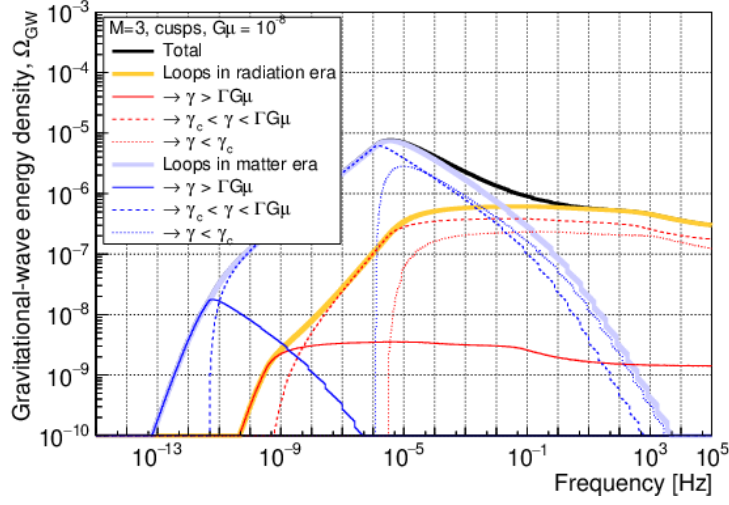


Figure 5.12: Gravitational wave energy density  $\Omega_{\text{GW}}^{(M)}(f)$  from cusps predicted by the loop distribution model  $M=3$  for  $G\mu = 10^{-8}$ . The contributions from loops in the radiation ( $z > 3366$ ) and matter ( $z < 3366$ ) eras are separated.

## 5.4 Results

No gravitational waves produced by cosmic strings was identified in the LIGO-Virgo O1/O2 burst search. However, we can use the detection efficiency estimation to constrain the string tension  $G\mu$  for topological strings, and the intercommutation probability ( $p < 1$ ) for superstrings. The general idea is to scan the two-dimensional parameter space for a given loop distribution model  $M$ , of the dimensionless string tension  $G\mu$  ( $10^{-12} < G\mu < 10^{-6}$ ), and the intercommutation probability  $p$  ( $10^{-3} < p < 1$ ). For each point in this parameter space, we compute the effective rate  $\mathcal{R}_{\text{eff},q}^{(M)}$ . It represents the rate of detectable events in the burst search, which is obtained by convolving the detection efficiency curve with the cosmic string rate given by Eq. 5.29. Then the parameter space is ruled out at 95% level when the effective rate exceeds the expected rate from a Poisson process over an observation time  $T_{\text{obs}}$ . In parallel, for each point in this parameter space, we calculate the predicted gravitational-wave energy density  $\Omega_{\text{GW}}^{(M)}$  and compare it to the stochastic gravitational-wave spectrum predicted by the different and complementary observations: LIGO-Virgo stochastic search, pulsar timing arrays (PTA), big bang nucleosynthesis (BBN), and cosmic microwave background (CMB).

## 5.4.1 Constraints

### 5.4.1.1 LIGO-Virgo measurements

The effective detection rate defined for a loop distribution model M is given by:

$$\mathcal{R}_{\text{eff},q}^{(M)}(G\mu, p) = \int_0^{+\infty} dA_q e_q(A_q) \times \int_0^{+\infty} dz \frac{d^2 R_q^{(M)}}{dz dA_q}(A_q, z, f^*; G\mu, p). \quad (5.39)$$

Here  $e_q(A_q)$  is the detection efficiency to cusp/kink gravitational wave events, which is estimated by injecting simulated signals of known amplitude  $A_q$  in the data, as described in Sec. 4.7.2. The detection efficiency is measured as the fraction of simulated signals recovered with  $\Lambda > \Lambda_h$ , where  $\Lambda_h$  is the ranking statistic value associated to the loudest event of the search, see Sec. 4.9 and Sec. 4.10. The predicted detection rate is given by Eq. 5.29. The frequency  $f^* = 30$  Hz, is the lowest high-frequency cutoff used in the search template bank, see Sec. 4.4.2. This frequency provides the maximum angle between the line of sight and the cusp/kink on the loop, as shown in Sec. 3.3. We can compute upper limits based on the loudest observed event following the method described in 176. If we assume that the cosmic string burst events are Poisson distributed, the probability that no events have been detected by the burst pipeline with a ranking statistic  $\Lambda > \Lambda_h$ , in an observation time  $T_{\text{obs}}$  is 177:

$$P = \exp\left(-T_{\text{obs}} \times \mathcal{R}_{\text{eff},q}^{(M)}\right). \quad (5.40)$$

Therefore, the probability  $\eta$  that at least one event with  $\Lambda > \Lambda_h$  shows up is  $\eta = 1 - P$ . Then if  $\eta = 0.95$ , 95% of the time we would have expected to detect an event with  $\Lambda > \Lambda_h$ . The rate expected from a random Poisson process with  $\eta = 0.95$  over an observation time  $T_{\text{obs}}$  is:

$$\mathcal{R}_{\text{eff}}^{(M)} \Big|_{95\%} \simeq \frac{2.996}{T_{\text{obs}}}. \quad (5.41)$$

We scan the parameter space of model M of the dimensionless string tension  $G\mu$  ( $10^{-12} < G\mu < 10^{-6}$ ), and the intercommutation probability  $p$  ( $10^{-3} < p < 1$ ), and we say that the parameter space is excluded at 95% confidence level when the effective detection rate  $\mathcal{R}_{\text{eff},q}^{(M)}$  exceeds  $\mathcal{R}_{\text{eff}}^{(M)} \Big|_{95\%}$ . For example, if we take the observation time of O1 run,  $1/T_{\text{obs},\text{O1}} = 2.40 \times 10^{-7}$  Hz, our upper limit statement becomes  $\mathcal{R}_{\text{eff},q}^{(M)}(G\mu, p) > 7.2 \times 10^{-7}$  Hz.

Similarly for the stochastic search, the cosmic string parameter space  $(G\mu, p)$  is scanned and for each point in this parameter space, the gravitational wave energy density  $\Omega_{\text{GW}}^{(M)}(f_i; G\mu, p)$ , in the frequency bin  $f_i$ , is computed for a loop distribution model M. Frequency-dependent upper limits on the energy density  $\Omega_{\text{GW}}(f)$  are given by the stochastic gravitational-wave background search using the data of the initial LIGO and Virgo detectors 177 (science run S6), the first observing run O1 178 and the second observing run O2 147 of the Advanced LIGO and Advanced Virgo

detectors. To interpret these limits into constraints on cosmic string parameters, we use a likelihood function defined as:

$$\ln L(G\mu, p) \propto \sum_i \frac{-\left(Y(f_i) - \Omega_{\text{GW}}^{(\text{M})}(f_i; G\mu, p)\right)^2}{\sigma^2(f_i)}. \quad (5.42)$$

Here,  $Y(f_i)$  represents the expectation value of the cross-correlated detector data in each frequency bin, i.e. the measurement of the gravitational-wave energy density (cf. Sec. 1.5) and  $\sigma(f_i)$  is the standard deviation, i.e. the associated uncertainty. The likelihood function is the probability of the measurement of the gravitational-wave energy density  $Y(f_i)$ , given the the gravitational wave energy density predicted by the model. This function is evaluated at each point of the parameter space, and a 95% confidence contours is computed by maximizing  $\ln L(G\mu, p)$ . In addition, it is also possible to compute the upper limit on  $\Omega_{\text{GW}}(f)$  at design sensitivity for the Advanced LIGO and Advanced Virgo detectors.

#### 5.4.1.2 Other experiments

The stochastic background of gravitational waves is expected to imprint on the arrival time of pulses from the most stable millisecond pulsars. The basic idea behind Pulsar Timing Arrays (PTAs) is that, when a gravitational wave travels through space between the source and the observer it creates space-time perturbations that manifest as anomalies in the observed periodicity of the source. This principle can be used to search for gravitational-waves of large period. Here again, the bounds on the energy density apply in a specific frequency band at nanohertz frequencies. We use the results from the Parkes Pulsar Timing Array (PPTA) measurements [179, 180]:

$$\Omega_{\text{GW}}^{\text{PTA}}(f = 2.8 \times 10^{-9} \text{Hz}) < 2.3 \times 10^{-10} \quad (5.43)$$

The spectra predicted by the three loop distributions  $\Omega_{\text{GW}}^{(\text{M})}(f; G\mu, p)$  models is compared to this bound, to obtain constraints on the cosmic string parameter space.

In addition, two others limits on the total energy density of gravitational waves  $\Omega_{\text{GW}}(f)$  are derived with the Big-Bang Nucleosynthesis (BBN) and the Cosmic Microwave Background (CMB) observations. These bounds are said indirect, because they are upper limits for the integral of  $\Omega_{\text{GW}}(f)$ . The abundances of the lightest nuclei can be used to set constraints on the expansion rate of the Universe. This is done by constraining the effective number of degrees of freedom  $N_{\text{eff}}$  at the time of the BBN. Under the assumption that only photons and neutrinos contribute to the radiation energy density,  $N_{\text{eff}}$  is equal to the effective number of neutrino species during nucleosynthesis, corrected by a residual heating of the neutrino fluid due to electron-positron annihilation:  $N_{\text{eff}} \simeq 3.046$  [181]. Any deviation from this value can be attributed to an additional relativistic radiation, e.g. gravitational waves produced by cosmic string cusps or kinks generated before the BBN. The Big

Bang nucleosynthesis constraints provide an upper limit on the energy density of gravitational-wave given by:

$$\Omega_{\text{GW}}^{\text{BBN}}(G\mu, p) = \int_{10^{-10}\text{Hz}}^{10^{10}\text{Hz}} \Omega_{\text{GW}}^{(\text{M})}(f; G\mu, p) < 1.75 \times 10^{-5}. \quad (5.44)$$

Here, the lower bound on the integrated frequency region is determined by the size of the horizon at the time of the BBN [73]. The range of the redshift in Eq. 5.37 must be chosen properly for each measurement. For BBN bounds, the integration is performed for  $z > z_{\text{BBN}} = 5.5 \times 10^9$ , since we consider kinks and cusps generated before BBN. The presence of gravitational waves at the time of photon decoupling could alter the observed CMB. Similarly to the BBN bounds, the total energy density of gravitational waves at the time of the decoupling is [182]:

$$\Omega_{\text{GW}}^{\text{CMB}}(G\mu, p) = \int_{10^{-15}\text{Hz}}^{10^{10}\text{Hz}} \Omega_{\text{GW}}^{(\text{M})}(f; G\mu, p) < 3.7 \times 10^{-6}. \quad (5.45)$$

Once again, the lower bound on the integrated frequency region is determined by the size of the horizon at the time of decoupling. The integration of Eq. 5.37 is performed for  $z > z_{\text{CMB}} = 1089$ .

#### 5.4.2 O1/O2 results

Here we first present the constraints on the dimensionless string tension  $G\mu$  and the intercommutation probability  $p$  for the three cosmic string loop distribution models under consideration, using the data from the first observing run of Advanced LIGO detectors. The three models were developed for  $p = 1$ , for smaller intercommutation probability  $p$  we use a dependence  $1/p$  for the loop distributions presented in Sec. 5.1. Table 5.2 summarizes the different observations included in this work and specifies their frequency band and the type of loops to which they are sensitive. Figure 5.13 shows the excluded regions in the parameter space for  $M = \{1, 2, 3\}$ , based on the O1 LIGO burst and stochastic observational constraints. In addition to LIGO results, we also present the limits from PTA measurements and indirect limits from BBN and CMB.

Experiment	Frequency band	Type of loops
LIGO-Virgo burst	10-10 <sup>3</sup> Hz	Present in matter era but produced in radiation era.
LIGO-Virgo stochastic	10-10 <sup>3</sup> Hz	Present in radiation era.
PTA	1-10 <sup>3</sup> nHz	Present in matter era but produced in radiation era.
CMB	integrated	Present in radiation era.
BBN	integrated	Present in radiation era.

Table 5.2: Experiments used to derive the constraints on  $G\mu$  and  $p$  presented in [144] for the three loop distribution models considered  $M = \{1, 2, 3\}$ . In addition the frequency range of each experiment is given which informs us of the type of loops these experiences are likely to constrain.

For model  $M=1$ , the O1 LIGO burst search can not access to topological strings, i.e. strings with a probability of intercommutation  $p = 1$ . However, for superstrings  $p < 1$ , the loop distribution is larger and therefore the rate predicted by this model increases. Thus, the burst search is able to constrain this class of strings. Tighter constraints are obtained when probing the stochastic background of gravitational waves produced by cosmic strings. For this model, the topological strings are constrained by  $G\mu < 5 \times 10^{-8}$  by the O1 LIGO stochastic analysis. Indeed, we have seen that the LIGO stochastic search is sensitive to loops created in the radiation era for which the rate is much higher, than the loops present in the matter era, to which the burst search is sensitive. The indirect limits from CMB measurements are more restrictive than the one produced by the BBN measurements. This difference can be associated to the range of the redshift integral in Eq. 5.37: the integral is performed over a smaller interval in the case of BBN. Constraints from the pulsar timing array are the most competitive. For topological strings we get, the PTA bounds provide  $G\mu < 3.8 \times 10^{-12}$ . At nanohertz frequency, the PTA experiments are sensitive to loops produced in the matter where the gravitational wave energy density  $\Omega_{\text{GW}}^{(1)}(f)$ , reaches its maximum, cf. Fig. 5.11. The different experiment are complementary as they probe different regions of the loop distributions.

For model  $M=2$ , the cosmic string loop distribution model predicts a smaller density of loops and the LIGO constraints are therefore less strict. Thus, the O1 LIGO burst is still not able to put constraints on the string tension  $G\mu$  for topological strings. Assuming  $p = 1$ , the constraints is  $G\mu < 7 \times 10^{-7}$  for the indirect CMB bound, and  $G\mu < 1.5 \times 10^{-11}$  for the PTA measurements.

The last model,  $M=3$ , is the one that predicts the largest loop distribution for very small loops. As we have seen, for small loops the gravitational-wave detection rate for cusps and kinks is higher since the angle subtended by the line of sight and the cusp/kink is larger. Consequently, the parameter space studied here is almost entirely excluded by the LIGO stochastic O1 analysis. The PTA bounds also almost exclude all the region of the parameter space studied here, with  $G\mu < 5.7 \times 10^{-12}$  for

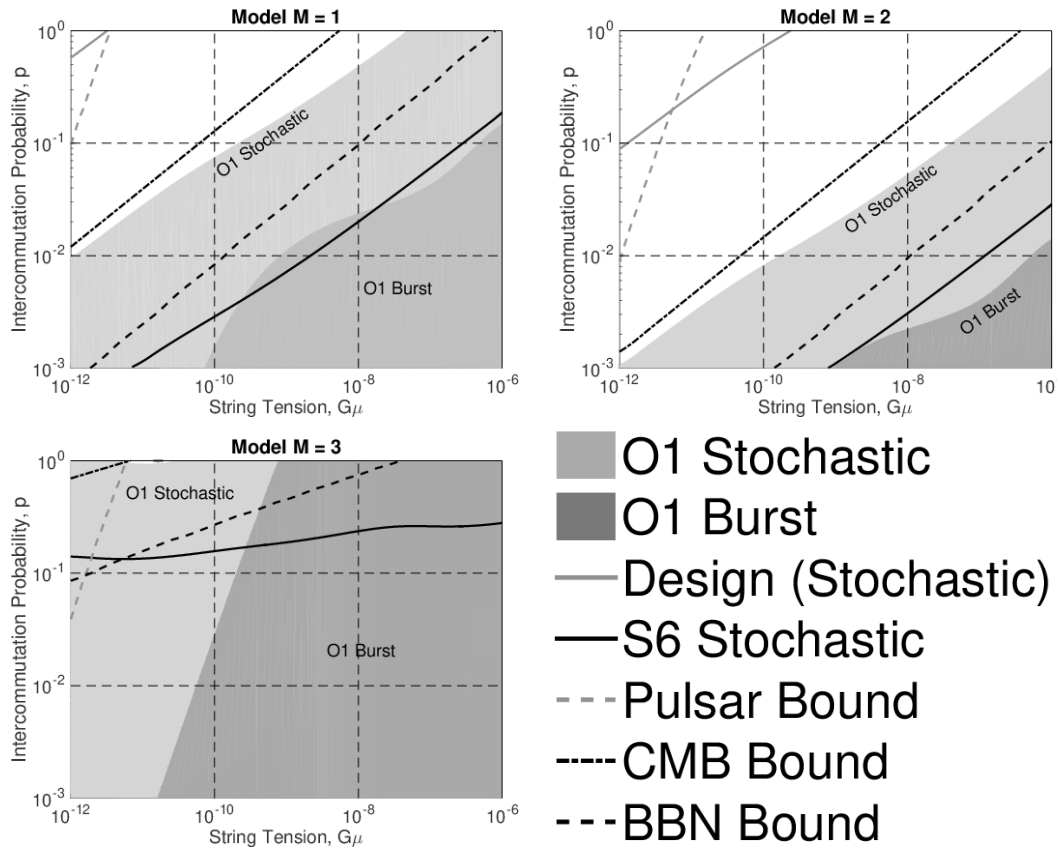


Figure 5.13: 95% confidence exclusion regions are shown for the three loop distribution models:  $M=1$  (top-left),  $M=2$  (top-right) and  $M=3$  (bottom-left). The regions excluded by the O1 LIGO burst and stochastic measurements are represented by shaded regions. To compare, the bounds from the previous LIGO-Virgo stochastic measurements (S6 science run) are also shown (solid black line). In addition, the bounds expected with an Advanced LIGO-Virgo detector network at design sensitivity are reported (solid grey line). Limits obtained directly with PTA measurements and indirectly with BBN and CMB measurements are represented by dotted line. The excluded regions are below the respective curves. Figure taken from. [144].

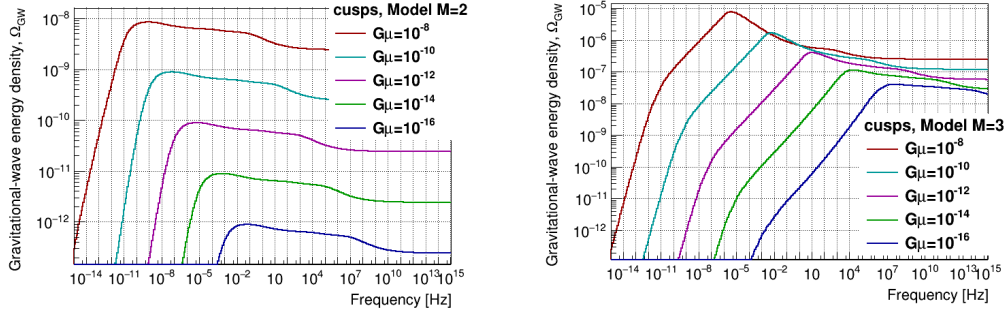


Figure 5.14: Gravitational wave energy density  $\Omega_{GW}^{(M)}(f)$  from cusps predicted by the loop distribution model M=2 and M=3 for different values of  $G\mu$ .

topological strings. The O1 LIGO burst constraint, although weaker, complements that result since the burst analysis is sensitive to gravitational waves produced in the matter era ( $z < 3300$ ). These gravitational wave bursts originate from small loops which used to be large when formed in radiation era. For this model and  $p = 1$ , the burst search constraints is  $G\mu < 8.5 \times 10^{-10}$  at 95% confidence level.

In O2 analysis, the sensitivity of this run being slightly better than that of O1 we combine the burst detection efficiencies, see Sec. 4.10. This time we consider only topological strings, because the dependence of models with the intercommutation probability is poorly known. In addition, similarly with O2 LIGO stochastic search, burst search consider only models M=2 and M=3, since model M=1 presented here, makes too simple assumptions to describe in a realistic way the loop distribution. As in O1, the burst search is not able to set constraints for M=2 since the predicted rate is too low at LIGO-Virgo frequencies. However, we update the upper limit on the string tension for model M=3 with  $G\mu < 4.2 \times 10^{-10}$  [146]. This O1+O2 upper limit has improved by a factor  $\sim 2$  with respect to the previous limit obtained with O1 data alone. Concurrently, the LIGO stochastic O2 analysis constrains these models with  $G\mu < 1.1 \times 10^{-6}$  and  $G\mu < 2.1 \times 10^{-14}$ , respectively for model M=2 and M=3 [147]. The O1+O2 LIGO stochastic limit obtained for model M=3 is stronger than that derived with PTA measurements.

The constraints on the cosmic string tension are tightening to very low  $G\mu$  values. In the near future, even if the next round of pulsar timing observations could improve the constraints on  $G\mu$ , it is not expected to be the most competitive bounds. Indeed, at lower  $G\mu$  values the gravitational-wave energy density peak shifts to high frequencies as observed on Fig. 5.16, which are out of reach of PTA experiments [174]. Furthermore, the indirect limits from BBN and CMB data will also be limited by the precision on the  $N_{\text{eff}}$  parameter which can be achieved. However the sensitivity of Advanced LIGO and Advanced Virgo will improve in the coming years. Figure 5.13 also shows the upper limits the stochastic search would achieve with an Advanced

LIGO-Virgo detector network working at design sensitivity. This bound is expected to surpass all the current bounds used in this work.

## 5.5 Searching for kink-kink collisions

In this section we present a preliminary work. When the number of kinks on a loop increases, two kinks can meet and produce a gravitational-wave burst. We study the impact of this new waveform on the burst and stochastic search. In the future, it can be used to set constraints on a new parameter space  $(G\mu, N_k)$ , where  $N_k$  is the number of kinks on a loop.

### 5.5.1 Burst search

So far we have only considered gravitational-wave bursts generated by single cusp/kink features. We have seen in Sec 3.2.6 that kinks can be created during string intercommutation by pairs. So, when the number of kinks per loop oscillation is  $N_k \geq 2$ , two kinks can meet, producing a gravitational-wave burst. In addition, other mechanisms may lead to the proliferation of kinks on a loop, for example the existence of junctions between strings [183, 184, 185] (cf. Sec 3.2.6). The waveform from this type of burst was given in Sec 3.3:

$$h(\ell, z, f) = A(z)_{q=2} f^{-q} \Theta(f_h - f) \Theta(f - f_\ell), \quad (5.46)$$

where in particular, we note that the amplitude of such a burst is independent of the loop size  $\ell$ :

$$A(z)_{q=2} = g_1 \frac{G\mu}{(1+z)r(z)}. \quad (5.47)$$

The dependency in  $\ell$ , the loop size, has disappeared in comparison with the predicted gravitational-wave amplitude produced by a cusp/kink. As mentioned above, cusps and kinks emit beamed gravitational-wave meaning, that the waveform is only valid for directions near the cusp or kink direction, and is cutoff for angle larger than the maximal gravitational-wave beam opening angle  $\theta_m$ . In contrast the emission at a kink-kink collision is isotropic.

This waveform has been added to the burst pipeline described in Sec 4. We then conducted an analysis using the data from the first and second observing run of Advanced LIGO and Advanced Virgo. We only analyzed the shifted data (close box analysis), since the purpose of this work, is simply to estimate the search efficiency curve as a function of the kink-kink collision signal amplitude, necessary to compute the constraints. There are one major difference with the previous analyses. We have seen that only one parameter is used to construct the set of matched-filter templates, the high frequency cutoff  $f_h$ . The previous analysis used 31 templates, spanning the range of frequency from  $f_{h,\min} = 30$  Hz to  $f_{h,\max} = 4096$  Hz. However, since kink-kink bursts are emitted in all direction, we only need one template characterized

by the largest high frequency cutoff  $f_{h,\max}$ , given the Nyquist frequencies. We applied the same list of vetoes used in O1 and O2 analysis. Figure 5.15 shows the detection efficiency  $e_{q=2}$  as a function of the injected kink-kink collision signal amplitude  $A_{q=2}$ .

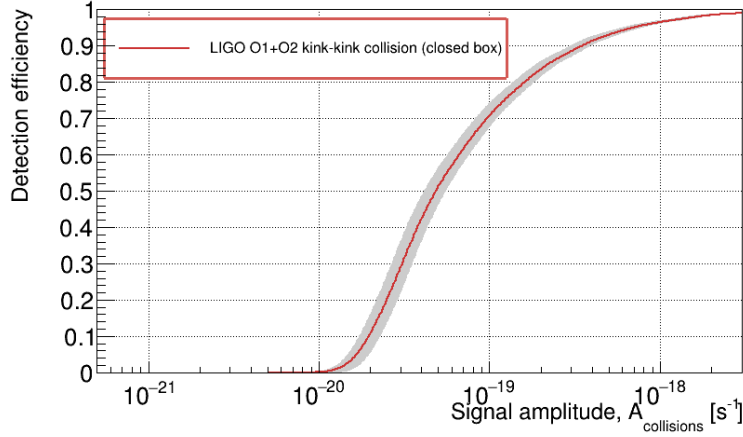


Figure 5.15: The sensitivity of the burst search as a function of the kink-kink collision signal amplitude. The uncertainties associated with the efficiency curve include binomial counting fluctuations, calibration uncertainties, and an amplitude binning uncertainty.

### 5.5.2 Constraints

In Sec 5.2 we derived the expression for the cosmological rate of burst events produced at cusp/kink features. Since the amplitude does not depend on the loop size  $\ell$ , we can not use the expression given by Eq. 5.29 which diverge at  $q = 2$ . Indeed, the change of variable used in Eq. 5.27 to pass from  $\ell$  to  $A_q$  is no longer valid. In this case instead of using the set of variables  $(A_q, z)$ , we work with  $(\gamma, z)$ , where we recall that  $\gamma$  is the relative loop size  $\gamma \equiv \ell/t$ . From Eq. 5.24 we get:

$$\frac{d^2 R_q^{(M)}}{dz d\gamma}(\gamma, z, f) = \frac{2N_q H_0^{-3} \varphi_V(z)}{(1+z)\gamma t^4(z)} \times \mathcal{F}^{(M)}(\gamma, t(z)) \times \Delta_q(\gamma, z, f). \quad (5.48)$$

Here, we recall that  $N_q$  is the average number of features producing gravitational waves per loop oscillation, namely the number of cusps  $N_c$ , the number of kinks  $N_k$  or the number of kink-kink collisions  $N_{kk}$ . We focus on the kink-kink collision case. The fraction  $\Delta_{kk}(\gamma, z, f)$  of observable bursts is well given by Eq. 5.25, for an isotropic gravitational-wave emission. The gravitational-wave rate is then integrated over the redshift  $z$  and the relative loop size  $\gamma$ . The variables  $(\gamma, z)$  define an integration domain that physically still depends on two conditions:  $\gamma < \gamma_{\max}$  and  $\theta_m < 1$ . This last condition imposes a lower cut-off in the size of loops:

$$\theta_m < 1 \Rightarrow \gamma > \gamma_{\min}(f, z) = \frac{1}{g_2 f t(z)(1+z)}. \quad (5.49)$$

The gravitational-wave energy density is now given by:

$$\Omega_{\text{GW}}(f; G\mu) = \frac{4\pi^2}{3H_0^2} f^3 \int_{z^*}^{\infty} h^2 dh \times \int_{\gamma_{\min}}^{\gamma_{\max}} dz \frac{d^2 R^{(M)}}{dz d\gamma}(\gamma, z, f; G\mu), \quad (5.50)$$

Once again, this computation should not include powerful and rare bursts. The condition on the rate in Eq. 5.38, which tells us that bursts are resolvable when their rate of occurrence is lower than the frequency, is now implemented by a cutoff on the redshift:

$$\int_0^{z^*} dz \int_{\gamma_{\min}}^{\gamma_{\max}} d\gamma \times \frac{d^2 R^{(M)}}{dz d\gamma}(z, \gamma, f) = f, \quad (5.51)$$

with  $z^*$ , the maximal redshift for which the bursts can be separated.

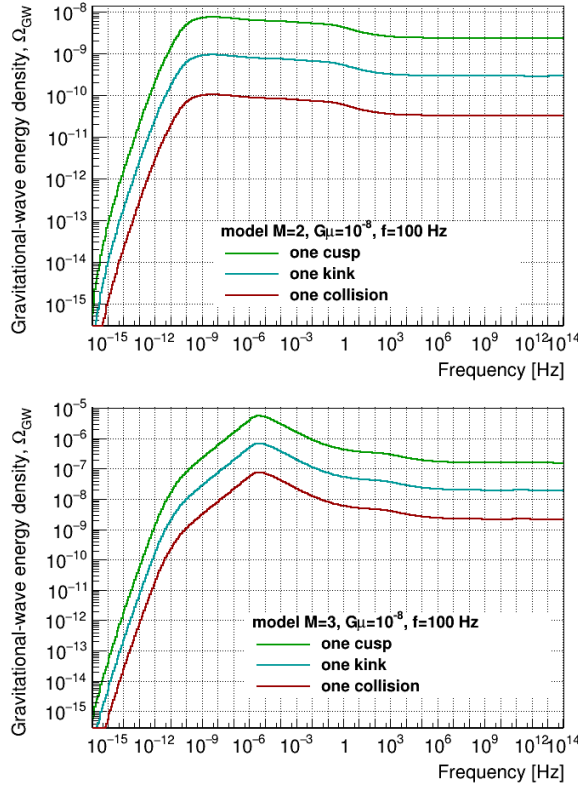


Figure 5.16: Gravitational-wave energy density  $\Omega_{\text{GW}}^{(M)}(f)$  from one cusp/kink/kink-kink collision feature, predicted by the loop distribution models  $M=2$ ,  $M=3$  for  $G\mu = 10^{-8}$ .

Figure 5.16 compares the gravitational-wave energy density  $\Omega_{\text{GW}}^{(M)}(f)$  for one cusp, one kink and one collision, at fixed  $G\mu = 10^{-8}$  and  $f = 100$  Hz, for the loop

distribution model  $M=2$  and  $M=3$ . The spectrum has the same shape for each type of bursts. In addition, for both model we observe that the cusp case dominates over the kink case by roughly an order of magnitude, which dominates by the same order the collision case, which seems to be in agreement with the results obtained for model  $M=3$  in [175]. If we consider that there are an even number  $N_k$  of kinks on a loop, there is  $N_{kk} = N_k^2/4$  collisions. Therefore, the number of collisions on a loop evolves as the square of the number of kinks, and consequently may be the major contribution to the stochastic gravitational-wave background produced by cosmic strings.

The number of cusps, kinks and collisions per loop oscillations is a non-trivial parameter to derive, and is the subject of ongoing work. Following [106], it is reasonable to consider that the number of cusps on a loop is  $N_c = \mathcal{O}(1)$ . In particular, as already mentioned, simulations shows that the presence of kinks render the appearance of cusps less likely. In addition, the smoothing of the loops through gravitational-wave backreaction effect, almost always introduces two cusps on each loop. On the other hand, the number of kinks can increase “freely”, so there is no real reason to consider that this number is  $N_k = \mathcal{O}(1)$ . Following the method described in Sec 5.4, we want to use the burst detection efficiency curve to constrain the parameter space  $(G\mu, N_k)$ . For simplicity, we consider loops without cusps. Thus, the gravitational-wave emission of these loops is dominated by bursts produced by kinks and collisions. We assume also that kinks are created in pairs, as it is observed in Nambu-Goto simulations such that the number of collisions is given by  $N_{kk} = N_k^2/4$ . In addition, as discussed in [175] the number of cusp/kink/collision features per loop oscillation cannot take arbitrarily large values. It is limited by the power lost into gravitational waves  $P_{\text{GW}} = \Gamma G\mu^2$ , see Sec. 3.3.3. In this work, we consider the limits determined in [175] with  $\Gamma = 50$  <sup>7</sup>:

$$N_k \leq 257, \quad N_{kk} \leq 4459. \quad (5.52)$$

These values depend on other parameters, and may underestimate the maximum number of kink or kink-kink collision events on a loop [175].

For each point in the parameter space  $(G\mu, N_k)$ , we compute the effective rate  $R_{\text{eff},q}^M$ , given by Eq. 5.39, namely the rate of detectable events by the burst search. We consider the contributions from gravitational waves produced by kinks and kink-kink collisions. We scan the parameter space of model  $M$  of the dimensionless string tension  $G\mu$  ( $10^{-14} < G\mu < 10^{-6}$ ), and the number of kinks  $N_k$ , and we say that the parameter space is excluded at 95% confidence level when:

$$R_{\text{eff},\text{kink}}^M \times N_k + R_{\text{eff},\text{collision}}^M \times \frac{N_k^2}{4} > \frac{2.996}{T_{\text{obs}}}. \quad (5.53)$$

Figure 5.17 shows the excluded regions in the parameter space  $(G\mu, N_k)$  for  $M=2,3$ , using the O1+O2 LIGO burst observations. We observe that for model  $M=2$ , the

---

<sup>7</sup>The idea at the time of the redaction, is to consider  $\Gamma$  as a free parameter as well. This is not included in this work.

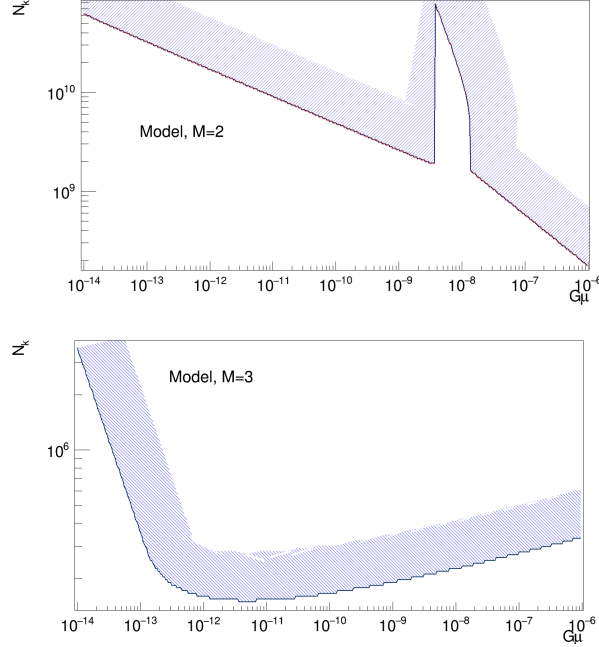


Figure 5.17: 95% confidence exclusion regions are shown for the loop distribution models: M=2 (at the top), M=3(at the bottom). Shaded regions are excluded by the latest (O1+O2) Advanced LIGO burst measurements.

bounds on  $G\mu$  become stronger for high values of the average number of kinks per loop oscillation  $N_k$ , which is expected. The observed peak around  $G\mu = 10^{-8}$  is artificial and should be ignored. It results from the discontinuous transition between the radiation and matter era (see also plots in Fig. 5.5 and Fig. 5.6), which gets amplified. For model M=3, this transition is smooth. The constraint on the number of kinks is high in comparison with theoretical predictions. This suggests that the burst search is not sensitive enough to gravitational-waves produced by kinks in the context of model M=2. We conclude that the burst search cannot constrain the number of kinks  $N_k$  for this model. The model M=3, predicts a larger gravitational-wave rate for very small loops. The constraint on the number of kinks is stronger but remains orders of magnitudes above theoretical expectations<sup>8</sup>. The burst search cannot constrain this model either. However, in [175] it is shown that the Advanced LIGO and Advanced Virgo stochastic search is able to severely constrain the number of kinks for this model, with  $G\mu < 8.8 \times 10^{-14}$  for a high number of kinks ( $20 < N_k < 133$ ). In summary, these results will be used for the O3 analysis. For O3 data, instead of targeting competitive upper limits, the burst search will be tuned to maximize the

<sup>8</sup>For the moment, we found no clear reason which could explain the change of behaviour in the shape of the derived curve. There is no peak in the burst rate as in the stochastic spectrum, which could move away from the observable frequency window with  $G\mu$ . However, we observed that the rate is not monotone with  $G\mu$ .

detection of individual bursts from cusps, kinks and, for the first time, kink-kink collisions. On the other hand, it is the LIGO-Virgo stochastic search that is expected to strongly constrain the parameters of the cosmic strings.

## Conclusion and prospects

The second generation of ground-based interferometric gravitational-wave detectors has incorporated several upgrades compared to the first generation. These developments have led to a significant increase in sensitivity, even if the detectors are not yet operating at design sensitivity. The first observing run (O1) began in september 2015, where Advanced LIGO collected data until January 2016. This run has culminated in the first direct detection of gravitational waves from a black hole coalescence, GW150914. The second observing run (O2) started on November 30, 2016 to August 25, 2017. Advanced Virgo joined the Advanced LIGO detectors, from the 1st of August until the 25th of August 2017. The addition of Advanced Virgo to the network of detectors played a crucial role on the source localization, in particular, for the case of the first detection of gravitational waves from a neutron star coalescence, GW170817. In this context, we carefully characterized the transient noise around the time of the gravitational-wave detections. These investigations were used to ensure that these transient noise did not affect the source localization and the event parameter estimation.

In addition to binary systems, there are various interesting gravitational-wave sources that could be detected in the future by current ground-based interferometric detectors. Cosmic strings are one-dimensional topological defects that can form during phase transitions in the early Universe. They are good candidates to bridge between cosmology and high energy physics. They may also form in string theory and are referred to as cosmic super-strings. The most potent gravitational-wave bursts are produced at regions of cosmic string loops called cusps and kinks, which acquire large Lorentz boost. We have performed a search for gravitational wave bursts produced by cusps and kinks in the data from the first and the second observing run of Advanced LIGO and Advanced Virgo.

A significant part of the O1 analysis was dedicated to understand the background of accidental triggers due to detector noise. The result of this work led to the application of DQ flags which improved the cosmic string search sensitivity. However, short transient noise events, that resemble the gravitational-wave signature of cosmic

string cusps or kinks, significantly reduce the sensitivity of the search. These are known as blip glitches. We investigated carefully these transient noise events, and we did not identify any particular subset of blip glitches correlated with a detector auxiliary or environmental sensor channels. In the future, it will become even more essential to mitigate these glitches from the data.

In the absence of a detection, the sensitivity of the search to cusp and kink signals was estimated. This was used to set constraints on the parameters which characterize a network of Nambu-Goto cosmic strings and super-strings, namely the dimensionless string tension  $G\mu/c^2$  and the probability of intercommutation  $p$ . To do this, we examined three models that predict the loop distribution, from which the detection rate was derived. We subsequently compared the burst constraints with those derived from other experiments, in particular from search for the stochastic gravitational-wave background with the LIGO-Virgo observations.

Similarly, we analyzed the data from the second observing run of Advanced LIGO. We also conducted a three-detector search using the data collected by Advanced Virgo in August 2017. We maximized the search sensitivity by performing specific data quality studies to reject part of glitches that mimic the waveform from cosmic string cusps/kinks. In particular, we showed that we have well understood the origin of the blip glitches in Virgo. However, the sensitivity of Virgo was not sufficient to perform a three-detector search. Finally, we used the O1 and O2 combined detection efficiencies to update constraints on the string tension for topological strings ( $p=1$ ).

The Advanced LIGO and Advanced Virgo have started their third observing run (O3) on April 1, 2019. The average BNS range increased for both detectors up to roughly 50 Mpc for Virgo, 110 Mpc for LIGO Hanford and 130 Mpc for LIGO Livingston. Thanks to the large gain in sensibility in Virgo, the O3 cosmic string burst analysis will be a full three-detector search. Since the first direct detection of gravitational waves, it became necessary to be able to claim a cosmic string detection at a  $5\sigma$  confidence level. The current pipeline cannot achieve such a high confidence level. To that purpose, a pipeline is in development which uses a new ranking statistic. It includes a model for the noise population without using the time slides method of background estimation [186].

In addition, a new type of gravitational-wave emission was studied. Indeed, when there is more than one kink per loop oscillation, kinks can meet and produce a gravitational-wave burst. While the bursts emitted at cusp/kink features are strongly beamed, the gravitational-wave emission at a kink-kink collision is isotropic. We included the new waveform in the pipeline and conducted the first search for bursts produced by the collision of two kinks. The number of kinks per loop oscillation is currently unknown and constitutes the main source of theoretical uncertainties on the predicted cosmological rate. Moreover, the new waveform amplitude does not depend on the loop size anymore. We then derived the new predicted rate by the models, to set constraints on the number of kinks per loop oscillation for different values of the string tension. This work will be used for the O3 LIGO-Virgo analysis.

In the more long-term, detectors will join to the ground-based interferometric gravitational-wave detectors: Kamioka gravitational-wave detector (KAGRA) in Japan, and LIGO India. This will provide various advantages, for example for the estimation of the parameters which is the next step after a cosmic string detection. Finally, it is expected that the Laser Inter-ferometer Space Antenna (LISA) will be able to probe cosmic strings by measuring the gravitational-wave background and improve even more the constraints on the cosmic string parameters [174], in case of non-detection.



# Bibliography

- [1] A. Einstein. Die Grundlage der allgemeinen Relativitäts theorie. *Annalen der Physik*, 6:769–822, 1916.
- [2] Albert Einstein. Approximative Integration of the Field Equations of Gravitation. *Sitzungsber. Preuss. Akad. Wiss. Berlin (Math. Phys.)*, 1916:688–696, 1916.
- [3] Hermann Weyl. Space, time, matter. <http://www.gutenberg.org/ebooks/43006>.
- [4] Jorge L. Cervantes-Cota, S. Galindo-Uribarri, and G-F. Smoot. A Brief History of Gravitational Waves. *Universe*, 2(3):22, 2016.
- [5] Arthur Stanley Eddington. The propagation of gravitational waves. *Proc. Roy. Soc. Lond.*, A102:268–282, 1922.
- [6] Ericourgoulhon. Relativité générale. <https://luth.obspm.fr/~luthier/gourgoulhon/fr/master/relatM2.pdf>.
- [7] Nathalie Deruelle. Introduction aux équations d'einstein de la relativité générale. <http://www.phys.ens.fr/IMG/pdf/docRG.pdf>.
- [8] Kostas D. Kokkotas. Gravitational waves physics. [http://www.tat.physik.uni-tuebingen.de/~kokkotas/Teaching/NS.BH.GW\\_files/GW\\_Physics.pdf](http://www.tat.physik.uni-tuebingen.de/~kokkotas/Teaching/NS.BH.GW_files/GW_Physics.pdf).
- [9] Thomas Moore. General relativity and gravitational waves. <http://pages.pomona.edu/~tmoore/LesHouches/>.
- [10] Bahram Houchmandzadeh. Variétés différentielles et champs de tenseurs. [https://www-liphy.ujf-grenoble.fr/pagesperso/bahram/Tenseur/rieaman\\_geometry.pdf](https://www-liphy.ujf-grenoble.fr/pagesperso/bahram/Tenseur/rieaman_geometry.pdf).
- [11] J. Grain A. Barrau. *Relativité générale*. Dunod, 2011.

- [12] S. Weinberg. *Gravitation and Cosmology*. John Wiley and Sons, 1972.
- [13] Sascha Husa. Michele Maggiore: Gravitational waves. Volume 1: Theory and experiments. *Gen. Rel. Grav.*, 41:1667–1669, 2009.
- [14] Ludvigsen. *La relativité générale : une approche géométrique*. Dunod, 2000.
- [15] E.ourgoulhon. *Relativité restreinte : des particules à l’astrophysique*. EDP Sciences / CNRS Éditions, 2010.
- [16] F. Bernardeau. *Cosmologie : des fondements théoriques aux observations*. EDP Sciences / CNRS Éditions, 2007.
- [17] Michal Was. *Searching for gravitational waves associated with gamma-ray bursts int 2009-2010 ligo-virgo data*. PhD thesis, Paris 11, 2011.
- [18] J. M. Weisberg, D. J. Nice, and J. H. Taylor. Timing Measurements of the Relativistic Binary Pulsar PSR B1913+16. *Astrophys. J.*, 722:1030–1034, 2010.
- [19] Russell A. Hulse. The discovery of the binary pulsar. *Rev. Mod. Phys.*, 66:699–710, 1994.
- [20] S. E. Woosley and J. S. Bloom. The Supernova Gamma-Ray Burst Connection. *Ann. Rev. Astron. Astrophys.*, 44:507–556, 2006.
- [21] D. Rickles C. DeWitt. *The Role of Gravitation in Physics: Report from the 1957 Chapel Hill Conference*. Berlin: Edition Open Access, 2011.
- [22] Peter R. Saulson. Physics of gravitational wave detection: Resonant and interferometric detectors. *eConf*, C9808031:05, 1998. [,113(1998)].
- [23] Tilman Sauer. Albert Einstein’s 1916 review article on general relativity. 2004.
- [24] F. A. E. Pirani. On the Physical significance of the Riemann tensor. *Acta Phys. Polon.*, 15:389–405, 1956. [Gen. Rel. Grav.41,1215(2009)].
- [25] J. Weber. Evidence for discovery of gravitational radiation. *Phys. Rev. Lett.*, 22:1320–1324, 1969.
- [26] V. B. Braginsky, Yu. I. Vorontsov, and K. S. Thorne. QUANTUM NONDEMOLITION MEASUREMENTS. *Science*, 209:547–557, 1980.
- [27] Allan Franklin. Gravity waves and neutrinos: The later work of Joseph Weber. *Perspectives on Science*, 18(2):119–151, 2010.
- [28] Julia Casanueva. *Control of the gravitational wave interferometric detector Advanced Virgo*. PhD thesis, Paris 11, 2017.
- [29] Peter R Saulson. *Fundamentals of interferometric gravitational wave detectors*. World Scientific, Singapore, 1994.

- [30] B. S. Sathyaprakash and B. F. Schutz. Physics, Astrophysics and Cosmology with Gravitational Waves. *Living Rev. Rel.*, 12:2, 2009.
- [31] B. P. Abbott et al. LIGO: The Laser interferometer gravitational-wave observatory. *Rept. Prog. Phys.*, 72:076901, 2009.
- [32] B. Sathyaprakash et al. Scientific Objectives of Einstein Telescope. *Class. Quant. Grav.*, 29:124013, 2012. [Erratum: *Class. Quant. Grav.*30,079501(2013)].
- [33] T. Accadia et al. Calibration and sensitivity of the Virgo detector during its second science run. *Class. Quant. Grav.*, 28:025005, 2011. [Erratum: *Class. Quant. Grav.*28,079501(2011)].
- [34] F. Acernese et al. Advanced Virgo: a second-generation interferometric gravitational wave detector. *Class. Quant. Grav.*, 32(2):024001, 2015.
- [35] Benjamin P. Abbott et al. Sensitivity of the Advanced LIGO detectors at the beginning of gravitational wave astronomy. *Phys. Rev.*, D93(11):112004, 2016. [Addendum: *Phys. Rev.*D97,no.5,059901(2018)].
- [36] J. Aasi et al. Advanced LIGO. *Class. Quant. Grav.*, 32:074001, 2015.
- [37] N. A. Robertson et al. Quadruple suspension design for Advanced LIGO. *Class. Quant. Grav.*, 19:4043–4058, 2002.
- [38] B. P. Abbott et al. GWTC-1: A Gravitational-Wave Transient Catalog of Compact Binary Mergers Observed by LIGO and Virgo during the First and Second Observing Runs. 2018.
- [39] J. Aasi et al. Enhancing the sensitivity of the LIGO gravitational wave detector by using squeezed states of light. *Nature Photon.*, 7:613–619, 2013.
- [40] J. Abadie et al. A Gravitational wave observatory operating beyond the quantum shot-noise limit: Squeezed light in application. *Nature Phys.*, 7:962–965, 2011.
- [41] H. Grote, K. Danzmann, K. L. Dooley, R. Schnabel, J. Slutsky, and H. Vahlbruch. First Long-Term Application of Squeezed States of Light in a Gravitational-Wave Observatory. *Phys. Rev. Lett.*, 110(18):181101, 2013.
- [42] J. Abadie et al. Sensitivity Achieved by the LIGO and Virgo Gravitational Wave Detectors during LIGO’s Sixth and Virgo’s Second and Third Science Runs. 2012.
- [43] T Accadia and B L Swinkels and. Commissioning status of the virgo interferometer. *Classical and Quantum Gravity*, 27(8):084002, apr 2010.
- [44] B. P. Abbott et al. Observation of Gravitational Waves from a Binary Black Hole Merger. *Phys. Rev. Lett.*, 116(6):061102, 2016.

- [45] B. P. Abbott et al. GW170814: A Three-Detector Observation of Gravitational Waves from a Binary Black Hole Coalescence. *Phys. Rev. Lett.*, 119(14):141101, 2017.
- [46] B. P. Abbott et al. GW170817: Observation of Gravitational Waves from a Binary Neutron Star Inspiral. *Phys. Rev. Lett.*, 119(16):161101, 2017.
- [47] B. P. Abbott et al. Tests of general relativity with GW150914. *Phys. Rev. Lett.*, 116(22):221101, 2016. [Erratum: *Phys. Rev. Lett.*121,no.12,129902(2018)].
- [48] B. P. Abbott et al. Astrophysical Implications of the Binary Black-Hole Merger GW150914. *Astrophys. J.*, 818(2):L22, 2016.
- [49] B. P. Abbott et al. The Rate of Binary Black Hole Mergers Inferred from Advanced LIGO Observations Surrounding GW150914. *Astrophys. J.*, 833(1):L1, 2016.
- [50] B. P. Abbott et al. Gravitational Waves and Gamma-rays from a Binary Neutron Star Merger: GW170817 and GRB 170817A. *Astrophys. J.*, 848(2):L13, 2017.
- [51] Brian D. Metzger. Kilonovae. *Living Rev. Rel.*, 20(1):3, 2017.
- [52] B. P. Abbott et al. Multi-messenger Observations of a Binary Neutron Star Merger. *Astrophys. J.*, 848(2):L12, 2017.
- [53] M. Soares-Santos et al. The Electromagnetic Counterpart of the Binary Neutron Star Merger LIGO/Virgo GW170817. I. Discovery of the Optical Counterpart Using the Dark Energy Camera. *Astrophys. J.*, 848(2):L16, 2017.
- [54] P. S. Cowperthwaite et al. The Electromagnetic Counterpart of the Binary Neutron Star Merger LIGO/Virgo GW170817. II. UV, Optical, and Near-infrared Light Curves and Comparison to Kilonova Models. *Astrophys. J.*, 848(2):L17, 2017.
- [55] M. Nicholl et al. The Electromagnetic Counterpart of the Binary Neutron Star Merger LIGO/VIRGO GW170817. III. Optical and UV Spectra of a Blue Kilonova From Fast Polar Ejecta. *Astrophys. J.*, 848(2):L18, 2017.
- [56] R. Chornock et al. The Electromagnetic Counterpart of the Binary Neutron Star Merger LIGO/VIRGO GW170817. IV. Detection of Near-infrared Signatures of r-process Nucleosynthesis with Gemini-South. *Astrophys. J.*, 848(2):L19, 2017.
- [57] Raffaella Margutti et al. The Electromagnetic Counterpart of the Binary Neutron Star Merger LIGO/VIRGO GW170817. V. Rising X-ray Emission from an Off-Axis Jet. *Astrophys. J.*, 848(2):L20, 2017.

- [58] K. D. Alexander et al. The Electromagnetic Counterpart of the Binary Neutron Star Merger LIGO/VIRGO GW170817. VI. Radio Constraints on a Relativistic Jet and Predictions for Late-Time Emission from the Kilonova Ejecta. *Astrophys. J.*, 848(2):L21, 2017.
- [59] P. K. Blanchard et al. The Electromagnetic Counterpart of the Binary Neutron Star Merger LIGO/VIRGO GW170817. VII. Properties of the Host Galaxy and Constraints on the Merger Timescale. *Astrophys. J.*, 848(2):L22, 2017.
- [60] W. Fong et al. The Electromagnetic Counterpart of the Binary Neutron Star Merger LIGO/VIRGO GW170817. VIII. A Comparison to Cosmological Short-duration Gamma-ray Bursts. *Astrophys. J.*, 848(2):L23, 2017.
- [61] B. P. Abbott et al. Estimating the Contribution of Dynamical Ejecta in the Kilonova Associated with GW170817. *Astrophys. J.*, 850(2):L39, 2017.
- [62] P. A. R. Ade et al. Planck 2015 results. XIII. Cosmological parameters. *Astron. Astrophys.*, 594:A13, 2016.
- [63] Adam G. Riess et al. A 2.4% Determination of the Local Value of the Hubble Constant. *Astrophys. J.*, 826(1):56, 2016.
- [64] B. P. Abbott et al. A gravitational-wave standard siren measurement of the Hubble constant. *Nature*, 551(7678):85–88, 2017.
- [65] Bernard F. Schutz. Determining the Hubble Constant from Gravitational Wave Observations. *Nature*, 323:310–311, 1986.
- [66] F. Robinet. Omicron: an algorithm to detect and characterize transient events in gravitational-wave detectors. Technical Report VIR-0545B-14, 2016.
- [67] Miriam Cabero et al. Blip glitches in Advanced LIGO data. 2019.
- [68] Daniel George, Hongyu Shen, and E. A. Huerta. Glitch Classification and Clustering for LIGO with Deep Transfer Learning. In *NiPS Summer School 2017 Gubbio, Perugia, Italy, June 30-July 3, 2017*, 2017.
- [69] J. Aasi et al. Characterization of the LIGO detectors during their sixth science run. *Class. Quant. Grav.*, 32(11):115012, 2015.
- [70] Tomoki Isogai. Used percentage veto for LIGO and virgo binary inspiral searches. *J. Phys. Conf. Ser.*, 243:012005, 2010.
- [71] Gary Hemming Didier Verkindt. Virgo interferometer monitoring (vim). <https://vim.virgo-gw.eu>.
- [72] Edwin Hubble. A relation between distance and radial velocity among extragalactic nebulae. *Proc. Nat. Acad. Sci.*, 15:168–173, 1929.

- [73] Pierre Binetruy, Alejandro Bohe, Chiara Caprini, and Jean-Francois Dufaux. Cosmological Backgrounds of Gravitational Waves and eLISA/NGO: Phase Transitions, Cosmic Strings and Other Sources. *JCAP*, 1206:027, 2012.
- [74] Alan H. Guth. The Inflationary Universe: A Possible Solution to the Horizon and Flatness Problems. *Phys. Rev.*, D23:347–356, 1981. [Adv. Ser. Astrophys. Cosmol.3,139(1987)].
- [75] Andrei D. Linde. A New Inflationary Universe Scenario: A Possible Solution of the Horizon, Flatness, Homogeneity, Isotropy and Primordial Monopole Problems. *Phys. Lett.*, 108B:389–393, 1982. [Adv. Ser. Astrophys. Cosmol.3,149(1987)].
- [76] Mairi Sakellariadou. Cosmic Strings and Cosmic Superstrings. *Nucl. Phys. Proc. Suppl.*, 192-193:68–90, 2009.
- [77] A. Vilenkin and E. P. S. Shellard. *Cosmic Strings and Other Topological Defects*. Cambridge University Press, 2000.
- [78] Alejandro Bohé. *Production d’ondes gravitationnelles par les cordes cosmique avec jonctions*. PhD thesis, Université Paris Diderot - Paris VII, 2011.
- [79] Christophe Ringeval. *Étude des courants fermioniques sur les objets étendus*. PhD thesis, Université Pierre et Marie Curie - Paris VI, 2002.
- [80] Tanmay Vachaspati, Levon Pogosian, and Daniele Steer. Cosmic Strings. *Scholarpedia*, 10(2):31682, 2015.
- [81] M. B. Hindmarsh and T. W. B. Kibble. Cosmic strings. *Rept. Prog. Phys.*, 58:477–562, 1995.
- [82] Erwann Allys. *Au-delà des modèles standards en cosmologie*. PhD thesis, Université Pierre et Marie Curie - Paris VI, 2017.
- [83] Holger Bech Nielsen and P. Olesen. Vortex Line Models for Dual Strings. *Nucl. Phys.*, B61:45–61, 1973. [,302(1973)].
- [84] P. Peter. Superconducting cosmic string: Equation of state for space - like and time - like current in the neutral limit. *Phys. Rev.*, D45:1091–1102, 1992.
- [85] Leandros Perivolaropoulos. Asymptotics of Nielsen-Olesen vortices. *Phys. Rev.*, D48:5961–5962, 1993.
- [86] E. B. Bogomolny and A. I. Vainshtein. Stability of Strings in Gauge Abelian Theory. *Sov. J. Nucl. Phys.*, 23:588–591, 1976.
- [87] Laurence Jacobs and Claudio Rebbi. Interaction energy of superconducting vortices. *Phys. Rev. B*, 19:4486–4494, May 1979.

- [88] Christopher T. Hill, Hardy M. Hodges, and Michael S. Turner. Bosonic Superconducting Cosmic Strings. *Phys. Rev.*, D37:263, 1988.
- [89] E. P. S. Shellard. Cosmic String Interactions. *Nucl. Phys.*, B283:624–656, 1987.
- [90] Steven Weinberg. Gauge and global symmetries at high temperature. *Phys. Rev. D*, 9:3357–3378, Jun 1974.
- [91] T. W. B. Kibble. Topology of Cosmic Domains and Strings. *J. Phys.*, A9:1387–1398, 1976.
- [92] T. W. B. Kibble. Some Implications of a Cosmological Phase Transition. *Phys. Rept.*, 67:183, 1980.
- [93] D.A.Kirzhnits and A.D.Linde. Macroscopic consequences of the Weinberg model. *Physics Letters B*, 42:471–474, 1972.
- [94] W. H. Zurek. Cosmic strings in laboratory superfluids and the topological remnants of other phase transitions. *Acta Phys. Polon.*, B24:1301–1311, 1993.
- [95] Yoichiro Nambu. Strings, Monopoles and Gauge Fields. *Phys. Rev.*, D10:4262, 1974. [,310(1974)].
- [96] Tetsuo Gotō. Relativistic Quantum Mechanics of One-Dimensional Mechanical Continuum and Subsidiary Condition of Dual Resonance Model. *Progress of Theoretical Physics*, 46(5):1560–1569, 11 1971.
- [97] Mairi Sakellariadou. Cosmic strings. *Lect. Notes Phys.*, 718:247–288, 2007.
- [98] R. A. Matzner and J. Mccracken. PROBABILITY OF INTERCONNECTION OF COSMIC STRINGS. In *IN \*NEW HAVEN 1988, PROCEEDINGS, COSMIC STRINGS\* 32-41.*, 1988.
- [99] Ana Achucarro and Roland de Putter. Effective non-intercommutation of local cosmic strings at high collision speeds. *Phys. Rev.*, D74:121701, 2006.
- [100] A. Achucarro and G. J. Verbiest. Higher order intercommutations in Cosmic String Collisions. *Phys. Rev. Lett.*, 105:021601, 2010.
- [101] L. M. A. Bettencourt and T. W. B. Kibble. Nonintercommuting configurations in the collisions of type I  $U(1)$  cosmic strings. *Phys. Lett.*, B332:297–304, 1994.
- [102] Mark G. Alford, Kai-Ming Lee, John March-Russell, and John Preskill. Quantum field theory of nonAbelian strings and vortices. *Nucl. Phys.*, B384:251–317, 1992.
- [103] Patrick McGraw. Evolution of a nonAbelian cosmic string network. *Phys. Rev.*, D57:3317–3339, 1998.

- [104] Mark G. Jackson, Nicholas T. Jones, and Joseph Polchinski. Collisions of cosmic F and D-strings. *JHEP*, 10:013, 2005.
- [105] T. W. B. Kibble and Neil Turok. Self-intersection of cosmic strings. *Physics Letters B*, 116:143, 1982.
- [106] Jose J. Blanco-Pillado, Ken D. Olum, and Benjamin Shlaer. Cosmic string loop shapes. *Phys. Rev.*, D92(6):063528, 2015.
- [107] Jeremy M. Wachter and Ken D. Olum. Gravitational smoothing of kinks on cosmic string loops. *Phys. Rev. Lett.*, 118(5):051301, 2017. [Erratum: *Phys. Rev. Lett.* 121, no. 14, 149901 (2018)].
- [108] D. Garfinkle and T. Vachaspati. FIELDS DUE TO KINKY, CUSPLESS, COSMIC LOOPS. *Phys. Rev.*, D37:257–262, 1988.
- [109] Thibault Damour and Alexander Vilenkin. Gravitational wave bursts from cosmic strings. *Phys. Rev. Lett.*, 85:3761–3764, 2000.
- [110] Thibault Damour and Alexander Vilenkin. Gravitational wave bursts from cusps and kinks on cosmic strings. *Phys. Rev.*, D64:064008, 2001.
- [111] Xavier Siemens, Jolien Creighton, Irit Maor, Saikat Ray Majumder, Kipp Cannon, and Jocelyn Read. Gravitational wave bursts from cosmic (super)strings: Quantitative analysis and constraints. *Phys. Rev.*, D73:105001, 2006.
- [112] C. J. Burden. Gravitational Radiation From a Particular Class of Cosmic Strings. *Phys. Lett.*, 164B:277–281, 1985.
- [113] Bruce Allen and Paul Casper. A Closed form expression for the gravitational radiation rate from cosmic strings. *Phys. Rev.*, D50:2496–2518, 1994.
- [114] David Garfinkle and Tanmay Vachaspati. Radiation From Kinky, Cuspless Cosmic Loops. *Phys. Rev.*, D36:2229, 1987.
- [115] Tanmay Vachaspati and Alexander Vilenkin. Gravitational Radiation from Cosmic Strings. *Phys. Rev.*, D31:3052, 1985.
- [116] R. Durrer. Gravitational Angular Momentum Radiation of Cosmic Strings. *Nucl. Phys.*, B328:238–271, 1989.
- [117] Bruce Allen and E. P. S. Shellard. Gravitational radiation from cosmic strings. *Phys. Rev.*, D45:1898–1912, 1992.
- [118] Paul Casper and Bruce Allen. Gravitational radiation from realistic cosmic string loops. *Phys. Rev.*, D52:4337–4348, 1995.
- [119] A. Vilenkin. Gravitational Field of Vacuum Domain Walls and Strings. *Phys. Rev.*, D23:852–857, 1981.

- [120] M. V. Sazhin, O. S. Khovanskaya, M. Capaccioli, G. Longo, Maurizio Paolillo, G. Covone, N. A. Grogin, and E. J. Schreier. Gravitational lensing by cosmic strings: What we learn from the CSL-1 case. *Mon. Not. Roy. Astron. Soc.*, 376:1731–1739, 2007.
- [121] M. Sazhin, Giuseppe Longo, J. M. Alcala', R. Silvotti, G. Covone, O. Khovanskaya, M. Pavlov, M. Pannella, M. Radovich, and V. Testa. CSL-1: A chance projection effect or serendipitous discovery of a gravitational lens induced by a cosmic string? *Mon. Not. Roy. Astron. Soc.*, 343:353, 2003.
- [122] George F. Smoot et al. Structure in the COBE differential microwave radiometer first year maps. *Astrophys. J.*, 396:L1–L5, 1992.
- [123] Alan H. Guth and David I. Kaiser. Inflationary cosmology: Exploring the Universe from the smallest to the largest scales. *Science*, 307:884–890, 2005.
- [124] Albert Stebbins. Cosmic Strings and the Microwave Sky. 1. Anisotropy from Moving Strings. *Astrophys. J.*, 327:584–614, 1988.
- [125] Richard Battye and Adam Moss. Updated constraints on the cosmic string tension. *Phys. Rev.*, D82:023521, 2010.
- [126] P. A. R. Ade et al. Planck 2013 results. XVI. Cosmological parameters. *Astron. Astrophys.*, 571:A16, 2014.
- [127] Robert H. Brandenberger. Searching for Cosmic Strings in New Observational Windows. *Nucl. Phys. Proc. Suppl.*, 246-247:45–57, 2014.
- [128] Michael Pagano and Robert Brandenberger. The 21cm Signature of a Cosmic String Loop. *JCAP*, 1205:014, 2012.
- [129] Peter Fritschel. Second generation instruments for the Laser Interferometer Gravitational Wave Observatory (LIGO). *Proc. SPIE Int. Soc. Opt. Eng.*, 4856:282–291, 2003.
- [130] F. Acernese et al. Calibration of Advanced Virgo and Reconstruction of the Gravitational Wave Signal  $h(t)$  during the Observing Run O2. *Class. Quant. Grav.*, 35(20):205004, 2018.
- [131] B. P. Abbott et al. Calibration of the Advanced LIGO detectors for the discovery of the binary black-hole merger GW150914. *Phys. Rev.*, D95(6):062003, 2017.
- [132] B.F.Schutz. *Gravitational-Wave Data Analysis*. Nato Asi, 1987.
- [133] Warren G.Anderson Jolien D.E Creighton. *Gravitational-Wave Physics and Astronomy*. Wiley VCH, 2011.
- [134] Piotr Jaranowski and Andrzej Krolak. Gravitational-Wave Data Analysis. Formalism and Sample Applications: The Gaussian Case. *Living Rev. Rel.*, 8:3, 2005. [Living Rev. Rel.15,4(2012)].

- [135] Bruce Allen.  $\chi^2$  time-frequency discriminator for gravitational wave detection. *Phys. Rev.*, D71:062001, 2005.
- [136] Yoichi Aso et al. Accurate measurement of the time delay in the response of the LIGO gravitational wave detectors. *Class. Quant. Grav.*, 26:055010, 2009.
- [137] Eric Thrane, Nelson Christensen, and Robert Schofield. Correlated magnetic noise in global networks of gravitational-wave interferometers: observations and implications. *Phys. Rev.*, D87:123009, 2013.
- [138] Yoshiaki Himemoto and Atsushi Taruya. Impact of correlated magnetic noise on the detection of stochastic gravitational waves: Estimation based on a simple analytical model. *Phys. Rev.*, D96(2):022004, 2017.
- [139] W. O. Schumann. [dx.doi.org/10.1515/zna-1952-3-404](https://dx.doi.org/10.1515/zna-1952-3-404).
- [140] Kipp C. Cannon. A Bayesian coincidence test for noise rejection in a gravitational-wave burst search. *Class. Quant. Grav.*, 25:105024, 2008.
- [141] D.S.Silvia. *Data Analysis a Bayesian Tutorial*. Clarendon Press, 1996.
- [142] B. P. Abbott et al. Characterization of transient noise in Advanced LIGO relevant to gravitational wave signal GW150914. *Class. Quant. Grav.*, 33(13):134001, 2016.
- [143] P. Hello. Robustness of templates for detecting gravitational wave bursts from cosmic strings cusps and kinks. Technical Report VIR-0361A-16, 2016.
- [144] B. P. Abbott et al. Constraints on cosmic strings using data from the first Advanced LIGO observing run. *Phys. Rev.*, D97(10):102002, 2018.
- [145] LIGO Scientific Collaboration. LIGO Algorithm Library - LALSuite. free software (GPL), 2018.
- [146] B. P. Abbott et al. All-sky search for short gravitational-wave bursts in the second Advanced LIGO and Advanced Virgo run. 2019.
- [147] B. P. Abbott et al. A search for the isotropic stochastic background using data from Advanced LIGO's second observing run. *Phys. Rev.*, D100(6):061101, 2019.
- [148] M. Hindmarsh and A. Rajantie. Phase transition dynamics in the hot Abelian Higgs model. *Phys. Rev.*, D64:065016, 2001.
- [149] Tanmay Vachaspati and Alexander Vilenkin. Formation and Evolution of Cosmic Strings. *Phys. Rev.*, D30:2036, 1984.
- [150] Edward Witten. Superconducting Strings. *Nucl. Phys.*, B249:557–592, 1985.

- [151] Richard Lynn Davis. Goldstone Bosons in String Models of Galaxy Formation. *Phys. Rev.*, D32:3172, 1985.
- [152] Andreas Albrecht and N. Turok. Evolution of Cosmic Strings. *Phys. Rev. Lett.*, 54:1868–1871, 1985.
- [153] David P. Bennett and Francois R. Bouchet. Evidence for a Scaling Solution in Cosmic String Evolution. *Phys. Rev. Lett.*, 60:257, 1988.
- [154] Bruce Allen and E. P. S. Shellard. Cosmic string evolution: a numerical simulation. *Phys. Rev. Lett.*, 64:119–122, 1990.
- [155] T. W. B. Kibble. Evolution of a system of cosmic strings. *Nucl. Phys.*, B252:227, 1985. [Erratum: *Nucl. Phys.*B261,750(1985)].
- [156] Christophe Ringeval, Mairi Sakellariadou, and Francois Bouchet. Cosmological evolution of cosmic string loops. *JCAP*, 0702:023, 2007.
- [157] Jose J. Blanco-Pillado, Ken D. Olum, and Benjamin Shlaer. The number of cosmic string loops. *Phys. Rev.*, D89(2):023512, 2014.
- [158] Anastasios Avgoustidis and E. P. S. Shellard. Effect of reconnection probability on cosmic (super)string network density. *Phys. Rev.*, D73:041301, 2006.
- [159] Mairi Sakellariadou. A Note on the evolution of cosmic string/superstring networks. *JCAP*, 0504:003, 2005.
- [160] Vitaly Vanchurin, Ken D. Olum, and Alexander Vilenkin. Scaling of cosmic string loops. *Phys. Rev.*, D74:063527, 2006.
- [161] C. J. A. P. Martins and E. P. S. Shellard. Fractal properties and small-scale structure of cosmic string networks. *Phys. Rev.*, D73:043515, 2006.
- [162] Jose J. Blanco-Pillado, Ken D. Olum, and Benjamin Shlaer. Large parallel cosmic string simulations: New results on loop production. *Phys. Rev.*, D83:083514, 2011.
- [163] Jose J. Blanco-Pillado, Ken D. Olum, and Benjamin Shlaer. A new parallel simulation technique. *J. Comput. Phys.*, 231:98–108, 2012.
- [164] Florian Dubath, Joseph Polchinski, and Jorge V. Rocha. Cosmic String Loops, Large and Small. *Phys. Rev.*, D77:123528, 2008.
- [165] Larissa Lorenz, Christophe Ringeval, and Mairi Sakellariadou. Cosmic string loop distribution on all length scales and at any redshift. *JCAP*, 1010:003, 2010.
- [166] Christophe Ringeval, Mairi Sakellariadou, and Francois Bouchet. Cosmological evolution of cosmic string loops. *JCAP*, 0702:023, 2007.

- [167] Joseph Polchinski and Jorge V. Rocha. Analytic study of small scale structure on cosmic strings. *Phys. Rev.*, D74:083504, 2006.
- [168] Jeremy M. Wachter and Ken D. Olum. Gravitational backreaction on piecewise linear cosmic string loops. *Phys. Rev.*, D95(2):023519, 2017.
- [169] Joseph Polchinski and Jorge V. Rocha. Cosmic string structure at the gravitational radiation scale. *Phys. Rev.*, D75:123503, 2007.
- [170] Pierre Auclair, Christophe Ringeval, Mairi Sakellariadou, and Daniele Steer. Cosmic string loop production functions. *JCAP*, 1906(06):015, 2019.
- [171] Xavier Siemens, Vuk Mandic, and Jolien Creighton. Gravitational wave stochastic background from cosmic (super)strings. *Phys. Rev. Lett.*, 98:111101, 2007.
- [172] S. Olmez, V. Mandic, and X. Siemens. Gravitational-Wave Stochastic Background from Kinks and Cusps on Cosmic Strings. *Phys. Rev.*, D81:104028, 2010.
- [173] Tania Regimbau, Stefanos Giampanis, Xavier Siemens, and Vuk Mandic. The stochastic background from cosmic (super)strings: popcorn and (Gaussian) continuous regimes. *Phys. Rev.*, D85:066001, 2012.
- [174] Pierre Auclair et al. Probing the gravitational wave background from cosmic strings with LISA. 2019.
- [175] Christophe Ringeval and Teruaki Suyama. Stochastic gravitational waves from cosmic string loops in scaling. *JCAP*, 1712(12):027, 2017.
- [176] Rahul Biswas, Patrick R. Brady, Jolien D. E. Creighton, and Stephen Fairhurst. The Loudest event statistic: General formulation, properties and applications. *Class. Quant. Grav.*, 26:175009, 2009. [Erratum: *Class. Quant. Grav.*30,079502(2013)].
- [177] J. Aasi et al. Improved Upper Limits on the Stochastic Gravitational-Wave Background from 2009–2010 LIGO and Virgo Data. *Phys. Rev. Lett.*, 113(23):231101, 2014.
- [178] Benjamin P. Abbott et al. Upper Limits on the Stochastic Gravitational-Wave Background from Advanced LIGO’s First Observing Run. *Phys. Rev. Lett.*, 118(12):121101, 2017. [Erratum: *Phys. Rev. Lett.*119,no.2,029901(2017)].
- [179] Paul D. Lasky, Chiara M. F. Mingarelli, Tristan L. Smith, John T. Giblin, Eric Thrane, Daniel J. Reardon, Robert Caldwell, Matthew Bailes, N. D. Ramesh Bhat, Sarah Burke-Spolaor, Shi Dai, James Dempsey, George Hobbs, Matthew Kerr, Yuri Levin, Richard N. Manchester, Stefan Osłowski, Vikram Ravi, Pablo A. Rosado, Ryan M. Shannon, Renée Spiewak, Willem van Straten, Lawrence Toomey, Jingbo Wang, Linqing Wen, Xiaopeng You, and Xingjiang

- Zhu. Gravitational-wave cosmology across 29 decades in frequency. *Phys. Rev. X*, 6:011035, Mar 2016.
- [180] R. M. Shannon et al. Gravitational waves from binary supermassive black holes missing in pulsar observations. *Science*, 349(6255):1522–1525, 2015.
- [181] Gianpiero Mangano, Gennaro Miele, Sergio Pastor, Teguyco Pinto, Ofelia Pisanti, and Pasquale D. Serpico. Relic neutrino decoupling including flavor oscillations. *Nucl. Phys.*, B729:221–234, 2005.
- [182] Luca Pagano, Laura Salvati, and Alessandro Melchiorri. New constraints on primordial gravitational waves from Planck 2015. *Phys. Lett.*, B760:823–825, 2016.
- [183] P. Binetruy, A. Bohe, T. Hertog, and Daniele A. Steer. Gravitational Wave Bursts from Cosmic Superstrings with Y-junctions. *Phys. Rev.*, D80:123510, 2009.
- [184] P. Binetruy, A. Bohe, T. Hertog, and Daniele A. Steer. Proliferation of sharp kinks on cosmic (super-)string loops with junctions. *Phys. Rev.*, D82:083524, 2010.
- [185] P. Binetruy, A. Bohe, T. Hertog, and D. A. Steer. Gravitational wave signatures from kink proliferation on cosmic (super-) strings. *Phys. Rev.*, D82:126007, 2010.
- [186] Kipp Cannon, Chad Hanna, and Jacob Peoples. Likelihood-Ratio Ranking Statistic for Compact Binary Coalescence Candidates with Rate Estimation. 2015.
- [187] Albert Einstein. Über Gravitationswellen. *Sitzungsber. Preuss. Akad. Wiss. Berlin (Math. Phys.)*, 1918:154–167, 1918.
- [188] Albert Einstein and N. Rosen. On Gravitational waves. *J. Franklin Inst.*, 223:43–54, 1937.
- [189] H. Bondi, F. A. E. Pirani, and I. Robinson. Gravitational waves in general relativity. 3. Exact plane waves. *Proc. Roy. Soc. Lond.*, A251:519–533, 1959.
- [190] Karl Schwarzschild. On the gravitational field of a mass point according to Einstein’s theory. *Sitzungsber. Preuss. Akad. Wiss. Berlin (Math. Phys.)*, 1916:189–196, 1916.
- [191] H. Reissner. Über die eigengravitation des elektrischen feldes nach der einsteinischen theorie. *Annalen der Physik*, 355(9):106–120, 1916.
- [192] G. Nordström. On the energy of the gravitational field in einstein’s theory. *Verhandl. Koninkl. Ned. Akad. Wetenschap., Afdel. Natuurk., Amsterdam.*, 26:1201–1208, 1918.

- [193] Peter R. Saulson. Josh Goldberg and the physical reality of gravitational waves. *Gen. Rel. Grav.*, 43:3289–3299, 2011.
- [194] R. Balasubramanian, B. S. Sathyaprakash, and S. V. Dhurandhar. Gravitational waves from coalescing binaries: Detection strategies and Monte Carlo estimation of parameters. *Phys. Rev.*, D53:3033–3055, 1996. [Erratum: *Phys. Rev.*D54,1860(1996)].
- [195] J. Aasi et al. Constraints on cosmic strings from the LIGO-Virgo gravitational-wave detectors. *Phys. Rev. Lett.*, 112:131101, 2014.
- [196] B. P. Abbott et al. First LIGO search for gravitational wave bursts from cosmic (super)strings. *Phys. Rev.*, D80:062002, 2009.
- [197] B. P. Abbott et al. GW150914: First results from the search for binary black hole coalescence with Advanced LIGO. *Phys. Rev.*, D93(12):122003, 2016.
- [198] Leo P. Singer. *The needle in the hundred square degree haystack: The hunt for binary neutron star mergers with LIGO and Palomar Transient Factory*. PhD thesis, Caltech, 2015.
- [199] T. Accadia et al. Virgo: a laser interferometer to detect gravitational waves. *JINST*, 7:P03012, 2012.
- [200] W.H. Press, S.A. Teukolsky, W.T. Vetterling, and B.P. Flannery. *Numerical Recipes: The Art of Scientific Computing*. Cambridge University Press, 3 edition, 2007.
- [201] N. Aghanim et al. Planck 2018 results. VI. Cosmological parameters. 2018.
- [202] K. Aylor et al. A Comparison of Cosmological Parameters Determined from CMB Temperature Power Spectra from the South Pole Telescope and the Planck Satellite. *Astrophys. J.*, 850(1):101, 2017.
- [203] F. R. Bouchet, P. Peter, A. Riazuelo, and M. Sakellariadou. Is there evidence for topological defects in the BOOMERANG data? *Phys. Rev.*, D65:021301, 2002.
- [204] Christophe Ringeval. Fermionic massive modes along cosmic strings. *Phys. Rev.*, D64:123505, 2001.
- [205] David P. Bennett and Francois R. Bouchet. HIGH RESOLUTION SIMULATIONS OF COSMIC STRING EVOLUTION: PART 1. NUMERICS AND LONG STRING EVOLUTION. PART 2. SMALL SCALE STRUCTURE AND LOOPS. In *Nuffield Workshop: Symposium on the Formation and Evolution of Cosmic Strings Cambridge, England, July 2-7, 1989*, pages 0321–386, 1990.

**Titre :** Recherche d'ondes gravitationnelles produites par des cordes cosmiques dans les données de LIGO-Virgo

**Mots clés :** Ondes gravitationnelles, cordes cosmiques, Virgo, LIGO.

**Résumé :** Cette thèse présente les résultats de la recherche de signaux d'ondes gravitationnelles produits par des cordes cosmiques dans les données des deux premières périodes d'observation des détecteurs de seconde génération Advanced LIGO et Advanced Virgo. Les cordes cosmiques sont des défauts topologiques unidimensionnels créés dans l'Univers primordial. Ces objets sont prédits par de nombreux modèles de physiques de très hautes énergies. La forme attendue du signal d'ondes gravitationnelles émis par des cordes cosmiques est prédite par la théorie. On utilise une technique de filtrage optimal pour rechercher la présence d'un signal dans les données des détecteurs Advanced LIGO et Advanced Virgo.

Cette technique est optimale si le bruit du détecteur est gaussien et stationnaire, ce qui n'est pas le cas. Une partie essentielle du travail de thèse a consisté à comprendre et réduire le bruit de fond de l'analyse. Ce travail sur la qualité des données a permis d'augmenter la sensibilité de la recherche. De plus on montre que la recherche de signaux transitoires d'ondes gravitationnelles produits par des cordes cosmiques est limitée par la présence d'une famille particulière de bruits qui miment le signal prédit pour les cordes cosmiques.

En l'absence de détection, nous avons placé des limites sur les paramètres qui caractérisent un réseau de cordes cosmiques pour différents modèles théoriques, afin de préciser les conditions d'existence de ces dernières.

**Title :** Searching for gravitational waves produced by cosmic strings in LIGO-Virgo data

**Keywords :** Gravitational waves, cosmic strings, Virgo, LIGO.

**Abstract :** This thesis shows the results of the search for gravitational-wave signals produced by cosmic strings using the data from the first two observation runs of the second generation detectors Advanced LIGO and Advanced Virgo. Cosmic strings are one-dimensional topological defects created in the primordial Universe. These objects are predicted by many models of very high energy physics. The gravitational-wave signal emitted by cosmic strings is predicted by theory. A matched-filter analysis is used to search for the presence of a signal in Advanced LIGO and Advanced Virgo data. This technique is optimal if the detector noise is Gaussian and stationary, which is not the case. An essential part of the thesis work was to understand and reduce the background noise analysis.

This work on data quality has increased the sensitivity of the search. Furthermore, we have shown that the search for transient signals of gravitational waves produced by cosmic strings is limited by the presence of a particular family of noises that mimic the predicted signal for cosmic strings.

In the absence of detection, we have placed constraints on the parameters which characterize a cosmic string network for different theoretical models, in order to specify the conditions of their existence.

